The Dense Interstellar Medium and Star Formation across the Nearby Galaxies NGC 3627 and NGC 253

Ivana Bešlić

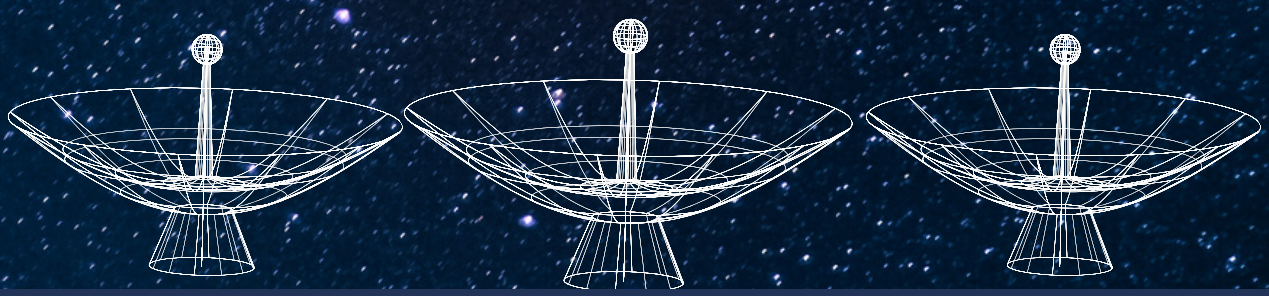

The dense interstellar medium and star formation across the nearby galaxies NGC 3627 and NGC 253

Dissertation
zur
Erlangung des Doktorgrades (Dr. rer. nat.)
der
Mathematisch-Naturwissenschaftlichen Fakultät
der
Rheinischen Friedrich-Wilhelms-Universität Bonn

von
Ivana Bešlić
aus
Obrenovac, Serbien

Bonn, 05.08.2022

Angefertigt mit Genehmigung der Mathematisch-Naturwissenschaftlichen Fakultät der Rheinischen Friedrich-Wilhelms-Universität Bonn

1. Gutachter:	Prof. Dr. Frank Bigiel
2. Gutachter:	Prof. Dr. Karl Menten
Tag der Promotion:	18.10.2022
Erscheinungsjahr:	2023

Mojoj porodici,
hvala vam na podršci.

Abstract

The star formation process is an essential aspect of galaxy evolution. Observations of star-forming regions from sub-pc to kpc scales revealed a tight correlation between star formation and the emission of high-critical density molecules (HCN, HNC and HCO^+). However, it is still unclear whether stars can form in regions where gas is overall denser or whether this gas is notably more efficient at producing stars. The missing piece in the star formation puzzle lies in understanding the properties of dense molecular gas at giant molecular cloud scales. Compared to the CO emission, high-critical density lines are faint, making them difficult to detect and approaching the sensitivity limits of current observing facilities. Despite recent major efforts to map molecular emission traced by the CO molecule at cloud scales, we still lack an equivalent study of high-critical molecular lines at these scales, covering a set of environments across nearby galaxies.

In this doctoral thesis, we expand the previous efforts in recent extragalactic studies to bridge the gap between our knowledge of star formation in the Milky Way and across unresolved systems at high redshifts. This study presents the first attempt to constrain the role of dense molecular gas at a few hundred pc and its relation to star formation across two nearby galaxies, NGC 3627 and NGC 253, using observations of high-critical density molecular lines within the 3 mm regime obtained by NOEMA and ALMA.

The major results of this doctoral thesis are that the intensity ratio of high-critical density lines (i.e. HCN) to the CO(2–1) appears sensitive to molecular cloud surface density changes, which makes them an excellent tool for constraining the density contrast. In studying the star formation efficiency of dense molecular gas, we found that environmental conditions play a crucial role. For example, the centres of NGC 3627 and NGC 253 contain the largest amount of dense molecular gas, yet their star formation efficiency is significantly reduced, whereas we found more efficient gas in other regions of these galaxies, such as in the bar ends, ring and spiral arms. Our results could be a result of the kinematics of dense molecular gas playing a critical role in setting the ability of gas to form stars. The complex kinematics observed in the centre and bar of NGC 253 show that it can significantly decrease this dense gas star formation efficiency while converging dense gas flows can further enhance the star formation process, as seen in the bar ends of NGC 3627.

The results presented in this doctoral thesis further support the importance of understanding the properties of dense molecular gas in nearby galaxies. Together with the turbulent theory of star formation, the emission of these high-critical density lines relative to the mean gas densities and the role of the environment are essential drivers of local star formation at scales of molecular clouds. This work outlines the importance of obtaining a clearer picture of the dense interstellar medium, which is the major contributor to the baryon cycle of galaxies that ultimately dominates their cosmic evolution.

Contents

CHAPTER 1

Interstellar medium

"*The Interstellar Medium is anything not in stars.*"
D. Osterbrock [1984 Jan 13 – author's UCSC course notes]
taken from "Interstellar and Intergalactic medium", by R. Pogge

The interstellar medium (ISM) is a stunning constituent that fills the space between stars in galaxies. The ISM consists of gas, relativistic particles, and fields. Remarkable phenomena, some of them not yet fully understood, are discovered in the ISM. For example, the ISM is the place where stars are born, evolve and die. Particles accelerate in the ISM, reaching relativistic velocities and enormous energies. Strong shocks produce multiple ionization states of atoms. The low temperature of the cold ISM allows the formation of complex organic molecules, while several molecular emission lines get enhanced, which produce masers (e.g. OH). In the low-density medium like in the ISM, specific physical conditions are suitable for the existence of forbidden transitions of atoms and molecules.

Because of the constant cycling of matter through star formation, stellar evolution and feedback mechanisms, the ISM is an essential aspect of understanding galaxy evolution, from high redshift objects shortly after the Big Bang until the present day. The majority of the physical conditions in the ISM cannot be reproduced in laboratories on Earth. Therefore, much of our knowledge of the ISM comes from observing the electromagnetic radiation of its constituents.

This chapter is about the interstellar medium. We provide a brief description of its discovery in Section 1.1, and an overview of its constituents in Section 1.2. Next, we will mention the models describing the ISM in Section 1.3. In this section, we will also give an overview of each gas phase and their properties. Then, we will focus on the molecular gas, how to observe it, and molecular clouds in Section 1.4. The following section, Section 1.5 is about the dense molecular gas phase, which is the main scope of this doctoral thesis. Section 1.6 highlights the importance of the ISM in the baryon cycle, which regulates galaxy evolution. Finally, we briefly mention the galaxy classification and their structure in Section 1.7. If not stated otherwise, the majority of this chapter is based on the books Draine (2011); Tielens (2005); Vukićević-Karabin & Atanacković (2010), and reviews of Kennicutt & Evans (2012); Girichidis et al. (2020); Saintonge & Catinella (2022).

1.1 Historical perspective

The concept of the ISM did not entirely exist before the 20th century. Before the discovery of nebulae in the 19th century by the German family Herschel[1], it was widely believed that the space between stars was a vacuum. Nebulae are faint, irregularly shaped, diffuse patches on the sky. Initially, it was thought that nebulae are located in our Galaxy, yet more accurate measurements of distances toward astronomical objects revealed that several nebulae lie far beyond the boundaries of the Milky Way. This discovery paved the way for extragalactic astronomy and marked a major turning point in understanding the Universe.

The existence of absorbing media along the line of sight, initially suggested by F. G. W. Struve, was subsequently presented further in the studies of Hartmann and R. Trumpler. Their discoveries laid the groundwork for the concept of the ISM. Hartmann observed narrow absorption features of ionized Ca, K and H lines, in the stellar spectrum of a spectroscopic binary star, δ Orionis, located in the Orion belt. Unlike the spectral lines originating from the star, whose properties reflected the stellar rotation, the K and H lines remained stationary and narrow. Therefore, Hartmann concluded that ionized Ca lines must come from the colder, lower-density medium. In addition, R. Trumpler observed open stellar clusters in 1930. He studied how different methods for deriving distances of the open clusters impact the observed results. In particular, he compared distances derived from the luminosity of stellar clusters and from the assumption that they have the same size and found a discrepancy. The distances calculated from the measured luminosities were significantly lower, which yielded that there must be a medium that absorbs the light.

We now know that the first representations of the ISM at that time were significantly different from today. At first, the ISM was seen as a homogeneous material distributed in the Galaxy. The efforts toward conducting high-resolution spectroscopic measures in the 1930s revealed the clumpy nature of the ISM. Moreover, observations found that the ISM consists of gas, dust, cosmic rays, and fields. The physical conditions describing the ISM, like gas densities and temperatures, are so extreme that it is impossible to reproduce them in the laboratories on Earth. Therefore, to improve our understanding of the ISM, it is crucial to observe its features, which is a challenging task since some of these are difficult to detect. The joint efforts in developing the observing techniques, particularly at radio wavelengths, building bigger telescopes to achieve higher spatial resolutions, and more sensitive receivers to detect the faintest radiation significantly contributed to getting a more complete picture of the ISM.

In the last century, we developed a picture of how the ISM looks, how its components are linked, and the nature of the main physical processes. We gained significant knowledge. We have learned a lot so far. However, the ISM is far from being understood. As said at the end of Draine (2011) textbook: "*Much remains to be learned.*"

1.2 Constituents of the Interstellar medium

This section will list and briefly describe the main constituents of the ISM. As stated in the previous section, the ISM is an inhomogeneous medium with extreme physical conditions. Temperatures can range from close to absolute zero, to very hot gas with temperatures of tens of thousands of K. The densities we find in the ISM are so low that these are considered vacuum compared to terrestrial conditions. For example, the average density of the ISM is $\sim 1\,\mathrm{cm}^{-3}$, 10^{-20} times lower than the

[1] William Herschel, a well-known German astronomer, his sister Caroline and his son John.

density of Earth's atmosphere near sea level! Considering everything is made of baryonic matter that we find between stars and black holes in galaxies, the ISM consists of gas, particles and fields.

Interstellar gas

The total gas mass in the ISM in the Milky Way is around $M_{\rm gas} = 10^{10}\,{\rm M}_{\odot}$ (Kalberla & Kerp, 2009). The most abundant element in the Universe, hydrogen, is the main building block of the ISM. By mass, H occupies 67%, He 31%, and the rest of the elements−metals, only 2% (Draine, 2011). All chemical elements in the Periodic Table after H and He are called metals in astronomy. Light elements, like C, N and S, are in the gas phase, whereas heavier ones, like Si and Fe, are locked up in the dust grains. Interstellar gas shows a wide range of physical conditions, characterized by a range of temperatures (T), densities (n), and the ionization fraction. Therefore, we observe three gas phases: atomic, ionized and molecular. Each of these phases is unique and has its characteristic heating and cooling mechanisms, energy source, dominant radiation, and part of the electromagnetic spectrum in which we observe its radiation. Interstellar gas plays the main role in regulating the evolution of a galaxy and the cycle of baryonic matter (Section 1.6). We describe each gas phase in Sections 1.3.1-1.4.

Interstellar particles

Interstellar particles are in the form of dust grains and cosmic rays (CRs), and their in the ISM is essential. Dust grains absorb and scatter stellar radiation, causing interstellar extinction. The absorbed stellar light heats the dust grains, and they re-emit at longer wavelengths in the infrared (IR), revealing the obscured parts of the Universe hidden in the optical domain. The grain surface is crucial for the formation of molecules but also to "lock" (freeze) heavier elements, causing their depletion. We will describe dust properties in more detail in Section 1.3.3.

Austrian-American physicist V. F. Hess discovered CRs in 1912, for which he won the Nobel prize in physics in 1936. CRs are protons, and atomic nuclei accelerated in an explosion of supernovae (SNe), stellar winds, or active galactic nuclei (AGN) to relativistic energies (from 0.1 eV to 10 GeV). The most energetic CRs leave the Galaxy. The overall flux of CRs is weak, isotropic, and can be described with a power-law. The energies of CR can have several orders of magnitude. However, the significant impact on the interstellar gas comes from the low-energy CRs (<100 MeV), while a few MeV CRs collide with dust.

Interstellar fields

The ISM fields distribute throughout the gas and particles. We observe three fields: radiation, magnetic and gravitational fields. They shape the morphology of the ISM. The radiation field contains stellar light, thermal emission from dust, free-free emission of electrons, and the cosmic microwave background (CMB) radiation. These can be explained by the emission of a black-body, which is described with Planck's function, which means that its spectrum is completely determined by its temperature. In addition to thermal sources of radiation, non-thermal radiation, such as the synchrotron emission, caused by the change in the motion of a charged particle in the presence of magnetic field, is also an important contributor.

Historically, the first evidence of the presence of magnetic fields in the ISM came from observations of polarized starlight by Hall and Hiltner (Hall, 1949; Hiltner, 1949) in 1949. Beside the polarization effects, the synchrotron radiation and the Zeeman splitting of some spectral lines (e.g. H and OH) are

indicators of the existence of magnetic fields in the ISM. The magnetic field in galaxies is generally weak. We observe two distinct, equally strong components of the magnetic field in the Milky Way. The first component follows the spiral arm features whereas the second one is chaotic. However, we still do not know the origin of the magnetic field, and observing it remains challenging.

Everything we observe in the Universe moves due to the gravitational potential caused by other objects. Gravity is essential in the densest part of molecular gas since self-gravity leads to star formation, which is one of the focuses of this doctoral thesis. It is worth noting that recent discoveries in the field of gravitational astronomy are fundamental and deserve a brief description here. I. Newton first presented a theory of gravity in the 16th century, changing our perspective on nature. At the beginning of the 20th century, A. Einstein generalized the idea of the gravitational interaction in the general theory of relativity, in which gravity disturbs and shapes the geometry of space-time, further affecting the motion of everything we see. However, the first observational supports of the general theory of relativity were a few decades later. R.A. Hulse and J. H. Taylor won the Nobel prize in physics for observations of binary pulsars in the 1990s. Since the gravitational field is relatively weak, detecting gravitational waves remained challenging as it required observations of highly massive, relativistic objects (e.g. black holes) with very high precision to catch the disturbances in space-time. The first detection of gravitational waves was made in 2015 by the Laser Interferometer Gravitational-Wave Observatory (LIGO - Abbott et al., 2007, 2016), and it was produced in the collision of two black holes. This discovery made a step toward observing the Universe not just in the light but also in the gravity domain.

1.3 Models of the Interstellar medium

It is challenging to properly describe and model the ISM because of its complexity. Modeling the ISM requires considering several processes and components, but in reality we need simplistic approaches and a variety of assumptions. There are many models and attempts trying to describe the ISM. In this section we will mention two models of the ISM. Field et al. (1969) presented a two-phase model of the ISM in which the ISM is made of gas in two phases: the cold neutral (CNM) and the surrounding warm neutral medium (WNM). In this model, the hydrogen is in its atomic state, whereas other elements (e.g. C, S, Si) are primarily ionized because they have lower ionization potentials than the hydrogen atom (13.6 eV). The coexistence of two gas phases stems from the pressure equilibrium. Regions of lower temperatures will be denser (the CNM), as opposed to the warmer medium (WNM). The down-side of this model is that it does not account for SNe explosion, which is a significant source of mechanical energy in the ISM. Therefore, the two-phase ISM fails to explain the origin of high ionization states of oxygen (O VI[2]) in the ISM. In addition, the two-phase model is unstable on timescales of 10 Myr.

The importance of the two-phase model is that it sets the base for the three-phase model, known as the McKee&Ostriker model (McKee & Ostriker, 1977). In this representation of the ISM, the presence of SNe and their energy input is included (Figure 1.1). Besides the CNM and WNM, McKee & Ostriker (1977) introduced the hot ionized medium (HIM) as the third phase, whose existence was predicted by Spitzer in the middle of the 20th century. Such hot ionized gas originates from SNe and is not in equilibrium. The HIM has a very long cooling time (10^9 yr), especially compared to the timescales between the SNe events (around half a century). The HIM is distributed throughout the halo of the galaxy, whereas the CNM and WNM are embedded in the HIM and located in the lower

[2] O VI means that the oxygen is 5 times ionized.

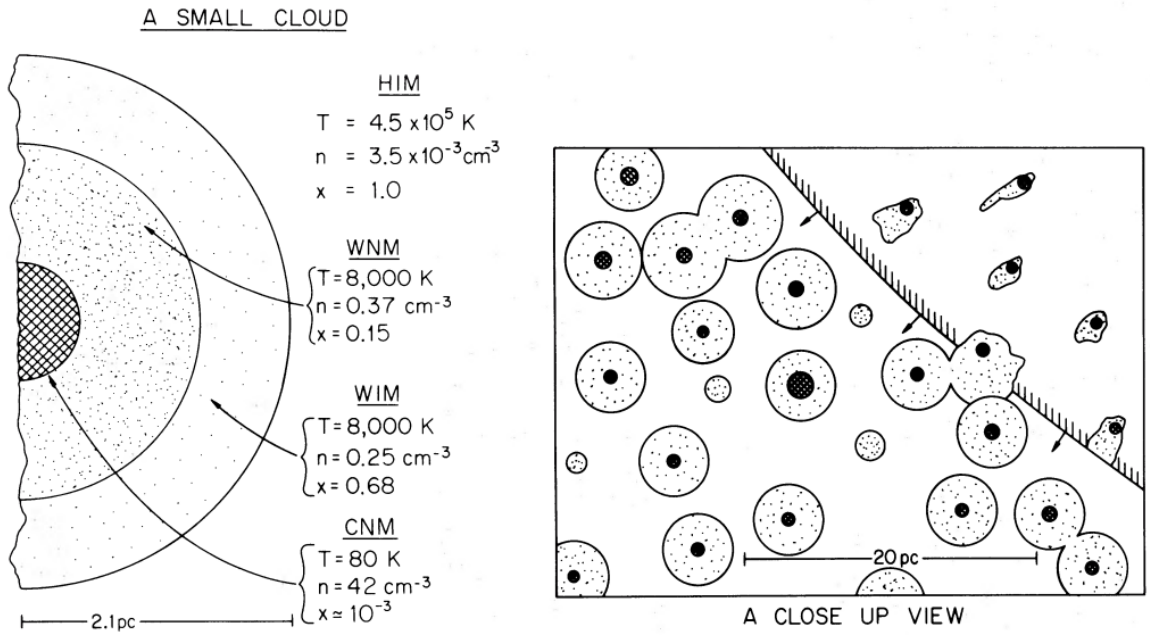

Figure 1.1: Illustration of the McKee&Ostriker three-phase model of the ISM is taken from the McKee & Ostriker (1977). The left panel shows a cross-section of a small cloud. We see different phases moving from the inside of the molecular cloud to its surface. The smallest circle shows the core of a cloud filled with the cold neutral medium, surrounded by the warm neutral medium (the following shell), and finally, the hot ionized medium. A small-scale ISM is shown on the right panel. The area of each feature is scaled to the filling factor, and the shade represents a range of densities: from low-density medium (brighter shade) to denser (darker shade) parts. The upper right side of this panel shows the supernova explosion and its impact on the surrounding matter.

halo. The CNM consists of dense clouds of gas in atomic state, surrounded by the WNM and WIM (left panel in Figure 1.1).

In addition to atomic gas, the CNM contains the denser phase, molecular gas, although it has different properties than atomic gas. In the following sections, we will describe all the phases of the ISM and provide information on their characteristics, temperature, density, and the filling factor. We will mention specific tracers, the leading heating and cooling mechanisms, in what part of the EM spectrum we observe each phase and what type of emission it is: continuum or spectral lines (emission or absorption). Figure 1.2 shows an example of a multi-wavelength image of the Milky Way disc and the distribution of various components of the ISM.

1.3.1 Hot coronal gas

This phase of the ISM takes up large part of the volume (80-90%), and it is the hottest ISM phase ($T \approx 10^6$ K). It was named coronal gas, after the Sun's corona, because they have similar temperatures and ionization conditions. More generally, it is called the hot ionized medium. The HIM consists of gas shocked to high temperatures, where some atoms are ionized multiple times. This phase is in the form of loops, bubbles and fountains, also present in the solar neighbourhood. In particular, the solar system is in the Local Interstellar cloud, which lies in the Local Bubble (or Local Cavity), a broad structure (92 pc in size), originating from a SNe a few tens of millions of years ago. In a galaxy, the

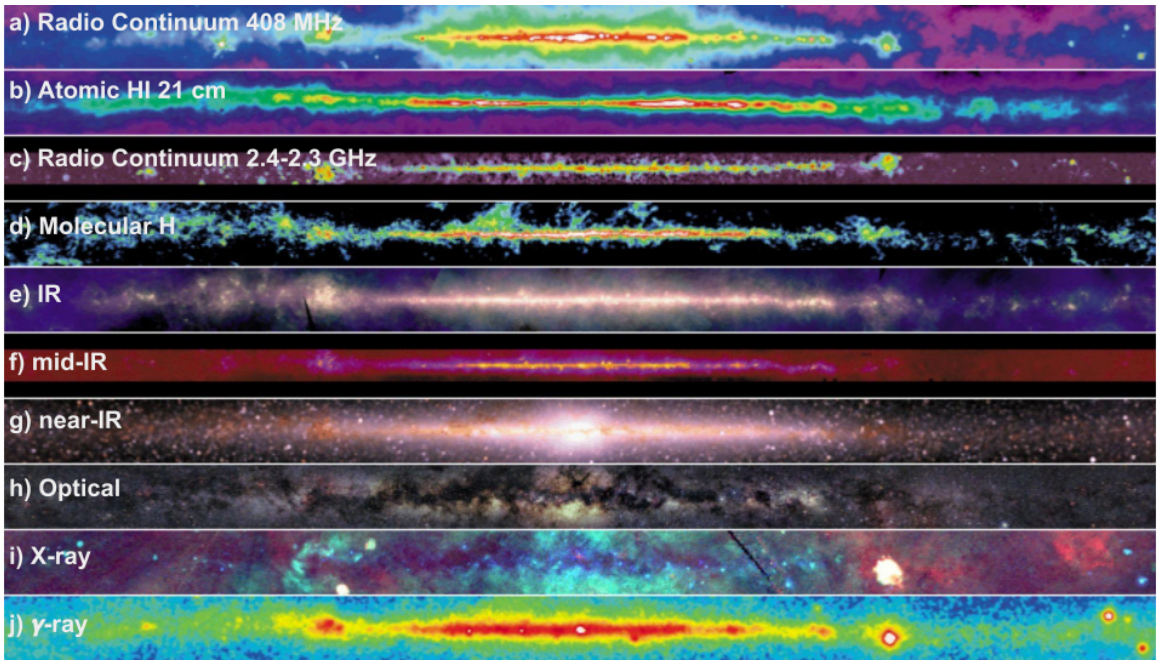

Figure 1.2: Images of the Milky Way observed at different wavelengths. It is striking that our Galaxy does not look the same in each domain of the electromagnetic spectrum. Each panel reveals a complex structure and distribution of different ISM components and stars. a) shows radio continuum at 408 MHz (Haslam et al., 1982), b) distribution of atomic HI (Burton, 1985; Kerr et al., 1986; Hartmann & Burton, 1997), c) radio continuum emission from Furst et al. (1990); Reich et al. (1990); Duncan et al. (1995). Panel d) distribution of molecular hydrogen (Dame et al., 2001), e) IR image from Wheelock et al. (1994), f) mid-IR image (Price et al., 2001), and g) in near-IR (Hauser, 1995). Optical image is shown in panel h) (Mellinger, 2000). High-energy view of Milky Way is in panels i) and j) showing X-ray (Snowden et al., 1997) and γ-ray maps (Hunter et al., 1997; Hartman et al., 1999), respectively. Credits: this webpage.

HIM is mainly in the halo, but it is also found in the disc (see panel i) in Figure 1.2). Interestingly, the space between galaxies (the intergalactic medium - IGM) is filled with hot coronal gas, which is observed in galaxy clusters via X-ray emission.

The HIM is a result of production of hugely energetic processes at the final stages of stellar evolution. Stars with intermediate masses ($M \approx 8\,\mathrm{M}_{\odot}$) end their life in the explosion of supernovae. After the supernova explosion, a neutron star remains where the star was, and the supernova remnant (SNR) is in the surroundings. In such a scenario, the upper layers of the stellar atmospheres are ejected, causing a shock wave (see Figure 1.3). Such shocks mechanically heat and collisionally ionize the surrounding gas. As a result, the gas reaches extreme temperatures and expands due to the shock causing rapid changes in the physical conditions. Therefore, the timescales over which this phase cools are very long. The cooling happens through adiabatic expansion and X-ray emission.

We observe the HIM through the absorption features of five times ionized oxygen (OVI at 103 nm) and nitrogen, and in synchrotron emission. Unfortunately, this phase is only observable from space telescopes, as the Earth's atmosphere is blocking light at these small wavelengths (Chapter 2, Section 2.1). The Chandra X-ray Observatory, ROSAT (Röntgensatellit), and NASA's Far Ultraviolet Spectroscopic Explorer (FUSE) satellite observed hot gas in the ISM.

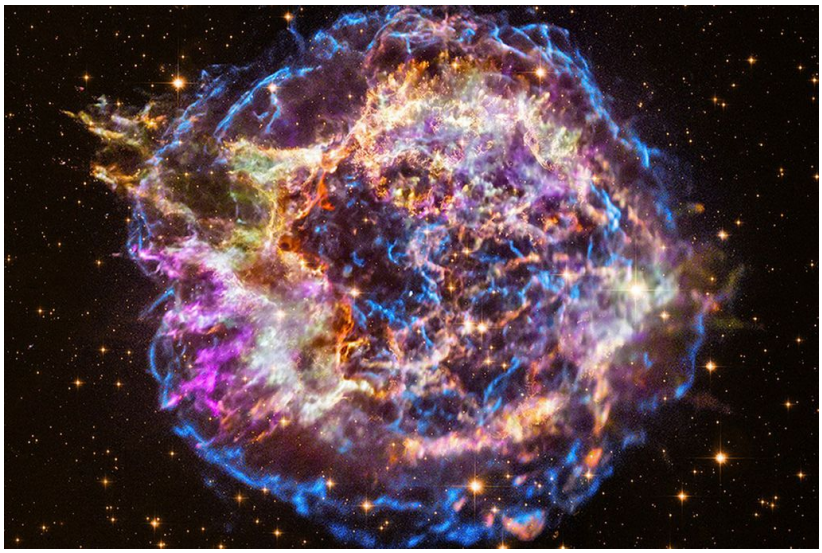

Figure 1.3: Supernova remnant Cassiopeia A, located in the Cassiopeia constellation at a distance of around 3.4 kpc. This object is the youngest SNR found in the Milky Way so far, and it was produced 400 years ago due to the supernova explosion of a star ~ 20 times more massive than our Sun. This supernova event was exactly the last one observed from Earth by the naked eye. Image credits: NASA/CXC/SAO; NASA/CXC/E.Jiang

1.3.2 Ionized medium

Ionized gas consists mainly of ionized hydrogen and takes up the majority of the volume in a galaxy (Haffner et al., 2009), although only 25% of the total mass of the ISM is in this phase. Hoyle & Ellis (1963) observed the ionized gas through absorption lines originating from the Galactic synchrotron emission. The presence of the ionized gas in the ISM is detected indirectly via the dispersion of radio emission from pulsars (Reynolds, 1989; Gaensler et al., 2008). In addition, observations of emission lines of ionized oxygen and hydrogen in the optical domain (Reynolds et al., 1973; Mierkiewicz et al., 2006) significantly contributed to understanding the properties of the ionized gas.

The ionized medium has temperatures up to 10^4 K. The warm ionized gas phase has two distinct features: a lower density ($n = 0.3\,\mathrm{cm}^{-3}$) diffused ionized gas, where the gas is collisionally ionized, and the denser medium ($\sim 10^4\,\mathrm{cm}^{-3}$) of ionized H, also known as HII regions. Young O and B stars, whose strong ultra-violet (UV) radiation field ionizes the surroundings, produce the HII regions. In addition, we consider planetary nebulae (PNe) and supernova remnants (SNR) part of this phase. PNe are the remains of the upper atmospheric layers of stars with low stellar masses ($<3\,M_\odot$)[3], a product of stellar expansion at the late stages of its evolution. SNRs are a product of much more energetic processes from massive stars, as explained in Section 1.3.1.

The photoionization of UV photons with wavelengths lower than 91.2 nm is the primary mechanism for the ionization of the gas. The ionized hydrogen reaches its atomic state by capturing one of the electrons. Such an atom will be in its excited state since the electron will be at one of the upper levels, which will move to the lower-energy levels. This process of converting the UV light to the combination of the optical photons from the follow-up de-excitations is called fluorescence. Photoelectrons from

[3] This is precisely the future of our Sun: after it burns all hydrogen into helium, its core will start collapsing and heating until helium starts burning. The upper layers of the solar photosphere will expand a few times in radius. In the end, the Sun will end its life as a white dwarf.

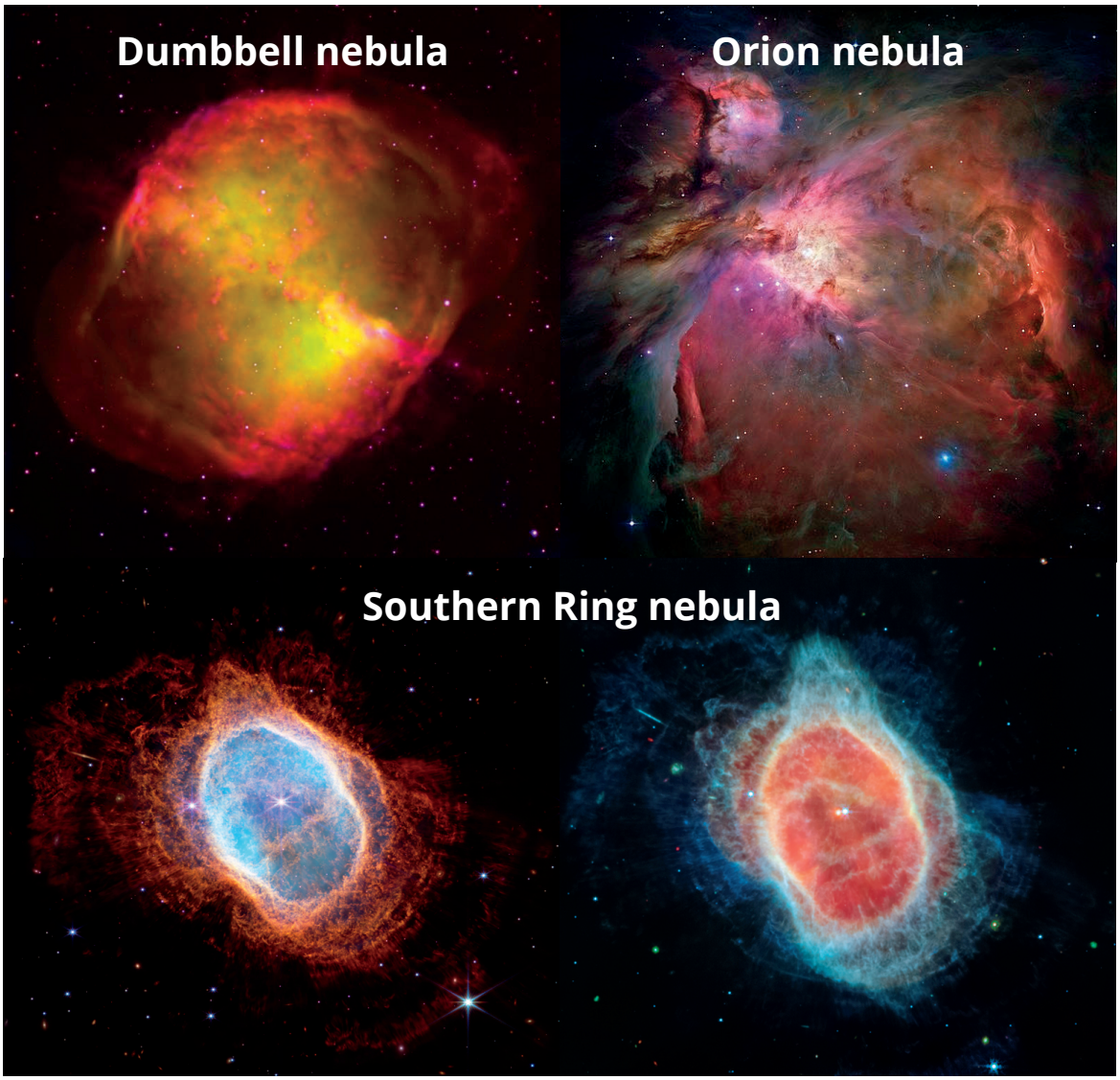

Figure 1.4: Examples of nebulae. The upper left panel shows a planetary nebula, the Dumbbell Nebula (M 27), imaged by the Very Large Telescope (VLT). This object is the first discovered planetary nebula, observed by Charles Messier in 1764. The upper right shows the image of the Orion nebula (M 42), taken by the Hubble Space Telescope (HST). M 42 is an HII region, one of the brightest nebulae in the Milky Way, also visible by the naked eye. The bottom image: planetary nebula, Southern Ring Nebula (NGC 3132) observed by James Web Space Telescope (JWST), released in July 2022. The left image shows emission observed by JWST's Near-Infrared Camera (NIRCam, Bagnasco et al., 2007), whereas the right image shows emission seen using the Mid-Infrared Instrument (MIRI, Kendrew et al., 2015).

H and He heat the gas. The ionized gas cools through the emission lines in the optical domain, fine structure lines, and free-free emission. HII regions are also characterized by the observed "forbidden" lines. Such emission lines are a product of radiative de-excitation of an atom in its metastable state (Osterbrock, 1989). The lifetime of the metastable state is very long in comparison to other excited states of an atom. Since the probability of radiative de-excitation is the inverse of the lifetime of

an excited atom, the probability of radiative de-excitation is very low. This transition can occur in low-density medium, such as the HII regions. So far, there are more than 100 known fine structure lines. One of the typical metastable lines are the from the twice ionized oxygen−OIII (~ 500 nm).

1.3.3 Interstellar dust

Dust is well-mixed with interstellar gas. Although dust contributes only 1% to the total mass of the ISM (Draine & Li, 2007), it plays a significant role in galaxy evolution, gas chemistry, dynamics, and regulating the gas temperatures. Dust particles are crucial for the formation of H_2, and other molecules. In addition, dust grains around young stars contribute to the gas heating, whereas they are the important coolant in the dense gas. A recent review provides an extensive literature summary of the dust emission and its properties in nearby galaxies (Galliano et al., 2018).

The mechanisms of dust production depend on the cosmic scale. In the early Universe, dust was mainly produced in stellar winds from the asymptotic giant branch stars, whereas grain growth in dense molecular clouds became the main production channel in the Local Universe (Triani et al., 2020). Heavy elements, like C, S, Si, and Fe, form dust grains, which explains their depletion in the ISM. Giant molecular species often build the dust grains, and some of these even look like "dirty ice mantels" or show complex molecular structures (e.g. polycyclic aromatic hydrocarbons−PAHs). The size of dust grains can vary from 0.01 to 1 μm, and its distribution is usually described via a power-law function, favouring smaller dust grains (Mathis et al., 1977; Draine & Lee, 1984).

Dust polarizes the stellar radiation, absorbs stellar light, and heats and re-emits electromagnetic radiation at longer wavelenghts. The effect where dust absorbs the stellar emission at shorter wavelengths, mainly in the UV and optical domain, is the "reddening", because stars appear redder. Unfortunately, it is not possible to directly observe each dust grain, but everything we know today about these ISM component comes from studying how dust impacts the stellar light, their emission in IR, characteristic emission bands and theoretical modelling (e.g. Draine & Li, 2007).

The dust emission significantly contributes to the total radiation field of the ISM (panels e)-g) in Figure 1.2) in the form of thermal continuum and emission features. Dust emission in the IR domain reveals obscured regions, invisible in the optical and UV. The development of IR astronomy and telescopes provided pictures of hidden parts of galaxies (see panel h) in Figure 1.2). We show an example of the spectral energy distribution (SED) across the galaxy NCG 3627 (Draine et al., 2007) in Figure 1.5. At sub-mm wavelengths, dust emits a thermal continuum, whereas, at shorter wavelengths, we see the presence of the non-thermal (blackbody-like) emission features. The most prominent one is the bump in the UV domain at 217.5 nm, possibly produced by small graphite, carbon grains (Draine, 1989), or even PAHs. Other strong features are silicate features seen at 9.7 μm and 18 μm. Heger (1922) discovered diffuse interstellar bands from 400 to 900 nm, still not identified. The UV-heated PAHs produce the IR peaks at 3.3, 6.2, 7.7, 8.3 and 11.3 μm.

There are many attempts to construct a proper dust model which can explain all emission features, their chemical composition (silicate or carbonaceous), their size (from small grains to PAHS) and geometry (spherical, non-spherical). A unique dust model cannot explain all observations. Dust models usually consider multiple components and include a contribution from various types of dust grains (Draine & Lee, 1984; Draine, 2009).

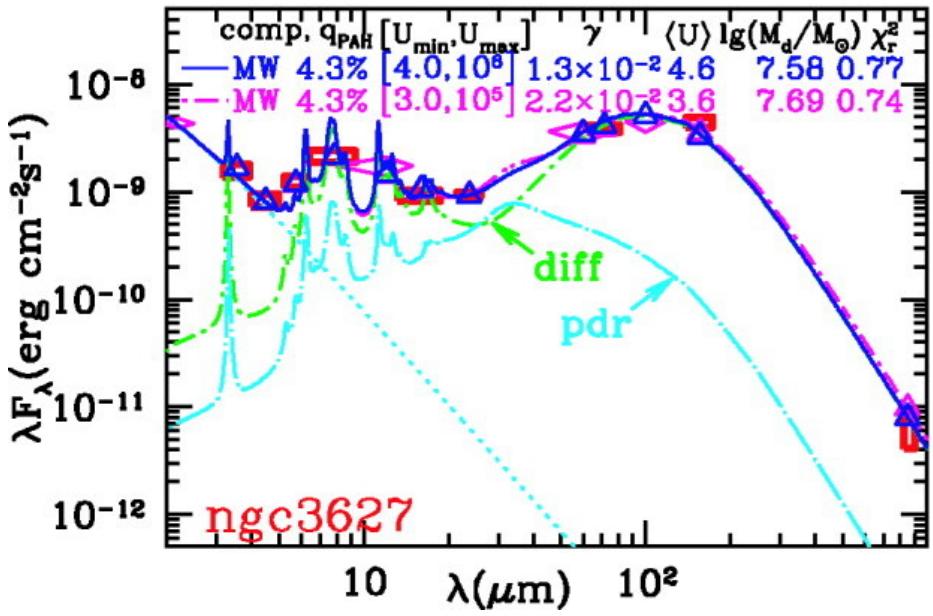

Figure 1.5: The spectral energy distribution of a nearby galaxy NGC 3627 (Draine et al., 2007). We show fluxes measured from the Infrared Array Camera (IRAC), and the Multiband Imaging Photometer (MIPS) from the Spitzer Space Telescope, the Infrared Astronomical Satellite (IRAS) at 12, 60, and 100 μm data, and Submillimetre Common-User Bolometer Array - SCUBA measurements. Fluxes are represented as rectangles and diamonds. The dotted-dashed lines show stellar emission, contribution from diffuse and the dust in photodominated regions.

1.3.4 Atomic phase

Atomic gas mainly consists of neutral hydrogen atoms (HI), while other atoms can be in the ionized state (e.g. C). On the one hand, the atomic phase together with molecular gas take up the majority of the total mass of the ISM. On the other hand, the volume filling factor of atomic gas is low (a few %). Atomic gas has typical densities of 50 cm^{-3}, and temperatures from 80 to 100 K. We see the atomic phase in the form of sheets and filaments, usually located in the outer parts of the galaxy and along spiral arms (Kulkarni et al., 1982). Atomic gas can be warm and cold, and it can be observed in emission (WNM) and absorption (WNM - in the front of bright quasars, and CNM). Warm gas is located in the photodissociation regions at the edges of HII regions.

We observe atomic gas in the well-known HI feature at 21 cm in the radio domain. This line arises from the hyperfine-structure transition of atomic hydrogen, where the electron spin flips from parallel to antiparallel. The HI line at 21 cm can be observed in both emission and absorption. Historically, the discovery of HI was of fundamental importance for studying the ISM and it opened the door to the development of radio astronomy. Observations of atomic hydrogen revealed the presence of large gas structures in the Milky Way ((panel b) in Figure 1.2) Burton, 1985; Kerr et al., 1986; Hartmann & Burton, 1997). The H atom is the most abundant element in the Universe since the Big Bang.

Astronomer van de Hulst theoretically proposed the existence of the HI 21 cm line in 1945 (van de Hulst, 1945). HI contains one electron orbiting around a proton, and their spins are antiparallel in the ground state. This result implies that the change of the electron's spin will emit a photon at the wavelength of 21 cm. However, the event where electron changes its spin is very rare, the transition occurs once every 10^7 years per excited hydrogen atom. Luckily, due to the high abundance of HI, it is

possible to observe this hyperfine transition. The first detection of interstellar atomic hydrogen had to wait until the first radio telescopes (Chapter 2, Section 2.3, 2.4.3) were built. Finally, Ewen and Purcell observed the HI hyperfine transition in the ISM in 1951 for the first time (Ewen & Purcell, 1951).

HI observations are important because they revealed the presence of atomic gas in the ISM. Moreover, the HI data can be used to calculate the total HI flux, total atomic gas mass, and velocity dispersion, even when the observed object is unresolved. Most importantly, HI data can be used to estimate the distance to other galaxies, via the Tully-Fisher relation (Tully & Fisher, 1977).

1.4 Molecular phase

Molecular gas has low temperatures (T = 10−50 K) and densities above $n = 10^3$ cm^{-2}. Similarly as the atomic gas, the molecular phase occupies even much smaller volume fraction but contributes around 30% of the total mass.

Molecules contain from two (diatomic) to several atoms or even aromatic rings (features made only of H and C atoms - PAHs). Atoms are held together via strong chemical bonds. Like atoms, molecules can get into the excited state and emit photons. There are three possible molecular transitions: electronic−caused by electron excitation in the molecule, which requires considerable energies; vibrational−caused by vibration of one of the nuclei and these transitions occur at moderate energies; and rotational transitions produced by nuclei rotation around the centre of mass of the molecule - the lowest energies. In the ISM, we predominantly observe rotational transitions of molecules, located in the mm and radio domains.

The first detected interstellar molecule is the methylidyne radical−CH, discovered by Swings and Rosenfeld in 1938 (Swings & Rosenfeld, 1937). After that, many other molecules in the ISM were discovered in the Milky Way, but also in other galaxies. The first extragalactic molecule, hydroxide (OH), was detected in the 1970s. We observe bright molecular emission even in very distant objects. For example, the furthest object in which astronomers detected molecular emission was at a redshift of $z = 6.42$. Up to the date of writing this doctoral thesis, the total number of detected interstellar molecules is 270 in the Milky Way and 74 within extragalactic sources (The Cologne Database for Molecular Spectroscopy - CDMS (Koeln, 2022); Table 1.1 in Williams & Viti 2013). The majority of detected interstellar molecules contain two atoms (diatomic molecules), with the most complex molecular features observed in the ISM contain more than 12 atoms.

Molecular gas is particularly interesting since their densest part is where star formation occurs (Chapter 3). The most abundant molecule is the hydrogen molecule, H_2. Unlike atomic hydrogen, it is impossible to observe H_2 molecule since its emission occurs only in hot regions. Therefore, observing the H_2 molecule directly will not provide information of the cold molecular gas. We explain this implication in more detail in Section 1.4.1. Fortunately, other abundant and easily observable molecules from Earth nicely trace molecular gas. One of these molecules is carbon monoxide, CO (see Section 1.4.2). The abundance of carbon monoxide scales with the amount of H_2 molecules ($n(H_2)/n(CO) \approx 10^4 - 10^5$), and it is observable in the mm domain.

The molecular gas content in the Milky Way is highly resolved and probed at sub-pc scales (panel d) in Figure 1.2). However, reaching the same physical scales across other galaxies is limited to small regions in the closest and brightest galaxies, while molecular gas remains mainly unresolved in many distant galaxies. The understanding of molecular gas properties is limited towards measuring the brightest molecular lines. Nevertheless, it is still possible to gain significant information by measuring various molecular line emission, because each molecule will originate from different processes, thanks

to the variety of formation and destruction mechanisms. Therefore, different molecular emission will originate from a specific region of a galaxy, and each will be sensitive to different physical conditions, and provide information about the physics and chemistry of the observed region.

The molecular gas is mainly concentrated in the inner parts of a galaxy. It has an inhomogeneous structure and is in the form of giant molecular clouds (GMCs), containing filaments with dense clumps and cores. The GMCs are relatively compact, not spherical, with sizes from a few to 100 pc and masses up to 10^5 $M_\odot$. We will elaborate more on this in Section 1.4.4. In the following, we briefly describe the H_2 molecule, its formation and why it is not easy to observe. Next, we will list and provide the properties of each molecular gas tracer.

1.4.1 Molecular hydrogen

H_2 formation

Several production mechanisms explain the formation of H_2 such as radiative association, ion-neutral collisions or three-body collisions. However, these fail to explain the relative H_2 abundance in the ISM. Therefore, the only production channel that can sufficiently explain the H_2 abundance is the formation of dust grains (Gould & Salpeter, 1963; Hollenbach & Salpeter, 1971). Dust grains act as catalysts in the H_2 formation. Hydrogen atoms are absorbed on the surface of dust grains. They can move along their surface or get trapped. The formation occurs when two hydrogen atoms meet, one trapped on the surface of a dust grain and the other bound with the dust grain. This reaction is exothermic, meaning that it releases energy. Dust grain absorbs part of the energy released in this reaction, while the rest of the energy increases the internal and kinetic energy of H_2. In the final stages, H_2 detaches from the grain surface (Bron et al., 2014). Other processes can further shorten the timescales for H_2 formation, such as the interstellar turbulence (e.g. Clark & Glover, 2014).

The issue of observing molecular hydrogen

The direct detection of H_2 emission in the ISM is far from easy. Eddington first commented on the existence of H_2 molecules in the ISM in 1926. However, the first successful detection of H_2 occurred almost half a century later (Carruthers, 1970). The problem with observing molecular hydrogen stems from its low mass. The energy separation between different states depends on the mass of a molecule as $E \propto m^{-1/2}$. This result implies that the energy levels of a low-mass molecule will be largely separated. Taking this into account, we find the first excited state of H_2 at temperatures of around 500 K. Therefore, to observe H_2 we need to look at the warm gas whose temperatures are high enough to excite H_2. In addition, because H_2 is a symmetric molecule, it has no dipole transitions. Consequently, the H_2 molecule will have two distinct states: the ortho and para-H_2[4]. According to selection rules for molecular transitions, the first allowed transition is quadrupole, which is incredibly faint.

Therefore, even if H_2 is observable, it will be only in the hot gas, such as in reflection nebulae and star-forming regions. We will thus observe H_2 in near-infrared (NIR) emission and towards hot stars in absorption in the UV (i.e. Lyman and Werner bands). In its strictest sense, properties of the H_2 emission will not provide any information about molecular gas. Therefore, observing other

[4] Ortho-H_2 has odd energy states, whereas para-H_2 has even. Based on the selection rules, the transitions from ortho to para-H_2 and vice versa are impossible.

abundant molecules with low rotational energy levels that can get excited at low temperatures typical for molecular gas is necessary.

1.4.2 Carbon monoxide

Other high−J CO transitions provide additional information about the physical conditions of molecular gas, such as the excitation and densities. These lines are commonly observed across galaxies at higher redshift because their observing frequencies shift toward the mm and sub-mm domain. By observing several different J−transitions of the CO emission across a source, we can construct the CO rotational ladder. In addition, a joint study of different CO transitions and emission of its isotopologues, such as ^{13}CO and C^{18}O is used to determine the optical depth of the molecular gas (Jiménez-Donaire et al., 2017a), and also to better understand excitation and chemistry (den Brok et al., 2022a).

1.4.3 The alternative ways of tracing molecular gas

[CII]

Apart from being sensitive to optical depth effects, another downside of using the CO molecule as a molecular gas tracer is that its emission does not probe numerous H_2 regions where the CO abundance is low, ("dark molecular gas"). The other way to trace molecular gas is by using its dominant coolant, the ionized carbon, which also probes dark molecular regions (Pineda et al., 2013). The [CII] line at 158 μm is a fine structure transition, which is bright at lower temperatures and it can be observed everywhere across the galaxy. [CII] emission is found in the envelopes of clouds, where the clouds are in the transition phase between atomic and molecular gas (Pineda et al., 2013). In addition, [CII] traces other phases of the ISM, such as the WIM, the warm and cold diffuse atomic medium, and warm and dense molecular gas. Therefore, using [CII] to trace molecular gas requires using other lines to trace and separate the [CII] contribution to other gas phases.

Dust tracers

Another way to trace molecular gas is to observe dust. Knowing the contribution from atomic gas (e.g. observing HI emission at 21 cm), it is even possible to calculate the amount of molecular gas. The following equations describe the way we use dust emission to constrain the gas mass in galaxies:

$$M_{\rm gas} = M_{\rm dust} \times \delta_{\rm GD}. \tag{1.1}$$

The relationship between gas and dust mass lies in the gas-to-dust ratio ($\delta_{\rm GD}$). A solution to the above equation lies in calculating the dust mass from dust emission and constraining the multiplication factor. On one hand, dust mass can be derived from the dust spectral energy distribution (SED), using various dust models (e.g. Draine, 2011). On the other hand, constraining $\delta_{\rm GD}$ is a challenging task. In general, $\delta_{\rm GD}$ depends on several parameters, particularly the metallicity, Z (e.g. Li et al., 2019). Observations show that the dust-to-gas ratio also varies across galaxies. Since Equation 1.1 can be written as a sum of atomic ($\Sigma_{\rm HI}$) and molecular gas ($\Sigma_{\rm H_2}$) surface densities, solving the Equation 1.1 and using measurements of atomic hydrogen, it is possible to constrain $\alpha_{\rm CO}$ (Bolatto et al., 2013b; Sandstrom et al., 2013).

1.4.4 Molecular clouds

Molecular gas can take the form of giant molecular clouds - GMCs (see Figure 2 in Leroy et al., 2021b). GMCs take a range of masses ($> 10^5$ $M_\odot$), sizes ($R > 20$ pc), temperatures, and densities (e.g. Blitz, 1993). Studying properties of GMCs is important in understanding the physics of molecular gas and mechanisms that regulate star formation (Chapter 3, Section 3.3). The gas density increases as we move towards the inner part of GMCs, where their structure is further organized into clumps and cores, which are the places of current or future star formation (Chapter 3, Section 3.1]). In the following sections, we will describe the mass distribution of the GMC, their properties, and recent results from the cloud-scale surveys of molecular gas.

Mass distribution

The mass distribution of GMCs can be described as a power-law function:

$$\frac{dN}{dM} = \begin{cases} N_u \left(\frac{M_u}{M}\right)^\gamma, & \text{for} \quad M \leqslant M_u \\ 0, & \text{for} \quad M \geqslant M_u. \end{cases} \tag{1.2}$$

In the above equation, N_u is the number of clouds with a mass close to the upper mass threshold, M_u. The value of a slope, γ, depends on the environment. In the inner parts of galaxies where a large amount of molecular gas is present, the slope has values from -2 to -1.5, whereas in systems with low H_2 it is from -2.5 to -2. The value of -2 of the slope marks the threshold between two molecular cloud regimes: the high and low mass clouds. In addition, the mass function of substructures within GMCs (the core mass function - CMF), can be described with both (see Dib et al., 2008, and references therein) a power-law (e.g. Beuther et al., 2004; Enoch et al., 2006) and a log-normal function (Reid & Wilson, 2006; Goodwin et al., 2008; André et al., 2009). We discuss the relation between the CMF and the initial mass function in Chapter 3, Section 3.2.1.

Describing GMCs

We can calculate several parameters to describe the GMC using molecular gas observations. We are particularly interested in knowing a cloud's size, R, its velocity dispersion, σ, and gravitational boundedness. The latter is described using the ratio between the kinetic (T) and gravitational energy (U) of a cloud, also called the virial parameter:

$$\alpha_{\rm vir} = \frac{T}{2U}. \tag{1.3}$$

The factor two comes from the virial theorem, which describes a bound system where kinetic and gravitational energies are equal. A gravitationally stable molecular cloud has $\alpha_{\rm vir} = 1$, whereas molecular clouds that collapse under the free-fall time have $\alpha_{\rm vir} = 2$ (Camacho et al., 2016). The alternative expression for the virial parameter considers a geometry of a cloud. If we assume a spherical geometry of a cloud, the above equation becomes (Bertoldi & McKee, 1992):

$$\alpha_{\rm vir} = \frac{5\sigma^2 R}{GM} \propto \frac{\sigma^2}{\Sigma}. \tag{1.4}$$

Equation 1.4 shows that the virial state of a cloud depends on its velocity dispersion and surface density. In addition, we can derive the turbulent pressure of a cloud:

$$P_{\rm turb} \propto \Sigma \cdot \sigma^2. \tag{1.5}$$

The ISM pressure regulates the properties of GMCs (Hughes et al., 2013). This means that molecular clouds in high-pressure environments will have higher velocity dispersions, which is the case in galaxy centres (Oka et al., 2001). In addition, velocity dispersion of a cloud and its surface density are related as: $\Sigma \propto \sigma^2$ (Heyer et al., 2009).

Larson's laws

To quantify the properties of molecular clouds, Larson analysed various molecular clouds in the Milky Way and proposed three laws to describe them (Larson, 1981). In this study, the properties of a molecular cloud are linked. All Larson's laws are co-dependent and stated as follows:
• **Size-velocity dispersion:** The first relation connects the internal velocity dispersion of a cloud with its size:

$$\sigma \propto R^{0.38}. \tag{1.6}$$

Studies of molecular clouds in the Milky Way (e.g. Solomon et al., 1987; Heyer & Brunt, 2004), and other galaxies (Bolatto et al., 2008) found different value for the power-law exponent: ~ 0.5. Lombardi et al. (2010) showed that molecular clouds have a universal structure, unlike their denser substructures.
• **Velocity dispersion-Mass:** This law describes the relation between the mass of a cloud and its velocity dispersion:

$$\sigma \propto M^{0.2}. \tag{1.7}$$

Equation 1.7 comes from the assumption of a virialized cloud, and observations found that molecular clouds are nearly virialized (Solomon et al., 1997; Bolatto et al., 2008). In such systems, the internal velocity turbulence prevents the cloud from collapsing; therefore, the free-fall timescale for star formation processes will not be dominant (Chapter 3, Section 3.3). The virial parameter of low-massive clouds is significantly higher than 1, suggesting that their existence is supported by strong external pressure. Molecular clouds can have various states besides being gravitationally bound, as pointed out in various observational and theoretical studies. Clouds can be marginally bound, and free-falling objects (Ballesteros-Paredes et al., 2011; Ibáñez-Mejía et al., 2016; Camacho et al., 2016), or their existence can be supported by being in the high-pressure environment (Oka et al., 2001; Field et al., 2011; Hughes et al., 2013; Schruba et al., 2019).
• **Density-size:** The volume density of a cloud is proportional to its radius cubed. Combining Equations 1.6 and 1.7, we get that the mass of a cloud is proportional to the radius by a power of 1.9. The mass density of a cloud is the ratio between the cloud's mass and its volume, which yields:

$$\rho \propto R^{-1.1}. \tag{1.8}$$

The above equation implies that the column density of a cloud must be constant since it is related to its volume density and linear size. Therefore, clouds have surface densities independent of their size (Roman-Duval et al., 2010; Rebolledo et al., 2012). On one hand, Lombardi et al. (2010) showed that molecular clouds do not have constant column density. Measurements of molecular clouds in the Milky Way showed that they have surface densities ranging from 10 to 200 $\mathrm{M_\odot\,pc^{-2}}$ (Heyer et al., 2009). Extragalactic studies showed that the surface density of molecular clouds varies within

the galaxy sample (Hughes et al., 2013; Leroy et al., 2015; Egusa et al., 2018), and across galaxy environments (Colombo et al., 2014).

1.4.5 Molecular emission at GMC scales

PHANGS-ALMA

There is a long list of observations of molecular gas across the Milky Way, local galaxies, nearby galaxies, and high-redshift objects. To probe molecular emission at GMC scales, it is necessary to focus on local and nearby sources. A literature summary of various CO surveys up to date is presented in Leroy et al. (2021b). Many key insights about molecular gas emission come from observing its large-scale ($\sim$ kpc) emission. However, a higher ($\sim$ 100 pc) spatial resolution is needed to resolve GMC structures in galaxies. Many studies focused on mapping galaxies in the Local Group and across the Milky Way. However, we still lack a sample of GMC population across a variety of galaxies. The era of resolving CO(2–1) emission in nearby galaxies at 50 − 100 pc scales started with the Plateau de Bure Interferometer (PdBI), its successor The NOrthern Extended Millimeter Array (NOEMA - Chapter 2, Section 2.5.4), and the Atacama Large Millimeter Array - ALMA (Chapter 2, Section 2.5.5). The most recent huge effort towards providing a comprehensive sample of GMC across an extensive sample of 90 nearby galaxies is made in the Physics of High Angular resolutions across Nearby GalaxieS (PHANGS survey, PI: E. Schinnerer Leroy et al., 2021a,b).

GMC properties

The PHANGS-ALMA CO(2–1) survey provided studies of individual molecular clouds across a sample of 90 galaxies. In Figure 1.6, we show the relation between the velocity dispersion of a cloud and its surface brightness measured at 120 pc resolution across a subsample of 12 galaxies from the PHANGS sample, including additional data from three galaxies: Antennae, M 31, and M 33. To first order, we see that molecular clouds show a large dynamic range in the $\sigma - \Sigma$ plane, particularly in surface densities and turbulent pressures (the bottom right panel in Figure 1.6). Although clouds show a narrow range in virial parameter (bottom left panel in Figure 1.6). GMCs in Antennae are located in the top part of the $\sigma - \Sigma$ plane, whereas sightlines from M 31 and M 33 show higher velocity dispersions than those predicted from surface density based on the $\sigma - \Sigma$ relation (Heyer et al., 2009).

Figure 1.7 shows CO(2–1) sightlines from a sample of 56 galaxies in the $\sigma - \Sigma$ plane at 150 pc scales. Sun et al. (2020) showed that molecular gas properties at GMC scales are environmentally dependent. Galaxy centres show higher molecular gas surface densities than the disc sightlines, even though Sun et al. (2020) showed that gas in the centres is less bound. Even among the centres, there is a prominent separation between galaxies that contain bars and those that do not. Centres of barred galaxies have higher Σ_{H_2} because the stellar bar fuels the centre with gas (e.g. Padoan & Nordlund, 2002b).

1.5 Dense molecular gas

Molecular clouds show complex internal structures characterized by a wide range of densities. Carbon monoxide is a good proxy for the total molecular gas mass, as it is the second most abundant molecule after the hydrogen molecule. However, the CO emission does not provide any information about denser structures of molecular gas because it traces gas densities of 10^3 cm^{-3}. This is where other molecules

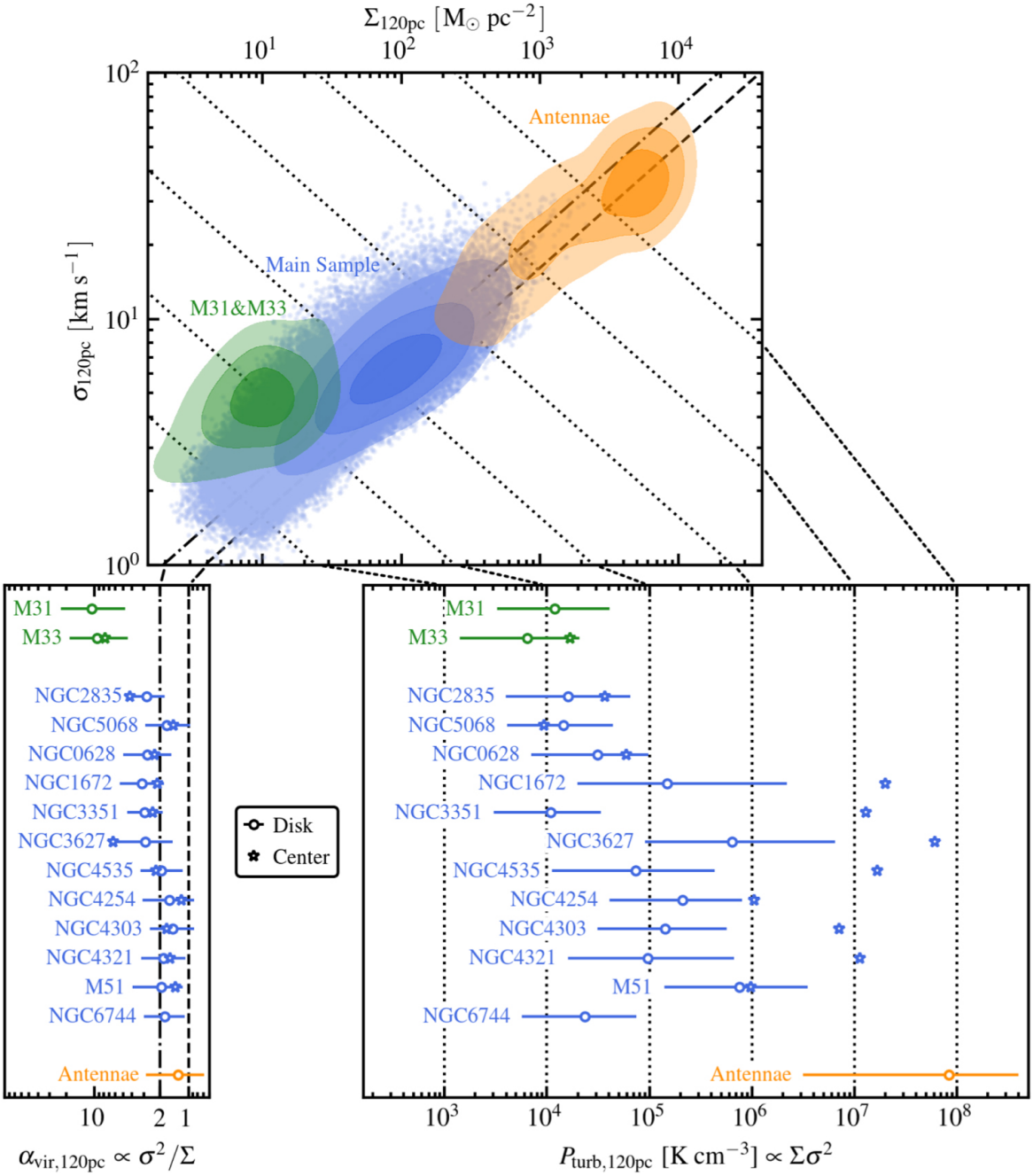

Figure 1.6: $\sigma - \Sigma$ relation of giant molecular clouds measured across a sample of 12 galaxies from the PHANGS survey (Leroy et al., 2021b), including sightlines from Antennae, M 31 and M 33 (Sun et al., 2018). The diagonal dashed line belongs to the virial parameter of 1, whereas the dotted-dashed line shows $\alpha_{vir} = 2$. The dotted lines show constant turbulent pressures.

become important, particularly molecules that show emission at higher gas densities, because they can be used as a tool to constrain the properties of dense molecular gas. In Chapter 3, we will further emphasize the importance of studying such lines since the observed star formation rate in the Milky

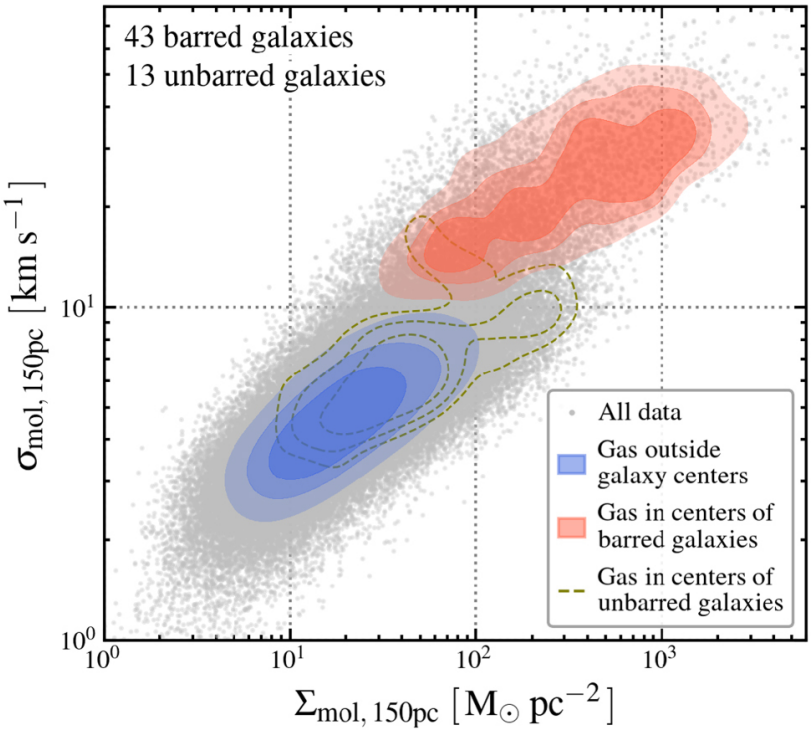

Figure 1.7: $\sigma - \Sigma$ relation of CO(2–1) emission at 150 pc scales across the PHANGS sub-sample of 56 galaxies, 43 of which have strong bars (Sun et al., 2020). All data is shown as grey points. Blue contours indicate sightlines from the galaxies disc. Centres from barred and non-barred galaxies are shown separately as red and brown contours.

Way, but also in other galaxies, shows a strong correlation with their emission (e.g. Gao & Solomon, 2004a), which puts star formation within the densest molecular phase.

The term dense gas tracer has a wide use within the literature. In galactic studies, the term dense gas tracers often refers to diazenylium, N_2H^+, a molecule that emits at densities higher than 10^5 cm^{-3}. The N_2H^+ emission in other galaxies is very faint, making it difficult to detect its emission. Other molecules whose ground transitions are in the range of $3 - 4$ mm are commonly used as dense gas tracers for studying this gas in nearby galaxies. The brightest molecule among these is the hydrogen cyanide, HCN. However, the HCN emission is $\sim$ 30 times fainter than the CO emission (Gao & Solomon, 2004b), which makes it challenging for observations (Chapter 2, Section 2.4.1, and 2.5.1). In addition, extragalactic studies also focus on other molecular lines, such as hydrogen isocyanide, HNC, formyl cation, HCO^+, and sulphur monosulfide, CS, which is exactly the focus of this doctoral thesis.

1.5.1 High-critical density molecules

Critical density

Before describing dense gas tracers, it is important to discuss the concept of a critical density, which provides understanding why CO tracers are good tracers of densities of 10^3 cm^{-3}, but cannot probe the densest regimes.

Molecules can get into the excited state via collisional or radiative processes. The physical conditions

of the molecular gas, such as the temperature and density, determine the dominant processes for molecular emission. Parameters describing collisional processes from the upper to lower energy levels are called collisional rate coefficients, C_{ul} for collisional de-excitation, and C_{lu} in case of collisional excitation. Radiative processes are described via Einstein coefficients, where A_{ul} is for de-excitation processes, whereas B coefficients are for photon absorption and stimulated emission (also called negative absorption). These coefficients will depend on the species. The Leiden Atomic and Molecular Database (LAMDA), CDMS (Koeln, 2022) and NASA Jet Propulsion Laboratory (JPL) contain tabulated coefficients for various atoms, molecules and their transitions.

In molecular gas, molecules collide predominantly with the H_2 molecule. The density at which collisional de-excitations balance radiative de-excitation is called the critical density, $n_{\rm crit}$:

$$n_{\rm crit} = \frac{A_{\rm ul}}{C_{\rm ul}}. \tag{1.9}$$

Molecules emit at gas densities above the $n_{\rm crit}$. The critical density depends on the kinetic temperature of the gas, $T_{\rm kin}$, determined by the ratio between the number population of the upper and lower energy levels. The above equation is valid under the assumption that the line trapping is negligible (Shirley, 2015). In reality, a percentage of the emitted photons will not escape the source but rather be absorbed again, which will modify the Equation 1.9. The opacity effects, described by the optical depth, τ, will thus lower the critical density. The optically-thick emission lines emit at significantly lower densities than the critical density. The slightly modified $n_{\rm crit}$ is called the effective critical density, as defined in Leroy et al. (2017a).

For a given molecular species, its emission will be in the local thermodynamic equilibrium (LTE) at gas densities above the critical density. To describe a system, we use temperatures. Excitation temperature is defined from the ratio of a number of particles in two states (Boltzmann distribution). The kinetic temperature describes a system of the mean energy E, and it is derived from the Maxwell's distribution. In LTE, collisional processes are the dominant mechanism for molecular excitation and de-excitation. Under the LTE conditions, kinetic and excitation temperatures will be equal. In the non-LTE case, the excitation temperature of a system will be higher than the kinetic temperature, and radiative processes dominate.

Considering all of the above, the information about dense molecular gas will come from molecules emitting at densities higher than the critical density of the CO(1–0) line. In this doctoral thesis, the term "dense molecular gas" will be used to refer to gas with density above $\sim 10^4\,{\rm cm}^{-3}$. Similarly, we will use the term "dense gas tracers" to refer to high-critical density molecular lines that probe gas densities higher than the CO emission.

Emissivity

Emissivity is defined as the ratio between the line intensity and the column density of the gas (Leroy et al., 2017a). It represents how efficiently a molecule emits as a function of the gas density (Leroy et al., 2017a). We show how the emissivity of different molecules depends on the density for fixed kinetic temperature and opacities in Figure 1.8. Each molecule starts emitting and reaches a peak emissivity at different gas densities. This trend corresponds to the critical densities of these molecular lines. The emissivity of the CO(1–0) peaks at densities of $10^2\,{\rm cm}^{-3}$, after which it drops to 60%. A similar trend is observed in the case of the ^{13}CO emissivity. Moreover, the CO(2–1) emissivity drops to 90% of its peak emissivity at higher gas densities, while the emissivity of the remaining molecular lines steadily decreases after reaching its peak.

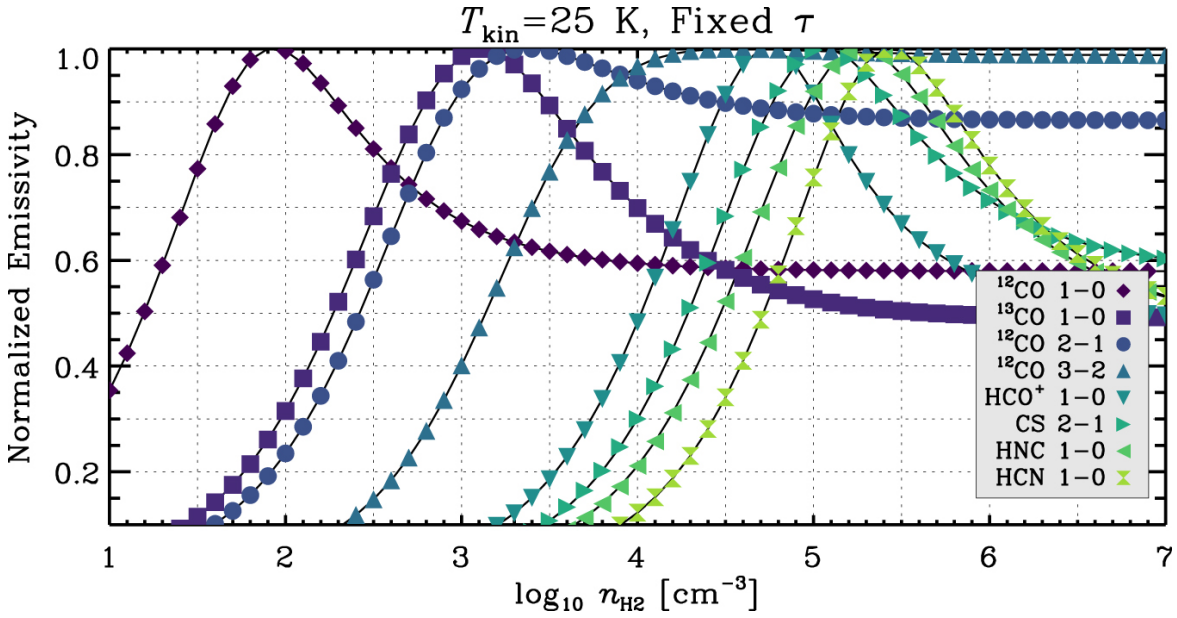

Figure 1.8: The normalized emissivity of various molecular lines as a function of the collider density, n_{H_2} at a fixed kinetic temperature of 25 K and a fixed, realistic optical depth, τ. Image credit: Leroy et al. (2017a).

Interestingly, all molecules shown in Figure 1.8 emit significantly at densities lower than their critical density. This result strongly implies its necessity to interpret the molecular emission with caution, as the contribution of their emission in the low-density regime is not negligible (Leroy et al., 2017a). The most effective critical density, $n_{\rm eff,crit}$, will thus be the density at which the molecule will reach 95% of its emissivity.

1.5.2 Molecular line emission as a tool for constraining physical conditions of molecular gas

Molecular line emission depends on the physical conditions of the gas. Each molecule is sensitive to the gas density (the information is contained in its critical density), temperature, radiation field, and chemistry. Therefore, constraining gas properties from interpreting the emission of only one line is not always enough. The intensity ratio of two molecular lines, measured along the same line of sight and integrated along the same frequency range (see Chapter 2, Section 2.6), is one of the tools providing information of the observed region.

For example, a recent study of a star-forming region in the Milky Way at sub-pc scales proposed HCN and HNC intensity ratio as a probe for gas temperatures (Hacar et al., 2020), since the production and destruction mechanisms of HCN and HNC are coupled and temperature sensitive.

HCN emission is sensitive to the metallicity (Rosolowsky et al., 2011). The intense radiation fields from young massive stars and cosmic rays can further increase the HCN abundance (Aalto et al., 2009; Pellegrini et al., 2009), similarly with the HCO$^+$ molecule. Therefore, numerous theoretical models and observations have attempted to interpret HCN and HCO$^+$ intensity ratio as a probe for PDRs and XDRs (Meijerink et al., 2007; Privon et al., 2015; Murphy et al., 2015), although recent studies did not find strong evidence to support that assumption (Bešlić et al., 2021; Eibensteiner et al., 2022). By studying the isotopologues of dense gas tracers, H^{13}CN, HN^{13}C, and H^{13}CO$^+$, it is possible to derive

the optical depths of dense molecular gas, as presented in (Jiménez-Donaire et al., 2017a), who found that dense gas tracers are optically thick.

One of the applications of high critical density molecular lines is determining gas densities. We use the line ratios between high- and low-critical density molecular lines to constrain the density constrast. A proxy for the dense gas fraction, $f_{\rm dense}$, can be the intensity ratio of HCN and CO(1–0)(Usero et al., 2015; Jiménez-Donaire et al., 2019, e.g.). This line ratio is commonly used within the literature to trace the dense gas fraction. As we will highlight later in Chapter 3 Section 3.6, several studies focused on trying to interpret the connection of dense gas fraction and star formation efficiency, which is also the scope of our work (Chapters 4 and 5).

Density distributions

Constraining the density probability distribution function (PDF) of molecular gas is the important step in understanding and modeling star formation (Chapter 3, Section 3.3). Both approaches in studying these: numerical simulations (e.g. Mac Low & Klessen, 2004; Elmegreen & Scalo, 2004; Molina et al., 2012) and observational studies (e.g. Kainulainen et al., 2009; Rathborne et al., 2014; Abreu-Vicente et al., 2015; Schneider et al., 2015, 2016; Pokhrel et al., 2016) mainly agreed that molecular gas density is well described via the log-normal density distribution:

$$dP(\ln\, n') \propto \exp\left(-\frac{(\ln n' - \overline{\ln n'})^2}{2\sigma^2}\right), \tag{1.10}$$

where n' is the ratio of the gas volume density and the mean gas density, n_0. σ is the width of the distribution, connected to the Mach number (Padoan & Nordlund, 2002a; Molina et al., 2012; Collins et al., 2012; Burkhart et al., 2015), a quantity proportional to the velocity dispersion of the gas. We show an example of density distributions of gas volume (solid blue line) and mass densities (solid green line) in Figure 1.9. The log-normal PDF is also seen when observing gas column densities (Lombardi et al., 2015), at a kpc, and $\sim$ 60 pc scales (Leroy et al., 2016). Large-scale turbulence produces this distribution on larger spatial scales than the scales of a typical molecular cloud (see Section 1.4.4), but also other effects can have an impact (Berkhuijsen & Fletcher, 2015).

In addition, observations of molecular clouds revealed that the high-density is described via a power-law tail (Federrath & Klessen, 2012):

$$dP(\ln n') \propto exp\left(\alpha\, \ln n'\right), \tag{1.11}$$

where α is the slope. Magnetic fields impact the slope of the power-law tail (Auddy et al., 2018). The power-law tail is shown on Figure 1.9 as the dashed line for both distributions. Although the log-normal distribution is universal, the presence and properties of the power-law tail depend on the cloud. In addition, the power-law tail is present at densities higher than the threshold density of $10^{3.8}$ cm^{-3} (Federrath & Klessen, 2012). The density threshold for a power-law tail depends on the value of Mach number (e.g. Ward et al., 2014; Auddy et al., 2018). Studies have found that star formation correlates with the mass of the gas within the power-law tail (Kainulainen et al., 2009).

The density of molecular clouds is often be described as a combination of the log-normal function (Equation 1.10) with the the power-law tail (Equation 1.11) at high densities (e.g. Federrath & Klessen, 2013; Girichidis et al., 2014; Kainulainen et al., 2014; Schneider et al., 2016).

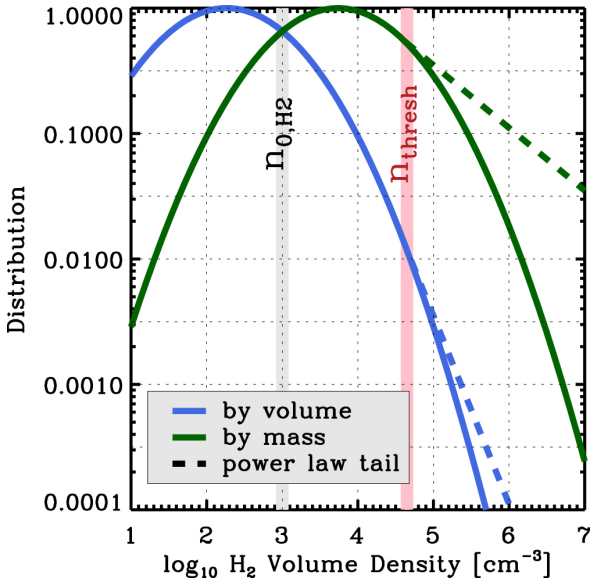

Figure 1.9: Volume and mass gas density distribution taken from (Leroy et al., 2017a). The distribution is described by a log-normal (solid line) with a power-law tail (dashed line) function at higher densities. The grey vertical line shows the mean gas density, $n_{0,\mathrm{H_2}}$, whereas the red line shows the density threshold at which the power-law tail starts.

Dense molecular gas in nearby galaxies, and the sub-beam density distributions

Studying resolved molecular line emission across molecular clouds in the Milky Way provides a detailed overview of various phenomena and diagnostics of these regions (Pety et al., 2017; Kauffmann et al., 2017; Barnes et al., 2020b; Evans et al., 2020). It is worth pointing out that molecular gas in the Milky Way can be probed at sub-pc scales even by using single-dish observations (Chapter 2, Section 2.4). This implies that it is easier to observe faint molecular lines (see Figure 2 in Barnes et al., 2020b), whose emission outside the Milky Way can only be detected towards the centre of the closest and brightest galaxies (e.g. NGC 253 - Martín et al., 2021). Molecular lines such as N_2H^+ probe the dense clumps of molecular gas, while the HCN emission can originate from regions of lower-density molecular gas (Pety et al., 2017; Kauffmann et al., 2017; Shimajiri et al., 2017). Another issue arises when considering the range of spatial scales we can probe in other galaxies. Until recently, studies observed global molecular gas properties at kpc and sub-kpc scales, averaging over large areas and different morphological environments (e.g. Gao & Solomon, 2004a; Bigiel et al., 2016; Gallagher et al., 2018a). Even though the use of new generations of interferometers (Chapter 2, Section 2.5) provided new insight into hundred pc scales in nearby galaxies, we still deal with averaging emission originating from different regions and clouds. Therefore, there is a need to overcome this and find a way to use molecular emission and various line ratios as a tool for constraining gas properties, particularly gas densities.

Leroy et al. (2017a) investigated line ratios as a probe to determine changes in density distributions. This tool is of great use for extragalactic observations since it is impossible to observe at similarly small scales as in the Milky Way. We show the main result from Leroy et al. (2017a) in Figure 1.10. The various line to CO(1–0) intensity ratios are shown, and these are ordered by the critical density, from the lowest (left part of each panel) to the highest (right part of each panel). The colour bar shows

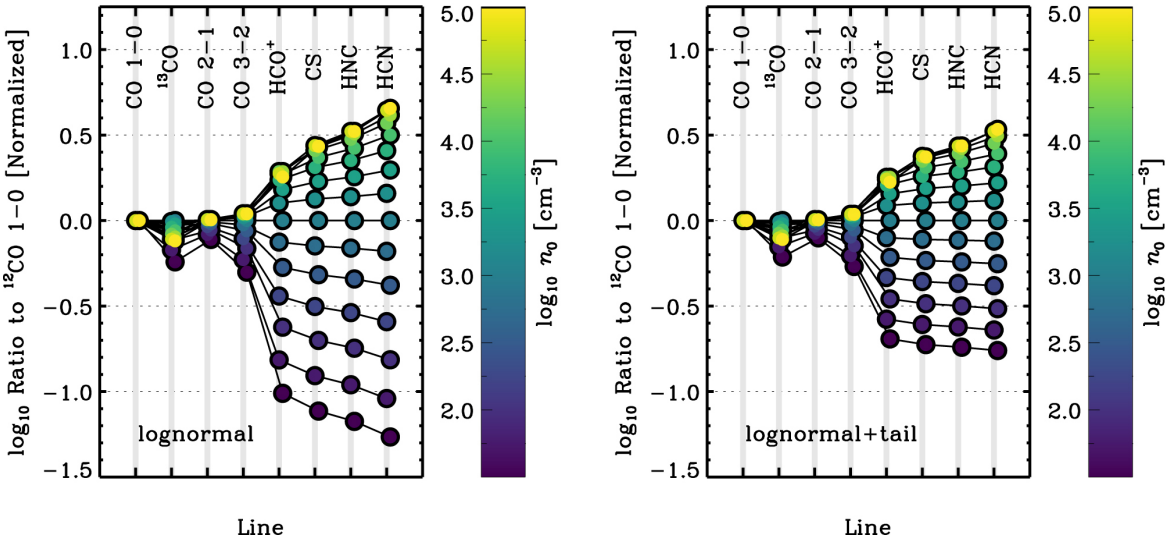

Figure 1.10: Line intensities relative to the CO(1–0) emission for two assumed density distributions: log-normal (panel left), and log-normal+power-law tail (panel left) (Leroy et al., 2017a).

the volume density, and points with the same volume density are connected. Figure 1.10 shows two examples of density distribution: log-normal and log-normal with a power-law tail, which describes part of the self-gravitating cloud. In both cases, we note that line ratios flare, and the flaring becomes more prominent at higher differences in critical densities. The higher the critical density of a line relative to CO, the greater the density contrast. The flaring pattern implies that the high-to-low critical density line ratios are sensitive to changes in the gas volume density. Therefore, they can be used as a probe of gas density variations. The gas density distribution will determine the magnitude of flaring. The flaring is more prominent if gas densities are described via a log-normal distribution.

1.6 The role of cold ISM in galaxy evolution: baryon cycle

The ISM considers everything that is visible and made of baryons[5] that are not stars and black holes. The ISM, particularly the cold phases, are essential to understanding the cycle of matter in the Universe. Similar to the space between stars in galaxies, the space between galaxies is not empty. Galaxies are in the forms of groups, clusters, and superclusters and are surrounded by the intergalactic (IGM) and circumgalactic (CGM) medium. The distance between galaxies is comparable to their sizes, which means that gravitational interaction and even galaxy mergers are frequently happening.

The processes of gas exchange between the galaxy, IGM and CGM are important in understanding galaxy evolution. As stars are made out of molecular gas, and molecular gas is produced from atomic gas, these two phases (cold ISM) will be substantial to understand how galaxies evolve. Importantly, all gas phases are connected, and one could not exist without others. Similarly is with dust and fields, as they are well mixed with the gas, and their coupling and impact on the gas phase cannot be neglected. The baryon cycle spreads across a variety of physical scales (from galactic flows at tens of kpc to molecular cores (sub)-pc), involves many different processes and mechanisms, and various gas

[5] We have to keep in mind that this is only the 2% of the total matter in the Universe, as there is the dark matter that is not visible, but it gravitationally interacts with everything, and dark energy, which we cannot observe, nor detect.

phases, and how these components are related and affect the matter in a galaxy, are a key asset in order to get a full picture of the lifecycle of matter in a galaxy. This is an extremely complicated task, and we still have not solved all the missing pieces of this puzzle. To better understand the following view of a lifecycle of the baryonic matter in a galaxy and how that affects its evolution, we show a sketch of relevant pieces of the puzzle in Figure 1.11. This figure is inspired by sketches in Draine (2011); Saintonge & Catinella (2022) and a brief overview of baryonic cycle in Tielens (2005).

Burbidge et al. (1957) connected the ISM to star formation and stellar evolution and explained their coexistence. In the simplest possible picture, galaxies are made of ISM and stars[6]. Due to cooling mechanisms, the gas changes its ionization state, density, and temperature. In particular, ionized gas becomes atomic, and later, molecular. The speed and efficiency of this gas conversion will depend on gas pressure and radiation fields (Blitz & Rosolowsky, 2004). As we previously mentioned, molecular gas is characterized by a wide range of densities, and its densest form is where star formation occurs. Therefore, due to the gravitational instability of such gas, the gas will collapse and eventually form a star. Chapter 3 provides all the relevant information about the star formation processes and theories.

New born stars impact the ISM that surrounds them, and this impact will depend on their mass. Low-mass stars will produce stellar winds and inject dust and PAHs. The presence of dust controls the molecule production. Photons from high-mass stars will ionize local surroundings, creating photon-dominated regions (PDRs). These high mass stars and young winds will contribute to the mechanical energy of the system in SNe. These will also produce heavier elements and enrich the ISM. Particularly enhanced star formation in the centre of galaxies (starburst) will produce galactic winds and outflows in various gas phases, e.g. work on understanding the outflow in local starburst galaxies NGC 253 (Bolatto et al., 2013a; Walter et al., 2017; Levy et al., 2021), and M 82 (Leroy et al., 2015). In this way, the matter will leave the galaxy and reach the CGM and IGM, where it will start cooling and eventually inflow and accrete back to the galaxy.

1.7 Galaxy structure and classification

In this section, we describe galaxy classification, types of galaxies, and their properties. It has been thought that the Milky Way is the only galaxy in the Universe until 1924, when E. Hubble found that the M 31 nebula is outside our galaxy. Later he discovered other galaxies, and the year 1924 may be considered as the beginning of extragalactic astronomy. All galaxies belong to one of the three groups of galaxies: elliptical, spiral or irregular. The illustrative representation of this classification is also called the Hubble fork, and is shown in Figure 1.12.

Elliptical galaxies are in a shape of a 3 dimensional ellipsoid. These systems are massive, show homogeneous structure, and show little substructures. We divide elliptical galaxies into 7 different categories, based on their shape: from E0, which are spherical galaxies, to E7, that are elongated. These galaxies contain old stars, and a very low fraction of cold ISM. Interestingly, they show very little emission of atomic hydrogen at 21 cm, but they contain significant amount of HIM. These galaxies are also called the "early-type" galaxies, and they are redder than the spiral galaxies since they contain more old stars.

Spiral galaxies can be divided into two main subcategories, based on the presence of a bar (suffix B) or not. Overall, spiral galaxies show substructures: they have a disc and a bulge in its centre. Spiral arms are in the plane of the galactic disc, they are rich in ISM, star-forming regions, old and young stars. Based on development of spiral arms and the bulge-to-disc ratio (Graham & Prieto, 2001), there

[6] Baryonic matter.

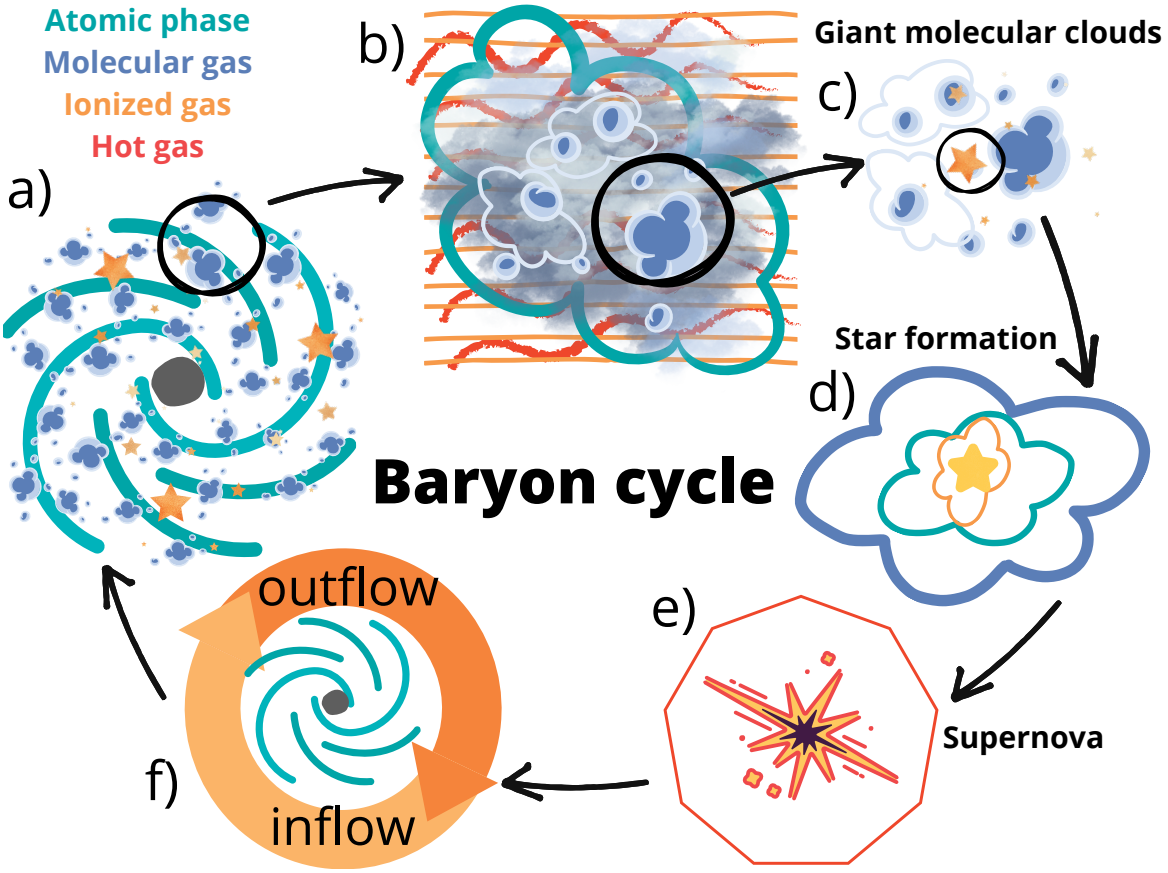

Figure 1.11: A cartoon representation of the baryon cycle of a galaxy. Panel a) shows a typical spiral-barred galaxy, like the Milky Way. Panel b) shows a close view at a spiral arm. Following the three-phase model (McKee & Ostriker, 1977), the HIM (red) and the WIM (orange) surround the atomic gas (green). When we look inside the atomic gas, we see molecular gas (blue). The transition from atomic to molecular state depends on a few parameters, as stated in the text—the darker shades of blue show different molecular gas densities, indicating the presence of clumps and cores. Panel c) shows a zoom-in of the molecular cloud and shows places of star formation, whose impact on the neighbouring area is shown in panel d). In this case, young, especially massive O and B stars ionize the local medium, and we see a gradient in densities and change in gas phases. Panel e) represents the SN and its way of enriching the ISM around it. Finally, panel f) is a spiral galaxy as shown in a). Orange and yellow arrows indicate galactic inflows and outflows into the CGM and IGM. This panel is connected to panel a) in a way that these red lines indicate gas inflows towards the galaxy from the surrounding medium, completing the circle of baryon matter.

are three different subcategories: type Sa has prominent nuclei and small spiral arms, whereas the type Sc contain relatively compact nuclei and prominent spiral arms. Galaxies that contain discs and nuclei, but no spiral arms are called lenticular galaxies, S0. Spiral galaxies are the “late-type” galaxies, and since they contain more young stars, they are bluer. According to this classification, our Milky Way is a strongly barred, spiral galaxy with moderate spiral arms, SBb.

The last category are irregular or dwarf galaxies, and they are not very common objects in the Local Universe. Overall they are faint, and do not show any specific shape of structure. However, they contain a significant amount of the ISM.

Another way to classify galaxies is based on their activity. At the very beginning, the majority of

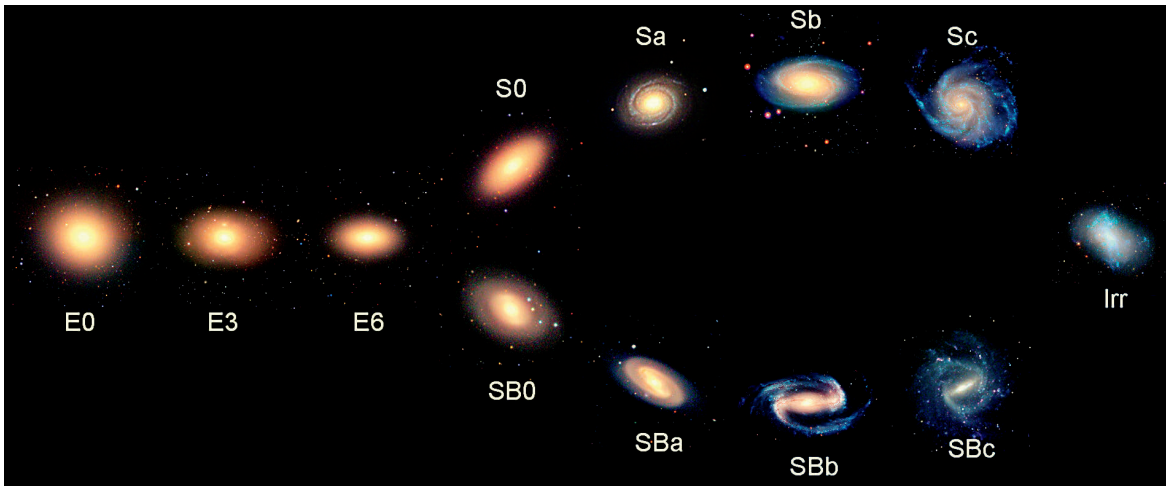

Figure 1.12: Hubble tunning fork. From left to the right: Elliptical galaxies, from type 0 (spherical), to type 7 (elongated), the S0 (transition zone between elliptical and spiral galaxies), and various types of spiral galaxies from non-barred to strongly barred and irregular galaxy. Imaga credit: ESO.

discovered galaxies did not show any peculiar behaviour. With detection of unusual activity in some galaxies observed in the second half of the 20th century, astronomers started diving galaxies into normal and active. Normal galaxies show emission as the sum of their stellar emission. Therefore the majority of radiation lies in the optical part of the spectrum. The luminosity of normal galaxies does not vary with time.

On the other hand, active galaxies show different properties. Although only 10% of galaxies are classified as active, these type of galaxies are very interesting to study. In particular, they show strong and bright emission that comes from their nuclei, variable flux, jets, and excessive radiation in the nuclei observed in X-ray, IR and radio domain. Active galaxies can be further split into different categories. These are: Seyfert galaxies (show emission lines in their spectrum), radio galaxies (giant elliptical galaxies that show strong non-thermal radio emission). Moreover, Luminous Infrared Galaxies (LIRGs) and Ultra-Luminous infrared galaxies (ULIRGs) are spiral galaxies with luminosities higher than 10^{11} $L_{\odot}$ and 10^{12} $L_{\odot}$ respectively. They show bright IR emission, and can be interacting galaxies.

CHAPTER 2

Radio and mm Spectroscopy

"*Omnia in numero et mensura.*"

The following important aspect of our work presents ways of observing the interstellar medium, particularly its molecular gas phase. The radio domain of electromagnetic radiation is crucial for understanding molecular ISM, star-forming regions, proto−planetary systems, and nearby and distant galaxies. This chapter aims to introduce the concept of radio astronomy, describe the observing techniques and how to produce the science−ready data set.

The knowledge about the Universe predominantly comes from the measured light, i.e., we need special "glasses" to observe various physical processes and astronomical objects. It is interesting to point out that before the 20th century, everything known in astronomy came from observations of only one small part of the electromagnetic spectrum−the optical light (Figure 2.1). The discovery of infrared light (W. Herschel), X-ray (W. C. Röntgen), and the existence of radio waves in interstellar space (K. Jansky) marked a major turning point in astronomy. The Universe looks different and unique observed at different wavelengths, as highlighted in Figure 1.2.

This chapter is structured as the following. In Section 2.1, we describe the electromagnetic spectrum, its domains and how the Earth's atmosphere impacts observations. Next, it seems appropriate to outline a history of discovering radio emission and radio sources, which motivated the development of radio astronomy (Section 2.2). Studying phenomena in this domain revealed great discoveries, some of which won Nobel prizes. Understanding the radiation mechanism and antenna theory to be able to interpret radio astronomy observations is fundamental (Section 2.3) because it yielded the construction of radio telescopes (Section 2.4), and receiving one of the first radio waves from space. The development of radio astronomy, single dish observations, and the need to probe small-scale features increased the resolving power of telescopes and significantly contributed to building the radio interferometers (Section 2.5). Unless stated otherwise, this chapter is based on Kraus (1966); Williams et al. (2000); Vukićević-Karabin & Atanacković (2010); Thompson et al. (2017).

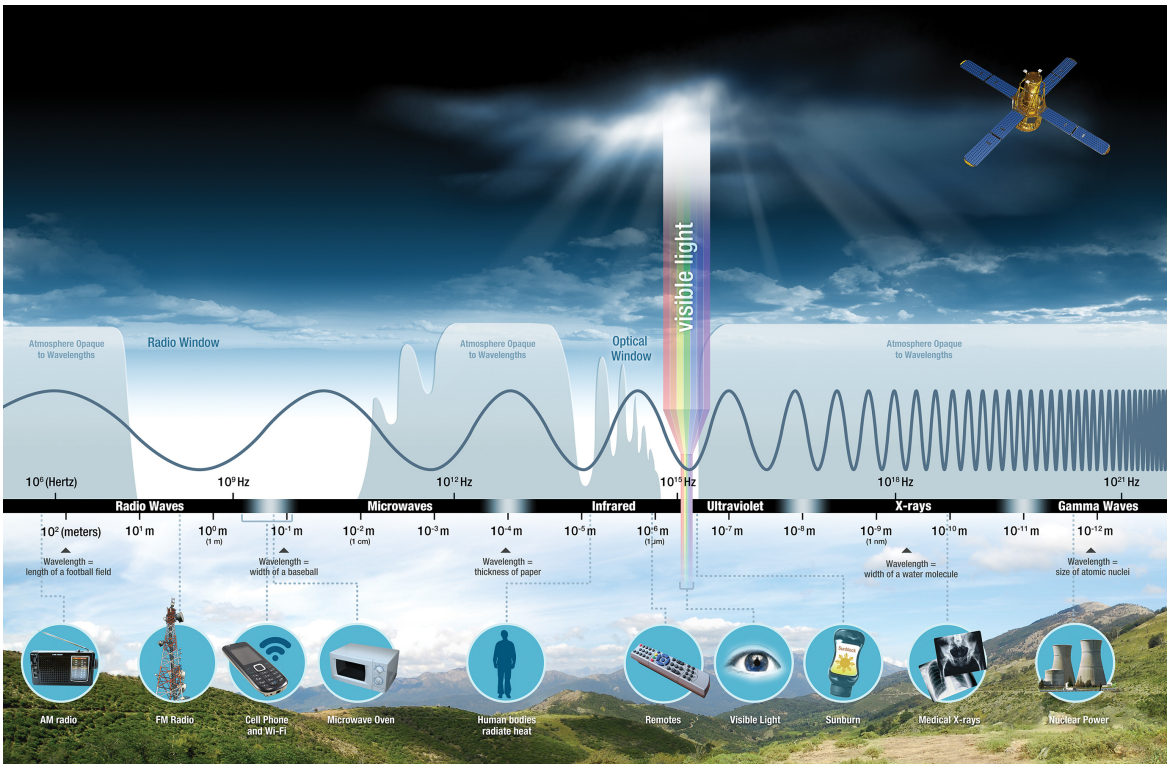

Figure 2.1: A representation of the electromagnetic spectrum, from long wavelengths (low energies) to low wavelengths (high energies). Image credit: NASA.

2.1 Radio emission

The electromagnetic spectrum consists of several domains. Each regime covers a different range of wavelengths (frequencies) and shows different behaviour. This implies the variety of detecting and observing techniques developed for each regime. We show the electromagnetic radiation and its components in Figure 2.1. We will use different units depending on the part of the EM radiation we want to study, i.e. whether we observe the particle or the wave nature of the light. For example, in the high energy regime (the left part of the upper panel in Figure 2.1), we express our measurements in the units of energies-electronvolts (eV). The UV and optical domains are commonly described in the units of wavelengths - either nanometers or angstroms (1 A = 10 nm). In the radio domain, characterized by the wave behaviour of the light, we deal with frequencies (MHz, GHz).

The longest wavelengths of electromagnetic radiation are referred to as radio waves. After the infrared light, radio waves are widely used for commercial purposes, such as radio and TV broadcasting, radars, and mobile phones. However, the wave nature of radio emission and its commercial use causes issues in the frequency domain and impacts astronomical observations in this domain. Therefore, the protection of specific frequency domains for radio observations is necessary.

We define several frequency ranges in the radio regime because the detecting techniques and impact of the Earth's atmosphere are different. The frequency range of the radio domain goes from a few MHz (the high-frequency domain), a range of 30–300 MHz (very high-frequency domain), 300 – 1000 MHz (the ultra-high frequency domain), 1 – 30 GHz (microwave), millimetre and sub-millimetre wave, to even 10^{13} Hz (terahertz). The emission of HI atom is in the ultra-high frequency domain. Microwaves

are often referred to as energetic radio waves. This part of the radio emission is not accessible from ground-based observations. Satellites sent to space can observe microwave emission, such as the Planck mission. Microwave astronomy is extremely important for observing the early Universe, particularly the cosmic microwave background emission (CMB).

It is essential to point out that radio emission is generally weak. Assuming that we collect all the energy emitted from all the astronomical sources ever observed from all radio telescopes we ever built, it would not be possible even to melt a snowflake!

The impact of the atmosphere

The Earth's atmosphere is, in fact, a set of four protective layers of gas, allowing only a tiny part of radiation (two frequency ranges) from space to reach the Earth's surface (Figure 2.1). The good side is that the atmosphere shields us from high-energy radiation. However, in terms of astronomical observations, the Earth's atmosphere acts as a considerable obstacle, and the only way to observe the rest of the electromagnetic radiation is to send satellites and telescopes to space. The most recent telescope launched to space is the James Webb Space Telescope (JWST - Doyon et al., 2019), the biggest telescope ever sent into space. JWST observes light in the near-IR (Bagnasco et al., 2007) and mid-IR (Kendrew et al., 2015) regimes and has impressive angular resolution and sensitivity. At the moment of writing this doctoral thesis, the JWST released the first images[1] and marked a major turning point in understanding the early Universe, but also provided a new perspective of the present day.

Some of the electromagnetic radiation from space is entirely blocked by the atmosphere, whereas the IR light can be observed in the upper parts of the stratosphere, for example, using the Stratospheric Observatory for Infrared Astronomy (SOFIA - Krabbe, 2000). Two ranges of wavelengths that can be observed from the Earth's surface are often referred to as the "windows": the optical and the radio window. As we will mention later, the Earth's atmosphere still impacts radio astronomy observations. In particular, the sub-millimetre domain is sensitive to water vapour in the atmosphere, which yielded the building of giant radio telescopes in deserts and at high altitudes.

2.2 Historical overview - the Universe through new eyes

"*...a steady hiss type static of unknown origin.*"
- K. Jansky, 1933.

Even before the 20th century, it was widely believed that there is radiation our eyes cannot detect. Humans have not developed sensors for detecting any other light besides the optical. H. Hertz produced radio waves in the laboratory. By investigating the properties of radio waves, Hertz found that radio emission shows similar properties to optical light, which confirms Maxwell's equations. The remarkable work of Serbian inventor N. Tesla on the alternate current and wireless methods in information transport paved the way for the production of radio receivers and commercial use of radio waves in the 1930s.

Cosmic radio emission was detected for the first time in the pioneering work of Karl Jansky at Bell Laboratories in 1933. Jansky was modelling the noise for transatlantic telephone communication. Using the dipole shown on the left panel in Figure 2.2, Jansky observed and detected a peculiar signal

[1] https://www.nasa.gov/webbfirstimages

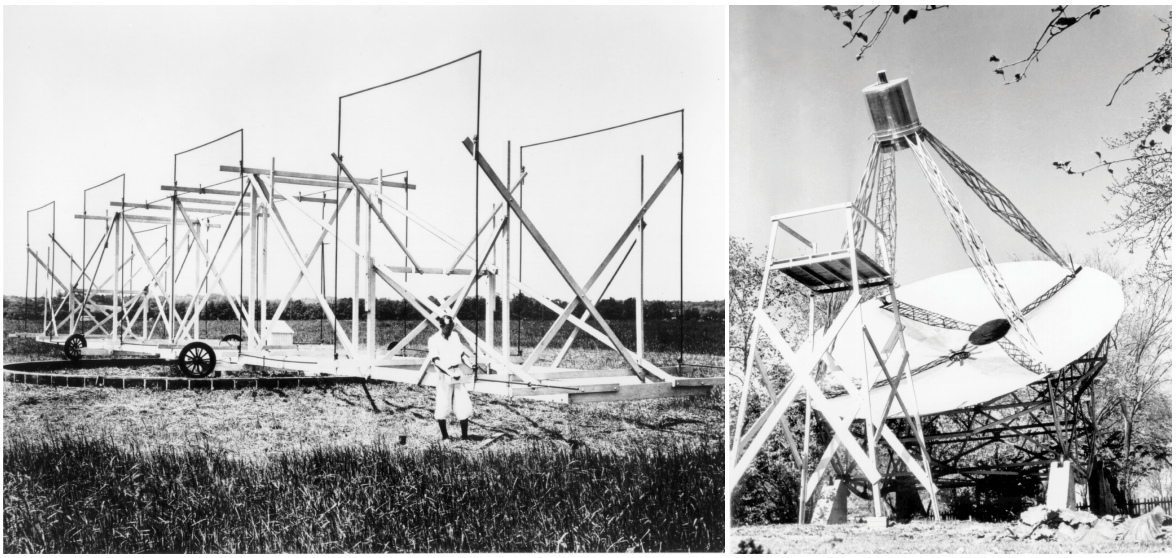

Figure 2.2: **Left:** Karl Jansky in front of the receivers he built to understand the origin of the interference of radio frequencies for transantlantic telephone signals and thunders, which led to discovery of radio emission from the centre of the Milky Way. **Right:** The parabolic-dish built by Grote Reber in his yard in order to detect radio emission from the Sun. He did not detect it, but the radio telescope he constructed is the base of later ones that were built.

at 21 MHz (∼15 m), like a hissing noise. The signal had a periodicity equal to the sidereal time, i.e. time needed for Earth to make a full rotation respective to the stars. Therefore, the origin of the noise was not from the Earth but space. Most importantly, the peak of the signal was reached every time the dipole was pointed to the centre of the Milky Way. Soon after this discovery, G. Reber observed radio emission at 1.89 m from the sky in 1939. Reber used the 9 m antenna he built in his yard (right panel in Figure 2.2). The main result of this work was that the radio emission is stronger with frequency, contrary to the predicted dependency that stems from the thermal emission. Later, V. L. Ginzburg further explained this finding as a synchrotron mechanism.

Despite several attempts to detect solar radio emissions, the first success was made during the second world war. The publication of J. S. Hey and G. C. Southworth in 1946 was the first one to confirm the solar radio emission observationally. Therefore, 1946 is commonly used as the beginning of radio astronomy. The development of radio astronomy followed a number of discoveries, some of them already mentioned in Chapter 1, Section 1.3.4. Among many others, one of the great achievements in the field of radio astronomy was the discovery of quasars by M. Schmidt in 1936 and pulsars in 1967 by J. Bell and T. Hewish. Moreover, N. Penzias and R. W. Wilson observed the cosmic microwave background radiation in 1965 (see the top panel in Figure 2.3). The recent significant joint efforts of several big radio telescopes around the world as the Event Horizon Telescope (EHT) provided the first images of supermassive black holes ever seen (bottom panel in Figure 2.3 Event Horizon Telescope Collaboration et al., 2019; Akiyama & Event Horizon Telescope Collaboration, 2022).

The 20th century brought outstanding achievements in scientific work, which could not be achieved without the improvement of observing techniques. Remarkably, the theory of aperture synthesis in the middle of 1940, developed and presented by M. Ryle, allowed radio interferometry and pushed radio astronomy observations to a higher resolution. The aperture synthesis demonstrated the power of using multiple telescopes all over the world at the same time. As we already mentioned at the beginning

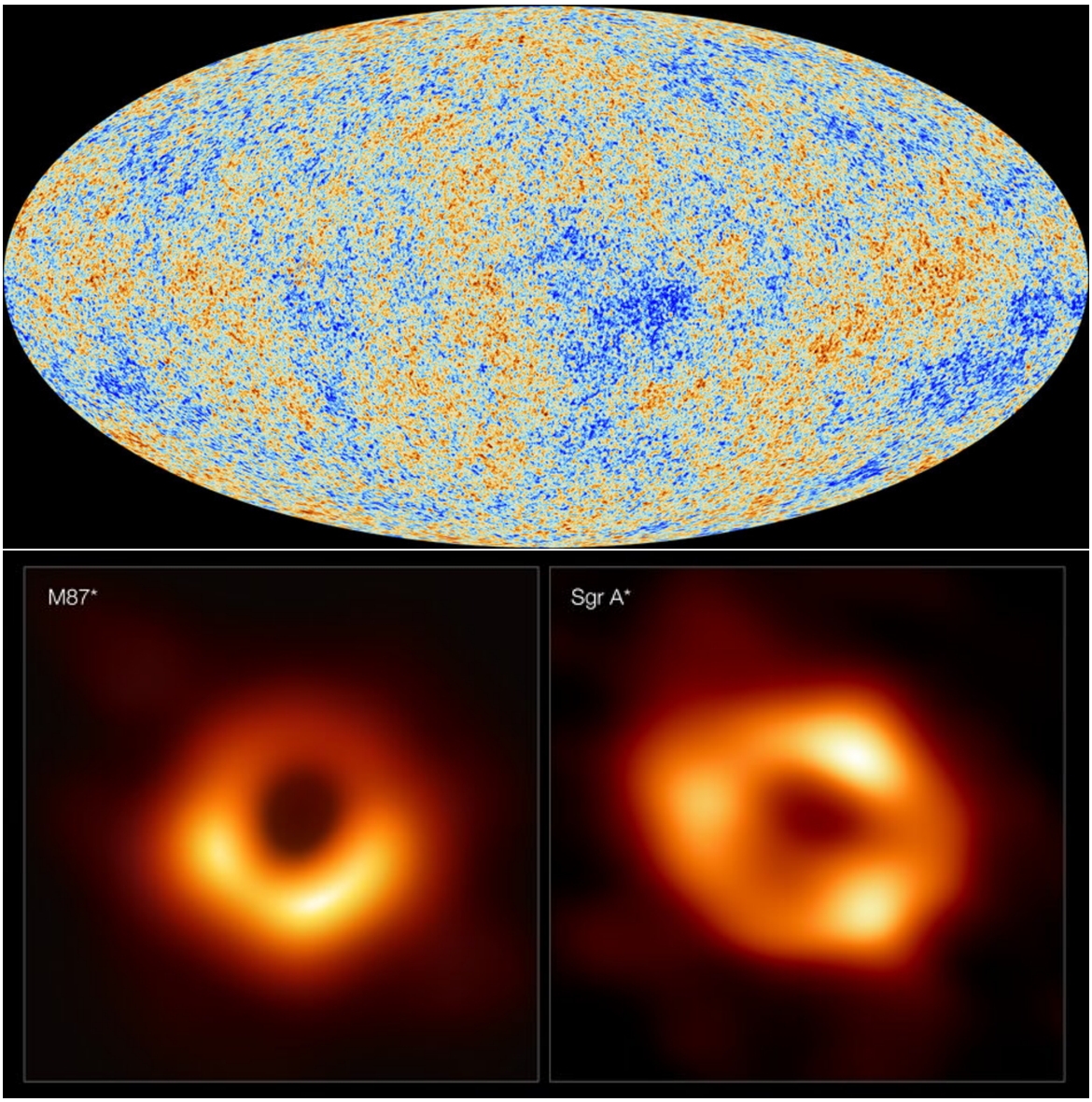

Figure 2.3: **Top:** the Universe at the epoch of recombination, the anisotropy of the cosmic microwave radiation at 2.3 K measured by Planck mission. Image credit: NASA. **Bottom:** The first-ever images of supermassive black holes in the centre of M 87 (left), and the Milky Way, Sagittarius A* (right). Image credit: EHT, European Space Observatory (ESO).

of this chapter, several discoveries in radio astronomy won the Nobel prize in physics. For example, synthesis imaging and the discovery of pulsars shared the Nobel prize in physics in 1974, and the discovery of the CMB won the prize four years later. There is no doubt that there will be many more in the upcoming years. Many places worldwide host institutes that are the leading radio-astronomy facilities, such as Bonn in Germany, which hosts two institutes: Argelander Institut für Astronomie and Max Planck Institut für Radio Astronomie.

2.3 Concepts of Radio Astronomy

In the following, we outline the basic concepts of radio astronomy, including definitions and theorems important for understanding the fundamental properties of radio telescopes. Everything listed below will be directly applied to single dish telescopes described in Section 2.4, while the relevant concepts for radio interferometers will be explained in Section 2.5.

Angular resolution

The angular resolution of any telescope will depend on the measured wavelength (λ) of the electromagnetic radiation and the diameter (D) of a telescope:

$$\theta \propto \frac{\lambda}{D}. \tag{2.1}$$

From the above equation, it is obvious that one of the main issues in radio astronomy is the low angular resolution because of the long wavelengths. A solution that increases angular resolution is to increase the diameter of a telescope. However, the limitation in the size of the main dish is present due to gravity effects. For example, a 90-meter Green Bank Telescope in West Virginia collapsed in November 1988 because its construction could not support the weight. Similarly, the 300-meter Arecibo telescope in Puerto Rico collapsed after severe support cable failures in 2020. To avoid these accidents and allow astronomers to observe objects at their finest details, the use of multiple single dish antennas simultaneously pointed to the same portion of the sky is widely used. We explain this concept in Section 2.5.

Flux density

In honour of K. Jansky, the flux density unit in radio astronomy is named after him: $1\,\mathrm{Jy} = 10^{-26}\mathrm{Wm}^{-2}\mathrm{Hz}^{-1}$. The flux density is defined as Power/(Area $\cdot$ Bandwidth), or integrated source temperature over the solid angle of the source:

$$S_\nu = \frac{c^2}{2k_B\nu^2} \iint T_\mathrm{B}\mathrm{d}\Omega, \tag{2.2}$$

where c, and k_B are the speed of light and the Boltzman's constant, respectively, ν the measured frequency, and T_B the source brightness temperature. The brightness temperature is the temperature of the observed source, under the assumption that its emission can be described via the Rayleigh-Jeans approximation of Planck's law. This means that it will be proportional to the flux density of a source and the inverse square of the observed frequency:

$$T_\mathrm{B} = \frac{2k_B\nu^2 S_\nu}{c^2\Omega_\mathrm{beam}}. \tag{2.3}$$

The measured brightness temperature will thus depend on the beam size of a telescope and if it is sensitive enough to detect the source. Therefore, the sensitivity of a radio telescope is one of the most critical properties because it defines possible sources that can observe and detect. At higher sensitivities, we detected fainter objects. The sensitivity will depend on several factors, such as the bandwidth, the observing time and the beam size.

Antenna and its properties

The antenna converts the input radiation to a current. In general, the antenna can be both the receiving and the emitting device, and the former is used in radio astronomy. Overall, many properties of receiving and transmitting antennas are the same. Therefore, it is convenient to use this advantage, particularly when trying to understand the measured signal.

Even though the antenna will collect electromagnetic radiation from all directions, it will not be equally sensitive. The antenna's power pattern shows how the antenna's sensitivity depends on the direction of the incoming radiation. It is commonly presented in the polar coordinate system. The power pattern is composed of lobes. The main lobe is the biggest and most dominant, whereas the other is the side lobes. The width at the half-power of the main lobe expressed in angular units determines the angular resolution of a telescope. The beam solid angle (Ω_{beam}) will then be the integration of the beam pattern over the whole sky, whereas the main beam solid angle ($\Omega_{\text{main beam}}$) will be the integration only over the main beam, and it will be measured in steradians.

The effective aperture, and the efficiencies

The effective aperture is defined as an area of the antenna with the efficiency of 100% (Stanimirovic, 2002):

$$A_{\text{e}} = \frac{\lambda^2}{\Omega_{\text{beam}}}. \tag{2.4}$$

The main beam efficiency ($\eta_{\text{eff,main}}$) is defined as the ratio between the main beam and the beam solid angle. This parameter determines the quality of the antenna because it shows the percentage of the power pattern contained in the main beam. The aperture efficiency is the ratio between the effective area and the geometrical area of the antenna.

Temperatures and noise

Here we define a few different temperatures commonly used in radio astronomy. The first one is the antenna temperature, T_{a}, which is a practical way to compute the power output from the antenna. The system temperature, T_{sys}, is a joint contribution of all the devices that are used for the transportation of the signal before reaching the backend. The antenna temperature will be the sum of all the temperatures as mentioned above and the temperature coming from the Earth's atmosphere, $T_{\text{atm,eff}}$, and the background emission from the sky, T_{sky}:

$$T_{\text{a}} = T_{\text{sys}} + T_{\text{atm,eff}} + T_{\text{sky}} + T_{\text{B}}. \tag{2.5}$$

Everything that does not have zero temperature emits some radiation and produces noise. This is particularly essential in radio astronomy since all the devices have some working temperature and add some noise to the weak signal.

Fourier transforms

The key component in radio astronomy is the Fourier transformation (FT), commonly used in signal processing. With convolution, cross-correlation and autocorrelation set the base for processing radio astronomy observations and getting information about the astronomical source.

The reciprocity theorem

Antennas are emitting devices used in radio broadcasting, but they can also receive the emission and transmit it. The reciprocity theorem can be easily explained using Maxwell's equations or the network analysis. The original form of this theorem, developed by Burke & Graham-Smith (1997) is slightly different from the one we state here since it describes the relationship between voltages and current of two antennas:

The power pattern of an antenna is the same for transmitting and receiving.

In other words, the antenna parameters are the same no matter if it receives or emits a signal. This theorem simplifies calculations to know the antenna power pattern and allows a better understanding of the relationships between the source and the antenna.

Sampling the data

The Nyquist theorem is also known as the sampling theorem (Nyquist, 1928). It comes from the signal theory but is commonly used in radio astronomy in the final stages of data reduction. This theory describes how to sample the data and properly keep all the relevant information.

2.4 Single dish telescopes, observations, and data reduction

Radio and optical telescopes differ from each other in various aspects. For example, due to the low energy of radio waves, and weak radio emission, larger collecting areas provide better sensitivities. The long wavelengths allow the quality of the surface of a telescope to be lower than for optical telescopes. The illustration representing the structure of a radio telescope is shown on the left part of Figure 2.4.

In the most simplistic form, a radio telescope consists of two main parts: the antenna and the radiometer. The antenna is a receiving device whose role is to collect radio waves. The radiometer is everything between the radio receiver and the power measuring tool. The antenna has a parabolic shape, whose suitable geometry allows the focusing of the incoming waves into a focal point. The secondary reflective surface is placed in the focal point, directing the waves to the feed horn, where we place the receivers. Before the signal reaches the receiver, it goes through the amplifier, which enhances the signal and sends it further to the mixer. In the mixer, the frequency band of a signal will be shifted and further transported to the intermediate frequency (IF) amplifier and then to the receiver. A receiving device depends on the type of observations. For example, for spectral line surveys, we use spectrometers, whereas, for continuum measurements, we use a continuum detector. The last stages of signal processing are performed in the digital converter, which is again amplified and sent to storage. The raw data is quite large, especially considering significant observing times of astronomical sources. All the above-described steps through which the input signal travels from the antenna to the spectrometer or continuum device are called the frontend, while the latter is called the backend. A typical frontend is the heterodyne receiver, whose primary goal is to collect the radio emission from the antenna and prepare the incoming signal for further processing. In addition, the role of a receiver is to minimise its contribution to the total noise.

Today, there are many operating single dish telescopes worldwide. In the following sections, we will describe two well-known and commonly used single dish telescopes in the radio and mm regime, the IRAM 30-meter and the Effelsberg telescope.

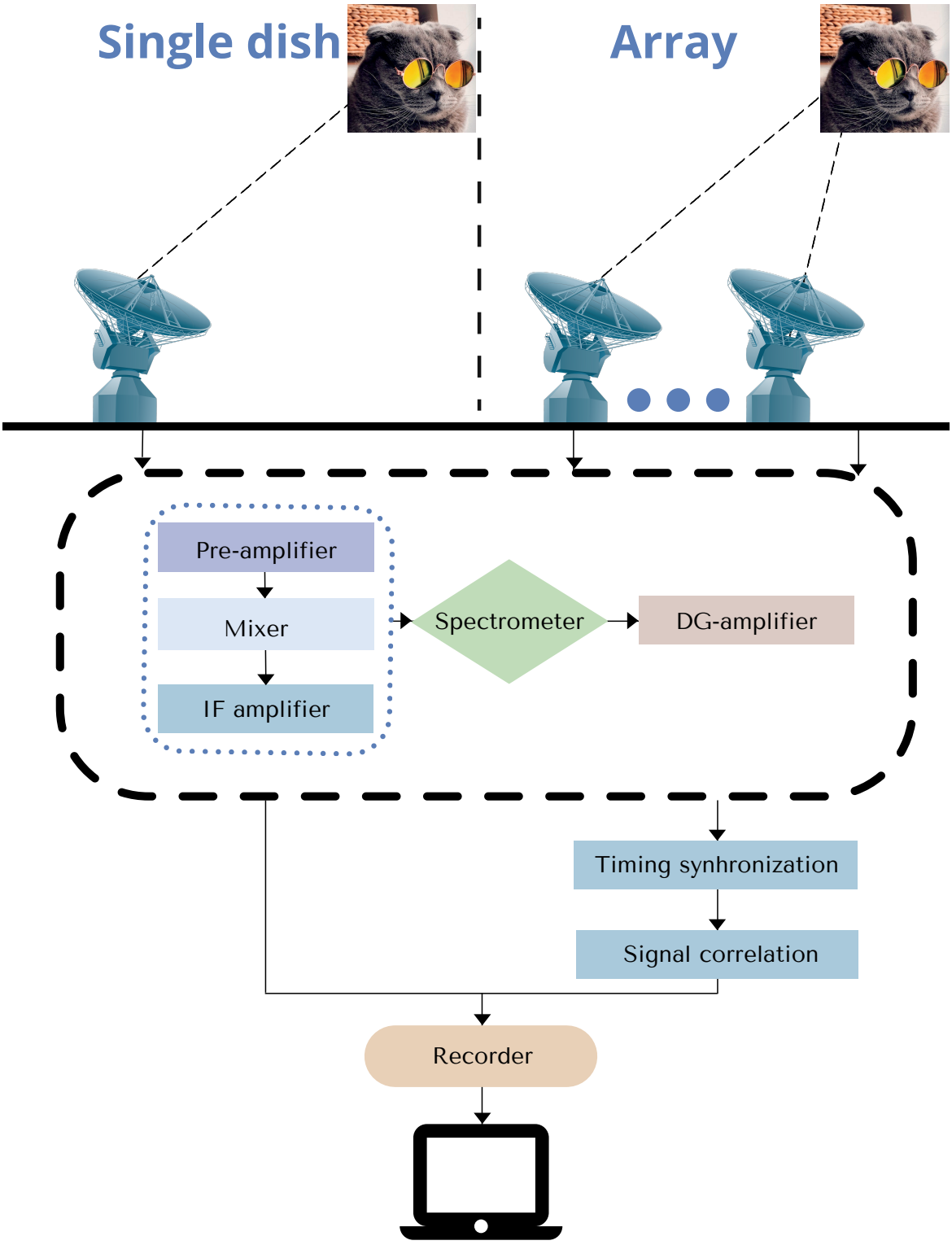

Figure 2.4: A simplistic view of radio telescopes and their relevant components. We show the example of a single dish on the left part of this figure and an array of N antennas on the right. The middle part of this figure shows the structure of the receiving system, while the bottom part shows the final stages of signal transportation before storing.

Single dish telescopes can map large areas of the sky, making them convenient for conducting galaxy surveys (EMPIRE - Jiménez-Donaire et al., 2019, CLAWS - den Brok et al., 2022b), or mapping star-forming regions in the Milky Way in great detail (Orion B- Pety et al., 2017). Moreover, several astronomical sources can be studied only using single dish measurements, such as pulsars. Single dish telescopes are sensitive to large-scale emission, which makes them essential for accounting for the missing flux (the short-spacing correction) in interferometric observations.

2.4.1 Single dish observations

The single dish observing procedure depends on the target source and emission type. In this chapter, we focus on observing techniques for spectral lines because they are the topic of this doctoral thesis. Weather conditions significantly impact single dish measurements. In the mm and (sub)-mm domain, the effects of the atmosphere have to be considered. The weather conditions have to be stable and favourable for observations. Each telescope has software specially developed for communication via observing scripts. In these scripts, the observer specifies steps the telescope has to take during observations. At the beginning of each observing shift, the telescope pointing and focus must be corrected. These steps are obtained on the bright, point sources close to the target source. The pointing corrections have to be calculated every hour and a half during the observing run, whereas focus has to be checked every few hours and an hour after sunrise and sunset.

The measured temperature, as shown in Equation 2.5, is a contribution of the receiver temperature, sky brightness temperature, source, and all the instruments used during observations. For extracting the source temperature, it is important to properly account for the additional contributions. Therefore, calibration is a crucial step in observations. To account for the contribution from the Earth's atmosphere and the effective temperature of the atmosphere, we have to know the optical depth towards the zenith measured by taumeter and calculate the air mass at the zenith distance. The next step is measuring the receiver temperature before observing the temperature of the whole system. Finally, to separate radiation coming from the sky and the source, it is necessary to observe part of the sky where there is no source and measure the cold sky temperature.

Several techniques are used to conduct single dish observations and different approaches to remove the background emission, depending on the target properties and the capabilities of the telescope. Two common ways to observe a target source are single pointing and on-the-fly mapping (OTF). The OTF mapping is used in mapping larger areas, such as whole galaxies or their parts. Each spectrum is measured in less than a second in this method. The OTF mapping is performed as follows. First, the telescope scans the source in one direction, usually along the right ascension. Next, the scanning is conducted in a perpendicular direction. The integration times for the OTF are usually short, which reduces the impact on the atmosphere. We repeat the OTF mapping until we reach the requested sensitivity.

The position, i.e. Wobbler switching and frequency switching, are used for correcting observations for the background emission. The position and Wobbler switching has a similar concept. The position switching is based on comparing the signal towards the source (ON the source) and the position of the sky close to the source (OFF the source). For position-switching, the telescope moves to ON and OFF positions, which requires stable receivers, and no line emission towards the OFF source. In this case, the Wobbler switching works on the same principle as the position switching, but only the secondary mirror moves between two positions in the sky. In Wobbler switching, the secondary mirror moves quickly. Therefore, Wobbler switching is suitable for observing compact sources in mm and sub-mm domains.

Figure 2.5: The image of the IRAM 30-meter telescope in Spain on the left panel. Image credits: J. Puschnig. The Effelsberg telescope located near Bonn in Germany is shown on the right panel. Image credit: T. D. Hoang.

2.4.2 IRAM 30-meter telescope

The IRAM 30-meter telescope (the left panel in Figure 2.5, Baars et al., 1987) is located on Pico Veleta in the Sierra Nevada in Spain, at an altitude of 2850 meters. It is one of the two facilities from IRAM (Institute for Radio Astronomy in the Millimeter Range). This is a single dish telescope with an antenna of a 30-meter diameter. It was built from 1980 to 1984, and it is one of the most sensitive and the largest single dish telescope in use. It is a classic single dish parabolic antenna. It consists of 420 aluminium panels, with the precision of 55 μm^2. It has a few heterodyne receivers. EMIR and HERA are used for spectral line measurements, whereas NIKA2 is the continuum camera. IRAM 30-m telescope can observe in a few different bands: from 0.9 mm, to 3 mm.

It is also possible to conduct a high-resolution spectroscopic measurement, which led to discoveries of new molecular species, such as the recent discovery of hydroxylamine, NH_2OH towards the centre of the Milky Way (Rivilla et al., 2020). The main beam of the IRAM 30-m is equal to 30 arcsec, which is sufficient enough to probe star-forming regions in the Milky Way at small scales: e.g. Orion B giant molecular cloud (Pety et al., 2017), The Line Emission as a Tool for Galaxy Observations (LEGO, Kauffmann et al., 2017; Barnes et al., 2020a), but also to observe molecular gas at high spatial resolution in nearby galaxies (M 51, PAWS survey - Schinnerer et al., 2013), conduct surveys of nearby galaxies in CO (HERA survey - Leroy et al., 2013), and the recent CLAWS survey (den Brok et al., 2022b), including dense molecular gas (EMPIRE survey - Jiménez-Donaire et al., 2019). IRAM 30-meter telescope is also a part of the EHT and was used to observe supermassive black holes (Figure 2.3).

2.4.3 Effelsberg telescope

The radio telescope Effelsberg (right panel in Figure 2.5) is located near Bonn in Germany. It has a 100-meter parabolic dish and is one of the biggest radio telescopes with a movable antenna in the world. It was built in 1971 and is operated by the Max Planck Institute for Radio Astronomy in Bonn. This massive construction is fully steerable and has computer support that deforms the antenna parts

[2] Comparable to the width of a human hair.

to preserve its parabolic shape. It operates at three wavelengths: 21 cm, 3 cm and 3.5 mm. Similarly, as the IRAM 30-meter telescope, Effelsberg contributes to the science operations of the VLBI. Using Effelsberg, it is possible to observe spectral lines, continuum emission and pulsars. The science that can be obtained with this telescope covers various topics. For example, using observations from this telescope, Kramer et al. (2021) measured parameters of an orbit of the binary pulsar with higher precision than the measurements that won the Nobel prize! Moreover, recent studies found fast radio bursts towards the outskirts of nearby galaxy M 81, exactly where the well-known globular cluster is located (Kirsten et al., 2022; Nimmo et al., 2022). This fast radio burst is the closest one ever detected.

2.5 Interferometry

In previous sections, we described the concept of radio astronomy and single dish telescopes. The biggest single dish antenna ever constructed is a 500-meter radio telescope FAST (Five-hundred-meter Aperture Spherical radio Telescope) in south-western China. Reaching high angular resolution in radio astronomy encounters several limitations. Because the angular resolution of a telescope depends on the observed wavelength, the diameters of radio telescopes need to be large to achieve considerable spatial resolution (Equation 2.1). An important aspect is a technical limitation in the size of a single dish telescope. The alternative solution to overcoming this issue is using the principle of interference and observing using several single dish antennas simultaneously. In the following sections, we will describe the concept of using interferometry in radio astronomy, the main properties of interferometers and outline why is excellent technical support essential when conducting interferometric observations.

The superposition of two light beams is interference. The general concept of interference is widely applied in several fields, including observational astronomy in the optical and radio domain. The combination of signals from several telescopes provides high angular resolution and the ability to resolve small-scale structures in the sky. Conducting interferometric observations is technically challenging, as it requires the simultaneous use of multiple telescopes. Next, it is crucial to understand the main principles of interferometric observations and their response to the source on the sky to properly perform the data reduction procedure and extract the information about the brightness of the observed target.

We mentioned the concept of angular resolution and the main beam for single dish telescopes in Section 2.3. In interferometry, we define the primary and the synthesized beam. The primary beam defines the angular size of the observed image and the entire field of view, defined in Equation 2.1. The synthesized beam is computed using the same equation, where instead of the diameter of the antenna, we insert the largest distance between two antennas of an array, called the baseline, B. The synthesized beam determines the angular resolution of an interferometer. Therefore, using multiple telescopes is equivalent to a single dish telescope with the size of the baseline. It is important to note that interferometric observations are more complex than single dish observations, as they require perfect time synchronization and precision. Time precision becomes crucial in the mm and sub-mm interferometric observations because Earth's atmosphere, small weather fluctuations, and the amount of water vapour significantly impact.

We show a schematic picture of an interferometric array of N antennas in the right part of Figure 2.4. The principle of interferometric telescopes is relatively similar to the case of the single dish: each antenna will collect the incoming radiation and send it further to the receiver. Before reaching the receiver, the signal will be amplified. In this case, conserving the input signal during the transportation is essential since the distance between antennas can be a few kilometres. Optical fibres are widely

used since there is almost no signal loss. After going through receivers and backends, the signal from all the antennas will be time-synchronized and sent to the correlator, where it will be combined. The final steps are storing the raw data, its reduction and the scientific use.

As shown in Figure 2.4, all telescopes in the array are pointed toward the source in the sky (in this case, the picture of a cat). The length of a path along which the incoming signal travels (solid blue lines) to the antenna is different for all antennas, which causes a time delay of the incoming signal. Several other factors must also be considered, such as time variation of the delay caused by the Earth's rotation, the finite bandwidth that causes a phase shift in the frequency domain, and instrumental response. Therefore, the incoming signal must be appropriately corrected for all the above impacts, which is unnecessary in single dish observations.

The power pattern of the interferometer, analogous to the antenna beam pattern of the single dish, where we see the main lobe and side lobes, will look like fringes (sinusoidal shape) that are the product of the response of the antenna pair. The length of the baseline determines the distance between fringes and their width. The more extended baseline causes narrower and denser fringes. The width of fringes from two antennae determines the spatial scales they can observe. Therefore, the interferometer provides a range of spatial scales determined by the array configuration. The downside is the limitation in spatial scales that interferometer can see: the largest angular scales they can probe is defined by the smallest distance between the antenna pair in a configuration, whereas the longest baseline defines the highest angular resolution (Equation 2.1). The direct consequence is that interferometric measurements will miss the emission of large-scale structures and will not provide information on the total flux of the observed target.

Depending on the array configuration and the integration time, the observed source will appear differently. The total number of antennas used for observations will determine a range of covered spatial scales and the sensitivity, which will further determine the required observing time based on the source target. We show how different shapes of an array configuration and the integration time impact the look of the source in Figure 2.6. Each configuration will produce a typical pattern on the final image. The reason for this "footprint" is that each configuration will sample the observed source differently, which impacts the sampling of the $u - v$ plane. We define an $u - v$ plane, which is perpendicular to the direction of a source and represents the baseline-projected directions towards the northeast direction.

The length of an array sets the sharpness and brightness of an image. For example, more distant antennas will provide a sharper image, whereas closely spaced antennas will provide a brighter image (see the third and fourth panel in Figure 2.6). Finally, the longer observing time increases the image brightness (the fourth and the fifth panel in Figure 2.6).

2.5.1 Interferometric observations

The strategy for interferometric observations depends on the source we want to observe, the sensitivity, and angular resolution. Based on that, we can decide between several ways to observe the source of interest. The main goals of all these approaches are to provide the best possible $u - v$ coverage and reduce the impact of the noise. In the case of small, compact sources that the beam can cover, it is possible to have short observing times and produce snapshots. For extended sources, we use full tracks that provide a sufficient $u - v$ sampling. In more extreme cases, like observing a nearby galaxy or mapping a larger portion of the sky, and when the field of view is significantly larger than the primary beam, we sample the map into smaller sub-maps, each matching the primary beam. We observe each sub-map separately. This procedure is called mosaicking. In addition, we use the multi-array

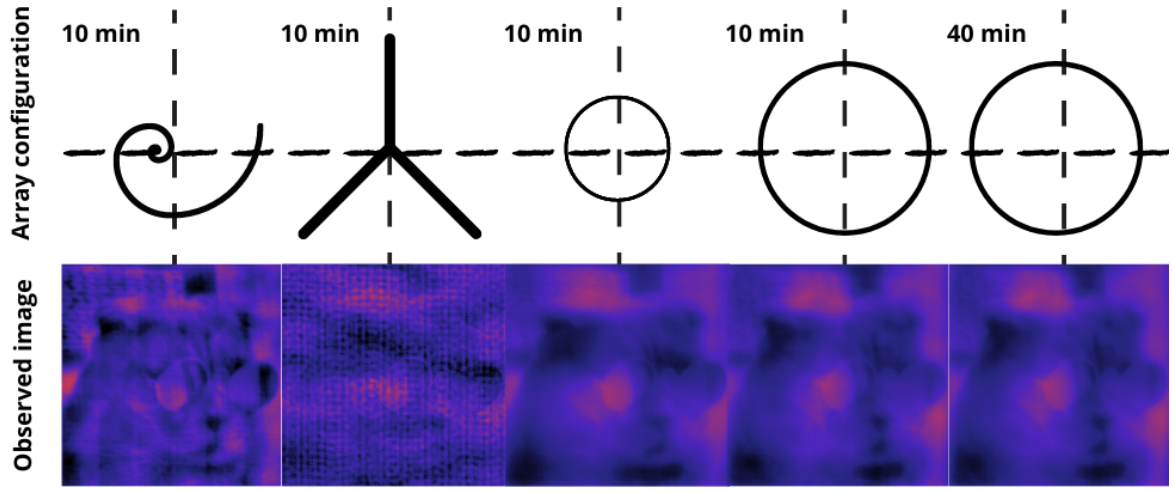

Figure 2.6: Example of a few different array configurations and their impact on the observed image of a cat. We show example of the spirally shaped, Y-shaped, and circular configurations. In addition, we show the integration time for each configuration. Source: NRAO

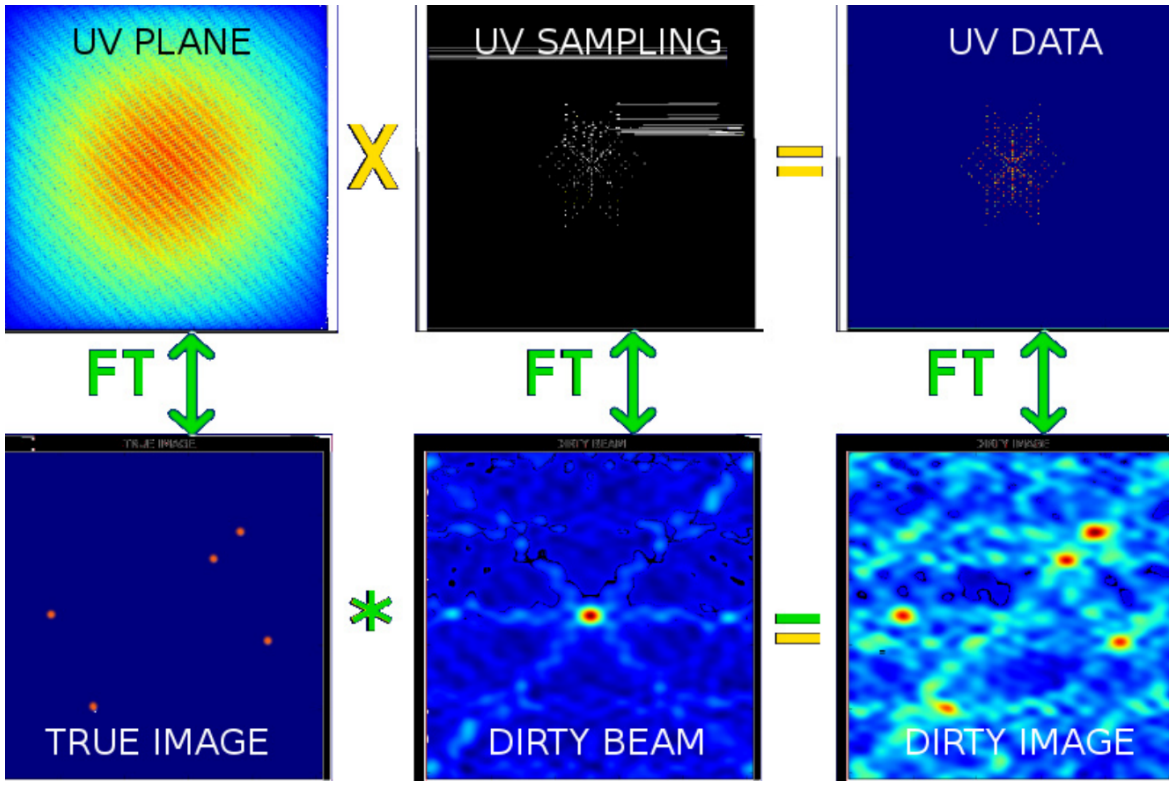

Figure 2.7: The relation between the $u - v$ data, image and the true brightness distribution of a source. Image taken from An Interactive Tool To Learn Interferometry (APSYNSIM - Marti-Vidal, 2017).

configurations to improve the quality of observations further and extend the range of physical scales we want to probe.

2.5.2 Interferometric data reduction

Interferometric data reduction is a complex, time-consuming procedure. In this section, we will briefly describe the stages of interferometric data reduction without providing further details. We refer to detailed descriptions of the data reduction steps and pipeline presented in Leroy et al. (2021a), which is also used for data reduction of ALMA ACA observations of nearby starburst galaxy NGC 253 in Chapter 5, Section 5.3.1.

The interferometric data reduction aims to convert the incoming signal into an image representing the observed source. The final output from an interferometer and the input for the data reduction procedure is the visibility function, V. The first step in the interferometric data reduction is called staging the visibility data. First, we calibrate the data and extract the source and spectral windows. Next, we select and extract spectral lines and remove the continuum. In the last step, we weight the data based on the noise models before moving to the imaging. Such prepared visibility data are ready for the following stages of the data reduction.

The visibility contains information about the following parameters: the antenna power pattern, the source brightness, and the coherence function for each measured frequency towards each direction. The main challenge is to produce the image of a source from the measured visibility function. The aperture synthesis technique (Kellermann & Moran, 2001) is developed to achieve this goal. The van Citter-Zernike theorem sets the main base for the aperture synthesis, as it connects the $u - \upsilon$ plane and the sky via Fourier transform. In the most straightforward representation of the van Citter-Zernike theorem, the brightness distribution of a source is the inverse Fourier transform of the visibility function, which is applicable for most astronomical sources, except for pulsars and masers.

We illustrate the relation between the visibility function (the top right corner) and the actual brightness of a source (the bottom left corner) in Figure 2.7. All images shown in the top row are connected with the images in the bottom row via the FT. As outlined in the previous section, the visibility function depends on $u - \upsilon$ coverage, and it is a set of discrete values. In reality, the $u - \upsilon$ sampling is never complete or continuous. Applying the van Citter-Zarnike theorem, we see the true image is the FT of the $u - \upsilon$ plane. The interferometers sample that plane and the sky emission and get the $u - \upsilon$ data. Mathematically, the $u - \upsilon$ data is the multiplication of the $u - \upsilon$ plane and the sampling function. The FT of the $u - \upsilon$ sampling gives the dirty beam, while the FT of the $u - \upsilon$ data is the dirty image (the bottom right corner in Figure 2.7).

Figure 2.8 shows the steps commonly taken in interferometric data reduction. We perform the data reduction using software specifically designed for conducting such tasks. These packages are usually developed to handle and reduce observations from specific telescopes. For example, NOEMA observations are reduced in the Grenoble Image and Line Data Analysis Software (GILDAS). Common Astronomy Software Applications (CASA - McMullin et al., 2007) is used for processing ALMA and the Very Large Array (VLA) observations.

The dirty image of a source is the convolution of the accurate source brightness distribution and the response of the interferometer. To reconstruct the proper source brightness distribution from the interferometer sampling, we have to calculate the inverse Fourier transform of the $u - \upsilon$ data. However, applying the inverse FT requires the full sampling of the $u - \upsilon$ data, which is never the case. Instead of applying the inverse FT, we use the Fast Fourier Transform (FFT), but this method requires a regularly sampled $u - \upsilon$ plane. The $u - \upsilon$ plane is irregularly sampled and can also

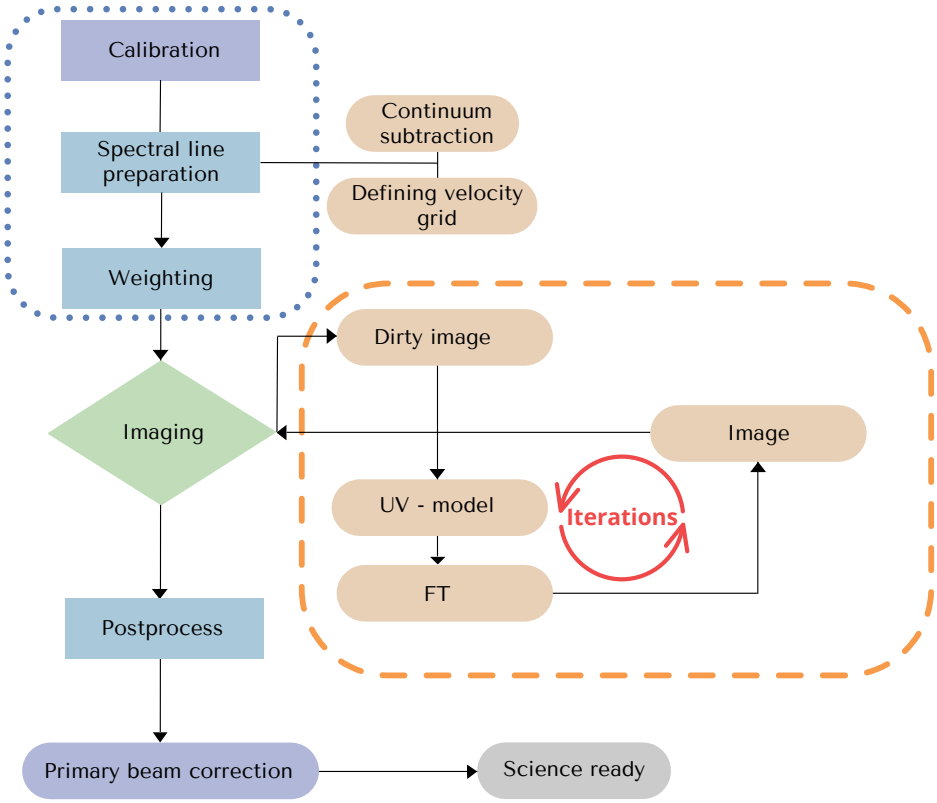

Figure 2.8: Stages of the interferometric data reduction. After extracting the spectral line and weighting the data based on the noise model, we perform deconvolution to produce the image of the observed source. After that, we do the postprocessing procedures to prepare the data set for science use.

contain areas that are not sampled, implying that values of the visibility function can be anything in non-sampled regions. Luckily, it turns out that even a lower number of observations are still enough to reconstruct the brightness distribution of a source correctly. The procedure in which we use the dirty image and the dirty beam of an array to produce the actual image of the source is called imaging or deconvolution/CLEAN (Högbom, 1974) (orangle rectangle in Figure 2.8). Following the work of Högbom (1974), several imaging algorithms were developed to improve the cleaning processes, such as the algorithm presented in Helfer et al. (2002) or the recent multi-scale cleaning (Cornwell, 2008). In CASA, the cleaning is an automated procedure containing several parameters and called by running the task `tclean`.

In the following, we explain the principle of the clean algorithm (orangle rectangle in Figure 2.8). The main goal of the cleaning algorithm is to construct source brightness distribution and reduce the noise as much as possible. Therefore, we can specify the region within which we expect to find the emission of the observed target. The initial step in cleaning is to assume a model of the true source brightness distribution - clean components. For example, a source can be described as a collection of point sources (Högbom, 1974), or as a combination of differently sized Gaussian functions - “multi SCALE” clean (Cornwell, 2008). We locate a peak emission on the dirty image, multiply it by the dirty beam, and remove it from it. We repeat this step as long as we do not match the stopping condition. The cleaning procedure is finished when we reach a total number of clean components or if the peak emission is below the threshold noise level. The remainder of the dirty beam is called the residual.

After leaving the loop, we multiply the map of clean components extracted during cleaning with the Gaussian beam and add the residual. In the postprocessing stage, we correct data for the missing flux (Section 2.5.3) and then proceed with the final steps in preparing the data for the science use.

The final stages of data reduction are performed to further improve the image for scientific use (the bottom part of Figure 2.8). The response of each antenna is still contained in the data. Thus, we need to correct our observations for a primary beam, and this task is done simply by dividing the image by the primary beam. Next, we convolve our image to a joint spatial resolution and sample the grid according to the Nyquist sampling to keep all the relevant information and reduce the data volume. In the end, we store the data as a Flexible Image Transport System (fits) file.

2.5.3 Combining with the single dish data - feathering

Interferometric observations provide information on small-scale structures in the sky. However, the limitation in using interferometers is that the largest spatial scales they can see are defined by the minimum distance between the two antennas, d_{min}. As a result, interferometric data will miss the extended emission, which can significantly contribute to the total flux of a source, as demonstrated in Pety et al. (2013). Therefore, combining interferometric with single dish observation measurements compensates for the missing flux. This process is called the short-spacing correction, or feathering (Stanimirovic et al., 1999; Koda et al., 2019; Cotton, 2017).

The angular size of the observed source to the primary beam determines the single dish observations needed for the short-spacing correction. For example, if the angular dimensions of a source are smaller than half of the primary beam, a single pointing towards the source is enough, whereas the OTF map is needed.

The feathering procedure is automatized in software used for data reduction, for example, the `feather` task in CASA (Cotton, 2017). The feathering process has a few steps. At first, the single dish data, beam size and interferometric data are Fourier transformed. Then the interferometric image is multiplied by the factor favouring short-spacing data less. The FT of the single dish data is rescaled according to the interferometric and single dish beam ratio. Such data sets are then combined and converted to the image plane.

2.5.4 NOEMA

NOrthern Extended Millimeter Array (NOEMA - Figure 2.9) is located at the Plateau de Bure in the French Alps and is the second facility run by IRAM. NOEMA is at an altitude of 2550 m, and it is the successor of the Plateau de Bure interferometer (PdBI), a six-antenna interferometer that operated from 1988 to 2014. NOEMA has 12 antennas, each with a 15-meter diameter. The last antenna started being fully operational in January 2022, and NOEMA reached its full capabilities and sensitivity.

Compared with the PdBI, NOEMA has higher spatial resolution and sensitivity by a factor of 4 and 10, respectively. NOEMA antennas can move along two tracks. One is in the north-south direction, whereas the other is on the east-west side. This relocation of telescopes allows a range of possible spatial resolution. For example, in its most extended configuration, NOEMA replaces a single dish telescope with a diameter of around 1200 meters. It can observe in several bands: at 0.8, 1, 2, and 3 mm.

NOEMA is part of many extensive surveys and can probe small spatial scales in nearby galaxies in dense molecular gas (i.e. NGC 3627 - Bešlić et al. (2021), M 82 - Krieger et al. (2021), the ongoing NOEMA M 51 large program (PIs: E .Schinnerer and F. Bigiel), but also cold molecular gas in more

Figure 2.9: NOEMA interferometer in the French Alps, near Grenoble, operated by the IRAM facility. Image credit: IRAM.

distant Universe (PHIBSS, PHIBSS2, e.g. Genzel et al., 2015), and the ongoing NOEMA3D survey (PIs: R. Genzel, R. Neri, and L. Tacconi). The high-resolution spectroscopy that NOEMA provides allows the detection of new molecular species, such as the first detection of the CCS molecule in the protoplanetary disc (Phuong et al., 2021). With a new `POLYFIX` receiver with a bandwidth of 32 GHz, it is now possible to observe at an even higher spectral resolution, observe two different bands simultaneously, and conduct more extensive spectral surveys.

2.5.5 ALMA

The Atacama Large Millimeter/Submillimeter Array (ALMA) is the interferometer operated by ESO. It is located in the Chajnantor plateau desert in the Chilean Andes, at an elevation from 4576 to 5044 m. This interferometer started working in the fall of 2011. ALMA has 66 antennas that, in the most extended configuration, are equivalent to a 16 km single dish telescope! The distance between antennas is a few hundred meters in its most compact configuration, which allows ALMA to provide an impressive range of measured spatial scales toward one object. ALMA facility breaks many records: it is the largest observing facility in the world, located at the highest altitude. Its location provides good quality observations in the mm and sub-mm regimes.

ALMA has three different types of antennas. It has 50 antennas with a diameter of 12-meter, providing the highest spatial resolution observations. Next, 12 antennas have a 7-meter dish and, together with the 4 remaining antennas (the total power), make the Atacama Morita Compact Array (ACA). ALMA operates in 10 bands, from 0.3 to even 8 mm, and can reach a high spectral resolution of 0.1 km s^{-1}. Therefore, ALMA telescopes are widely used for observing many different objects in the molecular line and continuum emission. Currently, there are a few big surveys conducted with ALMA. We mention a few of them, starting from surveys of high-redshift galaxies: ASPECS (The

Figure 2.10: ALMA telescope. Image credit: ESO.

ALMA Spectroscopic Survey in the Hubble Ultra Deep Field, PI: F. Walter - Walter et al., 2016), the ALMA Large Program to Investigate CII at Early Times (ALPINE, PI: O. Le Fèvre - Le Fèvre et al., 2020), and Reionization Era Bright Emission Line Survey (REBELS, PI: R. Bouwens - Bouwens, 2020), to nearby galaxies surveys such as PHANGS survey (PI: E. Schinnerer Leroy et al., 2021b), an ALMA Comprehensive High-resolution Extragalactic Molecular Inventory (ALCHEMI, PI: S. Martin - Martín et al., 2021), The Virgo Environment Traced in CO Survey (VERTICO - PI: T. Brown), to the Milky Way regions: The ALMA Central molecular zone (CMZ) Exploration Survey (ACES - PI: S. N. Longmore), ALMA IMF (PI: F. Motte Motte et al., 2022), and ALMA GAL (PI: S. Molinari).

2.6 Final processed data cubes - some definitions

The fits (Flexible Image Transport System) files are a way of digitally storing multidimensional data or tables. The fits file are organized in two parts. The first part describes the data set, called a header. Fits header is the ASCII (American Standard Code for Information Interchange) table and contains information about the data set, such as its dimensionality, length of arrays, units, the telescope used for observations, and history of previous processing of the data. The second part of the fits file is the multidimensional data.

The data have three dimensions in radio and mm astronomy, particularly for spectroscopic measurements. The first two dimensions are spatial information about the source and are expressed in equatorial or galactic coordinates. The spatial grid is divided into pixels. The third dimension is the observed frequency of velocity, which provides information about the emission (spectrum) of a source. The velocity axis is divided into channels. Such three-dimensional data is often called a spectral cube. We show the example of spectral cube in Figure 2.11. Any two-dimensional cut of the spectral cube is called a slice. When one dimension of the slice is in spatial coordinates and the other on the velocity, we refer to the position-velocity ($p - \upsilon$) slices.

It is worth pointing out that astronomical measurements, hence data cubes, contain noise, which can be significant when working with the faint molecular emission, as we will show in Chapters 4 and 5. Similarly, when conducting the data reduction, we aim to reduce the impact of the noise on our results, i.e. to increase the signal-to-noise ratio and analyse regions that contain signal. One way is by constructing masks and applying these to the data. There are many ways to create the mask, but the

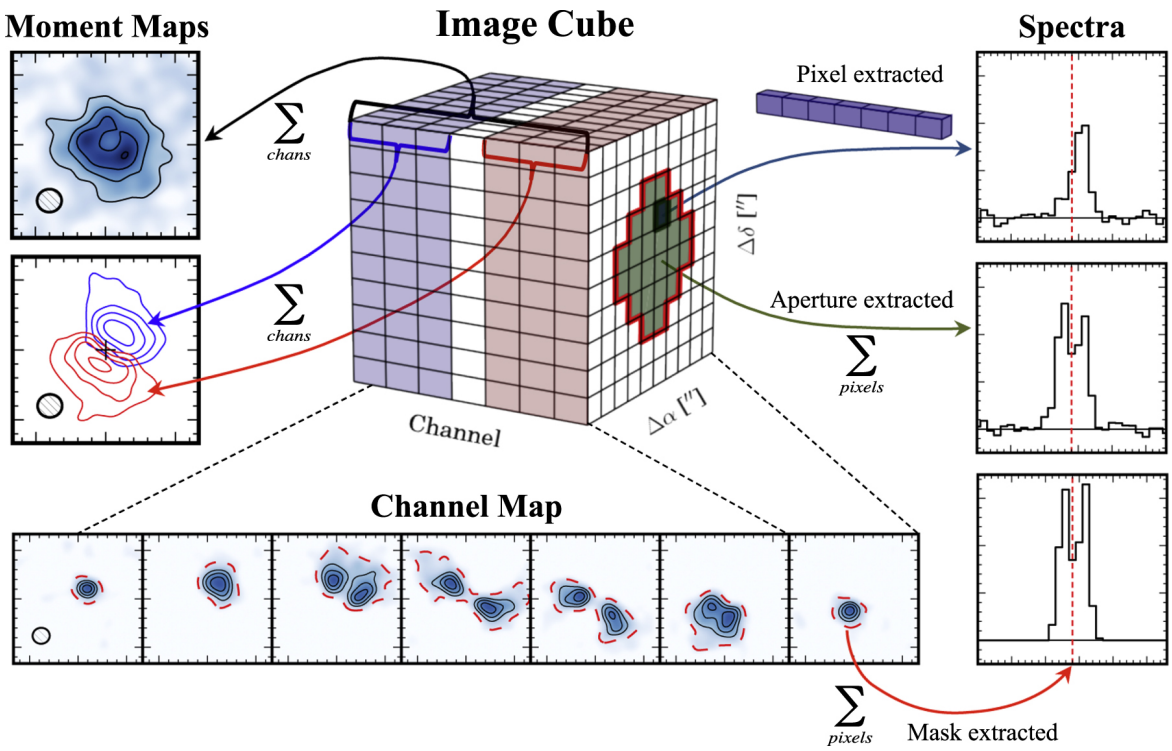

Figure 2.11: The example of the data cube. Two dimensions are spatial coordinates, usually right ascension (x-axis), and declination (y-axis). The third axis is the velocity (υ). The examples of zeroth and first moment maps are shown on the left part of this figure, whereas the spectrum of a selected pixel is on the right. Channel maps are shown in the bottom panels. Image credit: Loomis et al. (2018).

most common is a signal-to-noise-based mask of some bright emission line. In mm astronomy, the CO emission is the commonly used line for determining the signal-to-noise ratio. The noise is estimated by calculating the mean root square of the signal-free channels. Masks have the same dimension as the data and, in the simplest case, will contain only zeros and ones. All pixels and channels where the mask is set to zero will be masked.

The alternative way of dealing with the noise is averaging (binning) respective to some quantity, such as the radial distance, mass, and intensity. The three-dimensional binning in which we average spectra of several pixels and measure their properties is called spectral stacking. We will outline the spectral stacking principles in Chapter 4, Section 4.1.

Moments

In radio astronomy, three moments are used to analyze the data. The order zero is the integrated intensity (I) map, and it represents the sum of all emission along the velocity axis:

$$I = \Sigma_i (T_{\mathrm{B,i}} \cdot \Delta\upsilon), \tag{2.6}$$

where the $T_{\mathrm{B,i}}$ is the brightness temperature in the i-th velocity channel, and $\Delta\upsilon$ is the channel width in units of km s^{-1}. The integrated intensity has units of K km s^{-1}, or alternatively Jy/beam km s^{-1}.

Moment 1 map is also called the velocity map (υ_{mean}). It is intensity-weighted, and it overall shows

the velocity at which the intensity peaks in units of $\mathrm{km\,s^{-1}}$:

$$\upsilon_{\mathrm{mean}} = \frac{\Sigma_i (I_i \cdot \upsilon_i)}{\Sigma_i I_i}, \tag{2.7}$$

where υ_i is the velocity in the i-th channel. From this moment map, it is possible to reconstruct the rotation curve of a galaxy.

The second order of the moment map is the velocity dispersion of the spectral line, and the second moment map has the same units as the first order moment map. It is computed as:

$$\sigma = \frac{\Sigma_i (I_i \cdot (\upsilon_i - \upsilon_{\mathrm{mean,i}})^2)}{\Sigma_i I_i}, \tag{2.8}$$

where $\upsilon_{\mathrm{mean,i}}$ is the first moment from Equation 2.7. There are other ways to calculate the velocity dispersion. The second moment approach is sensitive to the noise, so the alternative way is to calculate it as:

$$\sigma = \frac{I}{\sqrt{2\pi} T_{\mathrm{peak}}}, \tag{2.9}$$

where the T_{peak} is the peak of the spectrum. This approach is not sensitive to the noise, but it does not assume the velocity profile and does not account for the potential spectral complexity. In that case, the observed emission along the line of sight has to be decomposed into individual components, as we will mention in Chapter 5, Section B.4.

CHAPTER 3

Star formation

"*It is unlikely that we will ever see a star being born. Stars are like animals in the wild. We may see the very young, but never their actual birth, which is a veiled and secret event. Stars are born inside thick clouds of dust and gas in the spiral arms of the galaxy, so thick that visible light cannot penetrate them.*"

— Heinz Pagels, American physicist

From the beginning of humankind, stars have intrigued us, which is still true a couple of hundred thousand years later (Figure 3.1). Traditionally, people used seasonal changes in the position of stars to determine the adequate time to perform botanical work and when the winter commences. The night sky was a compass for locating the north pole and guidance during long journeys. Today, we know that we owe our existence to stars because they provide conditions for planet formation and their habitability. In addition, stars are factories where elements heavier than H, He and Li are produced and released in the ISM at the final stages of stellar evolution. Stars spend their life being in a constant battle against the gravitational force that tends to collapse them. They fight back against collapsing via thermonuclear reactions and the degeneracy of matter. Most importantly, star formation is one of the fundamental processes in the Universe.

Crucial requirements for stars to form are gravity and molecular gas. However, the dominant mechanisms that lead to star formation, including the environmental impact on the physical condition of gas, are still unclear. Several theories have been developed to explain this phenomenon, supported by observational evidence, spanning ranges of physical scales, from sub-pc to a few kpcs. In this chapter, we give an overview of star formation. We describe a basic picture of star formation process in Section 3.1. In Section 3.2, we describe ways to quantify the star formation rate (SFR), introduce the initial mass function (Section 3.2.1), and describe star formation tracers (Section 3.2.2). Section 3.3 presents current theories of star formation. In Section3.4 we provide a literature overview of the cosmic evolution of star formation, from early galaxies to star formation in the Milky Way.

Furthermore, Section 3.5 presents studies aiming to understand star formation using observations of molecular gas across star-forming regions and how the molecular gas fits into the perspective of star formation theories. Section 3.6 highlights the importance of studying densest molecular gas phase. Finally, we will review several open science questions that this thesis addresses (Section 3.7). Until stated otherwise, this chapter is based on review (Kennicutt & Evans, 2012; Krumholz et al., 2016; Klessen & Glover, 2016).

Figure 3.1: The Cosmic Cliff, the edge of the star-forming region in NGC 3324. The IR image of Carina nebula, taken by James Webb Space Telescope. Image credits: NASA/ESA/CSA/STScI.

3.1 Star formation in a nutshell

Star formation is a multi-scale problem involving complex physical processes such as turbulence, galactic flows, magnetic fields, radiation fields, and a wide range of gas densities (Girichidis et al., 2020). Stars usually do not form alone (Hoyle, 1953; Kruijssen, 2012), but rather in stellar associations (Lada & Lada, 2003). Only one third of a core's mass turns into a star (Alves et al., 2007), a small fraction of the total mass of a molecular cloud. Within the GMCs, local structures that are overdense and gravitationally bound form clumps and cores. These are the progenitors of star formation (McKee & Ostriker, 2007). Clumps are the densest sub-structures of GMCs and are places of clustered star formation. Single stars and binaries form out of cores.

A star is being formed at the moment when the pressure cannot further suppress the molecular cloud from gravitational collapse. The initial stage of star formation begins in the molecular cloud, in the prestellar cores. These are the coldest, densest and gravitationally bound parts within the molecular clouds and filaments. To reach the physical conditions of a protostar, the density, temperature and radius of a core must change over many orders of magnitude. The only mechanism that can allow that to happen is gravitational compression. Therefore, the gravitational collapse of prestellar cores initiates star formation and eventually hosts a protostar. It can be induced in two ways: spontaneously or via external mechanisms. Spontaneous collapse is the so-called self-gravity, while the sources of external mechanisms are supernova shocks, winds from massive stars, cloud−cloud collisions (Fukui et al., 2021a,b), and spiral density waves.

Moreover, a magnetic field is crucial since it prevents the core from collapsing or further supports the infall. The collapse heats the surroundings and can ionize the gas. There are two primary sources of energy at these stages: the energy released from gravitational collapse and the energy released

from the thermonuclear burning of deuterium. As gas moves towards the protostar, the difference in energies heats the dust, which will start emitting at longer wavelengths. Therefore the IR and radio parts of the spectrum are the source of information about the early stages of star formation.

There are a few intermediate stages of a protostar between the quiescent core and the main-sequence star. We illustrate these steps in Figure 3.2. The temperature of a protostar rises as it goes towards later stages, and the accretion disc disappears. There are classes from 0 to III of a protostar. Apart from the dust that obscures the protostar with thermal emission, the protostar will create a stellar wind seen in the complex velocity structure of molecular line emission and shock tracers, such as SiO(2–1). This is class 0 of a protostar. Class I starts showing IR emission that can be distinguished between the dust emission and the protostar. However, the protostar is still highly obscured. The next stage is class II, within which the NIR and MIR emission comes from the protostar and the accretion disc. Protoplanetary discs form at this stage. Finally, class III protostars are the pre-main sequence stars with weak accretion disc and forming planetary systems. Once the core of a protostar reaches temperatures higher than 10^7 K, and densities of $10^5\,\mathrm{kg\,cm^{-3}}$ (McKee & Ostriker, 2007), the nuclear fusion of hydrogen will start, and the star will be born. This stadium is called the main-sequence star, the stage where the star is in equilibrium. The thermonuclear reaction in its core will support gravity, and as long as the core contains hydrogen, it will remain stable.

Finally, the lifetime of a star will be determined by its mass. Massive stars have short lifetimes but produce heavier elements and enrich the ISM. Less massive stars will remain stable for a longer time. It is thought that the first stars were massive because they can explain the presence of heavier elements in the early Universe.

3.2 Measuring star formation rate

In the previous section, we mention the existence of stellar clusters due to cloud fragmentation. Young massive stars are found within stellar clusters and predominantly contribute to the total stellar mass. On the other hand, single, low-massive stars are the most numerous. This unbalance significantly impacts how to parametrise the distribution of stellar masses, further impacting the estimation of the current SFR. In this section, we describe the recipe to calculate the SFR of a galaxy or a star-forming region.

In the most simplistic approach, the current SFR is measured by counting all the young stars across some star-forming region. However, that is not always possible. Even in the Milky Way, some regions are embedded in the dust. Observing and resolving individual stars in other galaxies is not possible due to the lack of high resolution needed to resolve these objects. Therefore, the main challenge in the case of unresolved stellar populations is distinguishing light between recently born and older stars.

A few assumptions are important in calculating the SFR. First, the SFR is constant over time because the lifetime of young massive stars is shorter than the typical dynamical time of a galaxy ($\sim 200\,\mathrm{Myr}$). The second assumption implies the stellar population is in statistical equilibrium, meaning the rate of born stars is balanced with the number of dying stars. Additionally, the star formation history (SFH) is assumed to be constant over time. The incoming light we observe towards some region is the sum of light from all the stars within that region. Thus, the measured stellar luminosity will depend on the SFR, the IMF, and the total energy output of a star. The latter is known from stellar evolution models. In the following, we describe the IMF (Section 3.2.1) and how we can be sure that we measure the light coming from the young massive stars (Section 3.2.2).

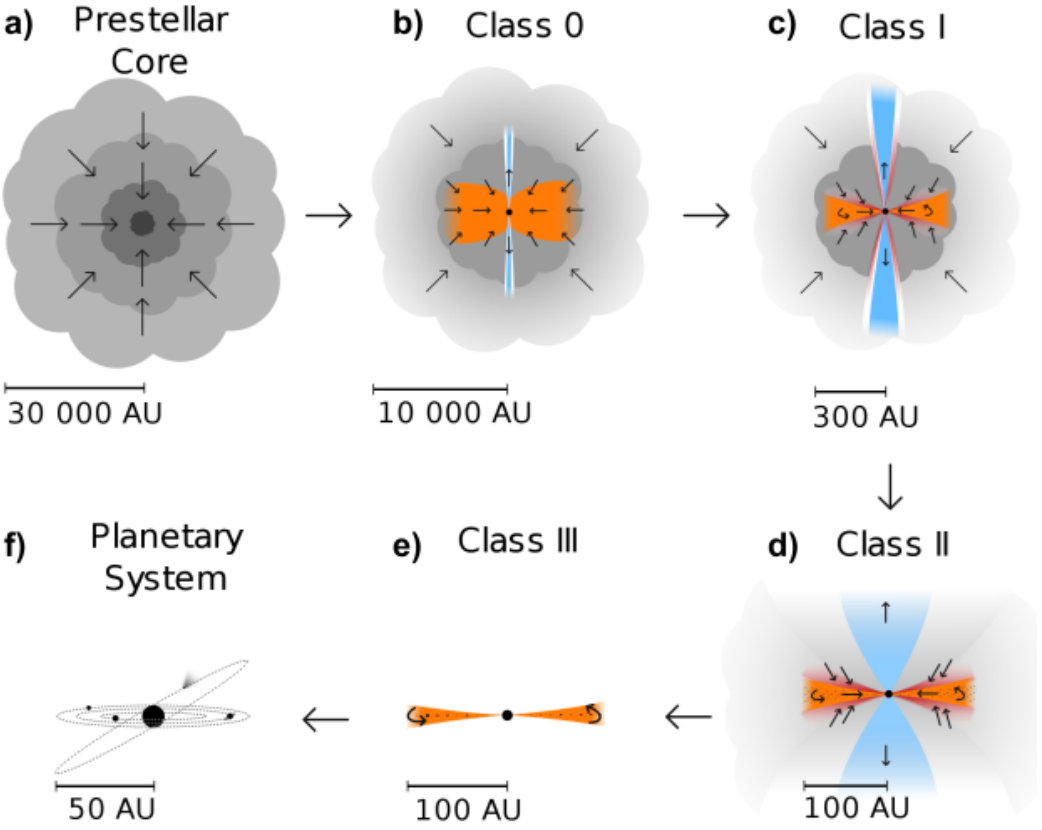

t!]

Figure 3.2: Phases of protostars. The process starts within a prestellar core (panel a) when pressure cannot balance gravity, and the gravitational collapse of gas produces a protostar. Panels from b) to e) show the classes of protostars. The remainder of the molecular cloud and accretion disc around a protostar disappear from Class 0 (panel b) to Class III (panel e). Finally, panel f) shows the final stage of star formation, with a system of a main-sequence star and planets. Image source: Persson (2013).

3.2.1 The initial mass function of cores and stars

The mass of a star determines its evolutionary path and death. Therefore, the first step is to accurately predict how many stars of a certain mass will form in a galaxy. The mass distribution of cores, CMF (see Chapter 1 Section 1.4.4) is a potential driver of the mass distribution of stars IMF_{*} and clusters $IMF_{clusters}$ (Sadavoy et al., 2010). Both can be described via a power-law function. Some studies showed that the slope of mass distribution of cores is closer to the mass distribution of stars than to the mass distribution of molecular clouds (Alves et al., 2007; Sadavoy et al., 2010). The observed offset between the CMF and IMF_{*} (Enoch et al., 2010) is explained by the low star formation efficiency of cores since a fraction of its mass contributes to star formation (Alves et al., 2007).

The IMF is a practical way to describe the distribution of initial stellar masses of stars and stars within clusters. It is expressed as the probability density distribution (PDF) for masses M, where M corresponds to the main-sequence star. In principle, the IMF can be calculated by counting all stars. In reality, it is difficult to do so since most mass is found within high-mass stars in stellar clusters and binaries, whereas the most numerous are single, fainter stars belonging to later spectral classes. Therefore, the low and high-mass end of this distribution is highly uncertain. Massive stars

are short-living objects, and their observation is limited to stellar clusters, whereas low-mass stars are faint and hard to observe, especially in a binary system where the companion star is much brighter.

Nevertheless, although it may appear surprising, the distribution of stars between 0.01 and 50 $M_\odot$ appears to be universal and environmentally independent (see, e.g. Bastian et al., 2010; Habibi et al., 2013). The first attempt to describe the IMF was made by Salpeter in 1955 (Salpeter, 1955) for main-sequence stars in the solar neighbourhood:

$$\xi(M)\Delta M = \xi_0 \cdot \left(\frac{M}{M_\odot}\right)^{-2.35} \cdot \frac{\Delta M}{M_\odot}, \tag{3.1}$$

which is a power-law function. ξ_0 is a constant, and the slope α is 2.35. The next one is represented in Kroupa (2001) and described as a broken power-law:

$$\xi(M) = M^{-\alpha}, \tag{3.2}$$

where α depends on the range of masses: $\alpha = 0.3$ for $M < 0.08\,M_\odot$, $\alpha = 1.3$ for masses between $0.08M_\odot$ and $0.5M_\odot$, and $\alpha = 2.3$ for masses higher than $0.5M_\odot$.

Another way to characterize the IMF is using the log-normal function - the Chabrier IMF (Chabrier, 2003, 2005):

$$\xi(\log M) \propto \begin{cases} \exp\left(-\dfrac{(\log M - \log 3.5)^2}{2 \cdot 0.2^2}\right), & \text{for} \quad M \geq 4M_\odot \\ M^{-1.7}, & \text{for} \quad M < 4M_\odot. \end{cases} \tag{3.3}$$

We show these IMFs in Figure 3.3. Overall, they all agree nicely for masses higher than $M_\odot$ and peaks between 0.2 and 1 $M_\odot$. The low and high-mass ends remain undefined, although there are some attempts to describe these parts. It was suggested that the IMF flattens for masses lower than the solar mass (Miller & Scalo, 1979). For the high-mass end, Zinnecker & Yorke (2007) found a physical cut-off in mass of about $150\,M_\odot$. Similarly, a mass cut-off is found for the IMF of stellar clusters (Gieles et al., 2006; Chandar et al., 2011).

The current main issues of the stellar IMF are the assumed evolutionary models and the population of brown dwarfs. In principle, the universality of the IMF is not yet fully understood since it is expected to vary from region to region, including variation with metallicity and even velocity dispersions within the stellar clusters. Villaume et al. (2017) found that the latter causes variations in the IMF, whereas there is no strong dependence on Z. There is no doubt that probing smaller scales in NIR will allow observing brown dwarfs and provide a better picture of the low-mass end of the IMF. Another issue in constraining the IMF is the poor sampling and the domain of low number statistics, as described in (Barnes et al., 2017). Low number sampling of the IMF affects the slope by ±0.1 (Elmegreen, 1999), which gives the variation in stellar masses by a factor of two.

3.2.2 Star formation tracers

The next step toward calculating the SFR lies in measuring the light from the young stars. One of the challenges with performing such a task is appropriately distinguishing stellar light from young and older stars. Here we describe the common ways to calculate the SFR by observing different tracers of young stars. Star formation can be observed in the UV, optical, infrared and radio domains in line or continuum emission. Some of these come directly from a star, while others are the effect of stellar

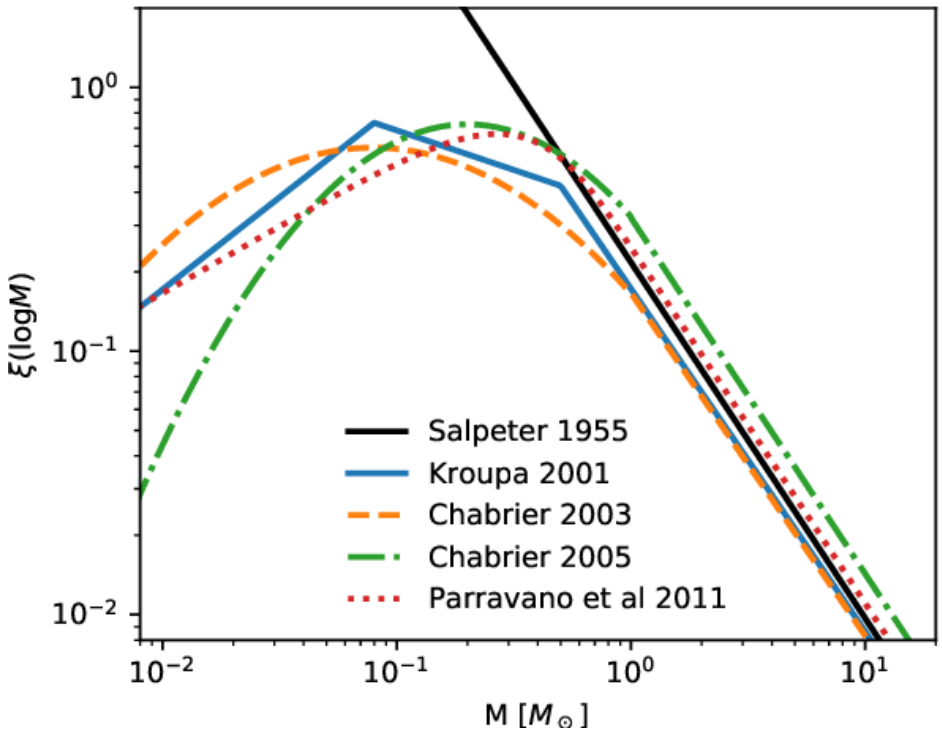

Figure 3.3: The examples of the IMF. Black line shows the Salpeter IMF (Salpeter, 1955), and blue line the Kroupa IMF (Kroupa, 2001). Orange and green lines represent Chabrier IMF, and dotted red line shows IMF from Parravano et al. (2011). Image credit: Colman & Teyssier (2020).

light on the ISM. Nevertheless, neither of these star formation tracers include all stellar light, and their use will depend on the observed system.

3.2.3 Hydrogen recombination lines

Recombination processes

Recombination is the inverse of ionization, i.e. an ion combines with an electron, releasing a photon. This process changes the ionization state of a particle from being ionized to an atomic state. After recombination, the atom is not necessarily in the ground state. Therefore, the electron captured in some of the excited states will move to lower energy orbits, releasing a photon with energy equal to the difference in energy levels. Hydrogen recombination lines can be divided into various series depending on the final energy state, and these lines can be found from UV to mm wavelengths. Transitions to the ground state belong to the Lyman series. The well-known Lyman α (Ly α) line is at 121 nm. The next are Balmer transitions in the optical domain. For example, Hα line at 656.2 nm is the $n = 3 \rightarrow 2$ and the $n = 4 \rightarrow 2$ is the Hβ at 486 nm. The Paschen series is mainly in the near-IR domain. Hydrogen recombination lines, particularly the Balmer series, are prominent in galaxies and accessible with ground-based observations.

Tracing recent star formation using hydrogen recombination lines

Hydrogen recombination lines are an excellent tracer for recent star formation. Strong radiation fields around young massive stars ionize local gas and produce HII regions. Free electrons will eventually be captured by the ions, which in turn will produce numerous recombination lines. Therefore, recombination lines are the product of young massive stars and direct tracer of star formation. However, the downside of using recombination lines is that some of these are sensitive to dust absorption. There are ways to correct observations for dust attenuation; for example, when using the Hα emission line as a star formation tracer, it is possible to calculate dust attenuation via the Hα/Hβ ratio, known as the Balmer decrement. The Hα/Hβ line ratio depends on the temperature and electron density (Osterbrock, 1993; Domínguez et al., 2013). Assuming a reddening law (i.e., the extinction curve - see, e.g. Calzetti et al., 2000), the Hα emission is corrected for dust attenuation. However, Hα is not a good tracer of star formation in circumnuclear regions of starburst and dust-rich galaxies. Another limitation of using Hα as a star formation tracer is that it does not trace the low star-forming regions where the IMF gets poorly sampled for massive stars (Section 3.2.1).

In cases when Hα is not a good tracer of SFR, lines from other hydrogen recombination series may be used to estimate the SFR. Other commonly used hydrogen recombination lines in the near-IR domain are Paschen α, β, and γ and Brackets α and γ lines. These lines are less sensitive to dust attenuation but are considerably fainter than the Hα. An alternative way to constrain the SFR is to use recombination lines found in the mm and radio domain - radio recombination lines (RRL), such as the H40α.

3.2.4 Radio free-free emission

Mechanisms for free-free emission

We briefly described free−free processes in Chapter 1, Section 1.3. In general, free−free emission is a thermal process where the particle (electrons, ions) remains in its unbound state. In the ISM, unbound electrons move in a medium consisting of ions, electrons and other particles. Since these are charged particles, they produce an electrostatic field which will determine the motion of other charged particles in a system. In such a field produced by ions, electrons accelerate as the force between ions and electrons (Coulomb's force)[1]. A change in an electron's speed implies a change in its energy. Therefore, the energy of an emitted photon is equal to the energy difference between the initial and final electron state.

Free-free emission as a probe for SFR

Like the recombination lines, free-free emission originates from HII regions. The spectrum of free-free emission in galaxies is flat in the radio domain. It is directly proportional to the ionization state governed by the flux from young massive stars. Therefore, the free-free emission indicates recent star formation (Condon, 1992; Murphy et al., 2011). Unlike the optical recombination lines whose emission can be absorbed by dust, free-free emission is not impacted by dust. Free-free emission is generally faint and must be separated from other sources of radio emission. For example, ultrasmall dust grains can impact the free-free emission, particularly at frequencies from 10 to 90 GHz (Draine & Lazarian, 1998; Planck Collaboration et al., 2011).

[1] The electron-electron and ion-ion interactions are neglected.

3.2.5 IR emission - Dust

Newly formed stars, particularly massive ones, emit in the UV and optical parts of the EM spectrum. This light is often highly obscured due to dust along the line of sight. Previously, in Subsections 3.2.3, and 3.2.4, we described two types of SFR tracers that are commonly used since they both originate from the ionized medium that surrounds the young massive star. The first tracer, recombination lines, are not good tracers of SFR is highly embedded regions. The latter, radio free-free emission, is not impacted by dust, but it is quite weak, limiting its use. The alternative approach is to use dust emission to estimate the total SFR of a galaxy. This works because stellar light heats the dust grains, which will then emit approximately as a black body at longer wavelengths.

Consequently, the total infrared luminosity from dust emission (L_{TIR}) tightly correlates with the stellar bolometric luminosity. However, dust absorbs only half of the stellar light, thus potentially underestimating the SFR. In metal-poor or dust-poor systems, using dust emission may overestimate total SFR (Hirashita et al., 2001). Another important factor that overestimates the SFR from dust emission is contribution to the dust heating from evolved stars (Hirashita et al., 2003; Bendo et al., 2010). Dust observations made by the space telescopes Herschel (Pilbratt et al., 2010) and Spitzer (Werner et al., 2004) have made a significant contribution to getting SFR for galaxies.

3.2.6 UV light

The peak emission of young massive stars is in the UV part, between 125 and 250 nm. Measuring such light originating from stellar photospheres is a direct probe of star formation since older stars emit mainly at longer wavelengths. However, our atmosphere is not transparent to UV light (Chapter 2, Section 2.1). Therefore, sending a telescope into space is necessary to measure the UV light from nearby stars and galaxies. Ground-based observations of UV emission from stars are possible only in the case of high-redshift galaxies because the emission will be shifted to the optical wavelengths. For example, the space satellite, "Galaxy Evolution Explorer" (GALEX - Martin et al., 2005), provided a deep understanding of UV emission in galaxies and one of the first SFR maps. GALEX observed a significant part of the sky in the far-UV (FUV, 150 nm) and near-UV (NUV, 230 nm). Similarly, as in the case of hydrogen recombination lines, UV light is highly impacted by dust emission. The FUV/NUV ratio is one of the ways to predict dust attenuation (Calzetti et al., 1994; Salim et al., 2007; Hao et al., 2011).

3.2.7 Combination of SFR tracers

Each of the previously described SFR tracers offers advantages and disadvantages. To include as many stars as possible and to compensate for the different disadvantages of each star formation tracer, we use a combination of a few of these to estimate the SFR. A combination of Hα emission with some of the IR tracers is one of the commonly used mixes of different SFR tracers (e.g. Kennicutt et al., 2007; Hao et al., 2011). Similarly, we can use a combination of UV and IR light, as well as use the combination of various dust bands (Calzetti et al., 2010; Galametz et al., 2013).

3.3 Star formation theories

Here, we provide an overview of current star formation theories, combining theoretical and observational points of view. It is worth pointing out that both theoretical and observational perspectives are equally

important and coupled. Theory and simulations provide explanations for observations, while the observations set the space of initial conditions for simulations.

3.3.1 The top-down approach

The top-down theory of star formation is one of the first attempts to explain observational results of the relation between star formation and gas in galaxies (Kennicutt, 1989). It puts global galactic-scale processes in focus as being responsible for star formation. For example, the disc instability, together with the dynamical timescale of the galaxy, are the drivers for star formation (Silk, 1997). The primary role of this approach is to explain the observed global KS law, including a strong correlation with $\Sigma_{\rm gas}/t_{\rm orb}$ (Kennicutt, 1998b), and a cut-off in star formation coincident with the transition phase of the gas stability, described by the Toomre Q parameter. From this point of view, the difference between low and intermediate density regimes is well explained by the gravitational instability of the gas disc, yet the top-down scenario does not distinguish between intermediate and high-density regimes. In addition, this approach also does not explain the star formation on sub-galactic and molecular cloud scales.

There are two relevant theories within the top-down direction for explaining star formation. One is that the star formation is completely governed by the hydrodynamics and self-gravity of the gas. This idea suggests the observed power-law trend between $\Sigma_{\rm SFR}$ and $\Sigma_{\rm gas}$ in Equation 3.4. However, later studies showed no correlation between $\Sigma_{\rm SFR}$ and the Toomre Q (e.g. Leroy et al., 2008) at sub-galactic scales. The other theory is the feedback regulated model for star formation (Ostriker et al., 2010), in which the star formation produces feedback that impacts the ISM. The different feedback mechanisms are dominant at various spatial scales, destroy clouds and shape the ability of gas to form stars. The downside of this theory was that models could not explain low star formation efficiencies and long depletion times of the gas. Additionally, as observed in the Large Magellanic Cloud (LMC), it cannot explain the metallicity dependence on star formation and variation of $f_{\rm dense}$ at small scales.

3.3.2 The bottom-up approach

The bottom-up approach provides an alternative idea for star formation, in which the internal structure of molecular clouds and gas densities drive the star formation (Krumholz & McKee, 2005). This point of view could explain everything that the top-down approach did not. For example, the bottom-up recognized three density regimes observed in Figure 3.6, and the transition between each of these is explained via atomic to molecular gas transition (the left vertical line in Figure 3.6) (Krumholz & McKee, 2008; Krumholz et al., 2009; McKee & Krumholz, 2010) and the point when we reach the required threshold for efficient star formation (the right vertical line in Figure 3.6).

Similarly, as in the top-down approach, we will mention the two most important theories of star formation within the bottom-up approach in the following. The density threshold model explains the observed correlation of star formation with the amount of dense molecular shown in Figure 3.7 (Lada et al., 2010, 2012). Clark & Glover (2014) have shown in simulations that star formation occurs in regions with molecular gas column densities higher than $10^{21}{\rm cm}^{-2}$. The increase in $f_{\rm dense}$ (Lada et al., 2012) or the decrease in relevant timescales (Krumholz et al., 2012) explain the observed non-linearity of the global KS law. Moreover, the low star formation efficiencies of the gas are because the mass of a cloud that contributes to star formation is small (Lada et al., 2012). However, even when considering the mass of a cloud from which star forms, the efficiencies are still smaller than expected.

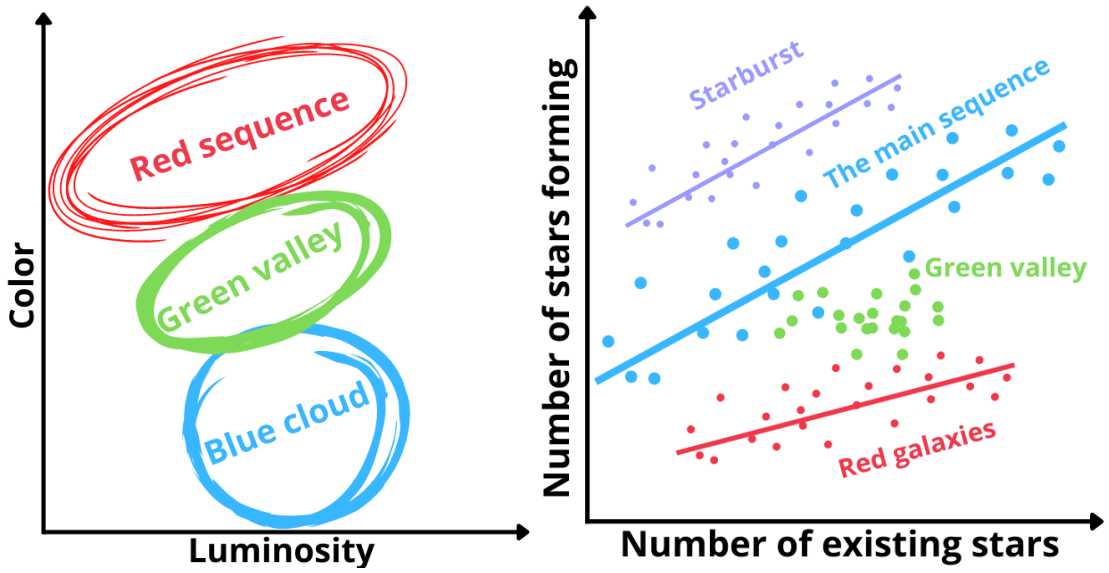

Figure 3.4: **Left:** A colour-magnitude diagram for galaxies. We observe a bimodality in distribution: red sequence, blue sequence and the green valley. **Right:** An illustration of the light-stellar mass diagram for galaxies. We see four different regimes here: the main galaxy sequence (blue points), red galaxies (red points), the green valley, and starburst galaxies (purple points).

The turbulence regulated model (Krumholz & McKee, 2005; Federrath & Klessen, 2012) tries to explain overall small star formation efficiencies at various spatial scales. This theory directly stems from the virial theorem of molecular clouds (Chapter 1, Section 1.4.4). The turbulence of gas has two roles depending on spatial scales. It can suppress the gas from collapsing at larger scales (shear motions), whereas it enhances star formation on small scales (Mac Low & Klessen, 2004). The turbulence will create local gas overdensities, and the velocity dispersion of the molecular cloud will have an important role in setting the ability of gas to collapse (Federrath & Klessen, 2012). In addition, these models contain magnetic field, as its impact is not negligible on these small scales (e.g. Padoan & Nordlund, 2011; Federrath & Klessen, 2012).

3.4 A cosmic history of star formation

Galaxy main sequence

It is important to consider star formation over cosmic time to explain and understand the evolution of galaxies. Similarly, as with stars, a mass of a galaxy has a crucial role in its evolution, particularly in its star formation history. We observe a bimodality when we look at the colour-magnitude diagram (left panel in Figure 3.4). The colour-magnitude diagram is a way to show the evolutionary state of galaxies. Light from actively star-forming galaxies appears to be bluer due to the high number of young stars than the light from more quiescent galaxies (red galaxies), mainly early-type galaxies. There is a region from red to blue galaxies called the “green valley”. Not many galaxies are located in this green valley, which indicates that this is mainly a transition zone in star-formation activity. The Milky Way is located in this area. The threshold in stellar mass for this transition to occur is around $3 \cdot 10^{10}\,\mathrm{M}_{\odot}$ (Kauffmann et al., 2003).

Similar bimodality is observed when we look at how the star formation rate varies due to stellar mass. We show this illustration on the right panel in Figure 3.4. Most galaxies are located on a line in this luminosity-stellar mass (proportional to SFR) plane, and this group is called the galaxy main sequence. This tight correlation between galaxies' SFR and stellar mass is observed in galaxies at redshifts of 4 (e.g. Tomczak et al., 2016). Galaxies that have lower star formation rates lie below this main sequence. Contrary to these less active star-forming galaxies, systems that show peculiarly high star formation rates are called a starburst. These galaxies are rare in the Local Universe but quite commonly observed features at higher redshifts and are mainly merger systems (Larson et al., 2016).

Variation of baryonic matter across cosmic time

Figure 3.5 shows the cosmic evolution of various baryonic densities, from $z = 4$ to the present day ($z = 0$) (Walter et al., 2020). The cosmic SFR density (Madau & Dickinson, 2014) and molecular density show similar trends. They rise through cosmic time, reaching the maximum at redshifts from 1 to 2, decreasing to values measured today. Interestingly, the peaks in $\rho_{\mathrm{H_2}}$ and Ψ_{stars} do not coincide. The peak of the star formation activity occurred shortly before galaxies contained the largest amount of molecular gas. On the one hand, the number of stars steadily increased over time. On the other hand, the amount of atomic gas (Neeleman et al., 2016) was higher in the early Universe than today, although the variation is not as prominent as in the amount of molecular gas (Decarli et al., 2019, 2020). Atomic and molecular gas cosmic densities were similar at the redshift of ~ 1.5.

In the first order, the variation in SFR and $\rho_{\mathrm{H_2}}$ is similar, so SFR/$\mathrm{H_2}$ ratio is roughly constant. Compilation of various studies Tacconi et al. (e.g. 2010); Genzel et al. (e.g. 2010, 2015) found that the star formation efficiency did not vary significantly over time, but the high star formation rate was explained by the presence of the larger amount of molecular gas.

3.5 Observations of star-forming regions - Scaling relations

This section presents an overview of all attempts to connect star formation with observations of gas and better understand its role in this process. Over the years, astronomers have been using various observations of molecular gas tracers across galaxies and star-forming regions in the Milky Way. The relationship between the star formation rate surface density and the gas mass surface density can be described via a power-law function, i.e. their connection is linear in the log-log space.

Since stars form out of molecular gas as a consequence of a gravitational collapse, it is obvious to think that the star formation rate will depend on the gas density, ρ. Although there are other physical quantities that also significantly impact star formation, such as magnetic fields (Shu et al., 1987) and turbulence (Mac Low & Klessen, 2004), in this simplistic form, M. Schmidt proposed the idea of a power-law relation between star formation rate and the gas density: $\rho_{\mathrm{SFR}} \propto A \cdot \rho^N$ (Schmidt, 1959a,b), where the power-law index, N, takes a value between 1 and 2. The slope depends on the choice of a star formation and selected gas tracers and physical scales probed by the observations (Kennicutt, 1997). However, measuring gas densities is challenging, as clarified in Chapter 1, Section 1.4, and 1.5. Instead, the slightly revised Schmidt relation, the Kennicutt-Schmidt star formation law (KS law - Kennicutt, 1998a) represents the relation between properties that we can directly observe. Using surface densities measured along the line of sight, we can quantify the relation between gas and star formation rate surface densities, Σ_{gas} and Σ_{SFR}:

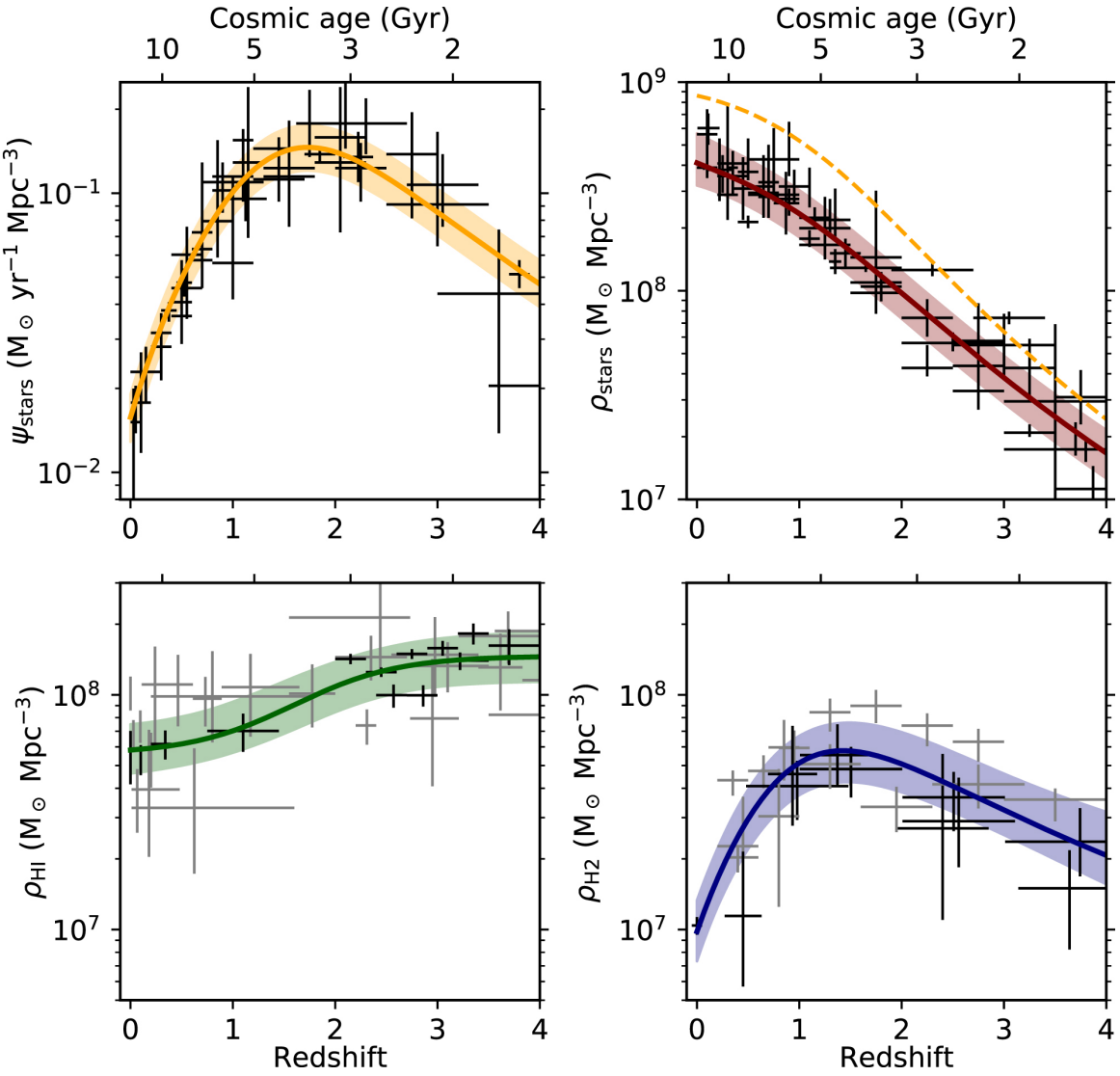

Figure 3.5: Cosmic variation of star formation rate density (yellow, top left), stellar density (red, top right), atomic (green, bottom left) and molecular gas density (purple, bottom right) (Walter et al., 2020). The solid line in each panel represents the best fit solution to each variable. The dashed line on the top right panel is the cosmic stellar mass density integrated from the star formation rate density model, shown on the top left panel.

$$\Sigma_{gas} = A \cdot (\Sigma_{SFR})^N. \tag{3.4}$$

This relation describes the global star formation rate as a power-law function of gas surface density:

$$\Sigma_{SFR} = (2.5 \pm 0.7) \cdot 10^{-4} \cdot (\Sigma_{gas})^{1.40 \pm 0.15}, \tag{3.5}$$

with Σ_{SFR} in units of $M_\odot$ yr^{-1} kpc^{-2}, and Σ_{gas} in $M_\odot$ pc^{-2}. Σ_{gas} is the summary of atomic and molecular gas surface densities (Chapter 1, Section 1.4). This relation is found using the observations of Hα, HI, and CO across the sample of 61 normal spiral star-forming galaxies and FIR and CO measurements of

36 starburst galaxies (Kennicutt, 1998a). Interestingly, the observed correlation is not sensitive to the atomic-to-molecular gas ratio. Equation 3.5 is also called the global KS law because the surface densities are measured and averaged over the entire optical disc. In addition, the global KS law can be parametrized using only $\Sigma_{\rm HI}$ or $\Sigma_{\rm H_2}$.

Moreover, numerous studies tried to constrain the power-law slope value better. The selection of gas and star formation tracers, properties of galaxies and clouds within the sample, but also resolving star-forming regions in galaxies significantly impacted the measured values. In Kennicutt (1998a), the measured slope varied based on the global galaxy' properties. For example, the slope is 2.47 ± 0.39 for a set of normal star-forming galaxies. Different SFR tracers yields the slope in ranges from 0.9 to 1.7 (Buat et al., 1989; Buat, 1992; Deharveng et al., 1994).

The relation is not linear, and there are many uncertainties, particularly the CO conversion factor (see Chapter 1, Section 1.4) that impacts metal-poor (Leroy et al., 2011) and starburst galaxies (Narayanan et al., 2012), but also the sampling of the IMF. Interestingly, the KS relation remains valid for various physical conditions: from low (Wyder et al., 2009) to very high-gas surface densities typical for starburst systems.

With the expansion of multiwavelength studies and extending the sample of observed galaxies, it was possible to quantify the KS relation further. Particularly sub-kpc measurements of atomic and molecular gas content in nearby galaxies: The HI Nearby Galaxy Survey (THINGS - Walter et al., 2008), and The HERA CO-Line Extragalactic Survey (HERACLES - Leroy et al., 2009) provided a better understanding of the role of the gas in star formation processes. Bigiel et al. (2008) observed how $\Sigma_{\rm SFR}$ correlates with both $\Sigma_{\rm HI}$ and $\Sigma_{\rm H_2}$, and found a weak correlation with $\Sigma_{\rm HI}$, and strong correlation with the latter. Particularly, Bigiel et al. (2008) found a linear relation between $\Sigma_{\rm SFR}$ and $\Sigma_{\rm H_2}$. This finding implied that star formation takes place in molecular gas. We show Figure 15 from Bigiel et al. (2008) in Figure 3.6, which also includes literature measurements at that time. Vertical dashed lines indicate at least two distinct (even three) regimes in KS relation: the low surface density regime, the intermediate regime, and the high (starburst) regime. All the observations of globally-averaged properties (Kennicutt, 1989, 1998a; Wyder et al., 2009; Genzel et al., 2010; Tacconi et al., 2010; Liu et al., 2015; Kennicutt & De Los Reyes, 2021), and sub-kpc scales measurements of star formation and gas (Bigiel et al., 2008; Leroy et al., 2008; Blanc et al., 2009; Bigiel et al., 2011; Schruba et al., 2011; Ford et al., 2013; Leroy et al., 2013; Kreckel et al., 2018; Williams et al., 2018; Dey et al., 2019) belong to the low and intermediate regimes.

KS relation at small scales

The overall linear relation between star formation and molecular gas surface density described above holds well and scales down to 200 pc. At smaller physical scales, the scatter becomes more prominent (Schruba et al., 2010; Chen et al., 2010; Onodera et al., 2010) and the star formation law "breaks" because the evolutionary timescales of star formation processes are statistically undersampled, i.e. the stochastic sampling domain. In this regime where it is possible to spatially resolve and distinguish locations of recent star formation from places where star formation will occur in the future (Schinnerer et al., 2019; Pan et al., 2022). Therefore, molecular cloud lifetimes become important contributors (Kruijssen et al., 2018, 2019; Chevance et al., 2020) in regulating the star formation efficiency.

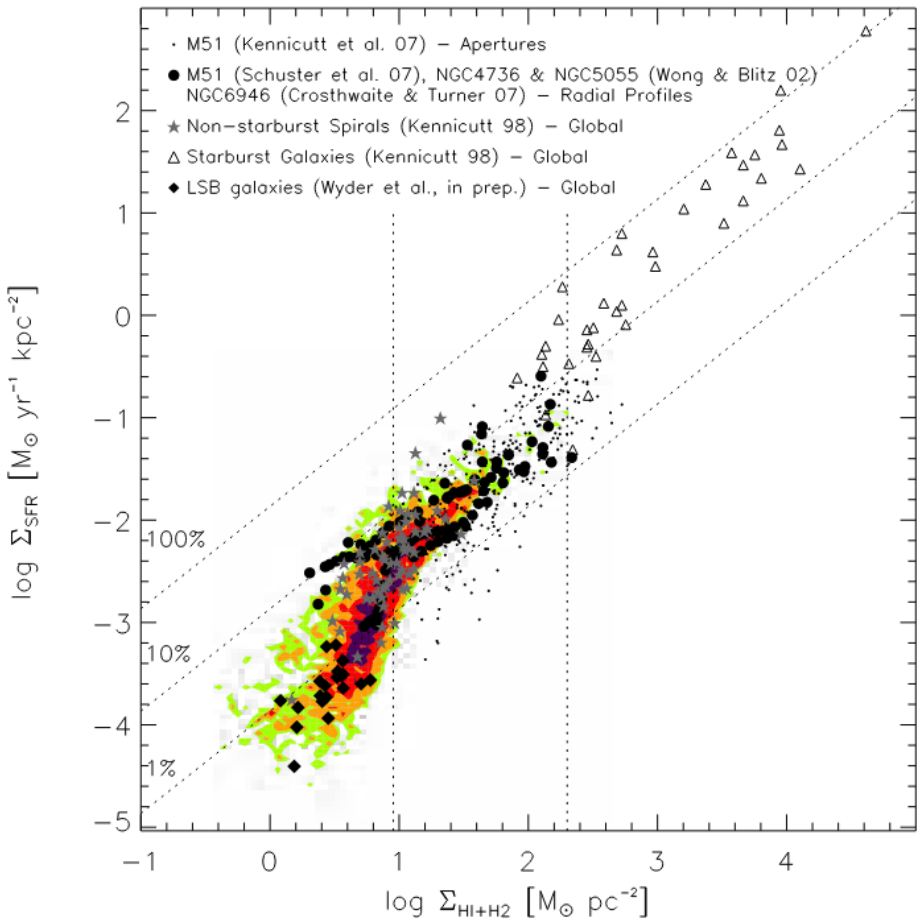

Figure 3.6: Σ_{SFR} as a function of total gas surface density, Σ_{gas}. Contours show sub-kpc measurements of HI gas and CO across the sample of 7 spiral galaxies and 11 late-type and dwarf galaxies from Bigiel et al. (2008). Black dots are individual aperture measurements in M 51 (Kennicutt et al., 2007), whereas points taken from its radial profiles are shown as black solid circles (Schuster et al., 2007). Moreover, black solid circles also show measurements across nearby galaxies NGC 4736, NGC 5055 (Wong & Blitz, 2002), and NGC 6946 (Crosthwaite & Turner, 2007). Diagonal dotted lines show constant depletion times (constant SFE) of gas. This figure includes measurements from Kennicutt (1998a), shown as open stars and triangles. Lines show times of 10^8, 10^9, 10^{10} years, from top to bottom. Vertical dotted lines indicate three different regimes of SF laws: the left line shows the regime where atomic gas gets saturated ($\Sigma_{gas} \approx 9\,M_\odot pc^{-2}$), while the right line shows surface densities at which gas is star-forming ($\Sigma_{gas} \approx 200\,M_\odot pc^{-2}$).

3.6 The role of dense molecular gas - Gao and Solomon relation

Observations of other molecular lines than CO, which get excited at higher densities - dense gas tracers (Chapter 1, Section 1.5), yielded discoveries in the role of molecular gas in star formation. The CO emission is a common tracer of the overall molecular gas content (Chapter 1, Section 1.4). However, star formation occurs in clumps and cores, the densest parts of molecular gas. Therefore, surveys of common dense gas tracers, such as HCN, and other high-critical density molecular lines found in the mm range, list a few new understandings of star formation processes in the Milky Way and other galaxies.

In the recent decade, many surveys mapped the emission of these high critical density lines across various sources and at different spatial scales. Overall, the main result from all of these studies is that $\Sigma_{\rm SFR}$ strongly correlates with the surface density of dense molecular gas, $\Sigma_{\rm dense}$. What is striking is that this correlation spans more than ten orders of magnitude in both HCN emission and SFR. We show various studies on the relation between star formation and dense molecular gas in Figure 3.7. In the following, we will summarise various studies and surveys shown in this figure.

3.6.1 Large spatial scales - whole galaxies and their centres

One of the most important studies in this field is the seminal study from almost twenty years ago, Gao & Solomon (2004a,b). They obtained a comprehensive study of HCN emission and total infrared luminosities of a sample of 65 galaxies: 34 normal star-forming spiral galaxies, 9 ULIRGs, and 22 LIRGs. The total infrared luminosity linearly scales with the HCN luminosity, putting dense molecular gas into focus. Soon after, other studies that also measured global properties of dense molecular gas and star formation confirmed the observed correlation: in high-redshift galaxies (Gao et al., 2007), active galaxies (Krips et al., 2008), samples of LIRGs and ULIRGs (Graciá-Carpio et al., 2008; García-Burillo et al., 2012; Privon et al., 2015), normal star-forming galaxies (Juneau et al., 2009). Similarly, as with the global KS law, the global measurements of HCN emission are a product of averaging over different environments.

Resolved galaxy discs - moderate spatial scales

First, (García-Burillo et al., 2012) found variation in $\rm SFE_{dense}$ among the sample between normal star-forming and starburst galaxies. Next, (Usero et al., 2015) observed 30 pointing of galaxy centres and discs, (Chen et al., 2014) observed M 51, same as (Bigiel et al., 2016). They found that together with $\rm SFE_{dense}$, also $f_{\rm dense}$ varies across galaxy discs. Lower $\rm SFE_{dense}$ were found in galaxy centres. Similarly, studies of CMZ observed low $\rm SFE_{dense}$ in comparison with the predicted one based on the amount of dense molecular gas that contains (Longmore et al., 2013; Barnes et al., 2017). These results suggest that the efficiency of gas for star formation depends on the environment, described by gas density, but also other parameters, pressure, stellar surface density, and shear motions.

Improvements in the angular resolution and sensitivity made it possible to resolve the HCN emission in nearby galaxies. First, studies of resolved dense gas in galaxy discs confirmed the global relation between $\Sigma_{\rm SFR}$ and $\Sigma_{\rm dense}$, in vigorous and typical star-forming systems. Moreover, resolved galaxy discs allowed for more comprehensive studies of the HCN distribution and how its emission relates to the molecular gas traced by CO emission. For example, Kepley et al. (2014) found a correlation between HCN and $\rm HCO^+$ emission with star formation and molecular gas in a local starburst galaxy M 82. Similar results were observed in a galaxy merger, the Antennae galaxy (Bigiel et al., 2015). The first systematic variations of the dense gas fraction ($f_{\rm dense}$, see Chapter 1, Section 1.5) were observed across a sample of 30 nearby galaxies at kpc scales in Usero et al. (2015). Galaxy centres contained a larger amount of $f_{\rm dense}$than the rest of the disc, but lower efficiency of gas to form stars, $\rm SFE_{dense}$, than in the outer parts. Similarly was found across the disc of the nearby galaxy M 51 (Bigiel et al., 2016): the efficiency of star formation depends on the local environment.

The major step toward better understanding the relationship between dense molecular gas and star formation was found in the "Emir Multiline Probe of the ISM Regulating galaxy Evolution" (EMPIRE) IRAM 30-meter survey of HCN emission at kpc scales across nine nearby galaxies (Bigiel et al., 2016; Jiménez-Donaire et al., 2019). The $f_{\rm dense}$ systematically varied among the galaxy sample and across

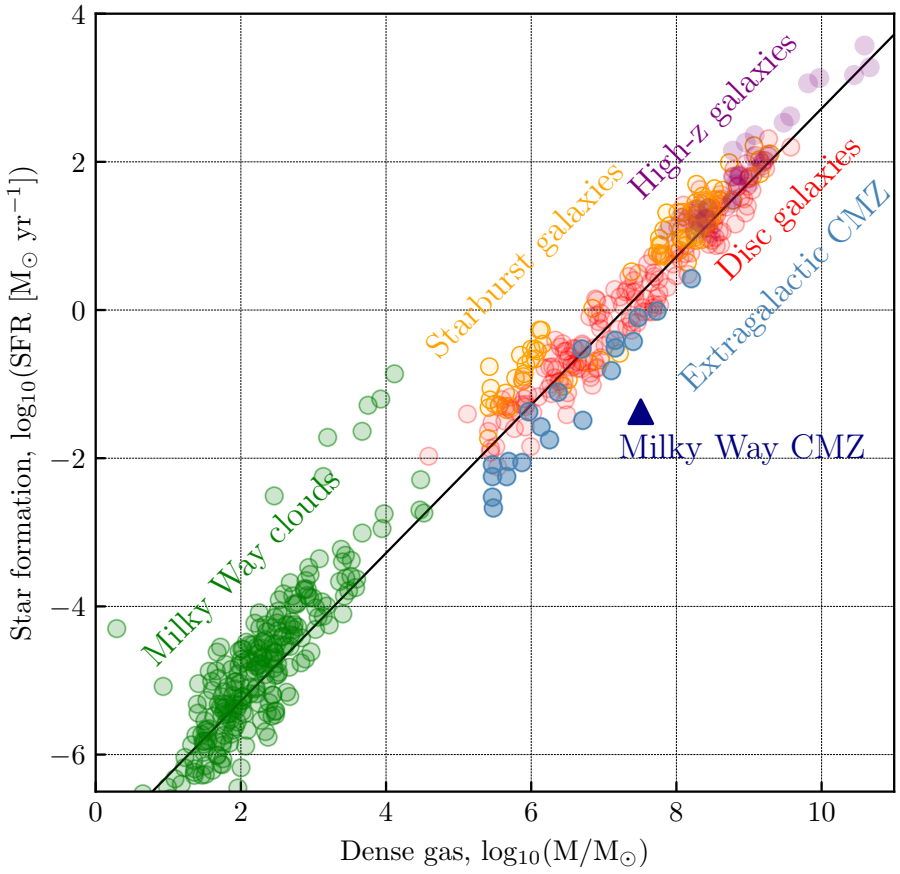

Figure 3.7: A literature overview of infrared luminosity (tracer for SFR) and dense gas (traced by the HCN emission) relation presented in Jiménez-Donaire et al. (2019). The upper right part shows measurements of whole galaxies and their centers, from high-z galaxies (purple points), to LIRGS, ULIRGS, starburst (yellow points) to normal spiral star-forming galaxies (red points). In addition, we include measurements of CMZ of nearby galaxies (Querejeta et al., 2019; Jiang et al., 2020). As we move towards the lower left part of this figure, we note centres of nearby galaxies (blue points), the CMZ (dark blue triangle) (Henshaw et al., 2022) and finally, reach measurements of clouds in the Milky Way (green points).

the galaxy disc. At the same time, the highest f_{dense} were found towards the centres of galaxies, and the $\mathrm{SFE}_{\mathrm{dense}}$ increased towards the outer parts. This result implies the anti-correlation between f_{dense} and $\mathrm{SFE}_{\mathrm{dense}}$, even though higher star formation is expected to be found in denser regions. Gallagher et al. (2018a) confirmed these results at slightly higher spatial resolution in a sample of 4 nearby galaxies, and Jiang et al. (2020) in the inner 2 kpc region of NGC 253. Additionally, all these studies found that f_{dense} is found in regions of high stellar surface density, Σ_* and high interstellar pressure, whereas $\mathrm{SFE}_{\mathrm{dense}}$ was significantly reduced in these regions.

3.6.2 Cloud-scale observations

Giant molecular associations in nearby galaxies

Resolving HCN emission at giant molecular cloud scales in nearby galaxies became possible with new generation of interferometers (ALMA, NOEMA - Chapter 2, Section 2.5). The following studies have seen the correlation mentioned above but at a scale of a few hundreds of pc. However, the sample of galaxies was limited to the nearest ones. For example, Brouillet et al. (2005) observed GMCs in Andromeda, and Buchbender et al. (2013) in M 33. Several studies observed HCN emission in M 51. Chen et al. (2017) found that the IR/HCN ratio varies across the outer spiral arm in M 51. On the other hand, Querejeta et al. (2019) observed variation of $f_{\rm dense}$ and $\rm SFE_{dense}$ across two different environments in the same galaxy: molecular ring and spiral arms. This study found that the amount of dense gas, but also its velocity dispersion anticorrelated with the $\rm SFE_{dense}$. Moreover, Sánchez-García et al. (2022) found two distinct regimes in the $\rm SFE_{dense}$ vs. $\alpha_{\rm vir}^{-1}$ plane in the ring of NGC 1068.

Molecular clouds in the Milky Way

The bottom left part of Figure 3.7 shows measurements of dense molecular gas within molecular clouds in the Milky Way. Due to their proximity, these studies started way before mapping HCN in nearby galaxies was possible. The $\Sigma_{\rm SFR}$ in star-forming regions in our Galaxy is proportional to the amount of dense molecular gas (e.g. Lada & Lada, 2003; Wu et al., 2005; Heiderman et al., 2010; Lada et al., 2010, 2012; André et al., 2014).

3.6.3 Systemic variation of the $f_{\rm dense}$ and $\rm SFE_{dense}$

The scaling between star formation and dense molecular gas (Figure 3.7) shows a scatter, although to a smaller magnitude than in the KS law. The star formation rate varies by two orders of magnitude for a fixed amount of dense molecular gas. Since Figure 3.7 covers a wide range of physical scales, the origin of the observed scatter is unknown but is due to the underlying physics. The scatter becomes more prominent when observing IR/HCN ratio, as shown on the right panel of Figure 3.7. In the following, we will describe the observed scatter and outline possible explanations.

Usero et al. (2015) mapped HCN emission across 30 normal star-forming galaxies at 1.5 kpc scales using IRAM 30m. This study showed that HCN/CO varies across galaxies, where higher values of HCN/CO are favoured in the high surface density regions, whilst the IR/HCN ratio is lower in high-density parts. Similarly, Chen et al. (2014); Bigiel et al. (2016) found environmental variation of $f_{\rm dense}$ and $\rm SFE_{dense}$ in M 51 at kpc scales. By extending observations of HCN across a larger sample of nearby galaxies at kpc scales, Jiménez-Donaire et al. (2019) found systematic variations in $f_{\rm dense}$, $\rm SFE_{dense}$with the distance to the centre of a galaxy, Σ_*, and $\Sigma_{\rm H_2}$. We show these variations in Figure 3.8.

The highest $f_{\rm dense}$ is observed towards the centre of galaxies, where the highest surface densities of stellar mass and molecular gas are present. Similarly, Gallagher et al. (2018a) found strong correlation between $f_{\rm dense}$ and $\Sigma_{\rm H_2}$ and Σ_* at 500 pc, and Gallagher et al. (2018b) confirmed the observed correlation using cloud-scale CO measurements. At the same time, Jiménez-Donaire et al. (2019) found the lower $\rm SFE_{dense}$ in galaxy centres and the anticorrelation with Σ_* and $\Sigma_{\rm H_2}$. All these studies imply the environmental dependence of $f_{\rm dense}$ and efficiency of gas to form stars, apparent separation in the behaviour of the gas in the centre and the rest of the disc of a galaxy.

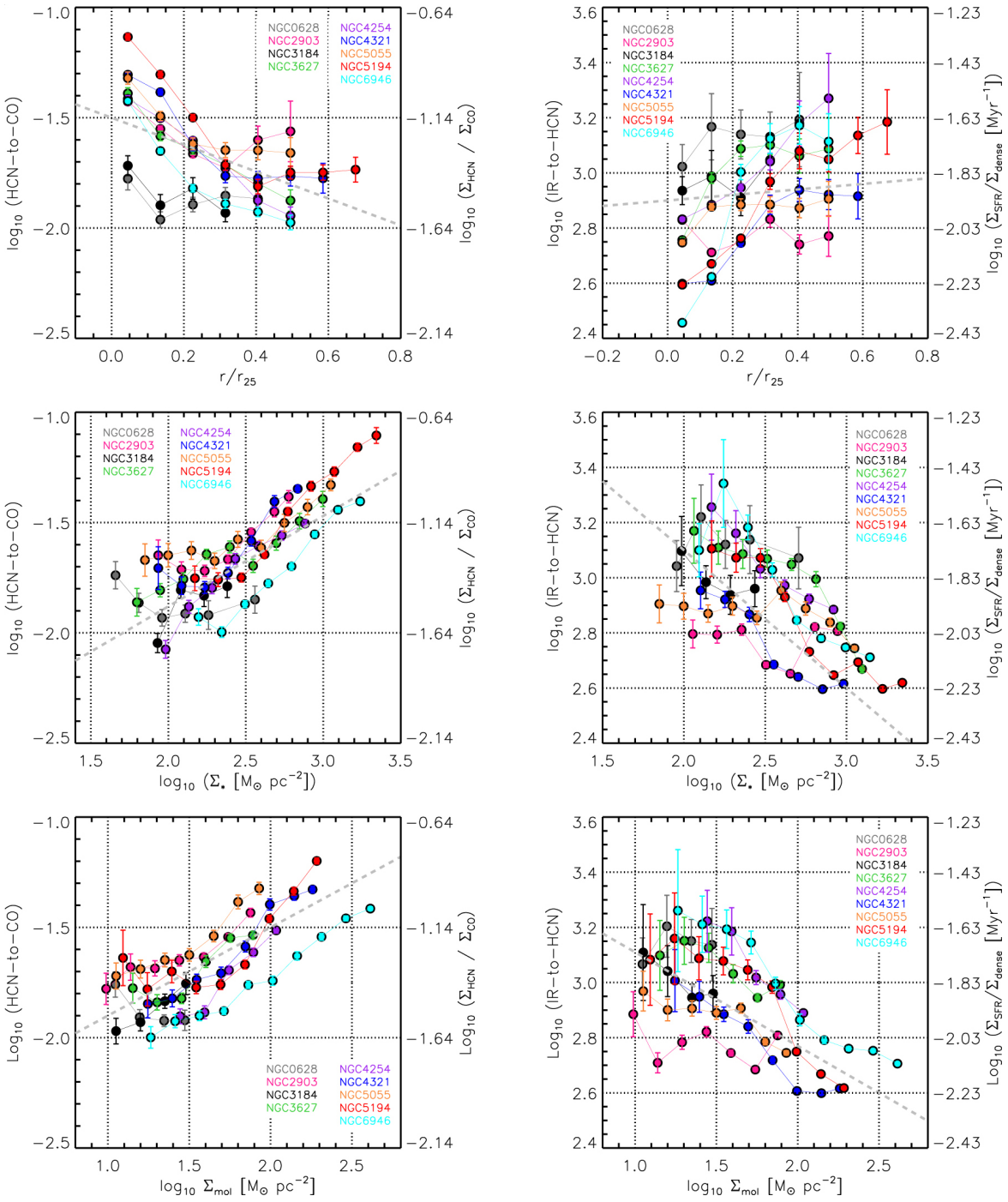

Figure 3.8: HCN-to-CO line intensity ratio (left column), and IR-to-HCN ratio (right column) as a function of distance from the centre of a galaxy (top row), Σ_* (middle row), and $\Sigma_{\rm mol}$ (bottom row) of nine nearby gaalxy from the EMPIRE survey (Jiménez-Donaire et al., 2019).

Galaxy centers, and the Central Molecular Zone

Galaxy centres are known to host the supermassive black hole, in which the gas is infalling, causing the relativistic jets or active galactic nuclei. Galaxy centres are the densest regions in galaxies and overall extreme physical conditions compared to the rest of the galaxy. Particularly, galaxy centres have the highest stellar and gas surface densities and high interstellar pressure. Thus, they show bright and rich emission, including emission of various molecular gas tracers, as observed towards the centre of, e.g. NGC 253 (Martín et al., 2021), NGC 6946 (Eibensteiner et al., 2022), M 51 (den Brok et al., 2022b).

Studies of HCN emission of galaxy centres found low efficiency of gas for star formation, despite containing a large amount of dense gas (Usero et al., 2015; Chen et al., 2014; Murphy et al., 2015; Bigiel et al., 2016; Gallagher et al., 2018a; Jiménez-Donaire et al., 2019). This result was also found in galaxy mergers, such as NGC 4038 and NGC 4039 (Kepley et al., 2018; Bemis & Wilson, 2019).

The inner 500 pc region of our Galaxy, also referred to as the Central Molecular Zone, was impossible to observe until recently due to high dust extinction. Recent studies of molecular gas in the CMZ confirmed what we observed towards centres of nearby galaxies: this region is the densest in our Galaxy, but its $\mathrm{SFE_{dense}}$ is lower than predicted from the amount of dense molecular gas that contains (Jones et al., 2012; Longmore et al., 2013; Kruijssen & Longmore, 2014; Barnes et al., 2017; Henshaw et al., 2022). As in the CMZ, centres of other galaxies have high Σ_*, $\Sigma_{\mathrm{H_2}}$ and interstellar pressure. Helfer & Blitz (1997) showed that more gas is located in regions described with deeper potential well. Therefore, f_{dense} will be higher in these regions.

Despite having the largest reservoir of dense molecular gas in centres of galaxies, its ability to produce stars is low. Galaxy dynamics plays an important role here (e.g. Meidt et al., 2018), as we will discuss later. For example, strong shear motions in the centre prevent gas from collapsing and lower the $\mathrm{SFE_{dense}}$.

Galaxies' discs

Unlike the centres of galaxies, the outer discs of galaxies show lower dense gas fraction, but considerably higher $\mathrm{SFE_{dense}}$ (e.g. Jiménez-Donaire et al., 2019). In the Milky Way, clouds outside the CMZ showed nearly constant $\mathrm{SFE_{dense}}$, yet different f_{dense} (Lada et al., 2012), which supports the idea about the universal density threshold for efficient star formation across the disc of the Milky Way.

Galactic bars and bar ends

Jiménez-Donaire et al. (2019) observed galaxy-to-galaxy scatter in the radial variation of IR/HCN and found that galaxy morphology shapes the observed relation (the top right panel in Figure 3.8). Galaxies containing a large-scale bar have smoother radial profiles than unbarred galaxies with nearly flat IR/HCN. The interaction of a bar with the spiral arms can cause gas inflows towards the inner parts, as shown in various simulations (Emsellem et al., 2015; Sormani et al., 2018; Sormani & Barnes, 2019; Díaz-García et al., 2020). From an observational perspective, to understand the impact of a bar on molecular gas and its ability to form stars, it is necessary to probe molecular gas and its dense content down to GMC scales. After galaxy centres, contact points between bars and spiral arms - bar ends, are the following brightest regions in a galaxy. Due to the convergence of orbits originating from the bar and spiral arms, gas transports and piles up in the bar ends. These are also places where we expect to see enhanced star formation, such as in the W 43 region in the Milky Way (Beuther et al.,

2012), located at the bar end. Moreover, due to the nature of bar ends, these are the environments where we expect to see collisions of gas motions and cloud-cloud collisions.

Recent work showed that the velocity dispersion of gas regulates its star formation efficiency. Murphy et al. (2015) showed that gas dynamics is important in setting the star formation efficiency on the example of bar ends in NGC 3627. Particularly, Murphy et al. (2015) studied HCN and HCO^+ emission in bar ends and how the observed SFE_{dense} varies with the line width. This study found higher SFE_{dense} and lower σ in the bar ends than in the centre of NGC 3627. Similarly, intersections of rings and bars have similar properties as the bar ends, as shown in NGC 1068 (Sánchez-García et al., 2022). Moreover, the study of a 100 pc HCN emission in spiral arms of M 51 (Querejeta et al., 2019) discovered that SFE_{dense} anticorrelates with the velocity dispersion. Northern and southern spiral arms in M 51 have similar Σ_*, but different σ. Interestingly, the southern spiral arm contains high f_{dense} but its SFE_{dense} is reduced. Observations of ~ 400 pc measurements of HCN emission across NGC 1068 found no such correlation between the SFE_{dense} and σ (Sánchez-García et al., 2022).

3.7 Current open questions

The star formation process is a multi-scale problem involving many different physical processes and gas densities (Girichidis et al., 2020). In previous sections, we outlined recent efforts toward better understanding the role of molecular gas in star formation, particularly the dense ISM. Various surveys and multi-wavelength studies significantly shaped the picture of our current view of the role of dense molecular gas. From measuring the UV, optical, to IR emission to correctly estimate star formation in galaxies to efforts in sub-mm, mm and radio astronomy to observe atomic, molecular and dense molecular gas. All these attempts followed each other. Each new step that has been taken was either towards including more galaxies in a sample, improving the spatial resolution, or gaining broader spatial coverage and increasing the signal-to-noise ratio. However, despite all these results, we still miss several important links. One is to explain the nature of scattering in the observed SFE_{dense}. Another missing link is understanding the scattering between dense gas and star formation in Figure 3.7. In the following, we outline some of the still open science questions that we will address in Chapters 4 and 5:

- What sets the density of molecular gas across a galaxy?
- How is the fraction of dense molecular gas, f_{dense} related to its efficiency to produce stars, SFE_{dense} on a cloud-scale? Does the local environment have an impact?
- How does the relationship between the IR to HCN look across a non-typical star-forming galaxy, i.e. a starburst?
- What is the role of dense molecular gas dynamics in setting the star formation?

The topic of this doctoral thesis is answering these questions, which are addressed by using two independent directions. The first is mapping the dense molecular gas content at GMC scales across various environments within the nearby galaxy. The other one is extending the sample from normal star-forming galaxies to include low metallicity galaxies and more extreme star-forming environments like starburst.

CHAPTER 4

NOEMA view of dense molecular gas at GMC scales across nearby galaxy NGC 3627

The first part of this chapter is based on the publication "Dense molecular gas properties on 100 pc scales across the disc of NGC 3627" (Bešlić et al., 2021), published in Monthly Notices of the Royal Astronomical Society (MNRAS) in June 2021. This published work is added at the end of this doctoral thesis in the Appendix A. In the following, we provide an overview of this study and highlight the most important results. The main data set used in this manuscript is obtained by NOEMA (PI: F. Bigiel). Additional measurements used in this work are from the PHANGS survey, PHANGS-ALMA (Leroy et al., 2021b) and PHANGS-MUSE (Emsellem et al., 2022), and the environmental mask based on dynamical modelling, published in Querejeta et al. (2021). I performed the data analysis, including preparing all figures and manuscript writing. J. Pety and C. H. Contreras provided the reduced data set. The manuscript has been under internal revision within the collaboration and externally reviewed by an anonymous referee. In Section 4.1 we present an overview of the work done in Bešlić et al. (2021).

In the remainder of this chapter, we describe the additional analysis of the data set published in Bešlić et al. (2021) that was beyond the scope of this study. In particular, we will present results on implementing the dense gas toolbox on the NOEMA observations of dense molecular gas in NGC 3627 in Section 4.2. We outline results on applying the GMC footprint to isolate HCN emission in Section 4.3.

4.1 Dense molecular gas properties on 100 pc scales across the disc of NGC 3627 - *Bešlić et al., 2021*

4.1.1 Introduction

The notion of the star formation process occurring within the dense, coldest parts of molecular gas derives from observations of star-forming regions in the Milky Way and the large-scale measurements of other galaxies. In the context of observations of the relation between dense molecular gas and star formation across molecular clouds in the Milky Way, the measured star formation rate surface density in these regions, $\Sigma_{\rm SFR}$, strongly correlates with the mass of dense molecular gas (Wu et al., 2005). Numerous studies found that gas above a certain surface density threshold is star-forming (e.g. Lada et al., 2012), suggesting a universal density threshold model for star formation. From the extragalactic point of view, the pioneering work of Gao & Solomon (2004a) found a tight correlation between star formation traced by total infrared luminosity and the amount of dense molecular gas traced by the HCN emission across a sample of 60 galaxies. Over the years, several studies have shown the

correlation between star formation and dense molecular gas independent of the physical scales: from star-forming cores to the measurements of whole galaxies and their centres.

Following the groundwork set by Gao & Solomon (2004a), and with the improvement of the spatial resolution and sensitivity, numerous extragalactic studies investigated the properties of dense molecular gas, traced by high-critical density molecular lines (e.g. HCN, HCO^+) and its relation to star formation. In particular, the available amount of dense gas, $f_{\rm dense}$, and how much of such gas turns into stars, $\rm SFE_{dense}$, were studied in the context of star formation theories (e.g. Usero et al., 2015; Chen et al., 2014; Bigiel et al., 2016; Gallagher et al., 2018a; Jiménez-Donaire et al., 2019). All these studies have found the environmental dependence on the $f_{\rm dense}$ and $\rm SFE_{dense}$. While the highest dense molecular gas fraction is observed towards the centres of galaxies, i.e. in the densest regions characterized by high stellar surface density, molecular gas surface density, and pressure, such gas appears to be the least efficient in star formation. On the contrary, gas sitting in the rest of the disc show high star formation efficiencies. The interpretation of this result is provided in the turbulent model of star formation (Federrath & Klessen, 2012). Gas turbulence and shear motions can prevent gas from collapsing and slow star formation. In addition, the environmental dependence of $f_{\rm dense}$ and $\rm SFE_{dense}$ across galaxies at kpc and sub-kpc scales (Bigiel et al., 2016; Gallagher et al., 2018a; Jiménez-Donaire et al., 2019) lies in the physics of molecular clouds.

Considering all the above, the next logical step is better to understand dense molecular gas emission at cloud scales. Molecular clouds in the Milky Way provided a great starting point toward understanding molecular cloud properties. However, observing molecular clouds across other galaxies is necessary to get the whole cloud population. First big efforts towards observing molecular emission, typically traced by carbon monoxide, CO, are already ongoing. Observing other molecular lines, such as the HCN molecule, is essential to probing the denser gas phase of such molecular clouds. Therefore, the missing puzzle in understanding the role of molecular gas in the context of star formation lies in mapping dense molecular gas at cloud scales across nearby galaxies. Conducting such studies faces many challenges. For example, the HCN emission is typically very faint compared to the bright CO emission, which requires significantly longer observing time, especially when probing small-scale emission.

The recently published study, Bešlić et al. (2021), take that next step and investigates the properties of high-critical density emission across galaxy NGC 3627. In this work, we use observations of $3-4$ mm molecular lines obtained by NOEMA interferometer, combined with the single dish data from the EMPIRE survey obtained by IRAM 30-meter telescope. The main goal of this work was to, for the first time, study the properties of dense molecular gas at GMC scales across a large part of the disc of the nearby galaxy, understand the link between dense gas and star formation, and bridge the gap between star-forming regions in the Milky Way, and nearby galaxies.

Galaxy NGC 3627

The galaxy NGC 3627, also known as M 66, is a nearby ($d = 11$ Mpc Anand et al., 2020), spiral (SABb - NASA Extragalactic Database), star-forming ($\Sigma_{\rm SFR} = 7.7 \cdot 10^{-3}\,\rm M_\odot\,yr^{-1}\,pc^{-2}$– Leroy et al., 2021b) galaxy. This galaxy is part of the Leo Triplet (Garcia, 1993). NGC 3627 contains a strong bar and two spiral arms (Querejeta, 2020). This galaxy has been well studied in recent years as part of the big surveys of dense molecular gas at kpc scales (EMPIRE – Jiménez-Donaire et al., 2019), cloud-scale molecular gas emission (PHANGS-ALMA – Leroy et al., 2021b), cloud-scale ionized gas (PHANGS-MUSE – Emsellem et al., 2022), and stellar population (PHANGS-HST – Lee et al., 2021).

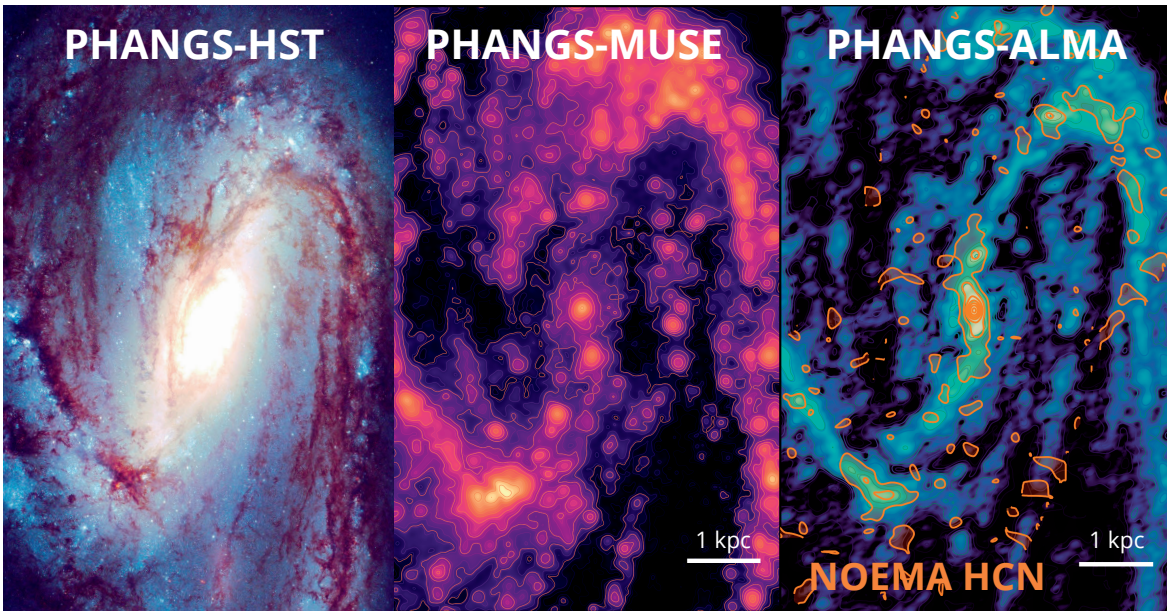

Figure 4.1: NGC 3627 observed at different wavelengths. **Left:** PHANGS-HST (Lee et al., 2021) composite (NUV–*U*–*B*–*V*–*I* bands) **The middle panel:** The ionized gas at 1.5 arcsec traced by Hα emission, a part of the PHANGS-MUSE survey (Emsellem et al., 2022). **Right panel:** The bulk molecular gas traced by CO(2–1) emission at 1.5 arcsec. Orange contours show the 100 pc scale (~ 2 arcsec) HCN emission obtained by NOEMA.

A synergy of high resolution datasets

Using the NOEMA interferometer, we mapped HCN, HCO^+, and HNC, including the CO isotopologues, ^{13}CO and $C^{18}O$ at 100 pc scales across the disc of the nearby star-forming galaxy NGC 3627. This data set represents the currently highest resolution observations of dense molecular gas across a large portion of a nearby star-forming galaxy, probing scales of individual GMCs. NOEMA observations were conducted in spring 2018 using the intermediate (C - 2arcsec at 100 GHz) and the most extended (A - 1arcsec at 100 GHz) configurations. Using the `POLYFIX` correlator, we simultaneously observed high-critical density lines and the CO isotopologues. The data reduction was obtained using `GILDAS` software (Pety, 2005). The imaging was done using the Högbom `CLEAN` algorithm within the ^{12}CO mask from the EMPIRE survey (Jiménez-Donaire et al., 2019). Our observations were combined with the single dish data from the EMPIRE survey, which added nearly 80% of the flux missed in interferometric observations.

This study uses the synergy between *state-of-the-art* high-resolution data sets using the most powerful observing facilities today. We show these datasets in Figure 4.1. In this work, we combined multi-wavelength datasets to compare properties of high-resolution datasets available at the moment: star formation from VLT/MUSE (PHANGS-MUSE survey - Emsellem et al., 2022), cloud-scale molecular gas (PHANGS-ALMA survey - Leroy et al., 2021b), and dense molecular gas emission at GMC scales obtained by NOEMA. Additionally, to identify each morphological environment in NGC 3627, we used an environmental mask generated from the IR data (Querejeta et al., 2021). These masks show that within the disc of NGC 3627, besides the centre, this galaxy has a bar and two spiral arms.

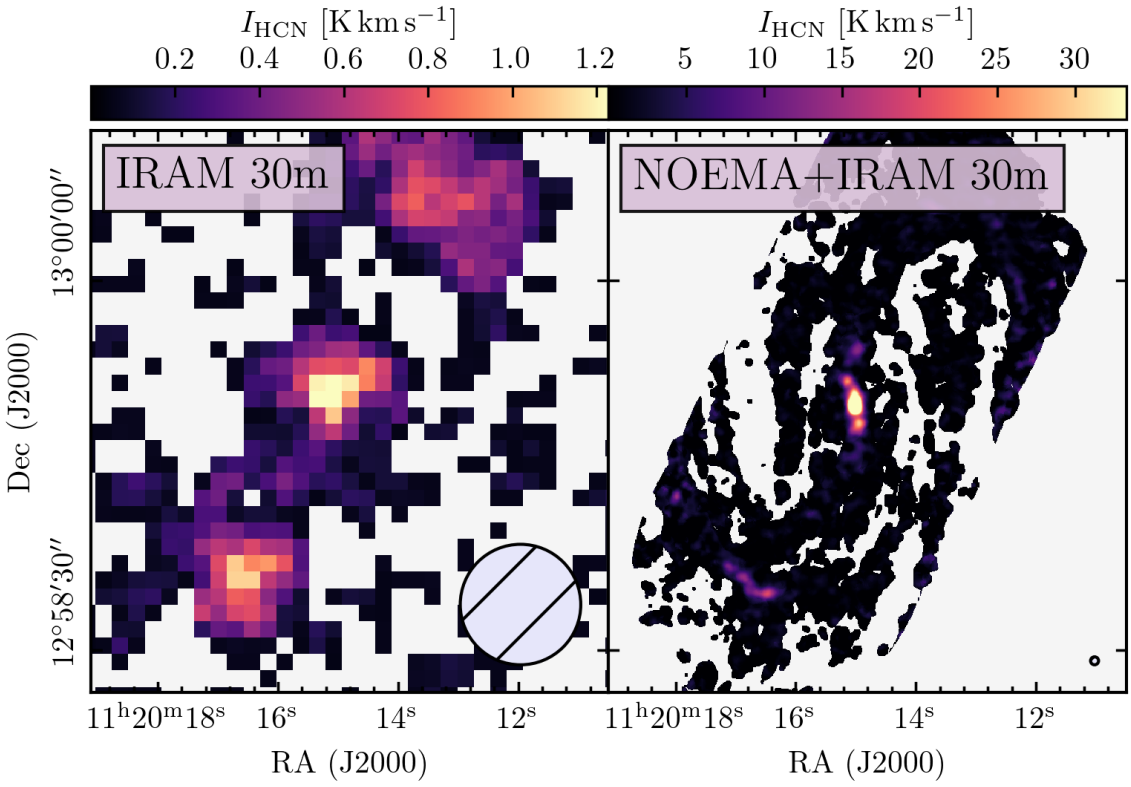

Figure 4.2: The HCN integrated intensity map of a nearby galaxy NGC 3627 observed by IRAM 30-meter telescope (left panel Jiménez-Donaire et al., 2019), and NOEMA+IRAM 30-meter data published in Bešlić et al. (2021). The circle in the lower right corner of each panel shows the beam size.

4.1.2 The benefit of mapping HCN emission at small scales

We show the impact of high spatial resolution measurements on the example of HCN emission across NGC 3627 in Figure 4.2 and demonstrate the need for mapping dense molecular gas at such spatial scales. The left panel of this figure shows the integrated intensity of HCN emission obtained by the IRAM 30-meter telescope from the EMPIRE survey (Jiménez-Donaire et al., 2019). The right panel shows the NOEMA+IRAM 30-meter data from Bešlić et al. (2021). On one hand, at kpc scales, the disc of NGC 3627 is resolved, and three bright spots in emission are noted. However, kpc scales are insufficient to provide detailed information about morphological environments. On the other hand, the jump in resolution by a factor of 10 provided additional information about structures in the disc of NGC 3627. For example, at 100 pc, we resolve different environmental features in this galaxy. HCN emission shows bright emission towards the centre and along the bar of NGC 3627. The following regions where we observe enhanced emission are the contact points between the bar and spiral arm features, also referred to in the literature as bar ends. We note, however, that due to the weak emission of such gas, our observations did not detect significant emission throughout the whole field of view. Therefore, to further analyse the data and investigate how the emission varies across the galaxy and how it compares with other high-resolution datasets, we needed to average the data to increase the signal-to-noise ratio.

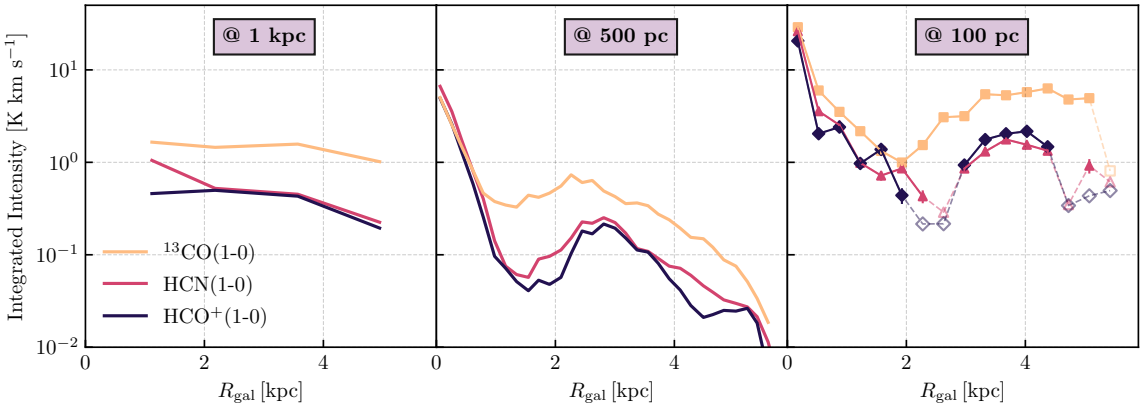

Figure 4.3: Comparison between different spatial resolutions of molecular emission across NGC 3627. Each panel shows the radial distribution of various molecular lines. The first panel shows kpc scale data points from the EMPIRE survey (Jiménez-Donaire et al., 2019). These points are radially stacked. The middle panel shows radially binned data from Gallagher et al. (2018a). The third panel shows radially stacked 100 pc measurements from Bešlić et al. (2021).

We used stacking to increase the signal-to-noise ratio and gain more information about the observed emission. Spectral stacking is introduced and described in Schruba et al. (2010), and it has been widely used within the literature (e.g. Jiménez-Donaire et al., 2019). In short, we measure integrated intensities from the averaged spectrum. To average (bin) spectra, we define the parameter space within which we want to stack. For example, averaging the spectrum of sightlines that have deprojected distance within a range of (r_1, r_2) from the centre of a galaxy is called radial stacking. Alternatively, it is possible to stack the spectra by the CO(2–1) integrated intensity or by the stellar surface density, $\Sigma_{\rm SFR}$. In Bešlić et al. (2021), we used all three approaches, allowing the following comparisons.

In all cases, our attempts to recover faint emission and gain a signal-to-noise ratio were mainly successful for the brightest emission lines in our sample (^{13}CO, HCN, HCO^{+}). However, spectral stacking could not further improve the emission of the two faintest molecular lines in our sample, HNC and C^{18}O.

Comparison with low resolution studies

We show the radial distribution of three measurements of the HCN emission and other molecular lines at different spatial resolutions in Figure 4.3: kpc-scale measurements observed by IRAM 30-m telescope from the EMPIRE survey (Jiménez-Donaire et al., 2019), a 500 pc scale measurements obtained by ALMA (Gallagher et al., 2018a), and 100 pc scale emission from Bešlić et al. (2021). The change in spatial resolution significantly impacts the observed radial distributions. We note, however, that in the case of Jiménez-Donaire et al. (2019) and Bešlić et al. (2021) data points are radially stacked, whereas the measurements from Gallagher et al. (2018a) are radially binned. At kpc-scales, we see that the centre of NGC 3627 shows the brightest molecular emission. As we move toward the outskirts of a galaxy, the emission smoothly decreases. At 500 pc scales, we note a difference. Centres remain the brightest, but we note a bump in the emission between the 2 and 3 kpc, after which the emission smoothly decreases up to several kpc. This difference in radial profiles becomes more prominent at 100 pc scales (Bešlić et al., 2021). At these spatial scales, we separate different

morphological environments and can study changes in radial distribution. In the first order, we see a sharp decrease in molecular emission between 1 and 2 kpc, along the bar. As we approach the edges of the bar, i.e. bar ends, the emission becomes enhanced. Unlike the kpc scales, where each data point represents averaging over a larger area, we observe the significant difference at GMC scales.

4.1.3 Intensity ratios as a proxy for tracing density changes

In Chapter 1, Section 1.5, we provided a brief overview of a study that highlighted using various molecular line ratios to trace density changes. In particular, Leroy et al. (2017a) showed, by modelling emission of various molecular lines within 3-4 mm regime, including a few different-J transitions of CO, that their intensity ratios reflect changes in the sub-beam density distribution. Leroy et al. (2017a) theoretically proved that these lines could be used as a tool for constraining changes in gas volume densities and even defining the density distribution. This is important for extragalactic measurements, where the typical beam size probes a few hundred pc. In addition, we needed observations of small spatial scales to probe sub-beam density changes to obtain such measurements.

In Bešlić et al. (2021), for the first time, we take that step and link molecular cloud surface density to molecular spectroscopy. We test whether molecular line intensity ratios are sensitive to changes in gas densities within a beam by deriving integrated line intensities from stacking by the CO(2–1) emission. The cloud-scale CO(2–1) is known to be a good trace of volume gas densities (e.g. Sun et al., 2018), assuming a constant scale height. We show results from theoretical modeling (Leroy et al., 2017a) in comparison to our measurements presented in Bešlić et al. (2021) in Figure 4.4. Following the idea presented in Leroy et al. (2017a), we calculated various line-to-CO(2–1) intensity ratios and placed them in order by accending critical density. In addition, we assigned the colour to each of our data points by its CO(2–1) intensity. Assuming all the above, we note that the colour bars from the left and right panels will be correlated.

Similarly, as in Leroy et al. (2017a), line ratios flare from low-critical to high-critical density regimes. This flaring reflects the changes in the cloud-scale surface densities, measured by the CO(2–1) emission. The variation with the cloud-scale surface density of molecular gas is the most prominent in the HCN/CO(2–1) line intensity ratio since the HCN has the highest critical density among our sample. On the contrary, we do not see any particular variation in the ^{13}CO/CO(2–1) which was expected because the ^{13}CO molecule has a lower critical density than the CO(2–1) molecule.

4.1.4 Drivers of local star formation

In our work, we investigated how gas is efficient at star formation depending on the local conditions. In particular, we examined the star formation efficiency of HCN-tracing gas across two bright regions in NGC 3627: the centre and across bar ends. In the previous section, we have shown that among our sample, the HCN/CO(2–1) intensity ratio is the most sensitive to changes in the cloud scale surface density. Therefore, we used the HCN/CO(2–1) as a proxy for the dense gas fraction. We show how Hα/HCN luminosity ratio varies as a function of HCN/CO(2–1)in Figure 4.5.

Our results are with findings from the literature. Even at 100 pc scales, we find the highest amount of dense gas fraction within the centre of NGC 3627. On the one hand, the HCN/CO(2–1) does not significantly vary between the centre and the bar. On the other hand, the difference in the Hα/HCN ratio is significantly different, suggesting that gas in the bar ends may be more efficient at star formation (Murphy et al., 2015).

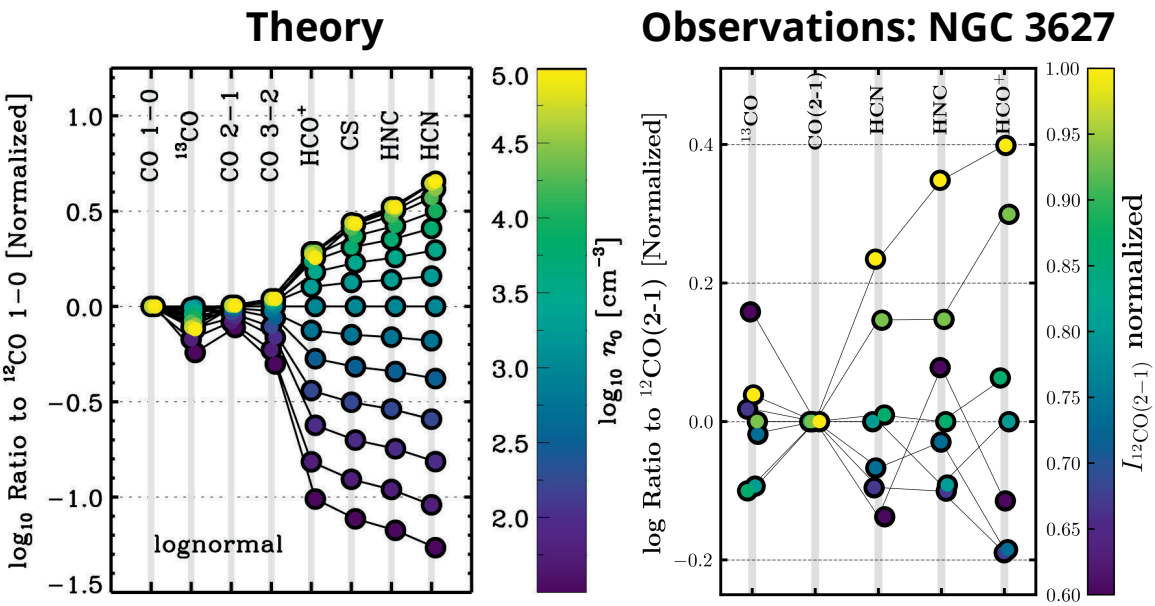

Figure 4.4: A comparison between theoretical results and observations in NGC 3627. The left panel shows line intensity to CO(1–0) ratios varying with the gas volume density, as shown on the colour bar. The left panel is the result from modelling Leroy et al. (2017a). On the right panel, we show the same as in the left but using observations of high-critical density molecules and the CO(2–1) emission across NGC 3627. In this case, we show the variations of these line intensity ratios as a function of the CO(2–1) intensity.

In the following, we will provide several possible explanations of our results. The highest dense molecular gas fraction is in the centres of galaxies, i.e. in the densest regions characterised by high stellar surface density, molecular gas surface density, and pressure. We show the illustration of two clouds sitting in two environments (disc of a galaxy and its centre) in Figure 4.6. The gas density increases from left to right. The mean gas density of a cloud in a bar end is n_1, whereas the mean gas density of a cloud in a galaxy centre is n_2. $n_{\rm crit}$ is the critical density of a dense gas tracer, like HCN. We assume that the gas density of both clouds is described via a log-normal and the power-law function. In the case of a cloud located in the bar end, the critical density of a dense gas tracer is considerably higher than the mean gas density. $n_{\rm crit}$ is on the high-density end and belongs to the power-law tail of the PDF and describes the density of the star-forming gas. In the other case, the molecular cloud is in a denser environment. $n_{\rm crit}$ is significantly lower than the mean gas density of a cloud in the centre of a galaxy, and it is on the low-density end, i.e. log-normal part. Such interpretations are contrary to the predicted density threshold for star formation (Lada et al., 2012). In this picture, knowing the mean gas densities is necessary to interpret the emission of a high-critical density line.

In addition, HCN emission can be further enhanced by strong IR emission, typical for AGN centres of galaxies. At 100 pc, unlike for the kpc-scale measurements, we enter a domain where star formation and molecular gas emission decouples, as shown in Schruba et al. (e.g. 2011); Schinnerer et al. (e.g. 2019); Pan et al. (e.g. 2022). The degeneracy comes from the timescales over which molecular clouds evolve and the free-fall time (Kruijssen et al., 2018; Chevance et al., 2020). We confirm these findings by finding the offset between the peaks of the HCN and CO(2–1) and Hα emission.

In respect of the turbulent of star formation, the dynamics of molecular gas have an impact on setting the local star formation. We found broad HCN and CO(2–1) emission lines within the centre

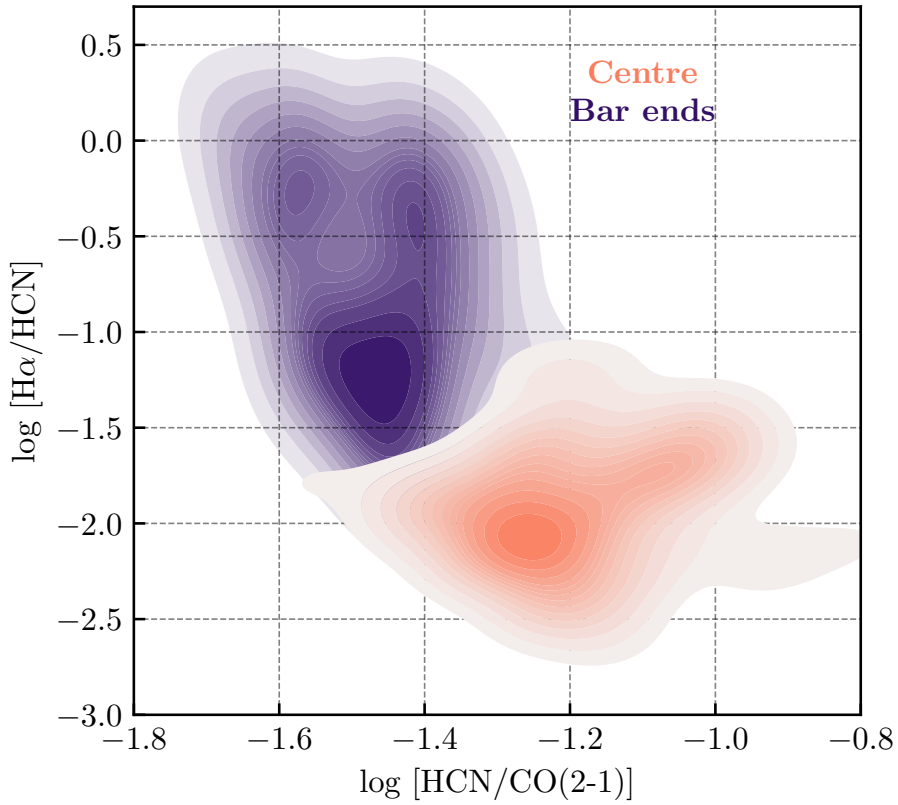

Figure 4.5: Comparison between star formation efficiency and the relative amount of the HCN-tracing gas across the centre and bar-ends in NGC 3627.

of NGC 3627. Similarly, HCN and CO(2–1) spectral lines are broad within the bar ends but show multiple velocity components. By inspecting the HCN and HCO^+ data cubes, we saw the presence of multiple velocity components in their spectra towards the bar end. We show these features towards several lines of sight across both bar ends in NGC 3627, including the spectra of CO(2–1) molecule in Figure 4.7. Beuther et al. (2017) identified these velocity components in the CO(2–1) emission and, using orbital models, concluded that these components belong to bar and spiral arm orbits. The presence of these complex emission features in the bar ends could explain the enhanced molecular emission and observed star formation efficiencies (e.g. Murphy et al., 2015) of dense molecular gas in these regions. Our results indicate the cloud-cloud collisions within the bar ends, which can explain the local enhancement in molecular emission and star formation. To prove that, we need higher spatial resolution observations of molecular gas.

4.1.5 Summary

In Bešlić et al. (2021), we probed for the first time the emission of high-critical density molecules across the disc of a nearby galaxy. Our study suggests that the local over-densities and gas turbulence are essential in stabilising the star formation. The work outlined in previous sections emphasises the strong relationship between the dense gas and environmental impact. We pointed out the necessity of understanding processes occurring in the bar ends. These regions are the following brightest regions

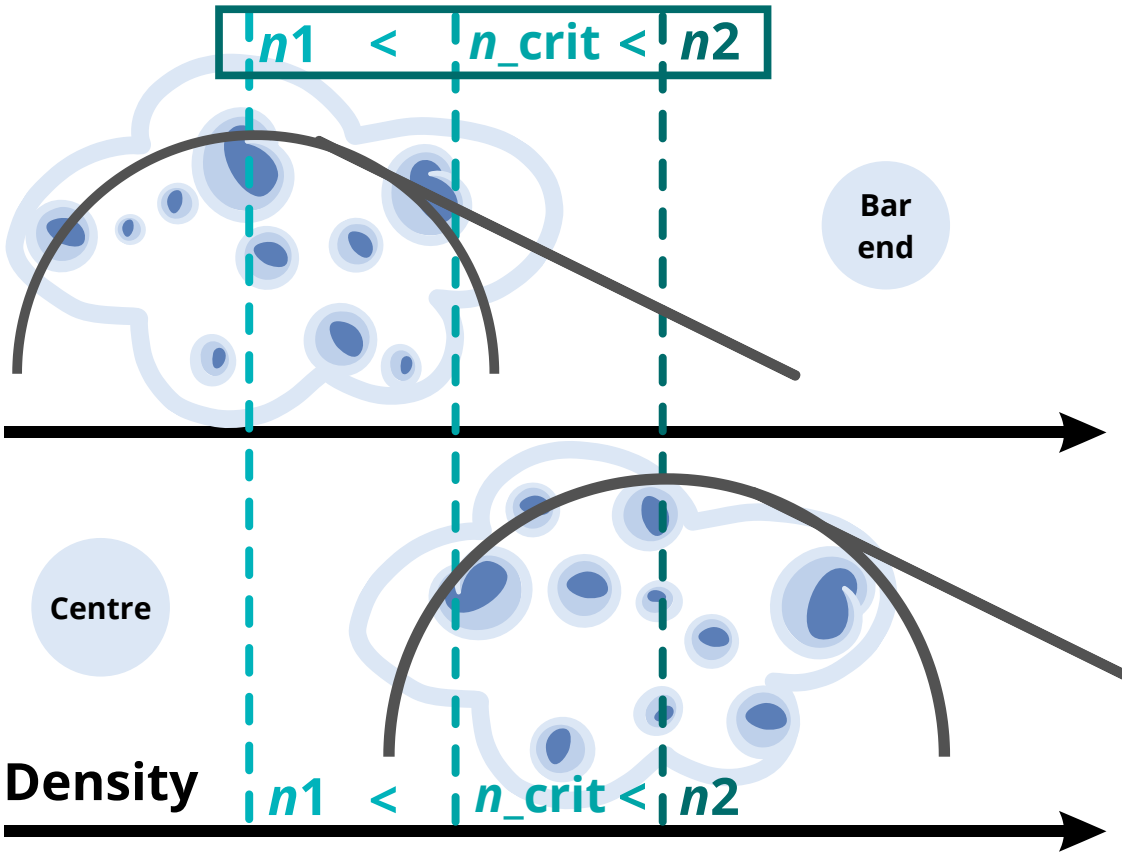

Figure 4.6: The example of environmental impact on a molecular cloud. We show a cloud from the disc of a galaxy and a cloud located in the centre. Gas densities in both clouds can be described via log-normal and a power-law tail (Chapter 1, Section 1.5), but with different mean gas densities - n_1 and n_3. The critical density of a dense gas tracer is n_2.

we observe in nearby galaxies after nuclear regions. In addition, bar end regions in nearby galaxies represent the analogues to the Galactic starburst region W 43 (Beuther et al., 2012). Another important aspect of studying bar ends is that these regions are potentially hosting cloud-cloud collisions, which are external triggers for star formation (e.g. Tokuda et al., 2020). Understanding these environments, including the influence of bar on the galactic dynamics and star formation in barred systems, should be investigated in more detail in future studies. Our work illustrates why it is crucial to probe dense gas content at cloud scales in nearby galaxies and initiated the ongoing NOEMA M 51 large program (PI: E. Schinnerer, F. Bigiel), which will provide more sensitive maps of these gas tracers across the Whirpool galaxy, M 51.

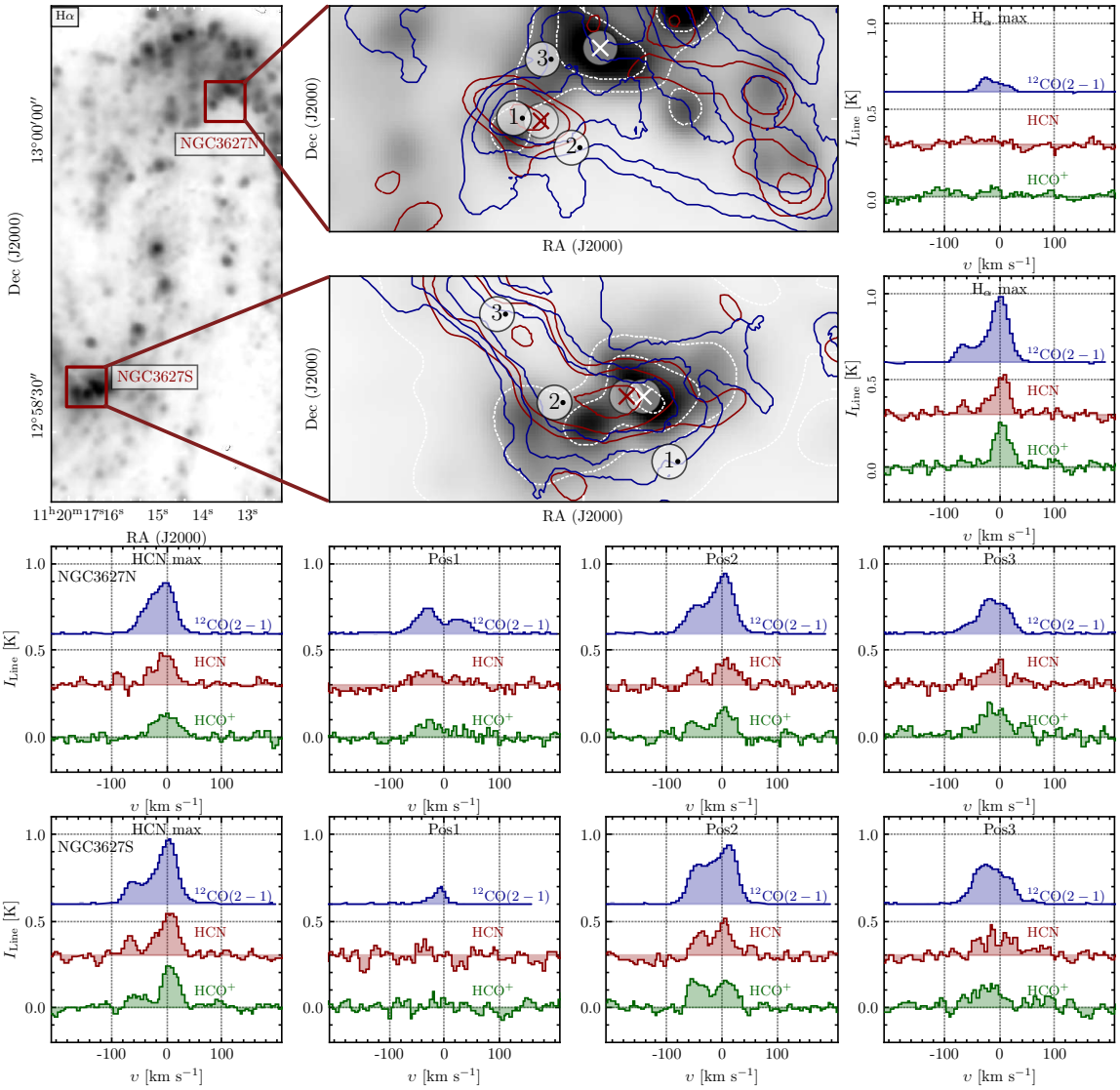

Figure 4.7: Spectra of the HCN (red), HCO$^+$ (green) (Bešlić et al., 2021) and CO(2–1) (blue) emission taken towards the bar ends in NGC 3627, shown in the upper left and middle panels (Bešlić et al., 2021).

4.2 Physical conditions of molecular gas in the centre and bar ends of NGC 3627

4.2.1 Introduction

In this section, we expand findings from Bešlić et al. (2021). In Bešlić et al. (2021), we shown that various line to CO(2–1) intensity ratios can trace changes on cloud scale surface densities, which is the proxy for gas volume densities, as previously presented in Leroy et al. (2017a). In particular, line ratios between high and low critical density lines are sensitive to various gas densities, and can be used as a proxy for determining the density contrast. High critical density molecules like HCN, HNC and HCO^+ have an effective critical density above or close to the mean molecular density and consequently, their line ratio to CO(2–1) shows more variation than the ^{13}CO/CO(2–1) ratio.

From Leroy et al. (2017a), it is known that gas PDFs differently impact the observed flaring of density-sensitive line ratios. For example, the log-normal density distribution has stronger impact on the line ratios sensitivity to density changes, whereas a combination of log-normal and the power-law tail less affects the flaring of these line ratios. Although we linked molecular gas spectroscopy with the cloud scale surface densities, results in Bešlić et al. (2021) could not provide any details on the gas density distribution. The reason for not determining the density distribution lies in the modest signal-to-noise ratio of the observed molecular emission. As previously explained in Section 4.1, data points we shown on the right panel in Figure 4.4 are intensity ratios measured from the spectral stacking by the CO(2–1) emission. Therefore, our data points are the result of averaging over regions with similar CO(2–1) emission. Due to the availability of a large number of molecular lines presented in Bešlić et al. (2021), here we take this exercise one step further and constrain the mean gas density via application of a radiative transfer model.

The dense gas toolbox

In this section, we present results on calculating gas density distributions from using the *Dense Gas Toolbox*[1] (`DGT`; Puschnig, 2020). The dense gas toolbox is based on the approach developed in Leroy et al. (2017a). Instead of assuming fixed, single density, this approach considers density distributions. For radiative transfer calculations, in which we solve the set of equations describing the gas conditions and how the medium impact the incoming radiation, `DGT` uses`RADEX` (van der Tak et al., 2007). `DGT` utilizes Bayesian inference to obtain model parameters, such as density and temperature. The input parameters are line intensities. Another assumption is that the emission lines emerge from an isothermal distribution of gas densities following a log-normal distribution with power-law tail.

First, we define density bins and calculate line emissivity in each density bin. To do so, we use the expanding-sphere escape probabilities (large velocity gradient approximation - LVG), already implemented in `RADEX`. Other important parameters, such as the line optical depths and abundances are calibrated using observations of the EMPIRE survey (Jiménez-Donaire et al., 2019). In this case, the temperature is the free parameter, whereas we fixed the width of the density distribution of 0.2 dex. A detailed description of the models will be presented in J. Puschnig et al. (in prep).

[1] `http://www.densegastoolbox.com`

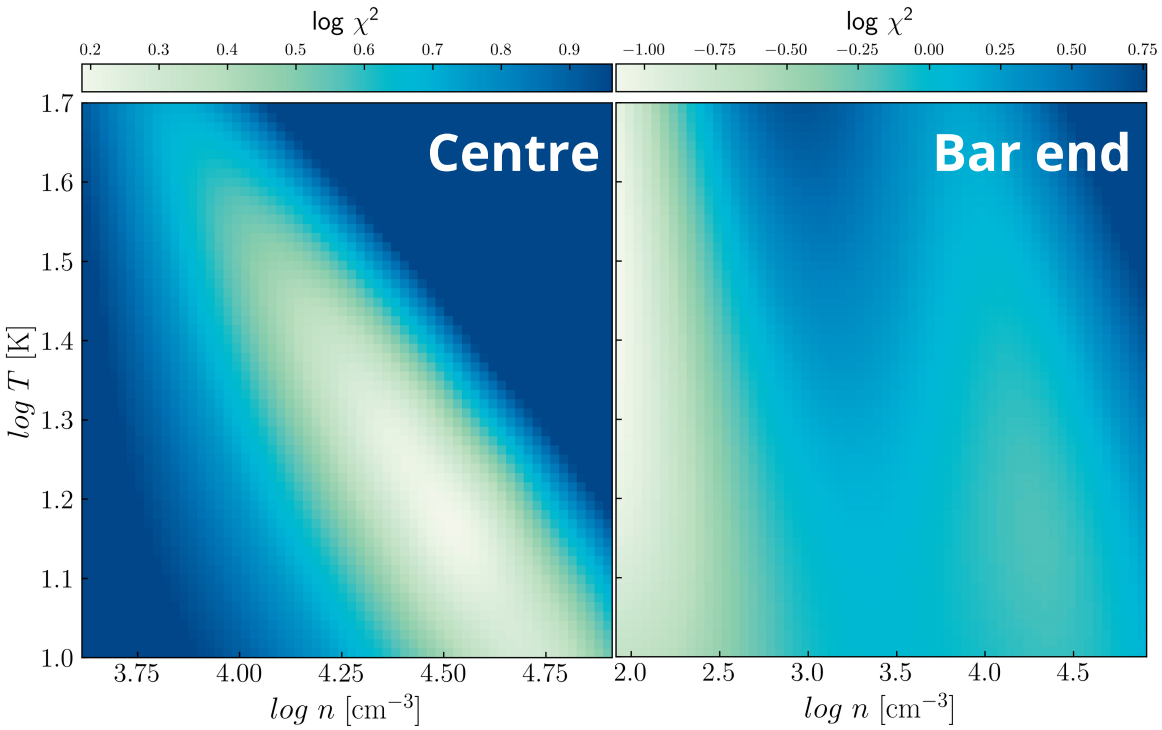

Figure 4.8: Results from the `Dense Gas Toolbox` that minimizes observed line ratios against radiative transfer models. Solution planes are shown for typical sight lines towards the centre of the galaxy (left panel). We show solution plane for the bar end located on the south, as the results from `Dense Gas Toolbox` are similar for both bar ends (right panel).

4.2.2 Results

We derived mean gas density from a DGT analysis for sight lines across two brightest regions in NGC 3627: the centre and both bar ends. Similar results are found for both bar ends. The models suggest a mean density of $\sim 10^4$ cm^{-3} for sight lines towards the centre of the galaxy and lower gas densities ($\sim 10^2$ cm^{-3}) in the bar ends. The observed emission of the densest gas tracers in our sample, however, may emerge from gas with even higher volume densities, as explained in Section 4.1. Given the derived width of the (assumed) log-normal ensemble of densities of 0.3 dex (for the centre and bar ends), a significant fraction of the gas in the centre and the bar ends is thus found at densities well above $\sim 10^5$ cm^{-3} and $\sim 10^3$ cm^{-3}, respectively. In Figure 4.8, we show the solution planes from the `DGT` for sight lines coming from the centre (left panel) and the southern bar end (right panel). While the results in the central part of the galaxy seem to be well constrained, the solution for the bar ends is less constrained, probably due to the presence of two distinct density regimes. In the bar ends, the low-density regime is dominant.

We thus argue that in the centre of NGC 3627 the HCN(1–0) line becomes a weak tracer of denser molecular gas, because its critical density is already close or even lower than the mean gas density. In such environments, HCN(1–0) traces the bulk molecular gas rather than only the densest fraction of it (which is the most susceptible to gravitational collapse and star formation). Hence, the apparent separation of the Hα/HCN and HCN/CO(2–1) of the centre and the bar end, as presented in Bešlić et al. (2021), could be explained by the large difference in the mean gas densities.

In addition, using the DGT, we estimate a kinetic temperature of the gas in the centre and bar ends. We found the temperature of ∼16 K in the centre of NGC 3627. The kinetic temperature computed in the bar ends is left unconstrained. The reason for unconstrained temperature estimates in bar ends originates from the presence of two density regimes in the solution plane (right panel in Figure 4.8). We note here, however, that a kinetic temperature in the centre derived with DGT mostly rely on our observations of ground state transitions (J=1-0) and should thus be considered as coarse estimates.

Moreover, we compare the kinetic temperature in the centre of NGC 3627 derived from the DGT with the temperature empirically estimated from the HCN/HNC intensity ratio (Hacar et al., 2020). Using the HCN/HNC intensity ratio and prescription from Hacar et al. (2020), Bešlić et al. (2021) estimated the temperature in the centre of ∼ 4 K. The discrepancy between empirical and DGT temperatures can be explained as following. Firstly, the input data for DGT mostly rely on our observations of ground state transitions (J=1-0). However, in order to better constrain the excitation temperature in the models, higher-J transitions are required. Secondly, the empirical temperature from Hacar et al. (2020) was determined using HCN and HNC observations on local clouds in the Milky Way at much higher spatial resolution (∼ 0.06 pc), probing larger dynamical range.

It is worth pointing out that the kinetic temperatures derived with DGT and thus taking into account the multitude of observed lines, contrast those from the empirical approach based on the HCN/HNC line ratio only. This discrepancy might be caused by the fact that HCN/HNC probes temperatures of the densest parts of the gas distribution, while DGT solves for an average temperature under the assumption of iso-thermalization.

4.3 GMC catalog analysis in NGC 3627

4.3.1 Introduction

In Chapter 1, Section 1.4.4, we described the properties of giant molecular clouds and recent results of studying the properties of molecular gas emission at giant molecular cloud scales. Molecular gas shows an inhomogeneous, clumpy structure. The first idea of extracting molecular clouds from measurements originates from Heiles (1971) who used dust extinction maps to isolate dark clouds. Rosolowsky & Leroy (2006) developed cataloguing algorithm in extracting molecular cloud from the CO emission - CPROPS. In short, the method for defining molecular cloud is based on finding local peaks of the CO emission and then including neighbouring pixels and velocity channels before reaching the signal-to-noise threshold. In the recent, updated version of the CPROPS, written in PYTHON, PYCPROPS (Rosolowsky et al., 2021), the method of cloud identification is improved to lower the impact of inhomogeneous noise and limited spatial resolution.

Rosolowsky et al. (2021) presents results on GMC properties using the PYCPROPS across a sample of ten PHANGS-ALMA galaxies, including NGC 3627. The key finding in Rosolowsky et al. (2021) is that the cloud properties depend on the morphological environment. For example, GMC located in the bar, like in the case of NGC 3627, have broader lines and have higher surface densities than the GMCs located along the spiral arms. Rosolowsky et al. (2021) identified slightly more than 500 GMCs in NGC 3627 at 90 pc resolution.

Moreover, in Bešlić et al. (2021) we investigated general properties of high-critical density molecular lines at scales of giant molecular clouds. This includes radial trends of the observed line intensities, how different line intensity ratios vary across NGC 3627, and how these correspond to the measured star formation rate. The relations between dense molecular gas, molecular gas and star formation

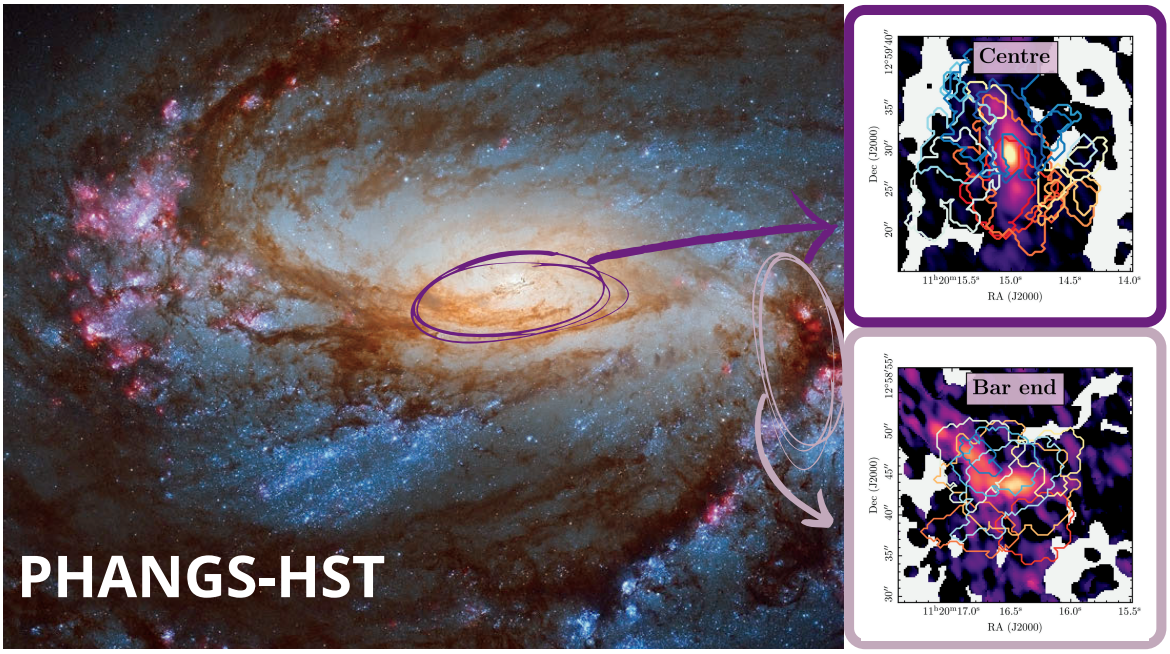

Figure 4.9: **Left:** The composite image of NGC 3627 obtained by Hubble Space Telescope (HST, image credits: PHANGS-HST Lee et al., 2021). We label the centre and southern bar end of this galaxy. **Right:** We show the HCN integrated intensity map in the background within the centre (top panel) and bar end (bottom panel). Overplotted contours are the GMC footprint calculated using PHANGS-ALMA CO(2–1) data (Leroy et al., 2021b) and PYPROPS (Rosolowsky et al., 2021).

presented in Bešlić et al. (2021) are based on pixel-by-pixel or stacked points comparisons (Figure 4.5). However, both approaches use emission averaged within regions and not from one GMC.

In this section, we take that next step and analyse HCN emission on a cloud-to-cloud basis. We use cloud identification to extract the HCN emission within each cloud. In the following, we will present results comparing the HCN emission encompassed within each GMC structure with properties of GMCs derived from PYCPROPS. We link cloud-to-cloud properties of dense molecular gas and star formation for the first time.

4.3.2 Extracting the CPROPS properties of the HCN emission

In this work, we used version 3.4 of the internal release of the GMC catalogue derived from PYCPROPS. To match our data presented in Section 4.1, we used the GMC catalogue generated using ALMA CO(2–1) 12m+7m+tp spectral cube at 100 pc resolution. The PYCPROPS identified around 500 GMCs in NGC 3627.

Due to the limitation in the signal-to-noise ratio of the HCN emission (Figure 4.1), we focus on the two brightest regions in NGC 3627: the centre and the southern bar end. By applying environmental masks (Querejeta et al., 2021), and positions of GMCs, we located 26 GMC: 18 in the centre and 8 GMC toward the bar end. To spatially isolate each GMC, we used the "cloud footprint" and applied it to the HCN spectral cube. The cloud footprint is a 3-dimensional array, equivalent to a mask. Each molecular cloud identified using PYCPROPS has assigned an id number. In this mask, all spaxels not associated with any GMC are set to zero, whereas other pixels will have a value equal to the id number

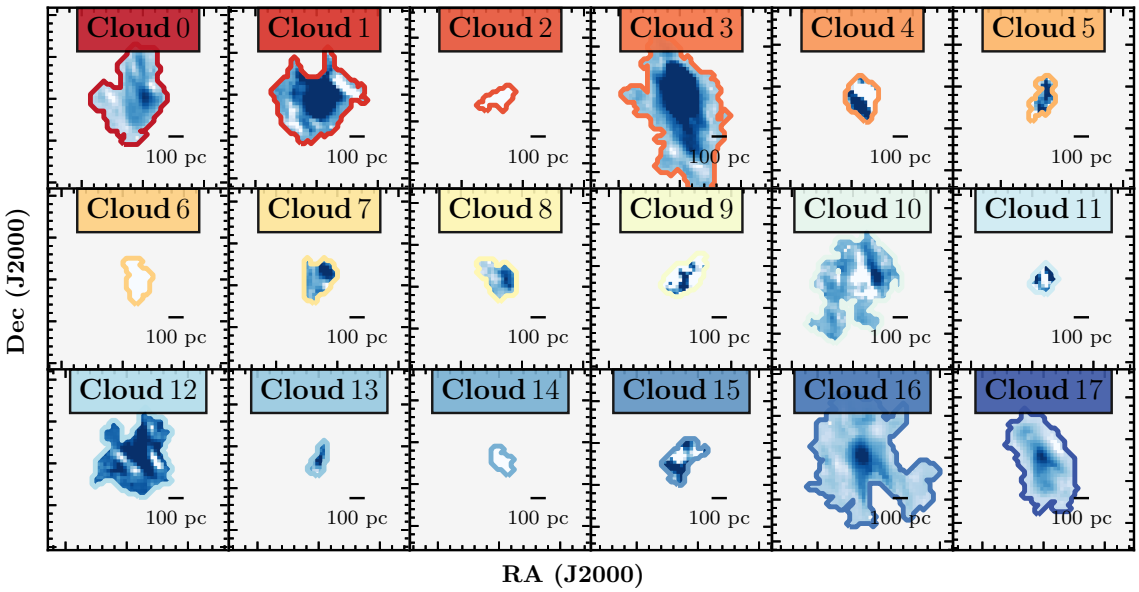

Figure 4.10: The HCN integrated intensity map of each cloud within the centre of NGC 3627. The colour within each cloud shows from 0 to 99.9% of the maximum HCN intensity within that cloud. We show a scale bar in the bottom right corner of each panel.

of their associated cloud. We apply this mask to our HCN cube and extract each cloud as a data cube - cloud cube.

We show clouds' two-dimensional footprint overplotted on the HCN integrated intensity map in Figure 4.9. Each cloud in the centre and bar end is shown as a contour using one colour. It is important to note that, even though it looks like some clouds spatially overlap, this might not be entirely the case since we show their projected boundaries as a map. In this case, we do not have information about velocity structures.

4.3.3 Comparison between molecular clouds in the centre and the bar ends

We use derived properties of the GMCs such as radius, mass and velocity dispersion to compare the HCN emission within each GMC. At the end of this work, we will include the star formation rate measured in NGC 3627 using Hα emission from PHANGS-MUSE (Emsellem et al., 2022). We computed the HCN integrated intensity within each cloud by collapsing the data of the cloud cube along the velocity axis and multiplying it by the channel width. Similarly, we calculate the CO(2–1) intensity within each cloud. For extracting star formation rate within each cloud, we use the 2-dimensional cloud footprint due to the coarse spectral resolution of the Hα measurements. Figures 4.10 and 4.11 show the HCN integrated intensity maps for each cloud previously shown in Figure 4.9. The boundary of each cloud is shown with the same colour as in Figure 4.9. To first order, we see in Figures 4.10 and 4.11 that the highest HCN integrated intensity lies within inner parts of each cloud. This does not hold for clouds where we did not find any or faint HCN emission, for example, as in clouds with numbers 7 and 8 within the centre (Figure 4.10). This result implies that molecular clouds have denser substructures. By comparing "by-eye" the projected size of each cloud with the scale bar located at the lower right corner of each panel, we see that clouds are predominantly

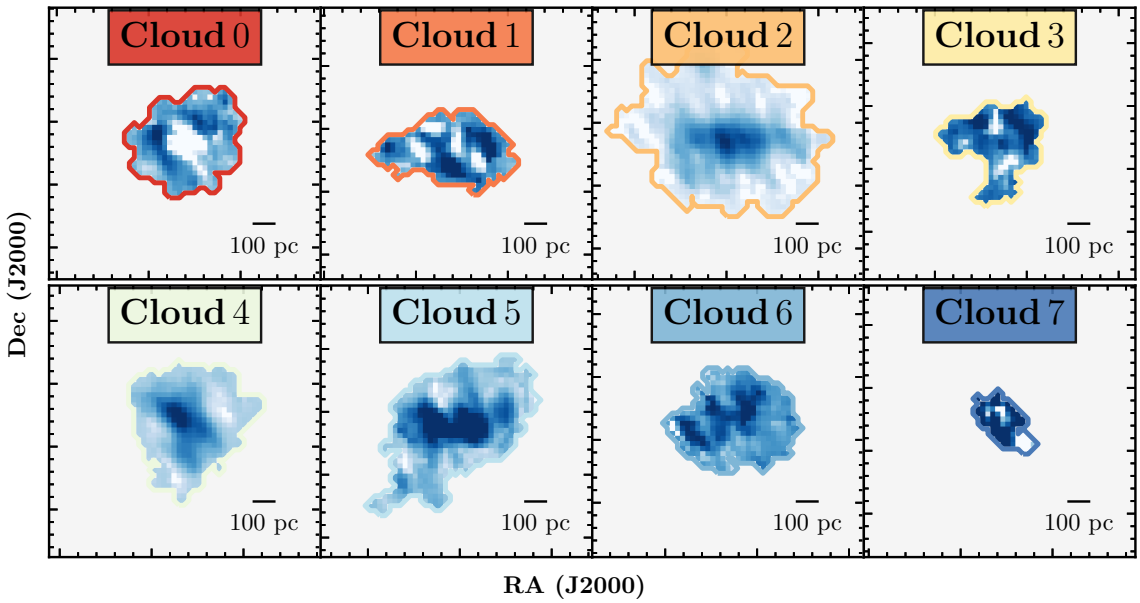

Figure 4.11: The same as in Figure 4.10, but for GMCs within the bar end.

larger than 100 pc. We note that we used the GMC output from a 100 pc resolution CO(2–1) data cube. Therefore, our results are biased and sensitive to the spatial scales our observations probe.

Using the GMC catalogue, we extracted the mass and radius of each. We show the luminous mass of the cloud and the intensity of the HCN emission related to the radius of a cloud in Figure 4.12. In the first order, mass positively correlates with the radius of a cloud, as expected and explained in Chapter 1, Section 1.4.4. There is no significant difference between the mass-size relation of GMCs located in the centre and the bar ends. In addition, the HCN emission appears to not correlate with the size of the cloud.

Next, as we show the pixel-by-pixel comparison in Figure 4.5, we show a cloud-cloud comparison between SFR/HCN and HCN/CO(2–1) intensity ratio in the centre and the bar ends. We note higher HCN/CO(2–1) than those measured in Bešlić et al. (2021). The reason is that in this case, we take into account emission identified in CPROPS, whereas in Bešlić et al. (2021) within each pixel/line of sight, we included diffused CO(2–1) emission, which contributes to total CO(2–1) emission and effectively lowers the observed HCN/CO(2–1) intensity ratio. We do not expect to see the diffuse HCN emission simply because it traces denser gas than the CO(2–1) molecule. In addition, we used information about two-dimensional Hα emission, which might bias our results.

Each point is coloured following the contour line that shows the borders of each molecular cloud in Figures 4.10 and 4.11, and the size of each point corresponds to the cloud's turbulent velocity dispersion, σ. We see that the turbulent velocity dispersion of clouds is similar in both environments.

We note an indication of two possible distinct regimes: the one where we see clouds from both environments with lower HCN/CO(2–1) intensity ratios and a wide range of Hα/HCN (several orders of magnitude). The other data points are clouds from the centre of NGC 3627 that show high HCN/CO(2–1) intensity ratio and nearly constant and low Hα/HCN.

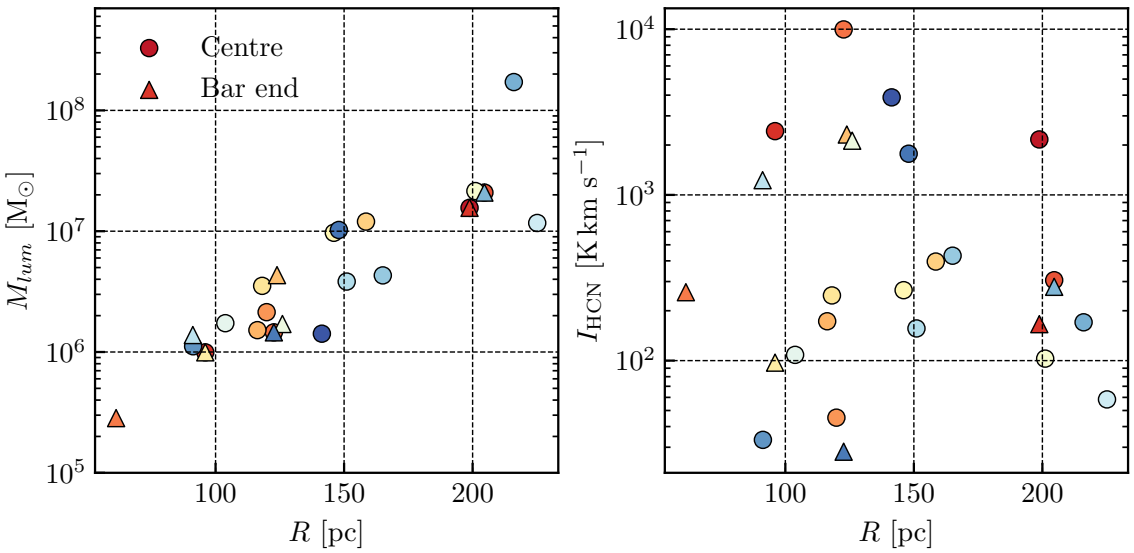

Figure 4.12: **Panel left:** Mass-size relation of GMC from the cloud catalogue. **Panel right:** The measured HCN integrated intensity of each GMC as a function of the size of a cloud.

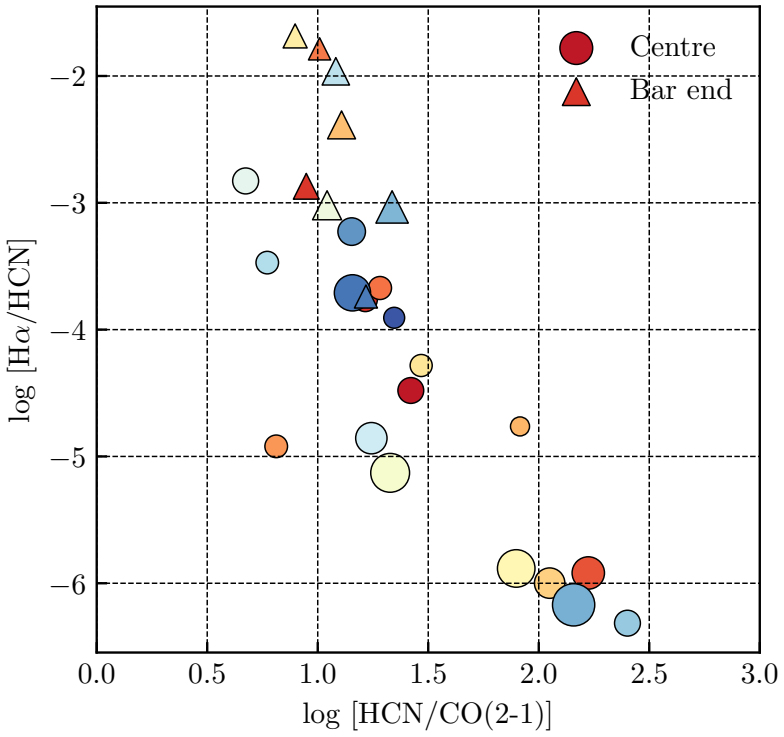

Figure 4.13: Star formation rate to HCN intensity ratio as a function of HCN/CO(2–1) intensity ratio within GMCs shown in Figures 4.10 and 4.11. The colour of each point correspond to the contour line of each cloud in Figures 4.10 and 4.11. The size of each point reflects the turbulent velocity dispersion of the respective cloud.

4.3.4 Discussion

The interpretation of our results, especially those shown on the right panel in Figure 4.12 is impacted by several factors. The HCN emission probes the internal structure of the GMCs and represents a small fragment of the total mass of a cloud. On the one hand, as stated in Section 4.1, the HCN emission in the centre of NGC 3627 is influenced by the AGN, whose impact is not extracted from the HCN emission. On the other hand, the cloud identification does not include the decomposition in emission along the velocity axis, which could affect measurements of clouds along the bar end (Beuther et al., 2017; Bešlić et al., 2021).

Moreover, by associating the Hα emission within each GMC, we did not follow the same approach as for the HCN data cube. By not considering the information along the velocity axis but taking just the total emission within each pixel, we might overestimate the star formation rate within each GMC. The presence of the AGN ionises gas means that not all Hα emission will trace star formation. To exclude the contribution of an AGN, it is first necessary to associate the Hα emission within HII regions (Santoro et al., 2022), and then, using the Baldwin, Phillips and Terlevich (BPT) cut (Baldwin et al., 1981), mask all Hα emission not coming from the star formation.

Future improvements

Overall, this work shows the potential for future studies using higher sensitivity observations of high-critical density lines. A higher signal-to-noise ratio will allow including more environments in the analysis so that it will be possible to perform the HCN cloud-by-cloud and environment-by-environment comparison and even use the cloud decomposition analysis on these data sets instead of CO(2–1). In a further development, the cloud decomposition algorithms, for example, including the decomposition along the velocity space (see Chapter 5, Section B.4) will provide the full potential of analysing dense molecular gas at cloud scales.

CHAPTER 5

The dense gas properties and kinematics of one the closest starburst galaxies (NGC253) observed with ALMA

In this chapter, we present results of our current work, Bešlić (prep), of recent ALMA Atacama Compact Array (ACA) observations across the closest starburst galaxy, NGC 253. This project is based on the PI-ed successful ALMA Cycle 7 proposal, project code 2019.2.00236.S. The preliminary results presented in this chapter went through the internal revision of PHANGS collaboration and will be submitted after completing this doctoral thesis. The complete data reduction, data analysis, figures and the manuscript is conducted by myself.

This chapter is is structured as following. In Section 5.3 we describe observations, data reduction, and the additional data sets used throughout this work. We show results on HCN emission in NGC 253 in Section 5.4 and briefly describe two methods we used to derive HCN intensity. Moreover, in Section 5.5 we present results on the HCN/CO(2–1) intensity ratio. Measurements of HCN velocity dispersion are shown in Section 5.6. We discuss our results in Section 5.7, and lastly, we summarize our work and highlight future implications in Section 5.8.

5.1 Introduction

Surveys of HCN in extragalactic systems found a tight correlation between HCN luminosity and star formation rate (SFR) (Gao & Solomon, 2004a). We show how IR luminosity (a tracer for the SFR) in the left panel of Figure 5.1, together with the IR/HCN luminosity ratio (the right panel in Figure 5.1) varies as a function of the amount of dense molecular gas traced by HCN emission (x axis) within the literature. The correlation between IR and HCN luminosities is approximately linear, spanning more than ten orders of magnitude. This covers a wide range of physical scales, from dense clumps and cores (a few pc - e.g. Wu et al., 2010; Stephens et al., 2016) within the Milky Way, to GMCs in local and nearby galaxies (Chin et al., 1997, 1998; Braine et al., 2017; Brouillet et al., 2005; Buchbender et al., 2013; Chen et al., 2017), to measurements of resolved galaxies' discs (a few kpc - Kepley et al., 2014; Usero et al., 2015; Bigiel et al., 2016; Chen et al., 2014; Gallagher et al., 2018a; Jiménez-Donaire et al., 2019) to whole galaxies and their centres (Gao & Solomon, 2004a; Gao et al., 2007; Krips et al., 2008; Graciá-Carpio et al., 2008; Juneau et al., 2009; García-Burillo et al., 2012; Crocker et al., 2012; Privon et al., 2015; Puschnig et al., 2020). The trend is such that the presence of more dense molecular gas implies a higher star formation rate. In Figure 5.1, we include measurements from this work on NGC 253, coloured by different dynamical ranges. Although it has been argued

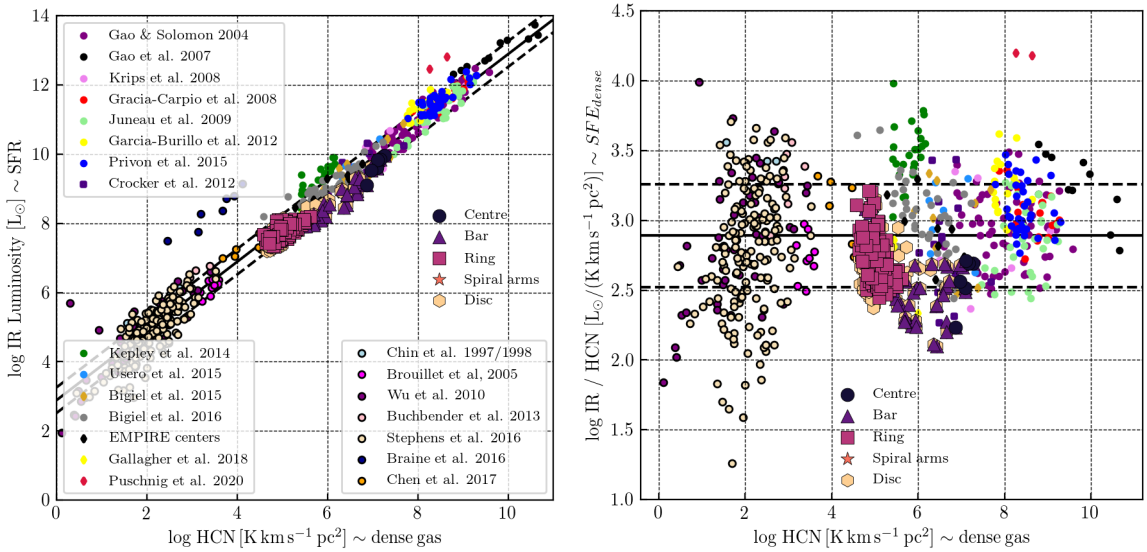

Figure 5.1: **Left:** A literature overview of the infrared luminosity (a proxy for star formation rate) as a function of HCN luminosity (a proxy for dense molecular gas), i.e. Gao & Solomon relation (Gao & Solomon, 2004a). We show measurements of whole galaxies and their centres at a few kpcs (see the legend in the upper and the lower-left part), Milky Way clouds (a few pc scales - see legend on the bottom right), including measurements across NGC 253 (this work - see the legend on the right central part) (Jiménez-Donaire et al., 2019). **Right:** The same as on the left panel, but we are showing $SFE_{\rm dense}$, traced by the IR/HCN luminosity ratio on the y axis. In both panels black solid line shows the mean IR/HCN luminosity ratio measured by the EMPIRE survey (Jiménez-Donaire et al., 2019). Black dashed lines show the 1σ RMS scatter of ±0.37.

that this relation suggests a universal density threshold above which gas starts to form stars (Lada et al., 2012), the scatter we observe in the right panel in Figure 5.1 implies that not all dense gas is equally efficient at star formation. Moreover, the central molecular zone (CMZ), known to be the densest region in our Galaxy, shows by an order of magnitude lower SFR than those predicted from measurements of dense molecular gas (Longmore et al., 2013; Henshaw et al., 2022). There are two possible explanations. In addition to gas density, the velocity dispersion of molecular gas is a second key parameter that determines the SFR (Federrath & Klessen, 2012). The other potential explanation lies at the scales of molecular clouds and their environmental dependence on star formation (Usero et al., 2015; Bigiel et al., 2016; Gallagher et al., 2018a; Querejeta et al., 2019; Bešlić et al., 2021).

To understand the underlying physical reason for the generally observed relation between dense molecular gas and star formation, it is important to conduct more studies of HCN-emitting gas. However, detecting HCN emission is not trivial, as it requires significant observing time to detect and map extended emission. One key step towards understanding star formation processes is connecting the wide range of relevant spatial scales as shown in Figure 5.1: studies of the Milky Way, where we can probe the substructure of individual molecular clouds, with those of more distant galaxies, which contain vastly different environments (e.g. starburst, García-Burillo et al., 2012). To achieve this, it is essential to observe nearby galaxies that span the range of scales needed to benchmark our understanding of local clouds and high-z galaxies.

Building up on work presented in EMPIRE survey (Jiménez-Donaire et al., 2019) and across NGC 3627 (Bešlić et al., 2021), the next logical step is to conduct deeper, more sensitive observations of high-critical density molecular lines across the disc of a non-typical star-forming galaxy. We present

new ALMA ACA observations of density-sensitive molecular lines within ~ 90−100 GHz range at 300 pc scales across the close starburst galaxy NGC 253.

Our observations (300 pc scales) are sufficient to probe different dynamical features in this galaxy, making it an excellent case study for investigating the dense molecular gas content in an extreme star-forming environment. This study aims to answer the following questions:

- What are the physical properties of the gas traced by HCN emission in such an extreme system?
- How does HCN emission relate to molecular gas and star formation across a large part of the disc in NGC 253?
- Do these properties vary across the inner disk of this galaxy, from center to ring to spiral arms?
- How does the bar fuel the nuclear starburst with dense molecular gas?
- Does the velocity dispersion regulates the SFE in these regions?
- Is there a surface density threshold after which the gas starts being efficient at star formation?

This section describes our source of interest, NGC 253, and provides a brief literature overview. Next, we will provide information about our ACA observations, describe the data reduction and list key properties of the final data product. Finally, we will describe additional data sets used in this work, environmental masks from the recent dynamical modelling results, new Physics of High Angular resolution in Nearby GalaxieS (PHANGS) ALMA CO(2–1) observations, and the recipe for the star formation rate and its relation to total infrared luminosity.

5.2 Target – NGC 253

We list main properties of the galaxy in Table 5.1. The Sculptor galaxy (NGC 253, see its composite image in Figure 5.2) is the closest, highly inclined, starburst galaxy (Rieke et al., 1980) located in the Southern hemisphere. Due to its proximity (1 arcsecond corresponds to 17 pc on a physical scale at distance of 3.6 Mpc, Anand et al., 2020), NGC 253 represents an ideal target for high-resolution studies, in particular when it comes to understanding the nature of its kpc nuclear region (Bolatto et al., 2013a; Leroy et al., 2015; Walter et al., 2017; Holdship et al., 2021) that appears to be undergoing an intense phase of active star formation (SFR=2 $M_{\odot}yr^{-1}$ Leroy et al., 2015). NGC 253 shows rich molecular gas emission, as demonstrated in ALCHEMI Large program (Martín et al., 2021). ALCHEMI uses ALMA ACA survey mapping a continuous frequency range from (sub)mm to mm wavelengths in the nuclear region of NGC 253. Several complex molecules such as C_2H_5OH, HOCN, HC_3HO were detected for the first time in an extragalactic source in NGC 253 (Martín et al., 2021). Moreover, this galaxy has a plethora of ancillary data covering a variety of gas phases, from atomic (e.g. Heckman et al., 2000), molecular (Houghton et al., 1997; Mauersberger et al., 1996; Paglione et al., 2004), and the most recent ACA observations of CO(2–1) which we will use in this work (Faesi et al in prep), to ionized gas (Arnaboldi et al., 1995).

The central 1 kpc of NGC 253 contains the nuclear region that shows complex molecular emission, demonstrated in Martín et al. (2006); Aladro et al. (2011); Meier et al. (2015), which detected 50 molecular species at 3 mm wavelength, of which almost 50 per cent remained difficult to classify. Meier et al. (2015) provided a schematic representation of the central region in NGC 253, demonstrating its

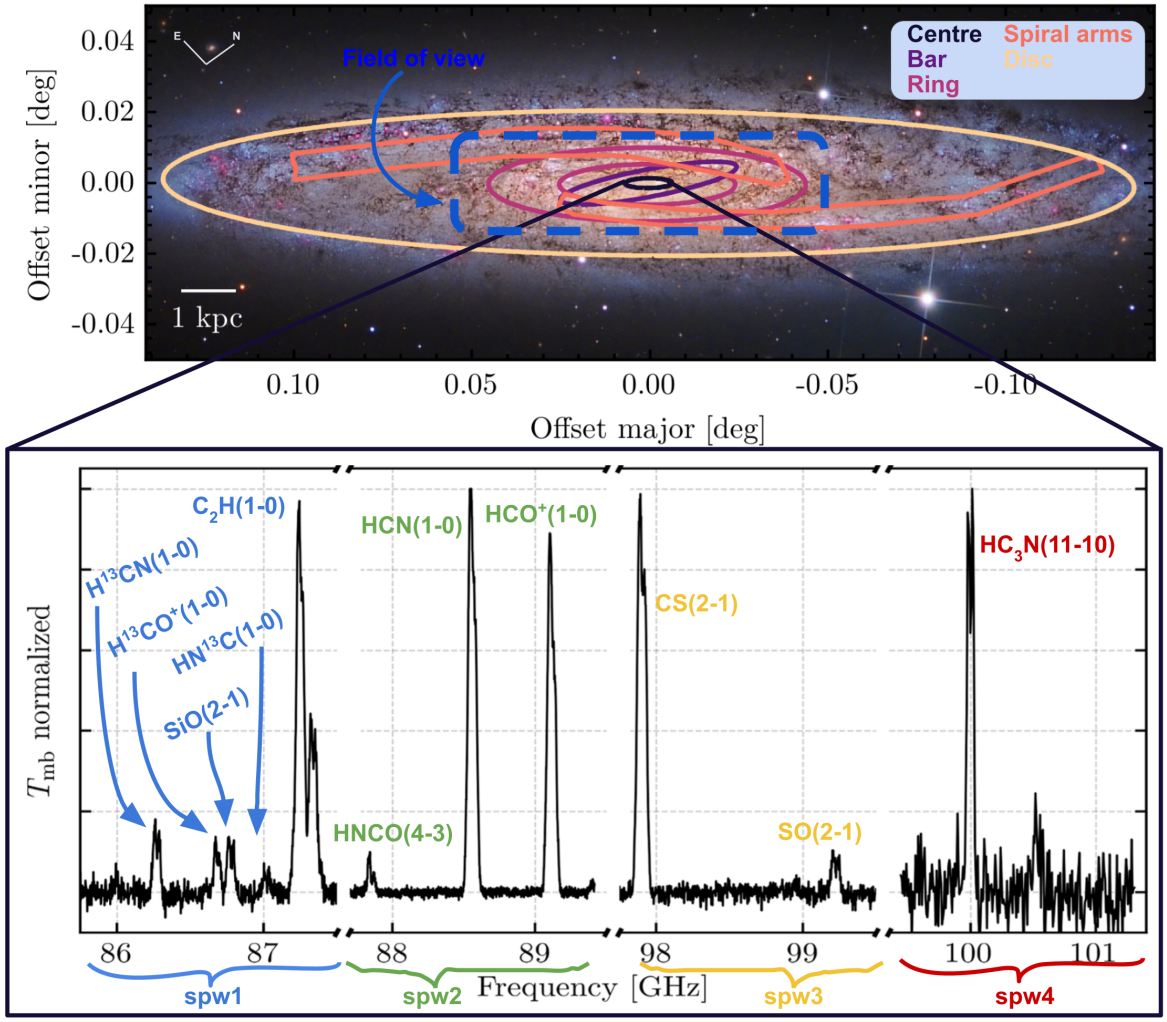

Figure 5.2: **Top panel:** NGC 253 composite image (credits: Terry Robinson). The overlayed blue dashed rectangle shows the ACA 25 7-meter pointings, with the antenna spacing of 57.6 arcsec. We show dynamical environments found in the disc of NGC 253: the centre, bar, ring, and spiral arms (Querejeta et al., 2021). **Bottom panel:** The observed spectrum taken towards the centre of NGC 253. We covered frequencies from 85.7 to 101.5 GHz. We label each spectral window, and mark all detected molecular lines.

interesting and complex structure. These authors found that the nuclear disc consists of the inner and outer regions. The inner nuclear disc contains high-density molecular gas and intense star formation. The central molecular zone (CMZ) lies within the inner nuclear disc, characterized by a strong dust continuum emission (Leroy et al., 2018). Giant molecular clouds are found in the CMZ of NGC 253 (Leroy et al., 2015), are more massive and have higher velocity dispersion than the GMCs in the Milky Way (Krieger et al., 2020). These clouds contain super stellar clusters, bright in continuum and line emission (Leroy et al., 2015, 2018), with detected outflow in dense molecular (Levy et al., 2021) and ionized gas (Mills et al., 2021).

The starburst in this galaxy drives the outflow towards the south-west direction, seen in various gas phases: in ionized gas (Hα and X-ray, Strickland et al., 2000, 2002; Westmoquette et al., 2011), neutral

Table 5.1: Source information.

Property	Value
Name	NGC 0253 (Sculptor galaxy)
Hubble type [(a)]	SABb
Centre RA (J2000)	00h47m33s
Centre DEC (J2000)	-25d17m19s
Inclination, i [°] [(a)]	76
Position angle, PA [°] [(a)]	52
Distance, D [Mpc] [(b)]	3.7
r_{25} [arcmin] [(b,c)]	5.12
$V_{\rm sys,hel}$ [km s^{-1}] [(d)]	258
SFR [M$_\odot$ yr^{-1}] [(e)]	4.2
$\log_{10}(M_*)$ [M$_\odot$] [(f)]	10.5

(a) McCormick et al. (2013)
(b) Distance Anand et al. (2020)
(c) Radius of the B-band 25th magnitude isophote
(d) Systemic velocity from Casasola et al. (2011)
(e) Star formation rate calculated from the IR luminosity (Sanders et al., 2003)
(f) Integrated stellar mass based on 3.6 μm emission, taken from the PHANGS-ALMA survey paper (Leroy et al., 2021b)

gas (Heckman et al., 2000), warm H_2 (Veilleux et al., 2009), OH in both emission and absorption (Turner & Ho, 1985; Sturm et al., 2011), and molecular gas (Krieger et al., 2020). Moreover, this wind contains significant amounts of dust (HST observations, Watson et al., 1996), molecular gas, based on ALMA CO(1–0) observations (Bolatto et al., 2013a), and dense molecular gas traced by HCN emission (Walter et al., 2017; Krieger et al., 2017).

The outer nuclear disc, on the other hand, contains gas with intermediate density and is thought to be the region where gas flows inward along the large-scale bar (Sorai et al., 2000; Paglione et al., 2004; Meier et al., 2015).

Although NGC 253 has been well-studied over the last few decades, most previous investigations have focused on its inner 1-2 kpc region, and particularly its starburst centre. The molecular gas outside the galaxy centre remains poorly understood, in particular its densest phase, properties and its kinematics on larger scales, and covering a wide range of environments.

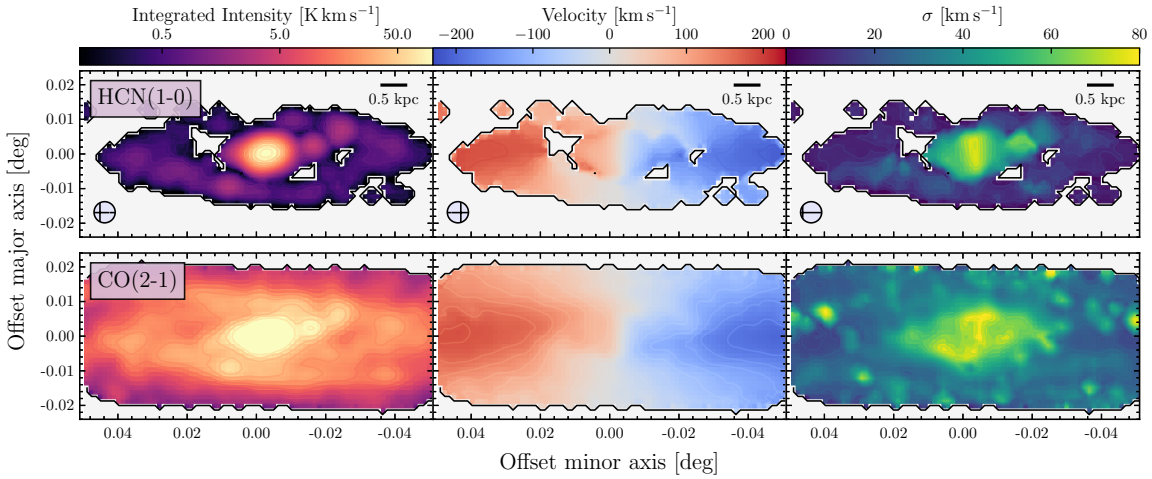

Figure 5.3: **Top row:** HCN(1–0) moment maps: integrated intensity map (left), centroid velocity map (middle), and velocity dispersion (right). The beam size of 22 arcsecond is shown in the left corner of each panel. **Bottom row:** CO(2–1) moment maps, in the same order as for HCN(1–0). CO(2–1) is convolved to a beam size of 22 arcseconds, and regrided to match the grid of HCN data. We fix the colorscale for each moment map to highlight the differences and similarities in HCN and CO(2–1) emission. All maps are rotated for the position angle and axes show the angular distance from the NGC 253's minor and major axis (see Table 5.1).

5.3 ALMA-ACA observations, data reduction and additional data

5.3.1 ALMA-ACA observations

Observations of NGC 253 are part of the ALMA Cycle 7, and they were obtained in December 2019 and January 2020. We observed molecular line emission using the Atacama Compact Array (7m - ACA) which included single-dish observations (total power - hereafter TP) in Band 3 (84 – 116 GHz). The total observing time was 22.9 and 44.1 hours for the 7 meter array and the TP antennas, respectively. The observed field of view contains 25 7-meter pointings - 114 arcsec ×516 arcsec (~2×9 kpc^2), which we show on NGC 253's composite image in Figure 5.2. The beam size is 21.40×10.36 arcsecond^2, the beam position angle is 83.51 degrees, and the primary beam full-width at half maximum is 57.6 arcseconds. These observations mapped the inner disc of NGC 253. We calculated the amount of CO flux found in the inner disc of NGC 253 covered by our observations using the ACA mosaics from ancillary observations (2018.1.01321.S; Section 5.3.3) convolved to the common spatial resolution to match the HCN observations. We found 90 % of CO(2–1) emission located in the inner disc of NGC 253. Similarly, we calculated the total star formation rate (SFR) using combination of dust tracers at 70, 160 and 250 μm (Section 5.3.4, Galametz et al., 2013) within our field of view and found 85%. Thus our observations covered the brightest regions in molecular gas and the most star-forming parts in NGC 253. Our interferometric observations were sensitive to emission from angular scales of ~14 arcseconds (~240 pc) to the largest angular scale filtered by the ACA-array of ~100 arcseconds (~1.7 kpc). The obtained sensitivity is 7.8 mJy/beam (~6 mK at requested beam size). The bandwidth is centered at 88.55 GHz, and the spectral resolution is 3.3 km s^{-1}. We detected three emission lines within this bandwidth: HCN(1–0) HCO$^+$(1–0), and HNCO(4-3) at the rest frequencies of 88.63 GHz, 89.125 GHz, and 87.8 GHz respectively (see spectral window 2 (spw2) in the bottom panel of Figure 5.2). Additionally, we detected other molecular lines

shown in the bottom panel of Figure 5.2. We summarize properties of these detected molecular lines in Table B.4 in the Appendix B, Section B.3.

The data reduction was done using PHANGS-processing pipeline (Leroy et al., 2021a) in Common Astronomy Software Applications (CASA - McMullin et al., 2007), version 5.6. Firstly, we flagged all the emission lines within the respective bandwidth to calculate the continuum emission and subtracted it. The imaging of the 7-meter data was done using CASA's standard *tclean* procedure. We used the strict CO(2–1)-based mask (Leroy et al., 2021a,b) within which we imaged our data. To perform our data imaging, we used the single-scale cleaning algorithm. The HCN 7-meter flux within the cleaning mask is 99% of the total flux within the full image. We show several diagnostic figures produced while doing the quality assessment during the data reduction in Appendix B, Section B.1.

The single-dish data were processed using the standard ALMA pipeline. In the final step of data reduction, we combined 7m observations with TP for the missing short-scales emission using the standard CASA task *feather*. The total flux from the interferometric data is 70 per cent of the total flux measured from the single-dish data. The final data cube was additionally primary beam corrected and convolved to have a round beam size of 22 arcseconds and channel width of 10 km s^{-1}.

5.3.2 Environmental masks

To separate environmental regions in NGC 253, we use environmental masks defined for NGC 253 based on dynamical modeling of infrared data (Querejeta et al., 2021). The environmental mask consists of four regions: the disc, nuclear ring, bar, and centre. Additionally, NGC 253 has two spiral arm features, visible in optical data (Pence, 1980) and also constrained from the 3.6 and 4.5μm observations obtained by Spitzer telescope, as part of the S4G survey (Muñoz-Mateos et al., 2015; Herrera-Endoqui et al., 2015). In this work, we additionally define spiral arms as follows. We used the unsharp-masked near-infrared Herschel The Photoconductor Array Camera and Spectrometer (PACS) 70μm data to locate spiral features, and then we fitted those in polar (ρ, θ) space as linear functions. The width of such constructed spiral arms is defined manually in SAO-NASA ds9 software (Joye & Mandel, 2003). Finally, we added these spiral arm regions to the already existing environmental mask, which we show in Figure 5.2.

5.3.3 ALMA-CO(2–1) observations from PHANGS

The CO(2–1) molecule has lower effective critical density than the HCN (Shirley, 2015). Therefore, the CO(2–1) emission can be found in molecular gas at lower densities than that in which HCN effectively emits. In this work, we use the CO(2–1) observations from the recent PHANGS-ALMA survey (PI E. Schinnerer, Leroy et al., 2021b). PHANGS-ALMA survey maps CO(2–1) emission across the sample of 90 nearby galaxies at a spatial resolution high enough to detect and isolate individual GMCs (Rosolowsky et al., 2021). The NGC 253 CO(2–1) observations (PI: C. Faesi, 2018.1.01321.S) were obtained with the ACA. The beam FWHM of this data set is 8 arcsec, and the channel width is 2.5 km s^{-1}. In the final step, we convolve the CO(2–1) data cube to match the working spatial and spectral resolution of 22 arcsec and 10 km s^{-1} and regrid to a common pixel scale.

5.3.4 Star formation rate

Dust in galaxies is heated from recently formed massive stars and re-emits at infrared wavelengths, making its emission commonly used estimate for SFR. To estimate star formation rate surface density

($\Sigma_{\rm SFR}$), we use a combination of IR Herschel data from the KINGFISH survey (Kennicutt et al., 2011). To compare our results with recent studies, we chose to calculate ($\Sigma_{\rm SFR}$) using Herschel bands at λ =70, 160, and 250 microns. Firstly, we convolved our Herschel maps to a final resolution of 22 arcseconds using the kernel defined in (Aniano et al., 2011) and matched the coordinate grid with the final HCN data image. We calculate the total infrared surface density ($\Sigma_{\rm TIR}$) following the prescription from (Galametz et al., 2013):

$$\Sigma_{\rm TIR}[{\rm W\,kpc^{-2}}] = \sum_j c_j \cdot \Sigma_j[{\rm W\,kpc^{-2}}], \tag{5.1}$$

where c_j is the coefficient and Σ_j is the surface density at a band ii. Finally, we calculate star formation rate surface density ($\Sigma_{\rm SFR}$) from $\Sigma_{\rm TIR}$ and correct for galaxy's inclination i:

$$\Sigma_{\rm SFR}[{\rm M_\odot\,yr^{-1}\,kpc^{-2}}] = 1.48 \cdot 10^{-10}\Sigma_{\rm TIR}[{\rm L_\odot\,kpc^{-2}}]\cos i. \tag{5.2}$$

Finally, we convolve SFR maps to a common spatial resolution, and matched wold coordinate system (WCS) grid.

5.4 Results

In this section, we present HCN moment maps in NGC 253 and compare it with the CO(2–1) emission. Next, we investigate how the HCN intensity varies across the galaxy using two different methods to analyse the data and determine the observed molecular emission properties.

Using the first approach, we calculate the integrated intensity by creating the moment 0 map, where we reduce the three dimensional data cube to two dimensions by summing the emission along each line of sight (i.e., we integrate along the velocity axis). In this method, we first create a CO(2–1) based mask. This mask is produced by selecting all voxels with signal-to-noise ratio higher than 4 and then expanding it to include all contiguous voxels with signal-to-noise > 2σ level. Next, we apply this mask to the HCN data cube. The HCN integrated intensity is then determined by summing all the emission found within the mask and multiplying it by the channel width.

In the second approach, we keep the 3-dimensional structure of our data set and extract all the information by decomposing the observed molecular line emission along each line of sight. To do so, we use the Semi-automated multi-COmponent Universal Spectral-line fitting Engine - SCOUSE (Henshaw et al., 2016a, 2019). We decompose the HCN and CO(2–1) emission using SCOUSE. This approach considers the complex emission in the data cube and gives the properties of each molecular gas component derived from the observed spectrum along the line of sight. This also includes numbers of lines of sight, total number of components, and the fraction of HCN components associated with the CO(2–1) emission. We provide a brief overview of the analysis steps taken when using SCOUSE in Appendix B.4.

5.4.1 Moment maps of HCN emission versus CO(2–1)

We show the integrated intensity (moment 0) map, centroid velocity map (moment 1), and velocity dispersion map (moment 2) in Figure 5.3 at the working resolution of 22 arcseconds (340 pc) for HCN(1–0) (top row) and CO(2–1) data (bottom row). To create these moment maps, we first produce a signal-to-noise-based mask for HCN and CO(2–1) cubes. Using the `python` package SpectralCube (Ginsburg et al., 2019), we produced the moment maps from the masked data cubes. We fix the colour

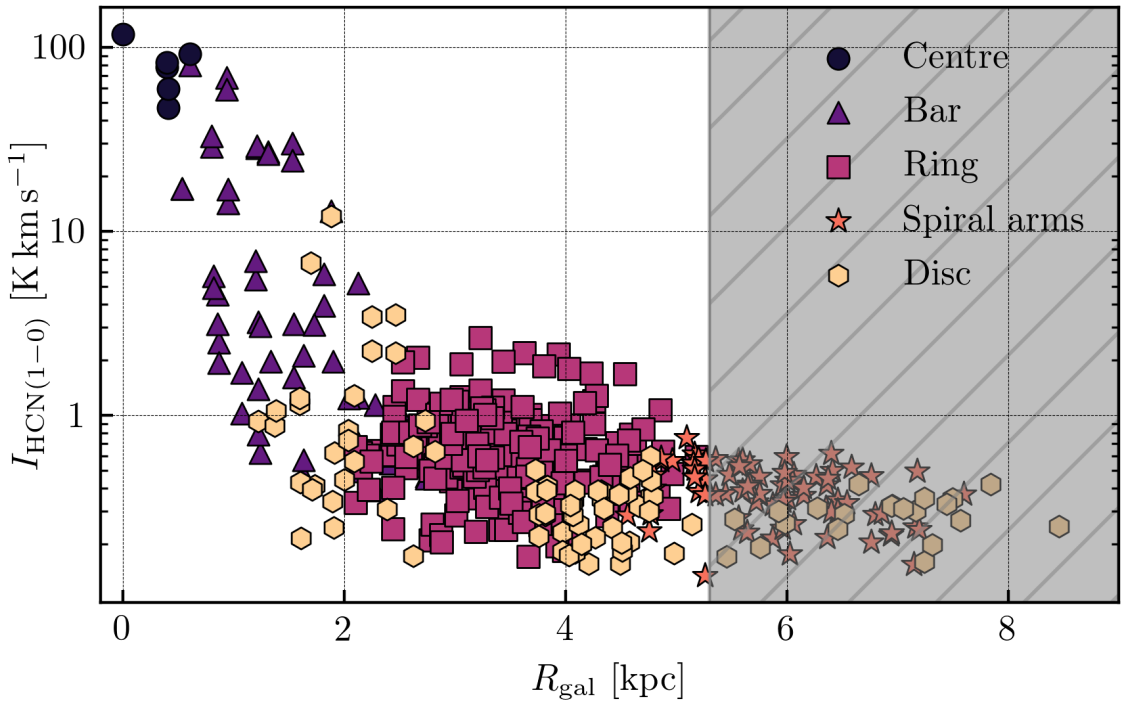

Figure 5.4: HCN integrated intensity as a function of galactocentric radii. The coloured, filled points represent pixels with signal-to-noise ratio of 3 and above, whereas open points have signal-to-noise ratio lower than 3. Due to the minor axis effect, we do not consider points at distances higher than 5.3 kpc, marked with the red shaded region.

scale for each set of moment maps (each column) to show the same range of values for HCN and CO(2–1).

We also see that HCN emission shows a clumpy structure and compact emission, very prominent in the centre of the galaxy and also concentrated along the ring and the bar. There are spots of bright HCN emission located in the contact points of the bar, dust lanes and ring, which we also see in the star formation map. These bright spots of HCN emission are expected to be found in the region where the bar and ring intersect, as these are interfaces where gas orbits converge (Kenney, 1994). Moreover, we see CO(2–1) bright spots co-spatial with those seen in HCN.

The moment 1 map is the intensity-weighted mean velocity map. We show these in the middle column of Figure 5.3 for both HCN and CO(2–1). The velocity map is corrected for the systemic velocity (Table 5.1). The outskirts of the map show the highest velocity gradient, i.e. along the major axis (around −230 and +230 km s^{-1} on the Eastern and Western parts, respectively). The southwestern side of the galaxy is blue-shifted, hence approaching us. HCN and CO(2–1) velocities look consistent (we will return to this in more detail in Section 5.4.3).

5.4.2 Radial distribution of pixel-by-pixel HCN intensity

Firstly, we hexagonally resample the HCN cube so that each pixel is half-beam spaced from its neighbouring pixels. Next, we use a CO(2–1)-based mask to select regions where we expect to find

emission. We calculate the HCN integrated intensity by summing the masked data along the velocity axis and multiplying it by the channel width. We show the radial distribution of the HCN integrated intensity in Figure 5.4. Sightlines with a signal-to-noise ratio of at least 3 in measured HCN integrated intensity are shown as filled coloured points, whereas the rest of the sightlines are shown as open points. Overall, we detected significant HCN emission over the whole field of view. The high inclination of this galaxy causes large deprojected distances from the centre along the minor axis (i.e. the minor axis effect). After inspection of the deprojected distances along the major axis, where we do not expect to encounter this issue, we concluded that the farthest data point from the centre of the map has a deprojected distance of 5.3 kpc. Therefore, we do not consider sightlines with galactocentric radii higher than 5.3 kpc when discussing the radial distribution of HCN emission, since these will not cover the full range of azimuthal angles. Thus, we detect significant HCN emission up to ∼5 kpc originating from all environments as described in Section 5.3.2.

We extract sightlines from each environment by applying the environmental mask (Querejeta et al., 2021) and colour-code the points by the environment, following the colour scheme we show in Figure 5.2. We distinguish five environments in NGC 253: the nuclear region lies within the inner ∼0.5 kpc region, then the bar feature is located in the inner 2 kpc region. The ring is at radii between 2 and 5 kpc, and finally, the dust lanes are at $r_{\rm gal}$=5 kpc. The brightest HCN emission is indeed towards the centre of the galaxy. There is a steep decrease in HCN intensity by two orders of magnitude along the bar. Moreover, HCN intensity varies by one order of magnitude at the $r_{\rm gal}$ >2 kpc, i.e., in the ring and spiral arms. Additionally, we see local enhancements in HCN at the intersection of the ring and spiral arms.

We compare our results with those within the literature in the following. The HCN intensity distribution in NGC 253 follows the CO distribution described in (Sorai et al., 2000; Paglione et al., 2004), i.e. the "twin-peaks" morphology, typical for barred galaxies (Kenney et al., 1992). The centre shows the brightest HCN emission, which is also seen in other galaxies: at kpc resolution in EMPIRE study (Jiménez-Donaire et al., 2019), in M 51 (Bigiel et al., 2016), in nearby galaxies at similar spatial scales (∼0.5 kpc) (Gallagher et al., 2018a), and higher spatial resolution (Bešlić et al., 2021). As we move out from the centre of NGC 253, we note the decrease in emission, in particular in the inner 1-2 kpc region within the bar HCN intensity steadily decreases, similarly as in NGC 3627 (Bešlić et al., 2021).

Observations of CO(1–0) emission at similar resolution (16 " ∼250 pc) across NGC 253 (Sorai et al., 2000; Paglione et al., 2004) found a similar radial distribution. This study observed a secondary peak in CO(1–0) surface density around $r_{\rm gal}$=2 kpc at the end of the bar. In our case, we note a slightly increase in CO(2–1) emission at distance between 3 − 4 kpc from the centre of NGC 253. The discrepancies between our results and those previously found in Sorai et al. (2000) stem from different distances (2.5 kpc) adopted for NGC 253. In addition, we observe local enhancements in HCN in regions that overlap the bar and ring and a decrease in HCN emission in the most outer parts of our map. On the other hand, Sorai et al. (2000) found a decrease in CO(2–1) surface brightness by two orders of magnitude in the inner 1-2 kpc region of NGC 253, and the intensity after the second peak observed at 2 kpc agrees well with the exponential decrease. The CO rotation curve of NGC 253 from Koribalski et al. (1995); Sorai et al. (2000) flattens in the ring. The flattening of rotation curve could indicate the pilling up of gas.

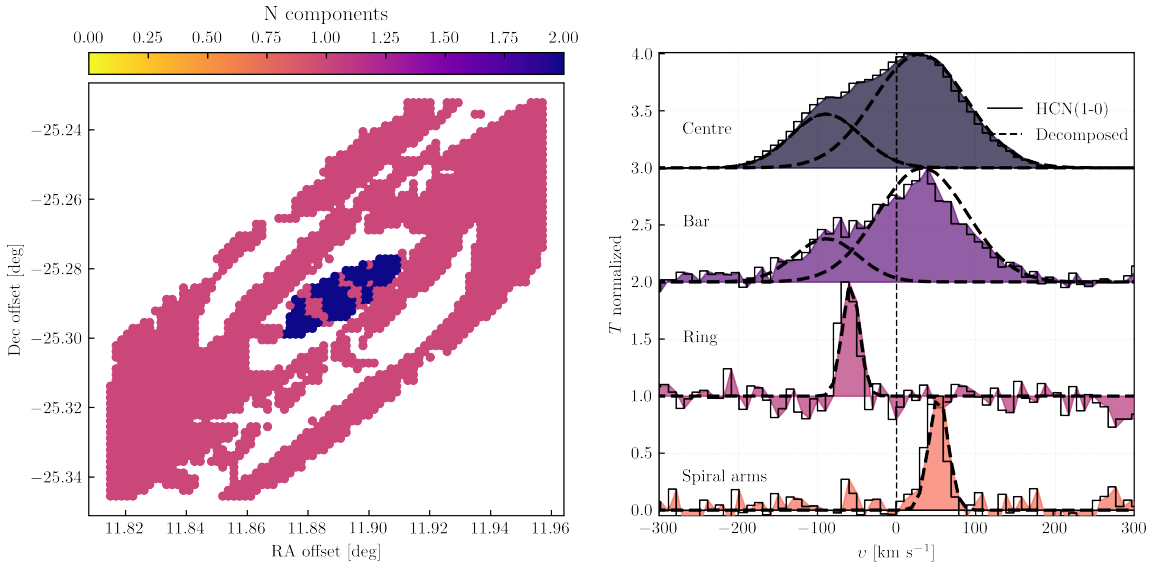

Figure 5.5: Map of NGC 253 showing number of velocity components in each pixel derived from SCOUSE. **Right:** Example of HCN spectra from each environment shown in Figure 5.2 and from coloured points on the left panel. The black dashed lines show each Gaussian velocity component derived from the SCOUSE spectra decomposition analysis (Henshaw et al., 2016a, 2019).

5.4.3 Radial distribution of HCN intensity determined from SCOUSE

We show spectra from 4 sightlines originating from different dynamical regions (each marked with a rectangle on the left panel of Figure 5.5) to illustrate the nature of the observed spectra. The black dashed lines show each Gaussian component derived from SCOUSE. In particular, sightlines from the nuclear region and the bar show double line profiles, whereas spectra towards the ring structure and spiral arms are narrow and single-peaked (the right panel in Figure 5.5). Similarly, Sorai et al. (2000) found compound velocity structures in CO(1–0), particularly within the bar. The separation between different components observed towards the same line of sight does not result from the separation resulting from the galactic rotation. Instead, Sorai et al. (2000) proposed a scenario in which the strong non-circular motions cause the existence of two velocity components.

We show our results from implementing SCOUSE analysis to both our datasets in Figure 5.6. Each panel shows the environmental distribution of solutions produced using SCOUSE: the peak brightness temperature of each spectrum (top row), the centroid velocity (the second row), the number of determined Gaussian components found within each pixel (the third row), and the velocity dispersion of each spectral lines (the bottom row). The first column shows solutions for the HCN emission, and the second column the output for CO(2–1).

In terms of the peak temperature, CO(2–1) profiles are brighter than HCN, and the central spectra, followed by those in the bar, have the highest temperature peaks. The distribution of $T_{\rm peak}$ within the centre has the largest dynamical range in comparison with the $T_{\rm peak}$ determined in spectra across other environments. These have considerably lower peak temperatures in their spectra, with similar median values of ~ 0.01 K.

The distribution of centroid velocities is similar in both HCN and CO(2–1). Median values are similar for all environments in both HCN and CO(2–1) and are in the (-20, 20) km s^{-1} range. The

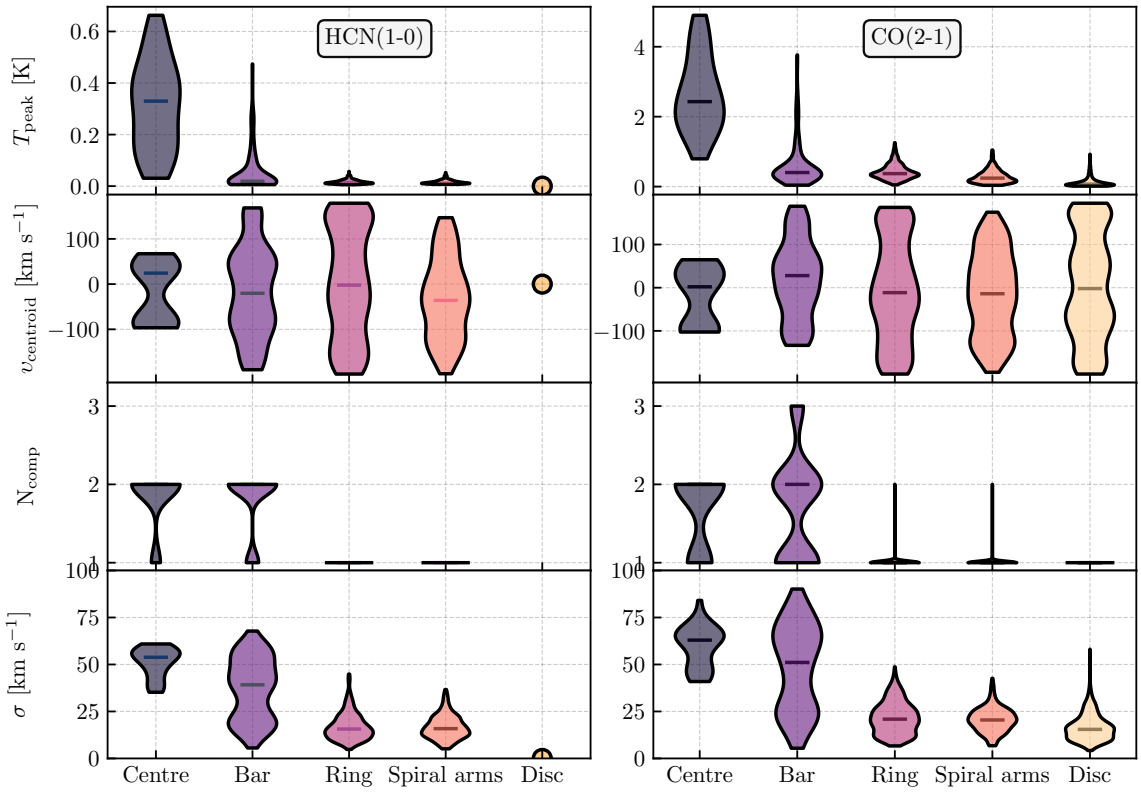

Figure 5.6: Results from applying the spectral decomposition analysis using SCOUSE (Henshaw et al., 2016a, 2019). We show output parameters of the fitted emission lines (left column for the HCN emission, and right column for CO(2–1) molecule) towards five environments in NGC 253.

effect of galaxy rotation is seen in the observed bimodality of centroid velocity distribution in all environments.

Each environment, as previously shown in Figure 5.5, shows a different amount of spectral features in both HCN and CO(2–1). The third row in Figure 5.6 summarizes what we already saw in Figure 5.5. The highest number of velocity components are seen towards the bar and nuclear region. HCN spectra are predominantly double-peaked in these regions, unlike HCN spectra in the ring and spiral arms. We see similar complexity in the CO(2–1) emission, although we identify up to three CO(2–1) velocity components in the bar. The number of CO(2–1) velocity components towards each sightline within the ring and spiral arms is mostly one. Except for a few sightlines where we identify two CO(2–1) velocity features within the same pixel.

Finally, we comment on the bottom row panels in Figure 5.6, where we show how the velocity dispersion of HCN (first column) and CO(2–1) spectra (second column). Here the environmental dependence becomes prominent as in T_{peak}. Central sightlines show the broadest lines, followed by sightlines originating from the bar. The distribution of velocity dispersion in the centre and the bar is bimodal. The σ distribution within the bar is elongated, similar to the distribution of HCN/CO(2–1) line intensity ratio within the bar (Figure 5.8). The distribution of σ in HCN and CO(2–1) is compact in the rest of the environments. The highest median in σ is found within the centre (55 km s^{-1} and 65 km s^{-1} for the HCN and CO(2–1)). Interestingly, we find higher median in velocity dispersion in

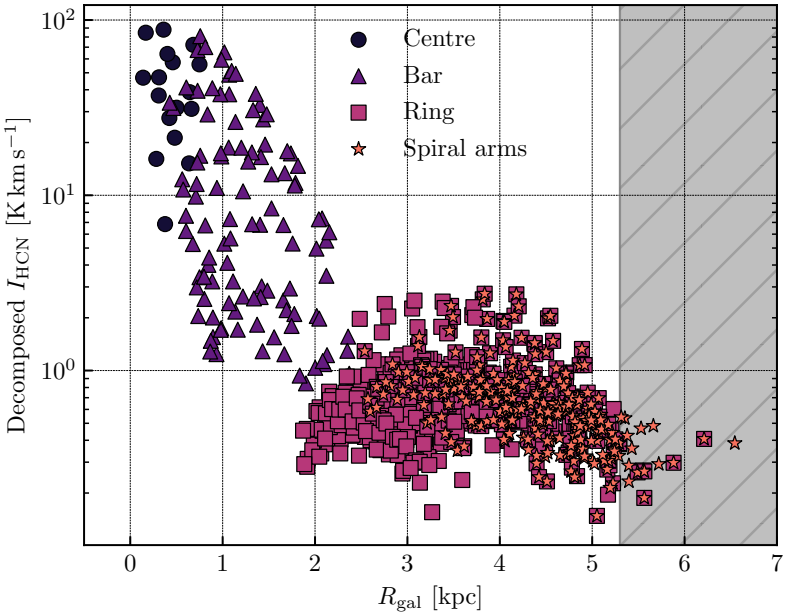

Figure 5.7: Same as in Figure 5.4, but we calculate the integrated intensity using SCOUSE.

HCN (40 km s^{-1}) than in CO(2–1) emission (30 km s^{-1}). In the ring and spiral arms, the median σ in CO(2–1) is higher than in HCN.

We calculate HCN integrated intensity using Gaussian parameters derived from SCOUSE and show how these very across galaxy in Figure 5.7. Overall, the HCN integrated intensity appears to be slightly lower than the one derived from the standard integration accounting emission along the whole velocity axis. Similarly as in Figure 5.4, we see the local enhancement in HCN emission in the overlap regions of bar, ring and spiral arms.

5.5 HCN/CO(2–1) intensity ratio

The HCN/CO(2–1) line ratio is, under the assumption that we know the CO(2–1)/CO(1–0) line ratio (R_{21}, see Sandstrom et al., 2013; den Brok et al., 2021) often used within the literature to constrain the density contrast (Leroy et al., 2017a), i.e., the dense gas fraction $f_{\rm dense}$. In the case of NGC 253, we are interested in seeing how this line ratio varies across the galaxy and any environmental dependence. In this section we present results on the observed HCN/CO(2–1) intensity ratio, its radial and environmental dependence. We determine HCN/CO(2–1) by using two approaches presented in Section 5.5.1.

5.5.1 Pixel-by-pixel HCN/CO(2–1) ratio

We calculate the HCN/CO(2–1) integrated intensity ratio using the hexagonally, half-beam sized sampled grid data points at 22 arcseconds. The HCN/CO(2–1) uncertainty is computed using the standard error propagation technique. To quantify HCN/CO(2–1) in these environments, we show the distribution of this line ratio in each region on the left panel of Figure 5.8. We also label the median value found in each environment. Points coming from the centre of NGC 253 have the highest

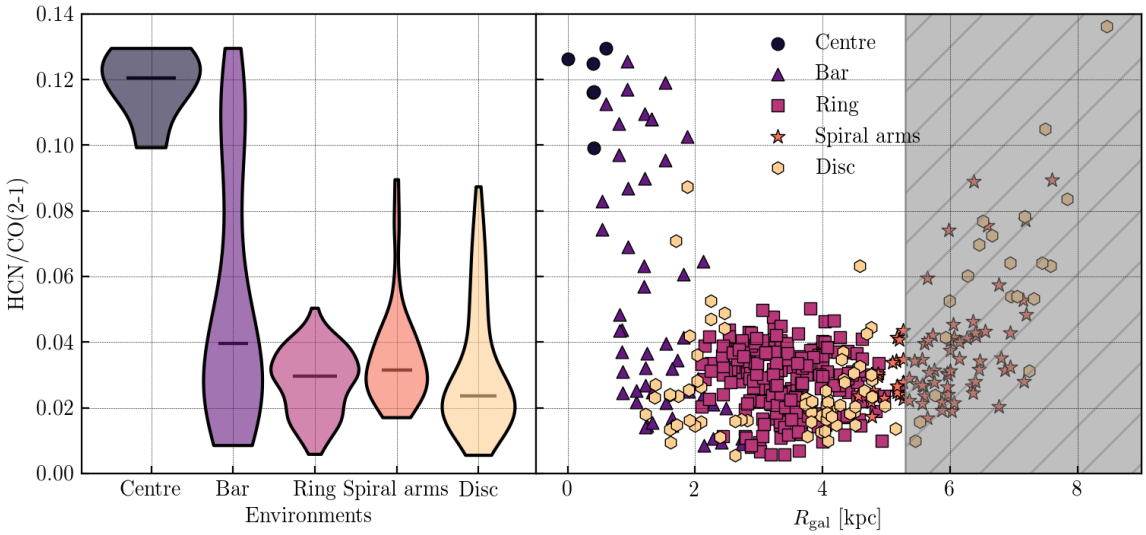

Figure 5.8: **Left:** Distribution of HCN/CO(2–1) line intensity ratio across several environments in NGC 253: the centre, bar, ring, spiral arms and disc. The mean line ratio in each environment is shown as dashed horizontal line. **Right:** Radial distribution of the same line ratio, sightlines are colour-coded as on the left panel. We show points with signal-to-noise ratio above 5. Similarly as in Figure 5.4, we do not consider points at radii higher than 5.3 kpc due to the minor axis effect.

median HCN/CO(2–1) of $(11.97\pm0.02)\times10^{-2}$, which is around 4 times higher than the median values found in the rest of the environments. We see that bar shows the most elongated distribution and a bimodal behaviour. The first group of sightlines shows a higher HCN/CO(2–1) ratio of 0.1 and above. The second group of points contains HCN/CO(2–1) values similar to those found in the ring and the rest of the regions (from 0.01 to 0.08). Therefore, the bar represents an intermediate region between the centre and the rest of the environments found in NGC 253. The bimodality and enhancement in HCN/CO(2–1) ratio found has a few possible implications, which we discuss in more detail in Section 5.7.1.

The right panel in Figure 5.8 shows HCN/CO(2–1) line intensity ratio as a function of a distance from the centre of NGC 253. Overall, the radial distribution of HCN/CO(2–1) follows the trends we see in HCN emission (Figure 5.4). We find the highest values of this line ratio within the centre of NGC 253. Similarly, there is a steep decrease in HCN/CO(2–1) ratio along the bar, after which HCN/CO(2–1) does not vary significantly (values between 0.01 and 0.05) in the nuclear ring and spiral arms. We find that HCN/CO(2–1) increases by two orders of magnitude in the inner 2 kpc region of NGC 253, similar to the results found at lower resolution studies Bigiel et al. (2016); Jiménez-Donaire et al. (2019); Gallagher et al. (2018a); Querejeta et al. (2019). On the contrary, weak radial variation of HCN/CO(2–1) intensity ratio across nearby galaxy NCG 3627 was found in Bešlić et al. (2021). We note, however, that Bešlić et al. (2021) used radially stacked measurements of the HCN and CO(2–1) emission in NGC 3627, whereas in our case we show the pixel-by-pixel emission.

Overall, the observed HCN/CO(2–1) line ratio shows agreement within the literature data. Similar to Gallagher et al. (2018a); Jiménez-Donaire et al. (2019); Bešlić et al. (2021), this line ratio has the highest values in the inner ~500 pc region of the galaxy, i.e., the immense amount of dense molecular gas relative to bulk molecular content is found within the centre of a galaxy. Knudsen et al. (2007) found HCN/CO(1–0) ratio in the inner 1 kpc region to be 0.08. By applying the R_{21} line ratio of 0.8

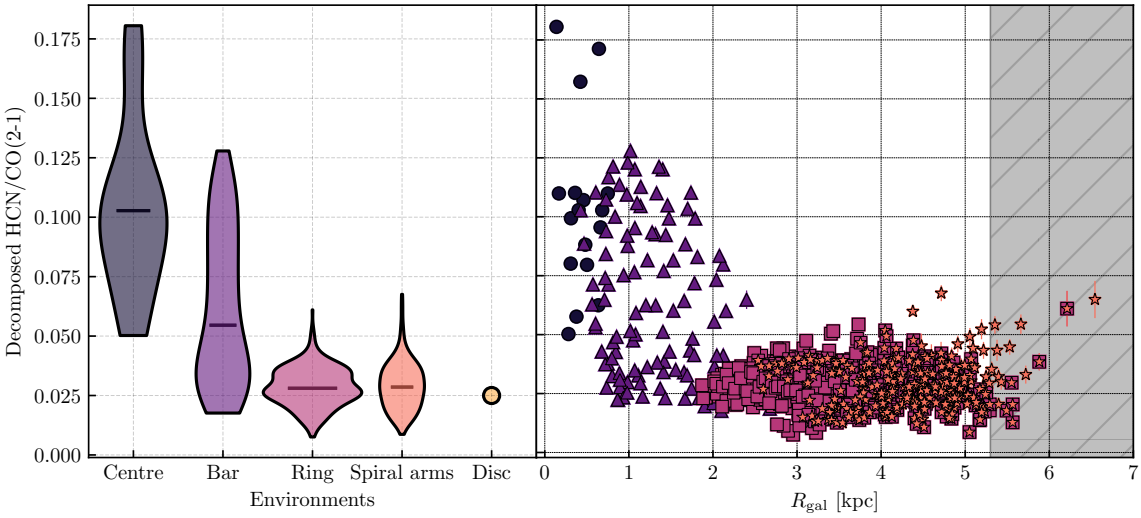

Figure 5.9: Same as in Figure 5.8, but the HCN/CO(2–1) intensity ratio is calculated using SCOUSE.

(Zschaechner et al., 2018) found in NGC 253, we find similar values of HCN/CO(1–0). As opposed to HCN/CO(2–1) in the barred galaxy NGC 3627 (Bešlić et al., 2021), we see a stronger environmental dependence of HCN/CO(2–1) and a significant decrease toward higher galactocentric radii.

5.5.2 HCN/CO(2–1) from SCOUSE

In this Section we compare results described in Section 5.4.3. In our work, we computed integrated line emission by summing emission throughout the whole velocity range. This approach impacts the observed HCN/CO(2–1) ratio, particularly in regions with complex kinematic structures, as seen in Figure 5.12. We noted sightlines with multiple CO(2–1) velocity components, whereas we found fewer of these in HCN emission. A higher signal-to-noise ratio impacts this result: CO(2–1) is very bright, and its emission is detected at a higher signal-to-noise ratio than the HCN. Therefore across such sightlines, the integration over the whole velocity range implies that we probed more CO(2–1) clouds along the line of sight than the HCN.

We show the component-by-component HCN/CO(2–1) intensity ratio computed using SCOUSE in Figure 5.9. The median HCN/CO(2–1) values have not changed in the ring and spiral arms. The distribution of this line ratio within the bar still shows a bimodality as in Figure 5.8.

5.6 HCN velocity dispersion

Molecular gas flows are essential in enhancing or suppressing local star formation (Meidt et al., 2018). Therefore determining the properties of molecular gas kinematics is important in understanding the ability of gas to form stars.

To directly compare HCN and CO(2–1) velocity dispersion at each sightline, we need to match the detected velocity components in HCN with those found in the CO(2–1) emission. As seen on the top left panel of Figure 5.6, the number of Gaussian components differ from region to region but is also different between HCN and CO(2–1). In particular, sightlines contain up to three Gaussian

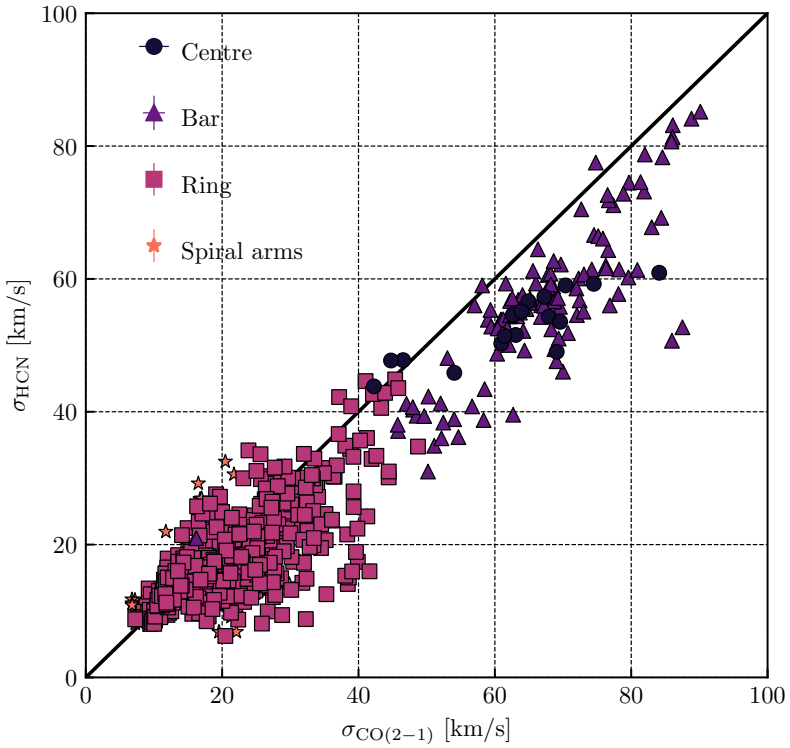

Figure 5.10: Pixel by pixel comparison between HCN (y-axis) and CO(2–1) (x-axis) velocity dispersion derived from spectral decomposition using SCOUSE. We colour-code each point by the environment. The most outer contours show 70% of all the shown data points. The diagonal black solid line shows where we would find data points in the case of the HCN and CO(2–1) having equal velocity dispersion.

components in CO(2–1), yet HCN towards these positions only contains one or two components. This could result from the CO(2–1) tracing more lower density gas at shifted velocity to which the HCN is not sensitive.

The first step in associating velocity components is to look at the centroid velocities determined for each component within each pixel in HCN and CO(2–1), particularly the difference in $\upsilon_{\mathrm{centroid,HCN}}$ and $\upsilon_{\mathrm{centroid,CO(2–1)}}$. When the HCN velocity component is associated with the CO(2–1), their centroid velocities will be similar. Therefore, we consider that the HCN line is associated with the CO(2–1)if $|\upsilon_{\mathrm{centroid,HCN}} - \upsilon_{\mathrm{centroid,CO(2–1)}}| < \sigma_{\mathrm{thresh}}\,\mathrm{km\,s^{-1}}$.

We define the σ_{thresh} as following:

$$\sigma_{\mathrm{thresh}} = \frac{\sigma_{\mathrm{CO(2-1)}} + \sigma_{\mathrm{HCN}}}{2}, \tag{5.3}$$

and calculate this value for each pixel where we decompose the emission. The Equation 5.3 represents the overlap of the clouds. Such introduced criterion assures us that clouds with higher line widths have a less strict association criterion. After applying this criterion, we match 99 % of HCN emission lines to those in CO(2–1) in all sightlines.

We show a comparison of the observed velocity dispersion in NGC 253 for HCN and CO(2–1) emission in Figure 5.10. We find that broader CO(2–1) lines have broader associated HCN emission. The solid black line represents the one to one ratio in HCN and CO(2–1) velocity dispersion. The

contours show the density of the data points for each environment. We see that $\sigma_{\mathrm{CO(2-1)}} > \sigma_{\mathrm{HCN}}$ on average. This result is expected assuming the HCN emission traces higher density gas than the CO(2–1), and coming from a more compact region than the CO(2–1)emission. Consequently, the turbulent velocity dispersion of the HCN-tracing gas is lower. We see this trend particularly pronounced in the center and the bar. At velocity dispersions below 50 km s^{-1} data points are scattered around the solid black line. The general positive correlation in HCN and CO(2–1) velocity dispersion in NGC 253 is in agreement with previous velocity dispersion measurements in M 51 (Querejeta et al., 2019), and across NGC 3627 (Bešlić et al., 2021).

Next, we focus more on the environmental comparison. We find that sightlines from the spiral arms (blue points) and the ring (green points) are primarily distributed in the lower values part of this figure. On the contrary, we see that central sightlines populate the higher-values region. Interestingly, we notice bar sightlines over the full range of the observed values along both axes and two distinct clusters of data points. The first group of bar data points is found in the bottom-left part of Figure 5.10 within the range from 5 to 35 km s^{-1}, together with the ring and spiral arms sightlines. The broader emission lines (from 40 to 65 km s^{-1}) within the bar are found around the central sightlines.

5.6.1 HCN velocity dispersion

In this section, we present results on measurements of HCN velocity dispersion (σ_{HCN}) in NGC 253 and comparison with CO(2–1) velocity dispersion ($\sigma_{\mathrm{CO(2-1)}}$). After inspecting HCN emission in position-position-velocity space, we find complex line profiles consisting of multiple Gaussian components at several positions across the map. To calculate σ, we use three different approaches. The first approach is estimating the velocity dispersion from the second moment of the data, using the signal-based masked data cubes (Section 5.3.2).

The second approach is to calculate velocity dispersion using the "effective width" approach (Heyer et al., 2001; Sun et al., 2018; Querejeta et al., 2019), which takes the ratio of integrated intensity and the peak brightness temperature. On the contrary to the velocity dispersion derived from the second moment, this approach is less sensitive to the noise in the spectrum. However, both the second moment and the effective width approaches are insufficient to determine the velocity dispersion in the case of multiple velocity components, particularly in the inner 2 kpc region of NGC 253. Lastly, we derive the velocity dispersion from SCOUSE (Henshaw et al., 2019) and the Gaussian fit of each spectral line.

5.6.2 Molecular gas flows

We show the position-velocity diagram in Figure 5.11 of the centroid velocities of HCN emission from the SCOUSE as a function of the offset from the galaxy's minor axis. Each point is colour-coded by the HCN/CO(2–1) integrated intensity and the environment (see colour bars). The HCN/CO(2–1) is derived from the integrated intensities calculated from SCOUSE (see Section 5.9) Bar sightlines show a "parallelogram"-shaped feature, previously seen in CO(1–0) (Sorai et al., 2000) and CS(2–1) emission (Peng et al., 1996). Gas motions in the bar are under the influence of the bar potential. Simulations and dynamical modeling showed that in bar gas moves along oval orbits ((e.g. Binney et al., 1991; Athanassoula, 1992; Peng et al., 1996; Sormani et al., 2015), which produces the parallelogram in the position-velocity diagram. We note more data points on the leading side of the bar, which is indicative of molecular gas concentrations caused by a non-axisymmetric bar potential (Kuno et al., 2000). The velocity gradient is the steepest in the bar and centre and more shallow in the ring and spiral arms. As the molecular gas travels from the outer disc, it starts losing angular momentum at galactocentric

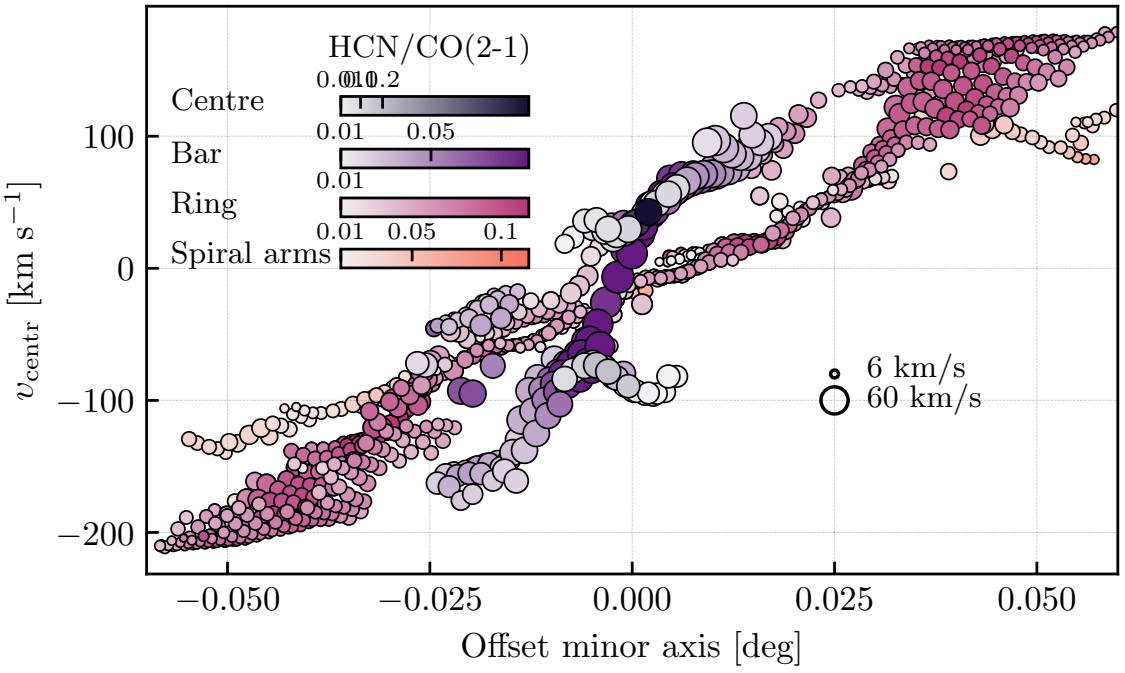

Figure 5.11: Position-velocity diagram (pυ) of HCN emission in NGC 253. Y-axis are the centroid velocities from the spectral decomposition, and on the x-axis are angular distances from the minor axis of NGC 253. We colour-code points by their HCN/CO(2–1) ratio derived from SCOUSE. The size of each point corresponds to the HCN velocity dispersion.

radii lower than the corotation radius $\sim 3-4$ kpc (e.g. Iodice et al., 2014), and comes to the ring. The rotation curve within the ring is almost flat, causing the crowding of molecular gas. This is also supported by the observed narrow single-peaked HCN spectral features.

5.7 Discussion

5.7.1 Enhancement in HCN/CO(2–1) ratio along the bar: Do we see the outflow?

The enhanced HCN/CO(2–1) in the bar towards the centre of NGC 253 and the bimodal distribution for the bar sightlines in HCN/CO(2–1) have a few possible implications. On the one hand, we might witness a molecular gas flow, and there is a chance that enhanced HCN/CO(2–1) points in the bar originate from the molecular wind. On the other hand, the beam smearing effects caused by a high galaxy inclination are not negligible. Therefore, we may detect the emission originating from the centre within the bar. Moreover, Paglione et al. (2004) found high gas densities traced by CO(1–0) emission near the inner Lindblad radius (~300 pc Iodice et al., 2014) and along the bar's minor axis. We investigate these sightlines to further explore and explain the enhancement in HCN/CO(2–1).

The bar's data points that form the bimodality have an HCN/CO(2–1) ratio above 0.1. After inspecting the data points that cause the bimodality in the HCN/CO(2–1), we find that these points lie along the minor axis in NGC 253, i.e., where we expect to see the outflow. It is worth noting that the probed spatial scales of our data are not sufficient to resolve the outflow. However, we might see the

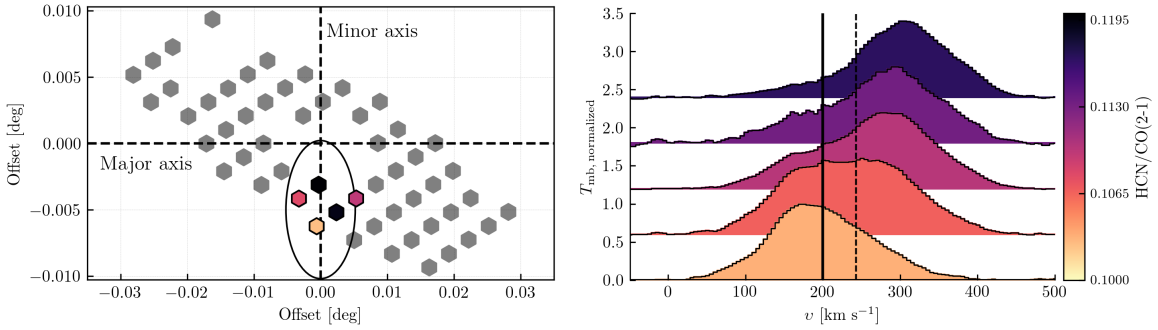

Figure 5.12: **Left:** Bar sightlines in NGC 253. We label major and minor axes. Coloured points are sightlines showing enhanced HCN/CO(2–1) emission in the direction of the SW streamer (Walter et al., 2017) and that contribute to the bimodality seen in Figure 5.8. Colors correspond to their HCN/CO(2–1) intensity ratio shown in the colorbar. **Right:** HCN spectra towards the data points located along the minor axis in NGC 253 shown on the left. Each spectrum is coloured by the HCN/CO(2–1) ratio shown on the colourbar. All these data points are located along the SW streamer (Walter et al., 2017). The black dashed line shows NGC 253 systemic velocity of 243 km s^{-1} (see Table 5.1). The black solid line represents the $v_{\rm lsr}$ = 200 km s^{-1} velocity at which Walter et al., 2017 observed the outflowing component in CO(1–0) emission.

outflow within the spectra. Walter et al., 2017 observed the wind in NGC 253 in CO(1–0) emission and found a separate velocity component at intermediate (−4" to −10") offsets from the major axis. Therefore we plot the HCN spectrum towards the sightlines with enhanced HCN/CO(2–1) found along the minor axis, towards direction where the south-western streamer (SW) of the outflow is located (negative offsets from the minor axis). We show these in Figure 5.12. Each spectrum is coloured by the HCN/CO(2–1) line intensity ratio.

Overall, we find that minor axis sightlines located towards the SW streamer have the following properties: broad emission lines that correlate with HCN/CO(2–1) ratio, with possible multiple velocity components within each point. This result implies that we see multiple gas flows within our beam. Walter et al., 2017 found the outflowing molecular component at $v_{\rm lsr}$ = 200 km s^{-1} ($\sim$ −48 km s^{-1}). We show this velocity as a solid black line in Figure 5.12, and systemic NCG 253 velocity as a black dashed line. At the velocity that corresponds to the previously detected molecular outflow (Walter et al., 2017), we see local peaks in HCN emission that could belong to the outflowing gas.

Walter et al., 2017 calculated HCN/CO(1–0) line intensity ratio in the outflow and the disc of NGC 253. This study found that the HCN/CO(1–0) is ∼0.1 in the outflow, instead of three times lower value in the disc (1/30). We estimate the HCN/CO(1–0) ratio from our measurements. To do so, we use R_{21} ratio of 0.8 found in NGC 253 (Zschaechner et al., 2018). After applying the R_{21} ratio, sightlines with enhanced HCN/CO(2–1) line intensity ratio (from 0.1 to 0.12) correspond to values within the 0.08 to 0.096 range. Therefore, the molecular outflow could influence the enhanced HCN/CO(2–1) intensity ratio found along the minor axis.

5.7.2 Environmental dependence of the star formation efficiency of the dense gas and CO(2–1) intensity

In this section, we investigate the relationship between tracers of dense gas and tracers of star formation and connect our understanding with the observed environmental dependence of the HCN/CO(2–1)

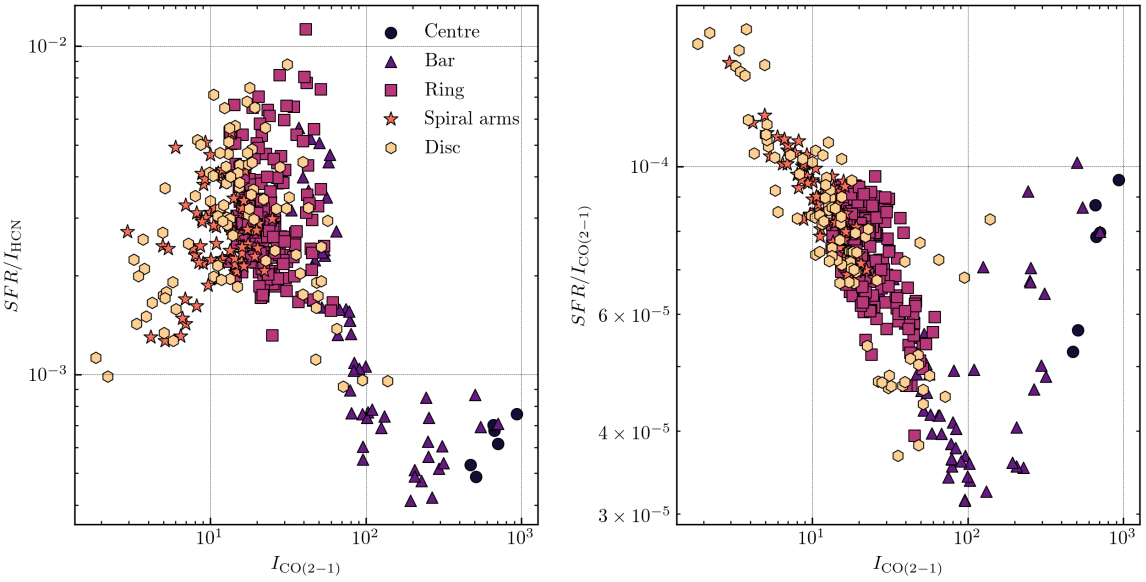

Figure 5.13: SFR/HCN luminosity ratio as a proxy for star formation efficiency of dense molecular gas (left) and SFR/CO(2–1) luminosity ratio as a proxy for star formation efficiency of molecular gas (right) as a function of CO(2–1) intensity. Points are colour-coded according to their environments.

line intensity ratio described in Section 5.5. Previous studies show that $f_{\rm dense}$, commonly traced by HCN/CO(1–0) line intensity ratio shows different star formation efficiencies $\rm SFE_{dense}$. For example, regions with high stellar surface density and interstellar pressure typically contain the highest $f_{\rm dense}$. However, these same regions tend to have relatively lower $\rm SFE_{dense}$, i.e. their ability to form stars is significantly reduced (e.g. Usero et al., 2015; Bigiel et al., 2016; Barnes et al., 2017; Jiménez-Donaire et al., 2019; Bešlić et al., 2021; Eibensteiner et al., 2022).

In Figure 5.13 we show the TIR/HCN luminosity ratio, which is expected to be a proxy for the star formation efficiency of dense molecular gas, $\rm SFE_{dense}$, as a function of CO(2–1) intensity (left panel). The right panel shows TIR/CO(2–1) luminosity ratio (star formation efficiency of bulk molecular gas, $\rm SFE_{mol}$) as a function of CO(2–1). CO(2–1) intensity is tracing the cloud-scale surface density, which is a good proxy for the gas volume density (Leroy et al., 2017b; Sun et al., 2018).

We colour-code data points by the environment, following the same colour scheme as in Figure 5.4. We observe a strong anti-correlation on the left panel, while we find no clear correlation on the right panel. We find the largest amount of HCN-tracing gas relative to bulk molecular gas to be located within the central and surrounding sightlines from the bar. However, these data points show the lowest TIR/HCN luminosity ratio. The bar sightlines show the broadest range of HCN/CO(2–1) as discussed in Section 5.5, but also an order of magnitude range in the TIR/HCN. Gas located in the ring, spiral arms and disc appear to be similarly efficient at producing stars, which is not surprising because they contain similar amounts of dense molecular gas. Similarly, these data points crowd in the SFR/CO(2–1)-HCN/CO(2–1) plane. We observe similar correlation on the right panel of Figure 5.13, with the exception of a few sightlines originating from the bar and the centre, which do not follow the trend and show high $\rm SFE_{dense}$. These data points originate from regions with significantly higher mean gas density than the effective critical density of CO(2–1) emission. At these high gas densities, CO(2–1) emission gets saturated (Leroy et al., 2017a), whereas star formation rate increases.

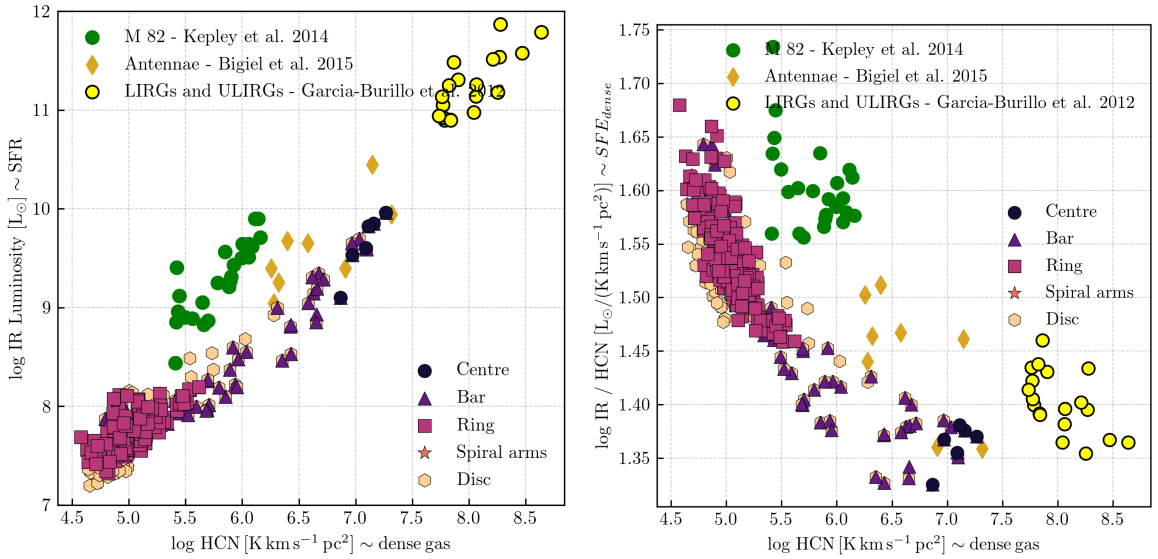

Figure 5.14: A zoom-in field from Figure 5.1, where we show NGC 253 sightlines, points from nearby starburst galaxy M 82 (Kepley et al., 2014), galaxy merger Antennae (Bigiel et al., 2015), and sample of LIRGs and ULIRGs (García-Burillo et al., 2012). Axes are the same as in Figure 5.1.

Figure 5.1 in Section 5.1 summarizes various HCN surveys and its relation to star formation (left panel), and how the TIR/HCN varies as the function of HCN-tracing gas that is present (right panel) (Jiménez-Donaire et al., 2019). We show data points from our work in Figure 5.1. Our measurements span ~ 3 orders of magnitude along both axes on the left panel, and overall they fit nicely into the SFR-HCN plane compared with the literature data. The centre of NGC 253 shows the brightest HCN emission and highest SFR, as opposed to the rest of the NGC 253's environments. On the other hand, on the right panel, we note that the brightest HCN-sightlines in NGC 253 show the lowest TIR/HCN.

We compare our results with other HCN observations across other extreme environments in Figure 5.14. We show measurements from Kepley et al. (2014) across the nearby starburst galaxy M 82 at slightly smaller physical scales than our work (200 pc), the sample of ULIRGs from García-Burillo et al. (2012), and sightlines from the galaxy merger, Antennae at 700 pc (Bigiel et al., 2015). LIRGs and ULIRGs show extensive IR and HCN luminosity, two orders of magnitude higher than starburst systems. M 82 sightlines appear to have higher IR luminosity than NGC 253. The Centre of M 82 shows the brightest HCN emission (Kepley et al., 2014), although it is fainter than the HCN emission towards the centre of NGC 253. M 82 and NGC 253 are typical starburst galaxies. However, they go through a different evolutionary phase (Rieke et al., 1988). NGC 253 is going through a more intense star formation episode than M 82; therefore, we expect a higher amount of HCN-tracing gas. On the other hand, HCN measurements across Antennae (Bigiel et al., 2015) show similar HCN as our data points, although we have to bear in mind the larger spatial scales of their observations.

Figure 5.15 shows how IR/HCN luminosity ratio varies as a function of HCN velocity dispersion and environment. Similarly, as in Figure 5.10, data points populate two distinct parts of this figure, and bar sightlines are found in both groups. Overall, we note that IR/HCN luminosity ratio decreases with increasing HCN velocity dispersion. Broader lines imply lower efficiency at star formation, implying that gas turbulence is important in suppressing star formation (Meidt et al., 2018), which is in agreement with the star formation theory of turbulent clouds (Federrath & Klessen, 2012). Similar

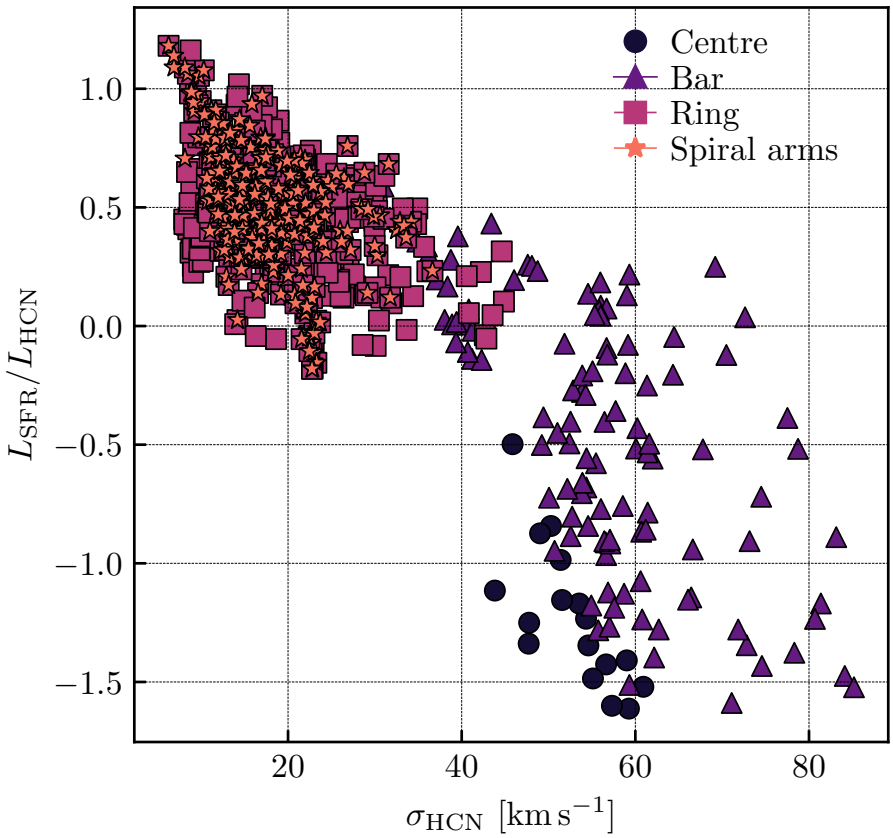

Figure 5.15: The ability of dense gas into forming stars, traced by *IR*/HCN luminosity ratio, as a function of HCN velocity dispersion measured from spectral decomposition analysis. We colour-code each point by the environment.

results are found in NGC 3627: central sightlines show broader emission lines, yet the ability of such gas for star formation is reduced (Bešlić et al., 2021). Murphy et al. (2015) compared SFR/HCO^+ with HCO^+ line widths in the nuclear region and bar ends in NGC 3627 and concluded that the gas kinematics is an important factor in setting star formation, not just its abundance.

5.8 Summary

We present new HCN emission at 300 pc scales obtained by ALMA ACA across the closest starburst galaxy NGC 253. These observations cover the large portion of NGC 253 disc that contains 95% of detected CO(2–1) emission obtained by ALMA ACA, and 85% of the star formation activity measured from ancillary infrared data at 70, 160, and 250 μm obtained by Herschel Space Telescope. We perform data reduction in using PHANGS pipeline in CASA. Our work focused on investigating the HCN line intensity distribution, its relation to CO(2–1) emission, gas kinematics, the ability of gas to form stars and its environmental dependence. Here we summarize our results:

- In our work, we used two approaches to calculate HCN integrated intensity: the first one is from calculating the zeroth moment map and extracting the information about HCN emission from it.

The second approach uses decomposition of observed emission along each line of sight. In this case, we got information about all gas components that contribute to the observed line emission.

- Using both approaches, we found strong enhancement of HCN emission towards the centre of NGC 253, and the change of intensity along the bar by two orders of magnitude. We observed a weak variation in HCN intensity along the ring and spiral arm, in contact points - bar ends.
- We observed strong environmental dependence on the HCN emission across the galaxy. In particular, the inner 2 kpc region shows complex HCN and CO(2–1). Using SCOUSE, we found up to three velocity components in central and bar sightlines, indicating that our observations probe multiple gas flows. On the other hand, we observe strong, single-peaked HCN emission lines in the ring and spiral arms. Our results support the idea that the molecular gas sits in the ring, after which it is inflowing towards the nuclear region along the bar.
- We investigated HCN/CO(2–1) line intensity ratio and its environmental distribution. We found that the HCN/CO(2–1) distribution within the bar shows a bimodality, which is a possible indication of the molecular outflow found in Walter et al., 2017. Flat HCN/CO(2–1) intensity ratio within the ring suggest that molecular gas traced by HCN emission gets pilled up in that region.
- Using SCOUSE to decompose the HCN and CO(2–1) emission, we found that 99% of all HCN velocity components have associated CO(2–1) component. We found that wider CO(2–1) profiles contain wider HCN emission lines. HCN velocity dispersion varies across the galaxy, together with spectral complexity and the HCN/CO(2–1) intensity ratio.
- We investigated ability of gas to form stars as a function of relative amount of HCN-traced molecular gas to bulk molecular gas and its environmental dependence. Sightlines with high HCN/CO(2–1) ratio appear the least efficient at star formation. This results has a few implications. The first one is that the mean gas density within the centre is considerably higher than the gas density traced by HCN emission. The second one is that the difference in kinematical complexity of the observed gas impacts the star formation.

CHAPTER 6

Conclusions

"*Space*", *it says,* "*is big. Really big. You just won't believe how vastly, hugely, mindbogglingly big it is. I mean, you may think it's a long way down the road to the chemist's, but that's just peanuts to space.*"
— Douglas Adams, "The Hitchhiker's Guide to the Galaxy"

The results presented in this doctoral thesis contribute to our understanding of the role of dense molecular gas in the context of star formation. It contains a detailed analysis of high-critical density molecular lines observed at GMC scales across two nearby galaxies: the strongly barred galaxy NGC 3627 and the closest starburst NGC 253. This work used observations from state-of-the-art facilities in mm astronomy, ALMA and NOEMA. We show how our observations of HCN emission across NGC 3627 (the centre) and NGC 253 (several environments) correspond to the literature overview presented in Chapter 3, Section 3.6 in Figure 6.1. To extend previous work on observing the dense molecular gas across nearby galaxies, the main goal of this work is to bridge the gap between the observations of resolved star-forming regions in our galaxy, the Milky Way, and the globally averaged measurements of other galaxies. Throughout our work, we take two directions in understanding dense molecular gas:

- **Mapping dense molecular gas at GMC scales** - study of dense molecular gas across NGC 3627, Chapter 4.
- **Expanding the sample of observed galaxies** - study of dense molecular gas in NGC 253, Chapter 5.2.

6.1 Main results of this doctoral thesis

In summary, we have shown the potential of studying mm molecular lines at a high spatial resolution and how molecular spectroscopy is a key tool to constrain dense gas properties. In the following, we outline the key findings of our work and answer questions asked in Chapter 3 Section 3.7:

6.1.1 Dense molecular gas across NGC 3627

In work presented in Chapter 4 and published in Bešlić et al. (2021), we take the next logical step built up from the EMPIRE survey (Bigiel et al., 2016; Jiménez-Donaire et al., 2019) and observed the nearby galaxy NGC 3627 in dense molecular gas tracers using the NOEMA interferometer. Our observations are at 100 pc scales, which is sufficient to resolve individual morphological environments

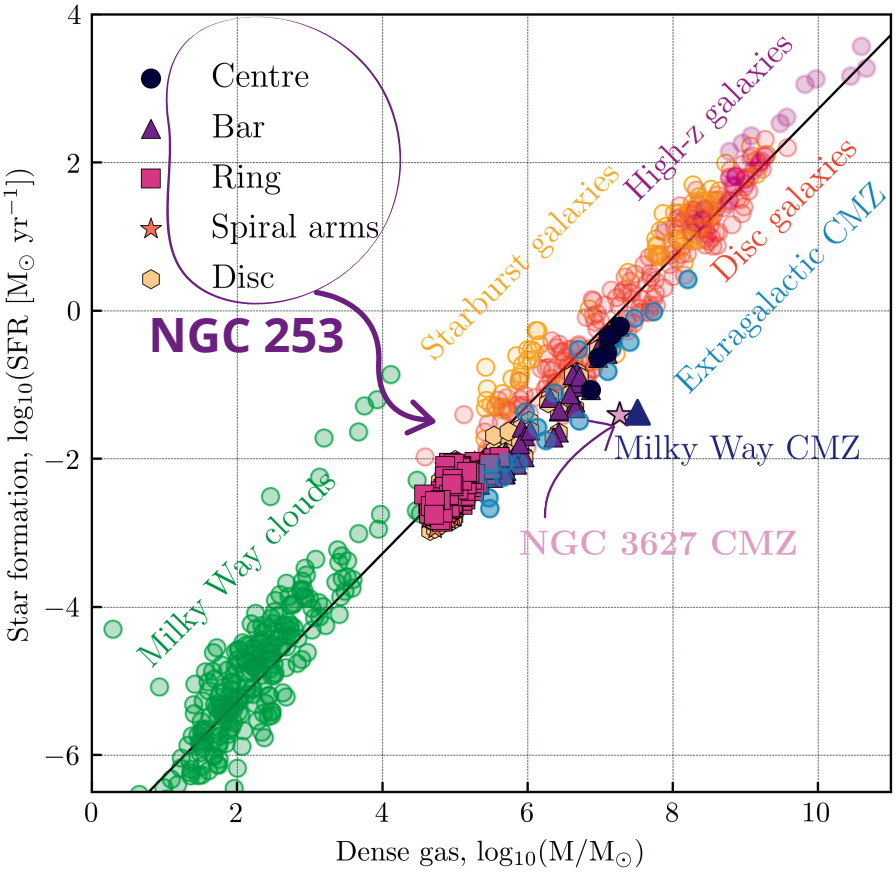

Figure 6.1: Correlation between star formation rate and dense molecular gas traced by the HCN emission. We show a compilation of literature measurements, presented in Jiménez-Donaire et al. (2019). We include measurements of central molecular zones in nearby galaxies (Querejeta et al., 2019; Jiang et al., 2020). The blue triangle represents the CMZ in the Milky Way (Henshaw et al., 2022). In addition, we include measurements from our work: The centre of NGC 3627 (Chapter 4 - Bešlić et al., 2021), and several environments across NGC 253 (Chapter 5).

within the disc of NGC 3627 and study the properties of dense molecular gas we found in these regions. This data set currently represents the highest resolution observations of dense molecular gas across a large part of a disc of a nearby galaxy. In addition, we use high-resolution measurements available of other gas phases, such as molecular gas emission traced by CO(2–1) at cloud scales from PHANGS-ALMA, high-resolution observations of ionised gas traced by the Hα emission from PHANGS-MUSE, and environmental masks presented in Querejeta et al. (2021). In the following, we describe our main findings presented in Chapter 4.

We observed bright emission of the observed molecular lines towards several regions of NGC 3627: the centre, along the bar, and spiral arms. Interestingly, molecular lines, HCN, HCO^+, and ^{13}CO show enhanced emission in the bar ends. In these regions, we expect to find gas shocked to higher densities since the bar ends features are the intersections of gas orbits from the bar and spiral arms. We see that line emission decreases along the bar, except for bar ends.

Next, we investigated the sensitivity of line intensity ratios to changes in cloud-scale surface

densities, traced by the CO(2–1) emission. We find that the line intensity ratios between high and low-critical density molecular lines reflect variations of the cloud-scale surface density, confirming the predictions shown in Leroy et al. (2017a).

Surprisingly, two distinct environments in NGC 3627, the centre and bar end, contain a similar amount of HCN-tracing gas relative to the bulk molecular emission (traced by CO(2–1) molecule). In contrast, the efficiency of such gas for star formation, traced by the Hα/HCN luminosity ratio, is significantly different across the centre and bar end. To explain this result, we suggest that other effects could be linked to the amount of dense gas, such as the gas dynamics, which play an essential role in setting the star formation efficiency. Mainly, in the bar ends of NGC 3627, we observe complex spectral molecular emission of high-critical density tracers, previously seen in the CO(2–1) emission (Beuther et al., 2017). Our findings imply that converging molecular gas flows in bar ends contain denser molecular gas. Bar ends are potential hosts of cloud-cloud collisions (e.g. Tokuda et al., 2020), and our results imply a presence of cloud-cloud collisions, which can further explain the local enhancement of star formation.

By applying the radiative transfer modelling to our observations using the `DGT`, we calculated the density and temperature in the centre and bar end of NGC 3627. We found that the gas densities in the centre can be described via lognormal function, whereas the gas densities in the bar ends show two distinct regimes, each describing the low and high-density regime.

6.1.2 Dense molecular gas across NGC 253

The second direction we took in this doctoral thesis was to expand the sample of galaxies covered in the EMPIRE survey Bigiel et al. (2016); Jiménez-Donaire et al. (2019), and map dense molecular gas across a more extreme galaxy, such as starburst. The benefit of this approach is in connecting nearby galaxies with more vigorous systems found at higher redshifts. Using ALMA ACA (PI: I. Bešlić), we detected various molecular lines at 300 pc scales in the inner disc (∼5 kpc) of local starburst galaxy NGC 253. The results are described and presented in Chapter 5.

This work used a new approach to analysing the observed emission. In particular, we used spectroscopy measurements to decompose the HCN(1–0) and the CO(2–1) emission along each line of sight. In such a method, we studied the component-by-component emission of these lines and how they relate to star formation calibrated from dust emission measurements. We found similar results as in the case of NGC 3627. Our results showed strongly enhanced HCN emission towards the centre of NGC 253 and a substantial decline in emission along the bar. The overlap regions between the bar, spiral arms and the ring show local enhancement of HCN emission, previously observed at CO(1–0) (Sorai et al., 2000).

In addition, we found multiple kinematical components of the HCN and CO(2–1) emission at the bar and the centre of this galaxy. The velocity separation of these components cannot be explained by the galactic rotation, which means we probe multiple clouds along the line of sight. By comparing velocity dispersions of decomposed components found in the HCN and CO(2–1) emission, we found that gas in the bar and centre shows different properties than in the ring and the spiral arms. In particular, gas from environments with simple kinematics (spiral arms and ring) have narrower lines than the gas in the central regions of NGC 253.

Furthermore, similar to the NGC 3627, we found the environmental dependence of the observed efficiency of star formation as a function of the total CO(2–1) emission. Regions with complex molecular emission show systematically different star formation efficiencies and suggest a possible threshold, after which the turbulence slows the star formation processes. This result suggests that the

kinematics of the gas plays a vital role in regulating star formation.

6.2 Outlook

Despite significant efforts from previous studies and their outstanding results, we must connect our results to our extensive knowledge of our galaxy, the Milky Way, and bridge the gap between the Galactic and extragalactic communities. Additionally, we lack specific information on dense molecular gas content at high spatial resolution in nearby galaxies. In particular, it is necessary to conduct a survey of various high-critical density lines at high spatial resolution across the disc of nearby galaxies (e.g. analogue to CLAWS survey, den Brok et al., 2022b) or focus on their brightest regions (e.g. centres, e.g. Eibensteiner et al., 2022; Martín et al., 2021) to provide a detailed picture of dense molecular gas properties, molecular line emission, kinematics, and cloud-cloud analysis.

The studies of dense molecular gas across the two nearby galaxies, NGC 3627 and NGC 253, constitute a significant step toward understanding the small-scale emission of dense molecular gas, the impact on the environment, and the role of gas kinematics. Our main findings in this work are the sensitivity of the observed molecular lines to gas densities, the role of the environment and gas kinematics in regulating the star formation at GMC scales. These results imply that the physics of individual molecular clouds is essential in further understanding star formation, as previously pointed out at lower resolution (e.g. Usero et al., 2015; Jiménez-Donaire et al., 2019).

The first step toward understanding the link between cloud-scale dense gas star formation is done in this work, which is a critical piece of the puzzle in completing the picture of galaxy evolution. Moreover, our key findings opened up new directions for studying the densest phase of the ISM. The next logical steps significantly depend on improving the current generation of interferometers, such as ALMA, NOEMA, SMA, APEX, and VLA. By achieving higher sensitivities and probing small spatial scales in nearby galaxies, the follow-up studies will focus on:

- Collecting more sensitive emission of high-critical density lines, HCN, HCO+, HNC, CS, N_2H^+, observing their isotopologues (e.g. $H^{13}CN$, $H^{13}CO^+$), including different$-J$ transitions of high-critical density lines.
- Further understanding of the impact of the environment on star formation.
- Constrain physical conditions of dense molecular ISM using radiative transfer modelling and prescription from (Leroy et al., 2017a).
- Identify dense molecular cloud by applying algorithms for defining GMCs (Rosolowsky et al., 2021).
- Study the impact of gas kinematics and investigate regions with peculiar kinematic features, such as bar ends and cloud-collision environments.

The following sections outline several critical aspects for future studies.

6.2.1 A study of emission and properties of various molecules in mm spectral-domain across nearby galaxies

In combination with other high-resolution observations covering various gas phases, e.g. the PHANGS survey, the currently missing piece is mapping the dense ISM at similar scales. As outlined in

Chapter 4, the first steps have already been taken. This goal is crucial for further bridging the gap between Milky Way and other galaxies.

The molecular gas phase of the ISM contains large number of molecules (Chapter 1, Section 1.4), primarily observable in the radio and mm domain. Today's radio observing facilities can detect molecules at high sensitivity and spatial resolution, probing faint regions within extragalactic sources that were not accessible before. Observing and detecting various molecules within a 90-250 GHz spectral window makes it possible to detect several low and high-J molecular transitions and their isotopologues, as shown in the centre of NGC 253 (Martín et al., 2021). By conducting these observations, we will understand gas chemistry in nearby galaxies further and link these results to Milky Way studies:

• The first part of this goal is to observe these molecules across the extensive sample of nearby galaxies and cover many environments (Querejeta et al., 2019) - centres, bars, nuclear rings, bar-ends, and dust lanes. By doing so, we will conduct a systematic analysis of molecular gas distribution globally (within the sample of galaxies) and locally (within each galaxy), as presented in the example of NGC 253 (Martín et al., 2021). In addition, it will be possible to test if galaxies' properties like morphology, star formation rate, and stellar and molecular gas mass affect the molecular emission. For example, expanding the findings described in Chapters 4 and 5, we will investigate how the presence of the bar, AGN, starburst, or a close companion - i.e. variety of environments impact molecular gas content. By investigating the origin of molecular emission across the galaxy, we can obtain more information about the processes that set molecular emission: the presence of cosmic rays, an intense radiation field, dust and other molecules and atoms. Additionally, we will use quantitative statistics to contrast and compare the relative spatial distribution of the emission across position-position-velocity (ppυ) space.

• The broad order of magnitude in the critical density of these molecules will allow the study of the density contrast and better model constraints in radiative transfer modelling. Following the work presented in Bešlić et al. (2021), the next step lies in conducting a systematic study of the sensitivity of molecular emission to changes in the mean gas density and further connecting observational work to theoretical studies (Leroy et al., 2017a). It is essential to highlight that other molecular lines like N_2H^+ have higher critical density than, e.g. HCN and probe denser molecular gas. Emission lines such as N_2H^+ are possible better tracers of star-forming gas in high-density regions (e.g. centres). N_2H^+ emission is the default "dense gas tracer" in local clouds in the Milky Way. Therefore, such observations would bridge the Galactic community's gap (Tafalla et al., 2021; Barnes et al., 2021).

• Each molecule is sensitive to different physical conditions, which means that studying various transitions of each molecule (e.g. HCN(2-1), HCN(2-3), HCN(4-3)) is essential in constraining the excitation conditions (Jiménez-Donaire et al., 2017b). Using radiative transfer modelling in RADEX, we will better constrain the gas temperatures and column densities. Moreover, studying isotopologues provides information on the observed gas's optical thickness (Jiménez-Donaire et al., 2017a). Shock tracers, e.g. SiO and temperature-sensitive lines, such as NH_3 in environments like the centres of galaxies that host an AGN, are critical to revealing the nature of molecular gas in such extreme radiation-dominated regions.

6.2.2 Unraveling the properties of gas flows in galaxies

Better understanding the mass flows is critical to knowing how gas reservoirs grow and how stars and clusters form. Global galaxy dynamics are fundamental in driving these mass flows, which in turn regulate the evolution of galaxies (Chapter 1, Section 1.6). Testing how gas flows on various

scales are connected to star formation theories is necessary. Therefore high-resolution observations are essential for resolving gas flows and gas structures. Bešlić et al. (2021) has shown the power of using high-resolution observations of dense molecular gas. In particular, by looking at the HCN and HCO^+ spectra towards bar-ends in NGC 3627, Bešlić et al. (2021) found multiple velocity components associated with gas flows along the bar and dust lanes, previously identified in CO(2-1) (Beuther et al., 2017). These molecular gas flows converge at the bar and spiral arms intersection, enhancing local star formation.

• Firstly, studying global dynamics and mass flows is crucial. Gas flows can further enhance or suppress star formation. For example, streaming gas motions in the bar and spiral arms converge and drastically increase gas surface densities and volume densities in the bar ends, inducing local star formation. On the one hand, the gas can get pilled up in the nuclear ring, which will start inflowing towards the centre along the bar (Sorai et al., 2000).

In addition, gas flows can prevent gas from collapsing, which might explain low star formation efficiency in centres of galaxies (Meidt et al., 2018). Composing the line emission and assessing the line width across the galaxies is necessary for associating dense gas emission to their molecular companions. Using the SCOUSE algorithm (Henshaw et al., 2016b, 2019), and following the work described in Chapter 5, a critical step forward will be decomposing each spectrum to its components and revealing which environments contain multiple gas flows and test the idea that contact points between different environments (e.g. bars, rings, spiral arms) are essential in bringing the gas towards the centres of galaxies. Additionally, by looking into the ppν picture, particularly along a galaxy's minor axis, we can search for indicators of outflowing gas and see how galactic winds affect the local environment in setting the mass transfers into the intergalactic medium.

• Stars are thought to form in clustered environments (Kruijssen, 2012). Super stellar clusters are products of high-mass star formation (Whitmore, 2003; Portegies Zwart et al., 2010), even starbursts in extreme cases, initiated via cloud-cloud collisions. Therefore, studying the local-scale kinematics and cloud-cloud collisions is crucial in understanding local enhancements of star formation. Cloud–cloud collisions are an essential modulator in the star formation processes (Elmegreen, 1998). They can inject energy into the gas, increasing the level of turbulence and producing a dense molecular layer that is gravitationally unstable (Takahira et al., 2018; Whitworth & Jaffa, 2018). As seen in numerical simulations (Fukui et al., 2021a), cloud–cloud collisions trigger star formation, and these can be identified in the position-velocity space (pν diagram) as broad bridging features (Haworth et al., 2015), V or U shaped (Figures 1 and 2 in Fukui et al., 2021a). Overall, even though the former studies (e.g. Tokuda et al., 2020; Muraoka et al., 2020; Kondo et al., 2021) demonstrated the importance of investigating molecular clouds in nearby galaxies, they focused on single clouds instead of studying environments set by dominant cloud–cloud collisions. For a detailed picture of cloud–cloud collisions and their role in regulating star formation, we need systematic and pc-scale studies of places characterized by high-massive star formation, as demonstrated in the nuclear region in NGC 253 (Leroy et al., 2015), the centre of NGC 4945 (Emig et al., 2020), and the centre of M 82 (Jimenez-Donaire, prep) natural cloud collision environments. This direction will do precisely this: by performing a detailed study of environments where we expect to observe cloud-cloud collisions (e.g. centres, bar-ends, galaxy mergers). By obtaining this scientific goal, we will test what drives these collisions, large-scale flows or supernovae (e.g. Cosentino et al., 2022).

• With high spatial and spectral resolution observations, it will be possible to resolve and separate gas flows between different regions and directly study how cloud-scale motions affect larger-scale gas flows. This step is crucial to understand how and why stars form from gas and the effects (on global-kpc and local-a few pc scales) driving the density enhancements. Most importantly, these

results are fundamental for star formation theories and an essential benchmark for simulations (e.g. see review Tan et al., 2014).

6.2.3 Systematic cloud analysis of high-critical density tracers

Star formation and dense gas phase relationship to each other over a wide range of physical scales: from clouds measured only in the Milky Way to measurements of whole galaxies and their centres. The comprehensive coverage of physical scales lies in the density structure of individual molecular clouds, which significantly contribute to extragalactic measurements. In particular, the averaging over more extensive areas mixes information over many environments and dynamical ranges (Spilker et al., 2021). The missing part is dense molecular gas content measurements at scales of individual molecular clouds in nearby galaxies. Additionally, the explanation for the observed systematic variation in dense gas efficiency lies in resolving molecular clouds in nearby systems (Kainulainen et al., 2009, 2014; Tafalla et al., 2021). Another important part is determining the density probability distribution function (PDF) at these scales. We will answer what drives the amount of dense gas and how that affects star formation. Changes in PDF may be related to the initial mass function (IMF). Here, we will do exactly this: using observations of dense molecular gas content at the high spatial resolution, covering an extensive dynamic range in spatial scale, we will take one step further than those outlined in Chapter 4 and apply cloud and structure identification tools like `CPROPS` (Rosolowsky, 2007; Rosolowsky et al., 2021) or a dendrogram analysis. In doing so, we will associate denser gas components homogeneously and cleanly with individual molecular clouds and their properties.

• This will link their sizes, masses, and viral state to star formation rates. In combination with the high-resolution optical observations from PHANGS, we can further directly measure spatial scales at which the relation between dense molecular gas and star formation breaks and estimate the lifetimes of this dense phase. This project will provide an extensive set of dense gas content information within the molecular clouds, covering a variety of galactic environments.

• We will investigate how the dense gas fraction and the star formation efficiency of dense gas of individual clouds are related. In this task, we will progress on better understanding if gravitationally bounder clouds have more dense gas and if the level of turbulence affects star formation efficiency. In turbulent models, the Mach number, the mean density, and the virial parameter of clouds determine the dense gas fraction and star formation efficiency (Renaud et al., 2012; Federrath & Klessen, 2013). Feedback-driven models make similar predictions and can be directly tested only with cloud-scale observations (Semenov et al., 2018). On larger scales, cloud collisions and gas flow through spiral arms and bars can prompt dense gas formation and stabilize the gas against collapse (e.g. Meidt et al., 2018), emphasizing the role of the environment. Moreover, the star formation efficiency of clouds, and their dense gas fraction, evolves with time (e.g. Murphy et al., 2011).

6.3 Conclusion remarks

In the previous sections, we have shown the contributions of our work in further understanding the dense molecular gas in nearby galaxies and several prospects for future investigations.

Our work highlights the importance of studying 3 mm molecular lines at high spatial resolution and the need for high spectral resolution in systems where we can resolve different morphological regions. Additionally, we demonstrated a broad use of investigating dense molecular ISM and linking it with the multi-wavelength data in answering several currently open science questions, mainly in the context

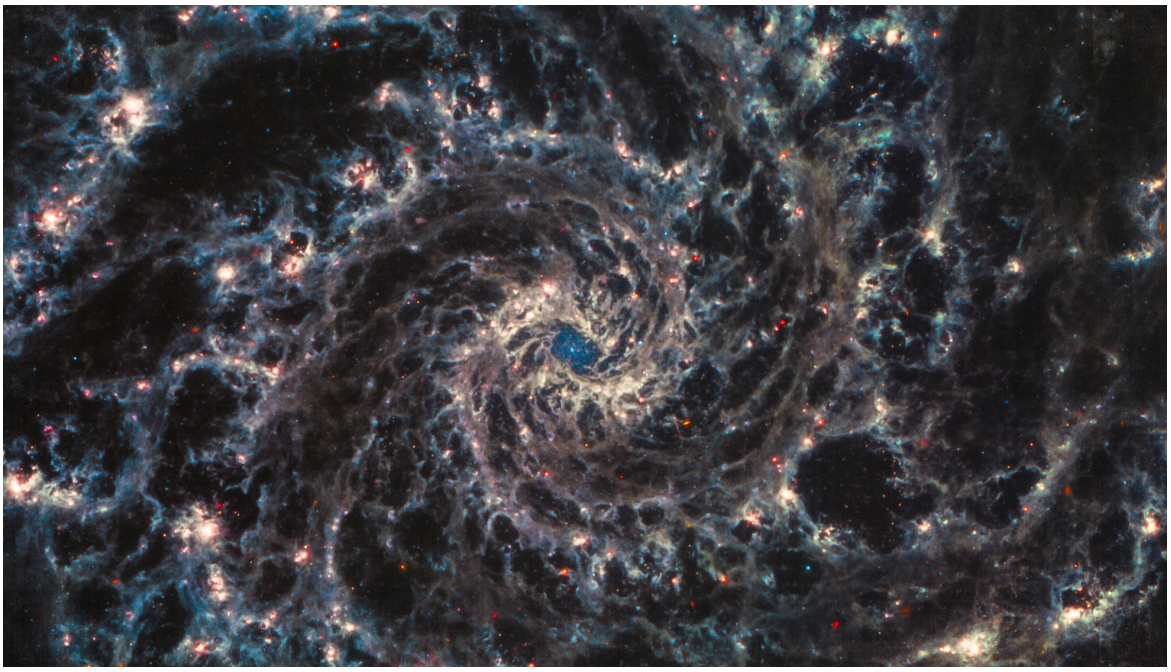

Figure 6.2: The outstanding JWST composite image of NGC 628. NASA/ESA/CSA/Judy Schmidt.

of the star formation process.

The pillars of future scientific projects in this field are based on the next generations of interferometers and the upgrades of current observing facilities. For example, the following steps for NOEMA's capability are reaching high sensitivity and high resolution, including building the exquisite capabilities and wide-band coverage of `POLYFIX`. ALMA telescopes will expand the maximum baseline length by a factor of a few, upgrade current receivers and significantly reduce the observing time. The EHT will soon include more observing facilities worldwide, such as NOEMA, Kitt Peak National Observatory (KPNO), and The Greenland Telescope. In addition, significant progresses in observing nearby galaxies in ionized gas, using, e.g. MUSE (currently ongoing Large Program of observing Hα across NGC 253, PI: E. Congiu), and recent efforts in mapping HI gas using the South African MeerKAT radio telescope (currently targeted several nearby galaxies from the PHANGS sample, including NGC 253), are critical assets in future studies.

The bright future with the JWST

We are witnessing a new era in astronomy. The most recent major event was the first image release from the James Webb Space Telescope, which revealed a great new perspective of the early Universe, but also the star-forming regions in our Galaxy (see Figure 3.1 in Chapter 3). The JWST collects light mainly in the infrared, revealing the dust-obscured regions in nearby galaxies, as seen across nearby galaxy NGC 628 in Figure 6.2, and even the most distant galaxies, whose confirmation we impatiently wait. In the future, by observing other galaxies, such as NGC 3627 (observation scheduled for December 2022 as part of the PHANGS-JWST survey), it will be possible to conduct even more comprehensive and detailed multi-wavelength studies of different components in the ISM and stellar populations at spatial scales for which we were always aiming.

Bibliography

Aalto S., Wilner D., Spaans M., Wiedner M. C., Sakamoto K., Black J. H., Caldas M., 2009, A&A, 493, 481

Abbott B., et al., 2007, ApJ, 659, 918

Abbott B. P., et al., 2016, ApJL, 818, L22

Abreu-Vicente J., Kainulainen J., Stutz A., Henning T., Beuther H., 2015, A&A, 581, A74

Akiyama K., Event Horizon Telescope Collaboration 2022, in American Astronomical Society Meeting Abstracts. p. 211.03

Aladro R., Martín-Pintado J., Martín S., Mauersberger R., Bayet E., 2011, A&A, 525, A89

Alves J., Lombardi M., Lada C. J., 2007, A&A, 462, L17

Anand G. S., et al., 2020, MNRAS,

André P., Basu S., Inutsuka S., 2009, in Chabrier G., ed., , Structure Formation in Astrophysics. p. 254

André P., Di Francesco J., Ward-Thompson D., Inutsuka S.-I., Pudritz R. E., Pineda J. E., 2014, Protostars and Planets VI, pp 27–51

Aniano G., Draine B. T., Gordon K. D., Sandstrom K., 2011, PASP, 123, 1218

Arnaboldi M., Capaccioli M., Cappellaro E., Held E. V., Koribalski B., 1995, AJ, 110, 199

Athanassoula E., 1992, MNRAS, 259, 345

Auddy S., Basu S., Kudoh T., 2018, MNRAS, 474, 400

Baars J. W. M., Hooghoudt B. G., Mezger P. G., de Jonge M. J., 1987, A&A, 175, 319

Bagnasco G., et al., 2007, in Heaney J. B., Burriesci L. G., eds, Society of Photo-Optical Instrumentation Engineers (SPIE) Conference Series Vol. 6692, Cryogenic Optical Systems and Instruments XII. p. 66920M, doi:10.1117/12.735602

Baldwin J. A., Phillips M. M., Terlevich R., 1981, PASP, 93, 5

Ballesteros-Paredes J., Hartmann L. W., Vázquez-Semadeni E., Heitsch F., Zamora-Avilés M. A., 2011, MNRAS, 411, 65

Barnes A. T., Longmore S. N., Battersby C., Bally J., Kruijssen J. M. D., Henshaw J. D., Walker D. L., 2017, MNRAS, 469, 2263

Barnes A. T., et al., 2020a, MNRAS, 497, 1972

Barnes A. T., Longmore S. N., Dale J. E., Krumholz M. R., Kruijssen J. M. D., Bigiel F., 2020b, MNRAS, 498, 4906

Barnes A. T., et al., 2021, MNRAS, 508, 5362

Bastian N., Covey K. R., Meyer M. R., 2010, ARA&A, 48, 339

Bemis A., Wilson C. D., 2019, AJ, 157, 131

Bendo G. J., et al., 2010, A&A, 518, L65

Berkhuijsen E. M., Fletcher A., 2015, MNRAS, 448, 2469

Bertoldi F., McKee C. F., 1992, ApJ, 395, 140

Beuther H., Schilke P., Wyrowski F., 2004, ApJ, 615, 832

Beuther H., et al., 2012, A&A, 538, A11

Beuther H., Meidt S., Schinnerer E., Paladino R., Leroy A., 2017, A&A, 597, A85

Bešlić I., et al., 2021, MNRAS, 506, 963

Bešlić I., in prep

Bigiel F., Leroy A., Walter F., Brinks E., de Blok W. J. G., Madore B., Thornley M. D., 2008, AJ, 136, 2846

Bigiel F., et al., 2011, ApJL, 730, L13

Bigiel F., Leroy A. K., Blitz L., Bolatto A. D., da Cunha E., Rosolowsky E., Sandstrom K., Usero A., 2015, ApJ, 815, 103

Bigiel F., et al., 2016, ApJL, 822, L26

Binney J., Gerhard O. E., Stark A. A., Bally J., Uchida K. I., 1991, MNRAS, 252, 210

Blanc G. A., Heiderman A., Gebhardt K., Evans Neal J. I., Adams J., 2009, ApJ, 704, 842

Blitz L., 1993, in Levy E. H., Lunine J. I., eds, Protostars and Planets III. p. 125

Blitz L., Rosolowsky E., 2004, in Johnstone D., Adams F. C., Lin D. N. C., Neufeeld D. A., Ostriker E. C., eds, Astronomical Society of the Pacific Conference Series Vol. 323, Star Formation in the Interstellar Medium: In Honor of David Hollenbach. p. 89 (arXiv:astro-ph/0408263)

Bolatto A. D., Leroy A. K., Rosolowsky E., Walter F., Blitz L., 2008, ApJ, 686, 948

Bolatto A. D., Wolfire M., Leroy A. K., 2013a, ARA&A, 51, 207

Bolatto A. D., Wolfire M., Leroy A. K., 2013b, ARA&A, 51, 207

Bouwens R., 2020, in The Build-Up of Galaxies through Multiple Tracers and Facilities. p. 17, doi:10.5281/zenodo.3756454

Braine J., Shimajiri Y., André P., Bontemps S., Gao Y., Chen H., Kramer C., 2017, A&A, 597, A44

Bron E., Le Bourlot J., Le Petit F., 2014, A&A, 569, A100

Brouillet N., Muller S., Herpin F., Braine J., Jacq T., 2005, A&A, 429, 153

Buat V., 1992, A&A, 264, 444

Buat V., Deharveng J. M., Donas J., 1989, A&A, 223, 42

Buchbender C., et al., 2013, A&A, 549, A17

Burbidge E. M., Burbidge G. R., Fowler W. A., Hoyle F., 1957, Reviews of Modern Physics, 29, 547

Burke B. F., Graham-Smith F., 1997, An introduction to radio astronomy

Burkhart B., Collins D. C., Lazarian A., 2015, ApJ, 808, 48

Burton W. B., 1985, A&AS, 62, 365

Calzetti D., Kinney A. L., Storchi-Bergmann T., 1994, ApJ, 429, 582

Calzetti D., Armus L., Bohlin R. C., Kinney A. L., Koornneef J., Storchi-Bergmann T., 2000, ApJ, 533, 682

Calzetti D., et al., 2010, ApJ, 714, 1256

Camacho V., Vázquez-Semadeni E., Ballesteros-Paredes J., Gómez G. C., Fall S. M., Mata-Chávez M. D., 2016, ApJ, 833, 113

Carruthers G. R., 1970, ApJL, 161, L81

Casasola V., Hunt L. K., Combes F., García-Burillo S., Neri R., 2011, A&A, 527, A92

Chabrier G., 2003, PASP, 115, 763

Chabrier G., 2005, in Corbelli E., Palla F., Zinnecker H., eds, Astrophysics and Space Science Library Vol. 327, The Initial Mass Function 50 Years Later. p. 41 (arXiv:astro-ph/0409465), doi:10.1007/978-1-4020-3407-7_5

Chandar R., Whitmore B. C., Calzetti D., Di Nino D., Kennicutt R. C., Regan M., Schinnerer E., 2011, ApJ, 727, 88

Chen H.-R., Liu S.-Y., Su Y.-N., Zhang Q., 2010, ApJL, 713, L50

Chen Y., Jiang B., Zhou P., Su Y., Zhou X., Li H., Zhang X., 2014, in Ray A., McCray R. A., eds, IAU Symposium Vol. 296, Supernova Environmental Impacts. pp 170–177 (arXiv:1304.5367), doi:10.1017/S1743921313009423

Chen H., Braine J., Gao Y., Koda J., Gu Q., 2017, ApJ, 836, 101

Chevance M., et al., 2020, MNRAS, 493, 2872

Chin Y. N., Henkel C., Whiteoak J. B., Millar T. J., Hunt M. R., Lemme C., 1997, A&A, 317, 548

Chin Y. N., Henkel C., Millar T. J., Whiteoak J. B., Marx-Zimmer M., 1998, A&A, 330, 901

Clark P. C., Glover S. C. O., 2014, MNRAS, 444, 2396

Collins D. C., Kritsuk A. G., Padoan P., Li H., Xu H., Ustyugov S. D., Norman M. L., 2012, ApJ, 750, 13

Colman T., Teyssier R., 2020, MNRAS, 492, 4727

Colombo D., et al., 2014, ApJ, 784, 3

Condon J. J., 1992, ARA&A, 30, 575

Cornwell T. J., 2008, IEEE Journal of Selected Topics in Signal Processing, 2, 793

Cosentino G., et al., 2022, MNRAS, 511, 953

Cotton W. D., 2017, preprint, (arXiv:1707.02272)

Crocker A., et al., 2012, MNRAS, 421, 1298

Crosthwaite L. P., Turner J. L., 2007, AJ, 134, 1827

Dame T. M., Hartmann D., Thaddeus P., 2001, ApJ, 547, 792

Decarli R., et al., 2019, ApJ, 882, 138

Decarli R., et al., 2020, ApJ, 902, 110

Deharveng J. M., Sasseen T. P., Buat V., Bowyer S., Lampton M., Wu X., 1994, A&A, 289, 715

Dey B., et al., 2019, MNRAS, 488, 1926

Díaz-García S., Moyano F. D., Comerón S., Knapen J. H., Salo H., Bouquin A. Y. K., 2020, A&A, 644, A38

Dib S., Brandenburg A., Kim J., Gopinathan M., André P., 2008, ApJL, 678, L105

Domínguez A., et al., 2013, ApJ, 763, 145

Doyon R., et al., 2019, in Canadian Long Range Plan for Astronomy and Astrophysics White Papers. p. 56, doi:10.5281/zenodo.3827472

Draine B., 1989, in Allamandola L. J., Tielens A. G. G. M., eds, Vol. 135, Interstellar Dust. p. 313

Draine B. T., 2009, in Henning T., Grün E., Steinacker J., eds, Astronomical Society of the Pacific Conference Series Vol. 414, Cosmic Dust - Near and Far. p. 453 (arXiv:0903.1658)

Draine B. T., 2011, Physics of the Interstellar and Intergalactic Medium

Draine B. T., Lazarian A., 1998, ApJL, 494, L19

Draine B. T., Lee H. M., 1984, ApJ, 285, 89

Draine B. T., Li A., 2007, ApJ, 657, 810

Draine B. T., et al., 2007, ApJ, 663, 866

Duncan A. R., Stewart R. T., Haynes R. F., Jones K. L., 1995, PASA, 12, 54

Egusa F., Hirota A., Baba J., Muraoka K., 2018, ApJ, 854, 90

Eibensteiner C., et al., 2022, arXiv e-prints, p. arXiv:2201.02209

Elmegreen B. G., 1998, in Woodward C. E., Shull J. M., Thronson Harley A. J., eds, Astronomical Society of the Pacific Conference Series Vol. 148, Origins. p. 150 (arXiv:astro-ph/9712352)

Elmegreen B. G., 1999, ApJ, 515, 323

Elmegreen B. G., Scalo J., 2004, ARA&A, 42, 211

Emig K. L., et al., 2020, ApJ, 903, 50

Emsellem E., Renaud F., Bournaud F., Elmegreen B., Combes F., Gabor J. M., 2015, MNRAS, 446, 2468

Emsellem E., et al., 2022, A&A, 659, A191

Enoch M. L., et al., 2006, ApJ, 638, 293

Enoch M. L., Lee J.-E., Harvey P., Dunham M. M., Schnee S., 2010, ApJL, 722, L33

Evans Neal J. I., Kim K.-T., Wu J., Chao Z., Heyer M., Liu T., Nguyen-Lu'o'ng Q., Kauffmann J., 2020, ApJ, 894, 103

Event Horizon Telescope Collaboration et al., 2019, ApJL, 875, L1

Ewen H. I., Purcell E. M., 1951, Nature, 168, 356

Federrath C., Klessen R. S., 2012, ApJ, 761, 156

Federrath C., Klessen R. S., 2013, ApJ, 763, 51

Field G. B., Goldsmith D. W., Habing H. J., 1969, ApJL, 155, L149

Field G. B., Blackman E. G., Keto E. R., 2011, MNRAS, 416, 710

Ford G. P., et al., 2013, ApJ, 769, 55

Fukui Y., Habe A., Inoue T., Enokiya R., Tachihara K., 2021a, PASJ, 73, S1

Fukui Y., Inoue T., Hayakawa T., Torii K., 2021b, PASJ, 73, S405

Furst E., Reich W., Reich P., Reif K., 1990, A&AS, 85, 691

Gaensler B. M., Madsen G. J., Chatterjee S., Mao S. A., 2008, PASA, 25, 184

Galametz M., et al., 2013, MNRAS, 431, 1956

Gallagher M. J., et al., 2018a, ApJ, 858, 90

Gallagher M. J., et al., 2018b, ApJL, 868, L38

Galliano F., Galametz M., Jones A. P., 2018, ARA&A, 56, 673

Gao Y., Solomon P. M., 2004a, ApJS, 152, 63

Gao Y., Solomon P. M., 2004b, ApJ, 606, 271

Gao Y., Carilli C. L., Solomon P. M., Vand en Bout P. A., 2007, ApJL, 660, L93

Garcia A. M., 1993, A&AS, 100, 47

García-Burillo S., Usero A., Alonso-Herrero A., Graciá-Carpio J., Pereira-Santaella M., Colina L., Planesas P., Arribas S., 2012, A&A, 539, A8

Genzel R., et al., 2010, MNRAS, 407, 2091

Genzel R., et al., 2015, ApJ, 800, 20

Gieles M., Larsen S. S., Scheepmaker R. A., Bastian N., Haas M. R., Lamers H. J. G. L. M., 2006, A&A, 446, L9

Ginsburg A., et al., 2019, radio-astro-tools/spectral-cube: v0.4.4, doi:10.5281/zenodo.2573901

Girichidis P., Konstandin L., Whitworth A. P., Klessen R. S., 2014, ApJ, 781, 91

Girichidis P., et al., 2020, Space Sci. Rev., 216, 68

Goodwin S. P., Nutter D., Kroupa P., Ward-Thompson D., Whitworth A. P., 2008, A&A, 477, 823

Gould R. J., Salpeter E. E., 1963, ApJ, 138, 393

Graciá-Carpio J., García-Burillo S., Planesas P., 2008, Ap&SS, 313, 331

Graham A. W., Prieto M., 2001, Astrophysics and Space Science Supplement, 277, 465

Habibi M., Stolte A., Brandner W., Hußmann B., Motohara K., 2013, A&A, 556, A26

Hacar A., Bosman A. D., van Dishoeck E. F., 2020, A&A, 635, A4

Haffner L. M., et al., 2009, Reviews of Modern Physics, 81, 969

Hall J. S., 1949, Science, 109, 166

Hao C.-N., Kennicutt R. C., Johnson B. D., Calzetti D., Dale D. A., Moustakas J., 2011, ApJ, 741, 124

Hartman R. C., et al., 1999, ApJS, 123, 79

Hartmann D., Burton W. B., 1997, Atlas of Galactic Neutral Hydrogen

Haslam C. G. T., Salter C. J., Stoffel H., Wilson W. E., 1982, A&AS, 47, 1

Hauser M. G., 1995, in Extragalactic Background Radiation Meeting. pp 135–144

Haworth T. J., et al., 2015, MNRAS, 450, 10

Heckman T. M., Lehnert M. D., Strickland D. K., Armus L., 2000, ApJS, 129, 493

Heger M. L., 1922, Lick Observatory Bulletin, 10, 146

Heiderman A., Evans Neal J. I., Allen L. E., Huard T., Heyer M., 2010, ApJ, 723, 1019

Heiles C., 1971, ARA&A, 9, 293

Helfer T. T., Blitz L., 1997, ApJ, 478, 162

Helfer T. T., Vogel S. N., Lugten J. B., Teuben P. J., 2002, PASP, 114, 350

Henshaw J. D., et al., 2016a, SCOUSE: Semi-automated multi-COmponent Universal Spectral-line fitting Engine, Astrophysics Source Code Library (ascl:1601.003)

Henshaw J. D., Longmore S. N., Kruijssen J. M. D., 2016b, MNRAS, 463, L122

Henshaw J. D., et al., 2019, MNRAS, 485, 2457

Henshaw J. D., Barnes A. T., Battersby C., Ginsburg A., Sormani M. C., Walker D. L., 2022, arXiv e-prints, p. arXiv:2203.11223

Herrera-Endoqui M., Díaz-García S., Laurikainen E., Salo H., 2015, A&A, 582, A86

Heyer M. H., Brunt C. M., 2004, ApJL, 615, L45

Heyer M. H., Carpenter J. M., Snell R. L., 2001, ApJ, 551, 852

Heyer M., Krawczyk C., Duval J., Jackson J. M., 2009, ApJ, 699, 1092

Hiltner W. A., 1949, Nature, 163, 283

Hirashita H., Inoue A. K., Kamaya H., Shibai H., 2001, A&A, 366, 83

Hirashita H., Buat V., Inoue A. K., 2003, A&A, 410, 83

Högbom J. A., 1974, A&AS, 15, 417

Holdship J., et al., 2021, A&A, 654, A55

Hollenbach D., Salpeter E. E., 1971, ApJ, 163, 155

Houghton S., Whiteoak J. B., Koribalski B., Booth R., Wiklind T., Wielebinski R., 1997, A&A, 325, 923

Hoyle F., 1953, ApJ, 118, 513

Hoyle F., Ellis G. R. A., 1963, Australian Journal of Physics, 16, 1

Hughes A., et al., 2013, ApJ, 779, 46

Hunter S. D., et al., 1997, ApJ, 481, 205

Ibáñez-Mejía J. C., Mac Low M.-M., Klessen R. S., Baczynski C., 2016, ApJ, 824, 41

Iodice E., Arnaboldi M., Rejkuba M., Neeser M. J., Greggio L., Gonzalez O. A., Irwin M., Emerson J. P., 2014, A&A, 567, A86

Jiang X.-J., et al., 2020, MNRAS, 494, 1276

Jimenez-Donaire M. J., in prep

Jiménez-Donaire M. J., et al., 2017a, MNRAS, 466, 49

Jiménez-Donaire M. J., et al., 2017b, MNRAS, 466, 49

Jiménez-Donaire M. J., et al., 2019, ApJ, 880, 127

Jones P. A., et al., 2012, MNRAS, 419, 2961

Joye W. A., Mandel E., 2003, in Payne H. E., Jedrzejewski R. I., Hook R. N., eds, Astronomical Society of the Pacific Conference Series Vol. 295, Astronomical Data Analysis Software and Systems XII. p. 489

Juneau S., Narayanan D. T., Moustakas J., Shirley Y. L., Bussmann R. S., Kennicutt R. C. J., Vanden Bout P. A., 2009, ApJ, 707, 1217

Kainulainen J., Beuther H., Henning T., Plume R., 2009, A&A, 508, L35

Kainulainen J., Federrath C., Henning T., 2014, Science, 344, 183

Kalberla P. M. W., Kerp J., 2009, ARA&A, 47, 27

Kauffmann G., et al., 2003, MNRAS, 346, 1055

Kauffmann J., Goldsmith P. F., Melnick G., Tolls V., Guzman A., Menten K. M., 2017, A&A, 605, L5

Kellermann K. I., Moran J. M., 2001, ARA&A, 39, 457

Kendrew S., et al., 2015, PASP, 127, 623

Kenney J. D. P., 1994, in Ishiguro M., Welch J., eds, Astronomical Society of the Pacific Conference Series Vol. 59, IAU Colloq. 140: Astronomy with Millimeter and Submillimeter Wave Interferometry. p. 282

Kenney J. D. P., Wilson C. D., Scoville N. Z., Devereux N. A., Young J. S., 1992, ApJL, 395, L79

Kennicutt Robert C. J., 1989, ApJ, 344, 685

Kennicutt R. C., 1997, in Astrophysics and Space Science Library. pp 171–195

Kennicutt Jr. R. C., 1998a, ARA&A, 36, 189

Kennicutt Jr. R. C., 1998b, ApJ, 498, 541

Kennicutt Robert C. J., De Los Reyes M. A. C., 2021, ApJ, 908, 61

Kennicutt R. C., Evans N. J., 2012, ARA&A, 50, 531

Kennicutt Robert C. J., et al., 2007, ApJ, 671, 333

Kennicutt R. C., et al., 2011, PASP, 123, 1347

Kepley A. A., Leroy A. K., Frayer D., Usero A., Marvil J., Walter F., 2014, ApJL, 780, L13

Kepley A. A., et al., 2018, ApJ, 862, 120

Kerr F. J., Bowers P. F., Jackson P. D., Kerr M., 1986, A&AS, 66, 373

Kirsten F., et al., 2022, Nature, 602, 585

Klessen R. S., Glover S. C. O., 2016, Saas-Fee Advanced Course, 43, 85

Knudsen K. K., Walter F., Weiss A., Bolatto A., Riechers D. A., Menten K., 2007, The Astrophysical Journal, 666, 156

Koda J., Teuben P., Sawada T., Plunkett A., Fomalont E., 2019, PASP, 131, 054505

Koeln U., 2022, CDMS, https://cdms.astro.uni-koeln.de/classic/molecules

Kondo H., et al., 2021, ApJ, 912, 66

Koribalski B., Whiteoak J. B., Houghton S., 1995, PASA, 12, 20

Krabbe A., 2000, in Melugin R. K., Röser H.-P., eds, Society of Photo-Optical Instrumentation Engineers (SPIE) Conference Series Vol. 4014, Airborne Telescope Systems. pp 276–281 (arXiv:astro-ph/0004253), doi:10.1117/12.389103

Kramer M., et al., 2021, Physical Review X, 11, 041050

Kraus J. D., 1966, Radio astronomy

Kreckel K., et al., 2018, ApJL, 863, L21

Krieger N., et al., 2017, ApJ, 850, 77

Krieger N., et al., 2020, ApJ, 899, 158

Krieger N., et al., 2021, ApJL, 915, L3

Krips M., Neri R., García-Burillo S., Martín S., Combes F., Graciá-Carpio J., Eckart A., 2008, ApJ, 677, 262

Kroupa P., 2001, MNRAS, 322, 231

Kruijssen J. M. D., 2012, MNRAS, 426, 3008

Kruijssen J. M. D., Longmore S. N., 2014, MNRAS, 439, 3239

Kruijssen J. M. D., Schruba A., Hygate A. e. P. S., Hu C.-Y., Haydon D. T., Longmore S. N., 2018, MNRAS, 479, 1866

Kruijssen J. M. D., et al., 2019, Nature, 569, 519

Krumholz M. R., McKee C. F., 2005, ApJ, 630, 250

Krumholz M. R., McKee C. F., 2008, Nature, 451, 1082

Krumholz M. R., McKee C. F., Tumlinson J., 2009, ApJ, 693, 216

Krumholz M. R., Dekel A., McKee C. F., 2012, ApJ, 745, 69

Krumholz M. R., Kruijssen J. M. D., Crocker R. M., 2016, preprint, (arXiv:1605.02850)

Kulkarni S. R., Heiles C., Blitz L., 1982, ApJL, 259, L63

Kuno N., Nishiyama K., Nakai N., Sorai K., Vila-Vilaró B., Handa T., 2000, PASJ, 52, 775

Lada C. J., Lada E. A., 2003, ARA&A, 41, 57

Lada C. J., Lombardi M., Alves J. F., 2010, ApJ, 724, 687

Lada C. J., Forbrich J., Lombardi M., Alves J. F., 2012, ApJ, 745, 190

Larson R. B., 1981, MNRAS, 194, 809

Larson K. L., et al., 2016, ApJ, 825, 128

Le Fèvre O., et al., 2020, A&A, 643, A1

Lee J. C., et al., 2021, arXiv e-prints, p. arXiv:2101.02855

Leroy A. K., Walter F., Brinks E., Bigiel F., de Blok W. J. G., Madore B., Thornley M. D., 2008, AJ, 136, 2782

Leroy A. K., et al., 2009, AJ, 137, 4670

Leroy A. K., et al., 2011, ApJ, 737, 12

Leroy A. K., et al., 2013, AJ, 146, 19

Leroy A. K., et al., 2015, ApJ, 814, 83

Leroy A. K., et al., 2016, ApJ, 831, 16

Leroy A. K., et al., 2017a, ApJ, 835, 217

Leroy A. K., et al., 2017b, ApJ, 846, 71

Leroy A. K., et al., 2018, ApJ, 869, 126

Leroy A. K., et al., 2021a, arXiv e-prints, p. arXiv:2104.07665

Leroy A. K., et al., 2021b, arXiv e-prints, p. arXiv:2104.07739

Levy R. C., et al., 2021, ApJ, 912, 4

Li Q., Narayanan D., Davé R., 2019, MNRAS, 490, 1425

Liu L., Gao Y., Greve T. R., 2015, ApJ, 805, 31

Lombardi M., Alves J., Lada C. J., 2010, A&A, 519, L7

Lombardi M., Alves J., Lada C. J., 2015, A&A, 576, L1

Longmore S. N., et al., 2013, MNRAS, 429, 987

Loomis R. A., Öberg K. I., Andrews S. M., Walsh C., Czekala I., Huang J., Rosenfeld K. A., 2018, AJ, 155, 182

Mac Low M.-M., Klessen R. S., 2004, Reviews of Modern Physics, 76, 125

Madau P., Dickinson M., 2014, ARA&A, 52, 415

Marti-Vidal I., 2017, arXiv e-prints, p. arXiv:1706.00936

Martin D. C., et al., 2005, ApJL, 619, L59

Martín S., Mauersberger R., Martín-Pintado J., Henkel C., García-Burillo S., 2006, ApJS, 164, 450

Martín S., et al., 2021, A&A, 656, A46

Mathis J. S., Rumpl W., Nordsieck K. H., 1977, ApJ, 217, 425

Mauersberger R., Henkel C., Wielebinski R., Wiklind T., Reuter H. P., 1996, A&A, 305, 421

McCormick A., Veilleux S., Rupke D. S. N., 2013, ApJ, 774, 126

McKee C. F., Krumholz M. R., 2010, ApJ, 709, 308

McKee C. F., Ostriker J. P., 1977, ApJ, 218, 148

McKee C. F., Ostriker E. C., 2007, ARA&A, 45, 565

McMullin J. P., Waters B., Schiebel D., Young W., Golap K., 2007, in Shaw R. A., Hill F., Bell D. J., eds, Astronomical Society of the Pacific Conference Series Vol. 376, Astronomical Data Analysis Software and Systems XVI. p. 127

Meidt S. E., et al., 2018, ApJ, 854, 100

Meier D. S., et al., 2015, The Astrophysical Journal, 801, 63

Meijerink R., Spaans M., Israel F. P., 2007, A&A, 461, 793

Mellinger A., 2000, Sterne und Weltraum, 39, 174

Mierkiewicz E. J., Reynolds R. J., Roesler F. L., Harlander J. M., Jaehnig K. P., 2006, ApJL, 650, L63

Miller G. E., Scalo J. M., 1979, ApJS, 41, 513

Mills E. A. C., et al., 2021, ApJ, 919, 105

Molina F. Z., Glover S. C. O., Federrath C., Klessen R. S., 2012, MNRAS, 423, 2680

Motte F., et al., 2022, A&A, 662, A8

Muñoz-Mateos J. C., et al., 2015, ApJS, 219, 3

Muraoka K., et al., 2020, ApJ, 903, 94

Murphy E. J., et al., 2011, ApJ, 737, 67

Murphy E. J., et al., 2015, ApJ, 813, 118

Narayanan D., Krumholz M. R., Ostriker E. C., Hernquist L., 2012, MNRAS, 421, 3127

Neeleman M., Prochaska J. X., Ribaudo J., Lehner N., Howk J. C., Rafelski M., Kanekar N., 2016, ApJ, 818, 113

Nimmo K., et al., 2022, Nature Astronomy, 6, 393

Nyquist H., 1928, Transactions of the American Institute of Electrical Engineers, 47, 617

Oka T., Hasegawa T., Sato F., Tsuboi M., Miyazaki A., Sugimoto M., 2001, ApJ, 562, 348

Onodera S., et al., 2010, ApJL, 722, L127

Osterbrock D. E., 1989, Annals of the New York Academy of Sciences, 571, 99

Osterbrock D. E., 1993, ApJ, 404, 551

Ostriker E. C., McKee C. F., Leroy A. K., 2010, ApJ, 721, 975

Padoan P., Nordlund Å., 2002a, ApJ, 576, 870

Padoan P., Nordlund Å., 2002b, ApJ, 576, 870

Padoan P., Nordlund Å., 2011, ApJ, 730, 40

Paglione T. A. D., Yam O., Tosaki T., Jackson J. M., 2004, ApJ, 611, 835

Pan H.-A., et al., 2022, ApJ, 927, 9

Parravano A., McKee C. F., Hollenbach D. J., 2011, ApJ, 726, 27

Pellegrini E. W., Baldwin J. A., Ferland G. J., Shaw G., Heathcote S., 2009, ApJ, 693, 285

Pence W. D., 1980, ApJ, 239, 54

Peng R., Zhou S., Whiteoak J. B., Lo K. Y., Sutton E. C., 1996, ApJ, 470, 821

Persson M., 2013, PhD thesis, University of Copenhagen, Natural History Museum

Pety J., 2005, in Casoli F., Contini T., Hameury J. M., Pagani L., eds, SF2A-2005: Semaine de l'Astrophysique Francaise. p. 721

Pety J., et al., 2013, ApJ, 779, 43

Pety J., et al., 2017, A&A, 599, A98

Phuong N. T., et al., 2021, A&A, 653, L5

Pilbratt G. L., et al., 2010, A&A, 518, L1

Pineda J. L., Langer W. D., Velusamy T., Goldsmith P. F., 2013, A&A, 554, A103

Planck Collaboration et al., 2011, A&A, 536, A1

Pokhrel R., et al., 2016, MNRAS, 461, 22

Portegies Zwart S. F., McMillan S. L. W., Gieles M., 2010, ARA&A, 48, 431

Price S. D., Egan M. P., Carey S. J., Mizuno D. R., Kuchar T. A., 2001, AJ, 121, 2819

Privon G. C., et al., 2015, ApJ, 814, 39

Puschnig J., 2020, Dense Gas Toolbox - Calculate Density and Temperature from Observed Molecular Lines, doi:10.5281/zenodo.3686329

Puschnig J., et al., 2020, A&A, 644, A10

Querejeta M., 2020, MNRAS in prep

Querejeta M., et al., 2019, A&A, 625, A19

Querejeta M., et al., 2021, arXiv e-prints, p. arXiv:2109.04491

Rathborne J. M., et al., 2014, ApJL, 795, L25

Rebolledo D., Wong T., Leroy A., Koda J., Donovan Meyer J., 2012, ApJ, 757, 155

Reich W., Reich P., Fuerst E., 1990, A&AS, 83, 539

Reid M. A., Wilson C. D., 2006, ApJ, 650, 970

Renaud F., Kraljic K., Bournaud F., 2012, ApJL, 760, L16

Reynolds R. J., 1989, ApJL, 339, L29

Reynolds R. J., Roesler F. L., Scherb F., 1973, ApJ, 179, 651

Rieke G. H., Lebofsky M. J., Thompson R. I., Low F. J., Tokunaga A. T., 1980, ApJ, 238, 24

Rieke G. H., Lebofsky M. J., Walker C. E., 1988, ApJ, 325, 679

Rivilla V. M., et al., 2020, ApJL, 899, L28

Roman-Duval J., Jackson J. M., Heyer M., Rathborne J., Simon R., 2010, ApJ, 723, 492

Rosolowsky E., 2007, ApJ, 654, 240

Rosolowsky E., Leroy A., 2006, PASP, 118, 590

Rosolowsky E., Pineda J. E., Gao Y., 2011, MNRAS, 415, 1977

Rosolowsky E., et al., 2021, MNRAS, 502, 1218

Sadavoy S. I., et al., 2010, ApJ, 710, 1247

Saintonge A., Catinella B., 2022, arXiv e-prints, p. arXiv:2202.00690

Salim S., et al., 2007, ApJS, 173, 267

Salpeter E. E., 1955, ApJ, 121, 161

Sánchez-García M., García-Burillo S., Pereira-Santaella M., Colina L., Usero A., Querejeta M., Alonso-Herrero A., Fuente A., 2022, A&A, 660, A83

Sanders D. B., Mazzarella J. M., Kim D. C., Surace J. A., Soifer B. T., 2003, AJ, 126, 1607

Sandstrom K. M., et al., 2013, ApJ, 777, 5

Santoro F., et al., 2022, A&A, 658, A188

Schinnerer E., et al., 2013, ApJ, 779, 42

Schinnerer E., et al., 2019, ApJ, 887, 49

Schmidt M., 1959a, ApJ, 129, 243

Schmidt M., 1959b, ApJ, 129, 243

Schneider N., et al., 2015, A&A, 575, A79

Schneider N., et al., 2016, A&A, 587, A74

Schruba A., Leroy A. K., Walter F., Sandstrom K., Rosolowsky E., 2010, ApJ, 722, 1699

Schruba A., et al., 2011, The Astronomical Journal, 142, 37

Schruba A., Kruijssen J. M. D., Leroy A. K., 2019, ApJ, 883, 2

Schuster K. F., Kramer C., Hitschfeld M., Garcia-Burillo S., Mookerjea B., 2007, A&A, 461, 143

Semenov V. A., Kravtsov A. V., Gnedin N. Y., 2018, ApJ, 861, 4

Shimajiri Y., et al., 2017, A&A, 604, A74

Shirley Y. L., 2015, PASP, 127, 299

Shu F. H., Adams F. C., Lizano S., 1987, ARA&A, 25, 23

Silk J., 1997, in Holt S. S., Mundy L. G., eds, American Institute of Physics Conference Series Vol. 393, The Seventh Astrophysical Conference: Star formation, near and far. pp 3–14, doi:10.1063/1.52807

Snowden S. L., et al., 1997, ApJ, 485, 125

Solomon P. M., Rivolo A. R., Barrett J., Yahil A., 1987, ApJ, 319, 730

Solomon P. M., Downes D., Radford S. J. E., Barrett J. W., 1997, ApJ, 478, 144

Sorai K., Nakai N., Kuno N., Nishiyama K., Hasegawa T., 2000, PASJ, 52, 785

Sormani M. C., Barnes A. T., 2019, MNRAS, 484, 1213

Sormani M. C., Binney J., Magorrian J., 2015, MNRAS, 449, 2421

Sormani M. C., Treß R. G., Ridley M., Glover S. C. O., Klessen R. S., Binney J., Magorrian J., Smith R., 2018, MNRAS, 475, 2383

Spilker A., Kainulainen J., Orkisz J., 2021, A&A, 653, A63

Stanimirovic S., 2002, in Stanimirovic S., Altschuler D., Goldsmith P., Salter C., eds, Astronomical Society of the Pacific Conference Series Vol. 278, Single-Dish Radio Astronomy: Techniques and Applications. pp 375–396 (arXiv:astro-ph/0205329)

Stanimirovic S., Staveley-Smith L., Dickey J. M., Sault R. J., Snowden S. L., 1999, MNRAS, 302, 417

Stephens I. W., Jackson J. M., Whitaker J. S., Contreras Y., Guzmán A. E., Sanhueza P., Foster J. B., Rathborne J. M., 2016, ApJ, 824, 29

Strickland D. K., Heckman T. M., Weaver K. A., Dahlem M., 2000, AJ, 120, 2965

Strickland D. K., Heckman T. M., Weaver K. A., Hoopes C. G., Dahlem M., 2002, ApJ, 568, 689

Sturm E., et al., 2011, ApJL, 733, L16

Sun J., et al., 2018, The Astrophysical Journal, 860, 172

Sun J., et al., 2020, ApJL, 901, L8

Swings P., Rosenfeld L., 1937, ApJ, 86, 483

Tacconi L. J., et al., 2010, Nature, 463, 781

Tafalla M., Usero A., Hacar A., 2021, A&A, 646, A97

Takahira K., Shima K., Habe A., Tasker E. J., 2018, PASJ, 70, S58

Tan J. C., Beltrán M. T., Caselli P., Fontani F., Fuente A., Krumholz M. R., McKee C. F., Stolte A., 2014, Protostars and Planets VI, pp 149–172

Thompson A. R., Moran J. M., Swenson George W. J., 2017, Interferometry and Synthesis in Radio Astronomy, 3rd Edition, doi:10.1007/978-3-319-44431-4.

Tielens A. G. G. M., 2005, The Physics and Chemistry of the Interstellar Medium

Tokuda K., et al., 2020, ApJ, 896, 36

Tomczak A. R., et al., 2016, ApJ, 817, 118

Triani D. P., Sinha M., Croton D. J., Pacifici C., Dwek E., 2020, MNRAS, 493, 2490

Tully R. B., Fisher J. R., 1977, A&A, 54, 661

Turner J. L., Ho P. T. P., 1985, ApJL, 299, L77

Usero A., et al., 2015, AJ, 150, 115

Veilleux S., Rupke D. S. N., Swaters R., 2009, ApJL, 700, L149

Villaume A., Brodie J., Conroy C., Romanowsky A. J., van Dokkum P., 2017, ApJL, 850, L14

Vukićević-Karabin M., Atanacković O., 2010, Opšta astrofizika. Zavod za udžbenike - Beograd

Walter F., Brinks E., de Blok W. J. G., Bigiel F., Kennicutt Robert C. J., Thornley M. D., Leroy A., 2008, AJ, 136, 2563

Walter F., et al., 2016, ApJ, 833, 67

Walter F., et al., 2017, ApJ, 835, 265

Walter F., et al., 2020, ApJ, 902, 111

Ward R. L., Wadsley J., Sills A., 2014, MNRAS, 445, 1575

Watson A. M., et al., 1996, AJ, 112, 534

Werner M. W., et al., 2004, ApJS, 154, 1

Westmoquette M. S., Smith L. J., Gallagher J. S. I., 2011, MNRAS, 414, 3719

Wheelock S. L., et al., 1994, IRAS sky survey atlas: Explanatory supplement

Whitmore B. C., 2003, in Livio M., Noll K., Stiavelli M., eds, Vol. 14, A Decade of Hubble Space Telescope Science. pp 153–178

Whitworth A. P., Jaffa S. E., 2018, A&A, 611, A20

Williams D. A., Viti S., 2013, Observational Molecular Astronomy

Williams J. P., Blitz L., McKee C. F., 2000, Protostars and Planets IV, p. 97

Williams G. M., Peretto N., Avison A., Duarte-Cabral A., Fuller G. A., 2018, preprint, (arXiv:1801.07253)

Wong T., Blitz L., 2002, ApJ, 569, 157

Wu J., Evans Neal J. I., Gao Y., Solomon P. M., Shirley Y. L., Vanden Bout P. A., 2005, ApJL, 635, L173

Wu J., Evans Neal J. I., Shirley Y. L., Knez C., 2010, ApJS, 188, 313

Wyder T. K., et al., 2009, ApJ, 696, 1834

Zinnecker H., Yorke H. W., 2007, ARA&A, 45, 481

Zschaechner L. K., et al., 2018, ApJ, 867, 111

den Brok J. S., et al., 2021, MNRAS, 504, 3221

den Brok J. S., et al., 2022a, arXiv e-prints, p. arXiv:2201.05165

den Brok J. S., et al., 2022b, A&A, 662, A89

van de Hulst H. C., 1945, Nederlandsch Tijdschrift voor Natuurkunde, 11, 210

van der Tak F. F. S., Black J. H., Schöier F. L., Jansen D. J., van Dishoeck E. F., 2007, A&A, 468, 627

Appendix

APPENDIX A

Dense molecular gas properties on 100 pc scales across the disc of NGC 3627

The paper Bešlić et al. MNRAS (2021), 506, 963-988 is reproduced below in its original form with permission by MNRAS.

Monthly Notices of the ROYAL ASTRONOMICAL SOCIETY

MNRAS **506,** 963–988 (2021) https://doi.org/10.1093/mnras/stab1776
Advance Access publication 2021 June 30

Dense molecular gas properties on 100 pc scales across the disc of NGC 3627

I. Bešlić [1★] A. T. Barnes,[1★] F. Bigiel,[1★] J. Puschnig [1] J. Pety,[2,3] C. Herrera Contreras,[2] A. K. Leroy,[4] A. Usero,[5] E. Schinnerer,[6] S. E. Meidt,[7] E. Emsellem,[8,9] A. Hughes [10,11] C. Faesi,[6,12] K. Kreckel [13] F. M. C. Belfiore [14] M. Chevance [13] J. S. den Brok [1] C. Eibensteiner,[1] S. C. O. Glover [15] K. Grasha [16,17] M. J. Jimenez-Donaire,[5] R. S. Klessen [15,18] J. M. D. Kruijssen [13] D. Liu,[6] I. Pessa,[6] M. Querejeta,[5] E. Rosolowsky [19] T. Saito,[6] F. Santoro,[6] A. Schruba,[20] M. C. Sormani [15] and T. G. Williams [6]

Affiliations are listed at the end of the paper

Accepted 2021 June 9. Received 2021 June 7; in original form 2020 December 22

ABSTRACT

It is still poorly constrained how the densest phase of the interstellar medium varies across galactic environment. A large observing time is required to recover significant emission from dense molecular gas at high spatial resolution, and to cover a large dynamic range of extragalactic disc environments. We present new NOrthern Extended Millimeter Array (NOEMA) observations of a range of high critical density molecular tracers (HCN, HNC, HCO^+) and CO isotopologues (^{13}CO, $C^{18}O$) towards the nearby (11.3 Mpc) strongly barred galaxy NGC 3627. These observations represent the current highest angular resolution (1.85 arcsec; 100 pc) map of dense gas tracers across a disc of a nearby spiral galaxy, which we use here to assess the properties of the dense molecular gas, and their variation as a function of galactocentric radius, molecular gas, and star formation. We find that the HCN(1–0)/CO(2–1) integrated intensity ratio does not correlate with the amount of recent star formation. Instead, the HCN(1–0)/CO(2–1) ratio depends on the galactic environment, with differences between the galaxy centre, bar, and bar-end regions. The dense gas in the central 600 pc appears to produce stars less efficiently despite containing a higher fraction of dense molecular gas than the bar ends where the star formation is enhanced. In assessing the dynamics of the dense gas, we find the HCN(1–0) and HCO^+(1–0) emission lines showing multiple components towards regions in the bar ends that correspond to previously identified features in CO emission. These features are cospatial with peaks of Hα emission, which highlights that the complex dynamics of this bar-end region could be linked to local enhancements in the star formation.

Key words: stars: formation – ISM: clouds – ISM: molecules – galaxies: evolution – galaxies: ISM – galaxies: star formation.

1 INTRODUCTION

Star formation occurs in the coldest, densest parts of molecular clouds. This is observed within star-forming regions in the Milky Way, where it has been shown that the star formation rate (SFR) surface density (Σ_{SFR}) of individual clouds is proportional to the dense gas mass surface density (Lada & Lada 2003; Wu et al. 2005, 2010; Heiderman et al. 2010; Lada, Lombardi & Alves 2010; Lada et al. 2012; André et al. 2014; Evans, Heiderman & Vutisalchavakul 2014). However, to study individual molecular clouds in other galaxies, extragalactic surveys have historically focused on the brightest observable molecular emission lines: the low-J transitions of ^{12}CO, which for simplicity we will refer to as CO. These transitions are sensitive to the total molecular gas mass, but cannot discriminate the gas mass in the densest regime. In order to probe the latter, less abundant molecules with transitions at higher critical densities (n_{crit}) are needed. We refer to the definition of critical density from Shirley (2015). In this work, we will also make use of the most effective critical density defined in Leroy et al. (2017b) (shortly the effective critical density, hereafter $n_{eff,\,crit}$). The effective critical density depends on a transition, kinetic temperature, and optical depth. Molecules such as HCN, HNC, and HCO^+ have higher dipole moments than CO and its isotopologues and hence higher $n_{eff,\,crit}$. Therefore, emission from these molecules has been used to probe the amount of denser molecular gas, which is more closely related to star formation than the lower density molecular medium traced by low-J CO emission. The ratios between these lines and CO(1–0), in particular HCN/CO(1–0), are assumed to be a good proxy for the dense gas fraction.

In the seminal study by Gao & Solomon (2004a,b), they obtained galaxy-integrated measurements of HCN and total infrared luminosities (TIR) to determine the dense gas mass and SFR, respectively. They found a linear relation between the HCN and TIR luminosities, therefore HCN(1–0) emission appears to be directly correlated to the level of star formation activity. Gao & Solomon (2004a,b) and other studies (Gao et al. 2007; Graciá-Carpio, García-Burillo &

★ E-mail: ibeslic@uni-bonn.de(I.B); abarnes@uni-bonn.de(ATB); bigiel@uni-bonn.de(FB)

Planesas 2008; Krips et al. 2008; Juneau et al. 2009; García-Burillo et al. 2012; Privon et al. 2015) investigated whole galaxies and their centres. These studies were focusing on the relation on global scales, i.e. averaging over different regions with different physical characteristics. However, studies of molecular lines other than CO within extragalactic sources are difficult. The emission of these molecules (HCN, HCO^+, HNC, etc.) is typically very weak (e.g. HCN is ∼20–30 times weaker than CO; Gao & Solomon 2004b), and for their detection more observing time is required.

Some other studies have investigated dense gas (HCN and HCO^+) in giant molecular associations in nearby galaxies: in M31 (Brouillet et al. 2005), M33 (Buchbender et al. 2013), and in the outer spiral arm of M51 (Chen et al. 2017; Querejeta et al. 2019). However, in order to understand the physics in galaxy discs, we need to resolve these in regions of faint molecular emission as well.

Over the last decade, many studies have focused on observing resolved galaxy discs in faint molecular lines. Kepley et al. (2014) mapped these lines in the starburst galaxy M82 using the Green Bank Telescope (GBT). These authors found that the HCN and HCO^+ emission correlates with star formation and more diffuse molecular gas. Usero et al. (2015) targeted HCN emission across 60 regions within 30 nearby galaxies at kiloparsec resolution using the Institut de Radio Astronomie Millimetrique (IRAM) 30-m telescope. This study investigated and found for the first time systematic variations in the dense gas fraction ($f_{\rm dense} = M_{\rm dense}/M_{\rm mol}$) traced by HCN/CO(1–0): higher values are seen in the centres of galaxies than in their outer parts. They also conclude that the star formation efficiency of dense molecular gas ($\rm SFE_{dense} = SFR/M_{dense}$) traced by the TIR/HCN luminosity ratio is lower in the centres of galaxies than in the outer disc.

The recent EMIR Multiline Probe of the ISM Regulating Galaxy Evolution (EMPIRE) IRAM 30-m EMIR survey was the first survey to obtain a sensitive wide-area mapping of so-called denser molecular gas tracers (e.g. HCN) across the discs of nine star-forming galaxies at 30 arcsec resolution (∼1–2 kpc; Bigiel et al. 2016; Jiménez-Donaire et al. 2019). Similarly, Bigiel et al. (2016) found that $\rm SFE_{dense}$ strongly depends on local environment in M51. Moreover, Jiménez-Donaire et al. (2019) showed that these variations are present in the full sample of nine galaxy discs. Gallagher et al. (2018a) mapped high critical density molecules (HCN, HCO^+, HNC, CS) and CO isotopologues (^{13}CO, C^{18}O) across four nearby galaxies at 8 arcsec or a few hundred parsec resolution using the Atacama Large Millimeter/submillimeter Array (ALMA). This study looked into the connection between the dense gas fraction, SFR, and the local environment. An important result from the above-mentioned studies was that while the fraction of denser gas increases towards the centres of galaxies, its efficiency to form stars is typically greatly reduced (Usero et al. 2015; Bigiel et al. 2016; Gallagher et al. 2018a; Jiménez-Donaire et al. 2019; Jiang et al. 2020). This result agrees well with studies in the Milky Way where it appears that the dense gas fraction and the star formation efficiency of dense gas within the Central Molecular Zone are higher and lower, respectively, compared to local Milky Way clouds (e.g. Longmore et al. 2013; Kruijssen & Longmore 2014; Barnes et al. 2017). The trend that has been seen between the TIR/HCN and HCN/CO in galactic centres, as shown in theoretical work by Kruijssen et al. (2014), and found in observations (e.g. Jones et al. 2012; Longmore et al. 2013; Usero et al. 2015), supports the idea that there is no absolute density threshold for star formation and that the overdensity relative to the background is important (e.g. Federrath & Klessen 2012). For example, going towards the centre of the galaxy, more dense gas is present, which increases the HCN/CO ratio, and, hence, it is expected to also form stars at a higher efficiency. However, in the centre, the HCN-emitting gas is not tracing the relative overdensities, but rather the bulk dense gas, which is mostly not star forming. The use of the HCN/CO ratio as a tracer for dense, star-forming gas in these regimes is then problematic (e.g. Bigiel et al. 2016; Jiménez-Donaire et al. 2019).

Together, the studies by Usero et al. (2015), Bigiel et al. (2016), Gallagher et al. (2018a), Jiménez-Donaire et al. (2019), and Jiang et al. (2020) provide the first resolved view of dense molecular gas in galaxy discs. However, the resolution that they achieve in the extragalactic studies is still only ∼500 pc to 2 kpc. This is enough to resolve galaxy discs and distinguish central and disc regions, but it is still much bigger than the size of an individual molecular cloud (e.g. ∼50–100 pc). As a result, observations like EMPIRE mix together many clouds in distinct evolutionary states (the typical distance between independent regions with distinct evolutionary states is ∼100–200 pc; see e.g. Kruijssen et al. 2019; Chevance et al. 2020; Kim et al. 2021) and physical environments (Hughes et al. 2013; Colombo et al. 2014). Recent decades and years have seen rapid growth in observations of CO (Heyer & Dame 2015), which have been undertaken with single-dish telescopes (e.g. Yamaguchi et al. 1999; Dame, Hartmann & Thaddeus 2001; Moriguchi et al. 2001; Regan et al. 2001; García-Burillo et al. 2003; Helfer et al. 2003; Mizuno & Fukui 2004; Gratier et al. 2012; Burton et al. 2013; Barnes et al. 2015), as well as with the current generation of interferometer telescopes [e.g. NOrthern Extended Millimeter Array (NOEMA) and ALMA; e.g. Engargiola et al. 2003; Rosolowsky et al. 2003, 2021; Rosolowsky 2007; Sheth et al. 2008; Hirota et al. 2011; Schinnerer et al. 2013; Schruba et al. 2017; Egusa et al. 2018; Faesi, Lada & Forbrich 2018; Sun et al. 2018; Maeda et al. 2020; Leroy et al. 2021b]. The big step forward in terms of sensitivity, resolution, and sample size is the current Physics at High Angular-resolution in Nearby GalaxieS with ALMA (PHANGS-ALMA) survey. The PHANGS-ALMA survey maps CO(2–1) emission across a sample of 74 nearby star-forming galaxies with resolution high enough to detect individual giant molecular clouds (GMCs) across galaxies' discs (PI: E. Schinnerer; Leroy et al. 2021b; Rosolowsky et al. 2021).

The next logical step is to also map the denser gas content of individual molecular clouds. The single-dish studies have provided an insight into how the dense molecular gas is distributed in nearby galaxies (Kepley et al. 2018; Viaene, Forbrich & Fritz 2018; Watanabe et al. 2019). Moreover, despite the difficulties attaining sensitivity at high angular resolution, several works have begun to map high critical density lines down to cloud scales in nearby galaxies using interferometers (e.g. Viti et al. 2014; Murphy et al. 2015; Chen et al. 2017; Walter et al. 2017; Gallagher et al. 2018b; Querejeta et al. 2019). Observations of high critical density molecules at a high spatial resolution allow us to measure dense molecular gas as a function of cloud surface density, dynamical state, and evolutionary state. Several studies have already taken pioneering steps in this direction, mapping HCN and HCO^+ emission at high physical resolution, and demonstrated the full potential of such observations despite the limited field of view, i.e. in chemical modelling (Viti et al. 2014), studying the outflows (Walter et al. 2017), investigating how the $\rm SFE_{dense}$ varies at 100 pc scales (Querejeta et al. 2019). Gallagher et al. (2018b) combined high-resolution CO measurements with lower resolution EMPIRE and ALMA (Atacama Compact Array – ACA) HCN maps to connect cloud properties to the dense gas fraction. However, a high resolution, sensitive, resolved HCN and HCO^+ map across a large portion of a galaxy disc is still lacking within the literature.

In this work, we present new observations using the NOEMA interferometer targeting one galaxy: NGC 3627 (source information

Table 1. Source information.

Property	Value
Name	NGC 3627 (Messier 66)
Hubble type[a]	SABb
Centre RA (J2000)	$11^{h}20^{m}14\overset{s}{.}867$
Centre Dec. (J2000)	$12^{\circ}59'34\overset{''}{.}05$
Inclination, i (°)[a]	62
Position angle, PA (°)[a]	173
Distance, D (Mpc)[b]	11.3
r_{25} (arcmin)[b, c]	5.1
$V_{\rm sys,\,hel}$ (km s^{-1})[d]	744
Metallicity ($12 + \log$(O/H))[e]	8.328 ± 0.004
$\langle\Sigma_{\rm SFR}\rangle$ ($M_\odot$ yr^{-1} kpc^{-2})[f]	7.7×10^{-3}
$\log_{10}(M_*)$ ($M_\odot$)[g]	10.5

[a]Morphology taken from the NASA Extragalactic Database (NED).
[b]Distance adopted from Anand et al. (2021).
[c]Radius of the B-band 25th mag isophote.
[d]Systemic velocity from Casasola et al. (2011).
[e]Metallicity calibration taken from Thuan & Izotov (2005) and metallicity value from Kreckel et al. (2019).
[f]Average SFR surface density inside $0.75\,r_{25}$, taken from the PHANGS-ALMA survey paper Leroy et al.(2021b)).
[g]Integrated stellar mass based on 3.6 μm emission, taken from the PHANGS-ALMA survey paper (Leroy et al.2021b).

Table 2. Properties of the observed molecular lines. We tabulate the molecular transition, rest frequency, and the effective critical density (Leroy et al. 2017a) taken at a temperature of 25 K for lines studied here.

Line	$\nu_{\rm rest}$ (GHz)	$n_{\rm eff,\,crit}$ (cm^{-3})
^{12}CO(2–1)[a,b]	230.53	1×10^3
^{13}CO(1–0)[a,c]	110.20	8×10^2
C^{18}O(1–0)[a,c]	109.78	8×10^2
HCO$^+$(1–0)[a,d]	89.19	4×10^4
HCN(1–0)[a,d]	88.63	2×10^5
HNC(1–0)[a,d]	90.66	1×10^5

[a]Calculated from the Leiden Atomic and Molecular Database (LAMDA; Schöier et al. 2005; van der Tak et al. 2007).
[b]The opacity of 100 adopted for this line (assuming the CO(1–0) is optically thick; Leroy et al. 2017a).
[c]We assume a fixed optical depth of 0.1.
[d]Here we assume a fixed optical depth of 1.

is listed in Table 1). This survey currently represents the highest resolution observations (1.85 arcsec = 102 pc) across a large part of a galaxy disc using high critical density molecules (line properties are given in Table 2). We use these observations to study the physical conditions of the denser gas at the scale of individual molecular clouds, to examine how the dense molecular gas is distributed across the galaxy's disc at these scales, and to study various density-sensitive line ratios. We investigate how dense molecular gas is linked to star formation at cloud scales. We also study various line ratios: the observed molecular lines relative to CO(2–1) and the line ratios among the high critical density molecules (HCN, HNC, and HCO$^+$). Investigating line intensities relative to CO(2–1) emission, in particular HCN/CO(2–1), we are able to determine where the more dense molecular gas is present relative to the molecular gas content and how it is affected by the environment and star formation. Moreover, by studying the line ratios among the high critical density molecular lines such as HCN, HNC, and HCO$^+$, we access the physical and chemical processes that set the cloud properties.

Table 3. NOEMA observation parameters.

Line	Beam (arcsec)	Beam (pc)	PA (°)	Noise[a] (mK)
HCN(1–0)	1.87×1.04	102.4×57.0	26	51
HCO$^+$(1–0)	1.86×1.03	101.8×56.4	27	54
HNC(1–0)	1.85×1.05	101.2×57.5	22	54
C^{18}O(1–0)	1.52×0.84	83.2×46	27	78
^{13}CO(1–0)	1.52×0.84	83.2×46	27	87

[a]Evaluated at the mosaic phase centre, which is close to the galaxy centre (the noise steeply increases at the mosaic edges after correction for primary beam attenuation), at a spectral resolution of 5 km s^{-1}.

NGC 3627 is a nearby, star-forming galaxy with a strong bar, part of the M66 group (Leo Triplet) (Garcia 1993). It is also classified as low-ionization nuclear emission-line region (LINER)/type 2 Seyfert galaxy (Ho, Filippenko & Sargent 1997; Filho, Barthel & Ho 2000). Watanabe et al. (2019) observed three regions in NGC 3627 (the centre, a bar end, and a spiral arm) in 3-mm band using IRAM 30-m and Nobeyama 45-m telescopes. They detected ∼10 molecular species in each region, finding that the chemical composition is similar among these regions. NGC 3627 has been mapped in HCN as part of the EMPIRE survey using the IRAM 30-m telescope (Jiménez-Donaire et al. 2019) and by ALMA (Gallagher et al. 2018a). Murphy et al. (2015) found a spatial offset between the peak intensity of HCN and HCO$^+$ and tracers of recent star formation in the centre and the bar ends in NGC 3627. This study also found that the dynamical state of the gas plays a more important role in star formation than the abundance of the dense gas. Beuther et al. (2017) investigated dynamics in NGC 3627 bar ends, finding multiple velocity components in CO(2–1) that originate from orbits coming from the bar and the spiral arm.

The paper is organized as follows. In Section 2, we outline the reduction and imaging of the NOEMA observations. We summarize the ancillary observations used throughout this work in Section 2.3. In Section 3, we present the moment maps for each line, and discuss trends of the integrated intensity as a function of radius, SFR surface density, and molecular gas surface density, as well as dense gas velocity dispersion and various line ratios. In Section 4, the results of this work are discussed in the framework of our current understanding of dense molecular gas properties and star formation. Finally, in Section 5, we summarize the findings of this work.

2 IRAM OBSERVATIONS, ANCILLARY DATA, AND THE PRODUCTION OF INTEGRATED INTENSITY MAPS

2.1 IRAM observations

The observations were taken at 3 mm using both the IRAM NOEMA interferometer at Plateau de Bure and the IRAM 30-m single dish. The 3 mm continuum emission was not detected. Since a multiplicative interferometer filters out the low spatial frequencies, i.e. spatially extended emission, we used the IRAM 30-m observations to recover the low spatial frequency ('short- and zero-spacing') information missed by NOEMA at a depth that matches the interferometric data. In the following sections, we describe the observing strategy, calibration, joint imaging, and deconvolution processes. Table 3 summarizes the parameters of the interferometric observations.

2.1.1 *Interferometric observations and calibration*

Interferometric measurements of NGC 3627 were obtained with NOEMA. The sideband separating receivers were tuned to observe from 86.9 to 94.6 GHz (lower sideband) and from 102.4 to 110.1 GHz (upper sideband). The POLYFIX correlator yielded a total bandwidth of 2×7.7 GHz per polarization at a spectral channel spacing of 2 MHz. Each intermediate-frequency baseband was further split into up to 16×64 MHz chunks of high spectral channel spacing. These chunks were centred around potential lines inside the lower and upper sidebands. This yielded spectra with a 62.5 kHz channel spacing that we further smoothed to reach three different spectral resolutions: 5, 10, and 20 km s^{-1}. In short, the frequency set-up was chosen to simultaneously cover the J = 1–0 lines of ^{13}CO and C^{18}O in the upper sideband, and the J = 1–0 lines of HCO$^+$, HCN, and HNC in the lower sideband. Their frequencies are listed in Table 2.

We observed a mosaic of six pointings aligned along the bar of NGC 3627 at a position angle (PA) of -26°. The neighbouring pointings were separated by 22.5 arcsec, which is half the primary beam size at 110 GHz. The mosaic thus covers a roughly rectangular field of view of about 2.7×0.9 arcmin^2 ($\approx 1.5 \times 0.5$ kpc^2). These measurements were carried out with eight or nine antennas in the C and A configurations (baselines from 15 to 750 m) from 2018 February to May. This amounts to 30.5 h of telescope time (12 h in C and 18.5 h in A configurations). The on-source time is equal to 8.8 h with a nine-antenna array. During the observations, the typical precipitable water vapour ranged from 1 to 3 mm in A configuration and 3 to 8 mm in C configuration. The typical system temperature was between 70 and 150 K, depending on the weather.

We used the standard algorithms implemented in the GILDAS/CLICsoftware to calibrate the NOEMA data.[1] The radio-frequency bandpass was calibrated by observing the bright quasars 3C 84 (∼14 Jy), 3C 279 (∼15 Jy), and 0851+202 (∼5 Jy). Phase and amplitude temporal variations were calibrated by fitting spline polynomials through regular measurements of two nearby quasars (1222+216 with a flux of about 2.0 Jy at 17.°5 distance, and 1116+128 with a flux of about 0.5 Jy at 0.°5 distance). One of the NOEMA secondary flux calibrators (either MWC 349 or LKHα 101) was observed during each track, which allowed us to improve the accuracy of the absolute flux scale of the interferometric data to ∼10 per cent.

2.1.2 *Joint imaging and deconvolution of the interferometric and single-dish data*

The single-dish observations were taken with the IRAM 30-m telescope as part of the EMPIRE large program (PI: F. Bigiel) from 2014 December to 2016 December. Jiménez-Donaire et al. (2019) describe in detail the observations and data reduction.

Following Rodriguez-Fernandez, Pety & Gueth (2008), the GILDAS/MAPPING software and the single-dish data from the IRAM 30-m were used to create the short-spacing visibilities not sampled by NOEMA using the UV_SHORT task. In short, the 30-m data cubes were first resampled around the redshifted frequencies observed with NOEMA and reprojected to the NOEMA phase centre. The data cubes were deconvolved from the IRAM 30-m beam in the Fourier plane, and corrected for the NOEMA primary beam response in the image plane. After a last Fourier transform, pseudo-visibilities were sampled between 0 and 15 m, the difference between the diameters of the IRAM 30-m and the 15-m NOEMA antennas. These visibilities were then merged with the interferometric observations.

Each mosaic field was imaged and a dirty mosaic was built combining those fields in the following optimal way in terms of signal-to-noise ratio (S/N; Pety & Rodríguez-Fernández 2010). The dirty cube is corrected for primary beam attenuation, which induces a spatially inhomogeneous noise level. In particular, noise strongly increases near the edges of the field of view. To limit this effect, both the primary beams and the resulting dirty mosaics are truncated. The standard level of truncation is set at 20 per cent of the maximum in GILDAS/MAPPING. The dirty image is deconvolved using the standard Högbom CLEAN algorithm. CLEAN components were only searched for inside a mask produced from the EMPIRE ^{12}CO(1–0) cube obtained at the IRAM 30-m telescope. Pixels within each channel with an S/N of the CO(1–0) line larger than 3 are included in this three-dimensional mask. This gives a shallow mask that loosely follows the galaxy velocity pattern as the angular resolution is 27 arcsec and the typical sensitivity is good (∼10 mK). The resulting data cubes are then scaled from Jy beam^{-1} to main beam brightness temperature (T_b) scale using the synthesized beam size (see Table 3). The channel width of the final data cubes is 5 km s^{-1}. The resulting beam size and corresponding noise values of the final combined maps used throughout this work are presented in Table 3.

2.2 The production of integrated intensity maps

We produce integrated intensity maps from masked spectral cubes for each line. The mask is based on the ALMA CO(2–1) cube (resolution 1.5 arcsec), because we expect to detect HCN emission only in regions of the galaxy with detected CO emission (Jiménez-Donaire et al. 2019; Querejeta et al. 2019). We convolve all NOEMA data cubes to a common working resolution of 1.95×1.95 arcsec$^2 \times$ 5 km s^{-1} (1.95 arcsec ≈ 102 pc). The ALMA CO(2–1) cube (see the following section for more details) has been spectrally and spatially smoothed and regridded to match the NOEMA observations.

We make use of an expanding masking technique in order to create masks for our data set (Pety et al. 2013). To construct the mask, we calculate the three-dimensional noise cube from signal-free parts of the spectrum. Then we define an initial mask where we select all pixels with S/N higher than 4 over at least two neighbouring channels. The mask is then expanded to cover all the pixels defined by a lower 2 S/N mask (Rosolowsky & Leroy 2006).

We apply the CO(2–1) mask to all of our line data cubes, and we determine the integrated intensity maps by summing intensities along the velocity axis for all lines of sight and multiplying by the channel width ($\Delta\upsilon = 5$ km s^{-1}). We construct a two-dimensional noise map ($\Delta_{\rm rms}$) based on the signal-free parts of each spectrum. Then we estimate the uncertainty in the integrated intensity by scaling this value by the channel width $\Delta\upsilon$ and the square root of the number of signal channels N:

$$\Delta_{\rm I} = \Delta_{\rm rms} \Delta\upsilon \sqrt{N}. \quad (1)$$

The S/N is then calculated by dividing the integrated intensity map by this uncertainty map.

2.3 Ancillary data

Throughout this work, we make use of a set of ancillary observations to determine the molecular gas and SFR surface densities. These are summarized in this section.

[1]See http://www.iram.fr/IRAMFR/GILDAS for more information on the GILDAS software (Pety 2005).

2.3.1 *PHANGS-ALMA CO(2–1)*

As a tracer of the molecular gas surface density in NGC 3627, we make use of CO(2–1) molecular line observations obtained with the ALMA interferometer. These were performed as part of the PHANGS-ALMA survey (PI: E. Schinnerer; Leroy et al. 2021b). Both 12-m array, 7-m array and the total power antennae (ACA) were used for the mosaic observations, therefore full spatial information is recovered for the whole CO disc of NGC 3627. The interferometric data were calibrated with the ALMA calibration pipelines and imaged with the PHANGS-ALMA pipeline (Leroy et al. 2021a). The total power data were calibrated following the method presented by Herrera et al. (2020). Then, interferometric and total power data were aligned, combined with the CASA feather task, and post-processed to T_b cubes using the PHANGS-ALMA pipeline. Moment maps were also generated with this pipeline. The data we used in this work are from the internal data release version 3.4 processed with the PHANGS-ALMA pipeline version 1. We refer the reader to Leroy et al. (2021b) for more details about the data processing. Imaging was done using CASA version 5.4.0. After calibration and imaging, the data cube was convolved to produce a round beam. The typical rms noise in brightness temperature units is $\sim$0.17 K per 2.5 km s^{-1} channel (see also Schinnerer et al. 2019). In our work, we use a CO(2–1) data cube convolved to 1.95 arcsec resolution with the channel width of 5 km s^{-1}.

2.3.2 *PHANGS-MUSE Hα data*

We determine the SFR in NGC 3627 from the 1.5 arcsec Hα map observed with the Multi-Unit Spectroscopic Explorer (MUSE)/Very Large Telescope (VLT). These observations were performed as part of the PHANGS-MUSE survey. We make use of data from internal release version 2.0 (PI: E. Schinnerer; see Emsellem et al., in preparation, for full details of data reduction). To estimate the SFR at each pixel, we make use of the MUSE extinction-corrected Hα map at 1.95 arcsec resolution. The extinction is calculated using the measured Balmer decrement assuming case B recombination, i.e. an intrinsic Hα/Hβ ratio of 2.86, which corresponds to a temperature of 10^4 K and electron density of 100 cm^{-3} (Osterbrock 1993; Domínguez et al. 2013). The recombination coefficients are robust to realistic changes in temperature and density (Osterbrock 1989). We make use of a Calzetti et al. (2000) extinction curve, and for the extinction-corrected map, only Hα and Hβ with an S/N better than 15 are used, whereas the values below this threshold are masked (see Faesi et al., in preparation, for full details on the extinction correction).

In addition to being produced in the nebulae ionized by massive young stars, Hα photons can originate from a wide range of other ionizing sources: gas ionized by an active galactic nucleus (AGN), older stellar populations, planetary nebulae (PNe), and supernovae. Thus simply adding up all Hα emission could overestimate the SFR and therefore bias our results. In order to ensure that we only make use of the Hα emission associated with star formation, we first match the H II region catalogue of Santoro et al. (in preparation), which uses two algorithms for finding spatially resolved (HIIPHOT; Thilker, Braun & Walterbos 2000) and point-like H II regions (DAOSTARFINDER; Stetson 1987) to isolate Hα emission associated with massive star formation. Then we mask our Hα map. However, this is not enough, since Hα photons within H II regions can still in principle originate from sources other than star formation. We further apply a Baldwin–Phillips–Terlevich (BPT; Baldwin, Phillips & Terlevich 1981) cut with line luminosity (in units of solar luminosity – $L_\odot$) ratio thresholds of log[N II]/Hα < 0 and log[O II]/Hβ < -0.09 (Baldwin et al. 1981; Kewley et al. 2001; Kauffmann et al. 2003). With these criteria, we remove all the pixels within the H II regions coming from ionizing sources other than the star-forming ones. All sightlines that do not satisfy these criteria are treated as a not a number (NaN). The H II mask and the BPT cut remove $\sim$40 per cent of the total Hα flux from the initial Hα map.

This map is then converted to the SFR surface density, $\Sigma_{\rm SFR}$, following Calzetti et al. (2007),

$$\Sigma_{\rm SFR} = \frac{10^{-41.27}(3.08 \times 10^{21})^2 S_{\rm H\alpha} 4\pi}{\Omega}, \quad (2)$$

where Ω is the pixel angular area in steradian (sr), $S_{\rm H\alpha}$ is the Hα flux per pixel in units of erg s^{-1} cm^{-2}, and $(3.08 \times 10^{21})^2$ is the kpc^2 to cm^2 scaling factor. The factor of 5.37×10^{-42} has been calculated with assumptions that the Hα has already been corrected for dust extinction, and a fully populated Kroupa initial mass function (IMF; Kroupa 2001) taken over the range of stellar masses 0.1–100 M$_\odot$ (Murphy et al. 2011; Kennicutt & Evans 2012). The use of Hα emission provides an almost instantaneous measure of the SFR, tracing activity over the past $\sim$0–10 Myr (see Kennicutt & Evans 2012).

We note here several issues related to the conversions of Hα emission to SFR, which are particularly relevant when assessing the SFR over small spatial scales (e.g. 100 pc scales). First, the high sampling rate at high resolution, can return regions with a low SFR ($\Sigma_{\rm SFR} < 10^{-3}$ M$_\odot$ yr^{-1} kpc^{-2}), within which the IMF can become poorly sampled. The conversion from Hα emission that assumes a fully sampled IMF may then under- or overestimate the SFR (e.g. Lee et al. 2009; Querejeta et al. 2019). The IMF can be poorly sampled on smaller spatial scales where we probe either lower mass clusters or lower SFRs, which can cause some stochastic variation in the calculated SFR (Kennicutt & Evans 2012). Secondly, the Hα line is subject to systematic uncertainties from dust attenuation and excitation variations in galaxies. Thirdly, the Hα emission relies on the production of ultraviolet (UV) photons from massive (>10 M$_\odot$) stars, which ionize the surrounding medium. Regions containing exclusively lower mass stars or which are well mixed with the diffuse ionized gas are, therefore, not seen in Hα emission, and not accounted for in our measurement of the SFR.

To estimate how much star formation is not traced by our extinction-corrected Hα emission due to extinction, we compare to SFR estimates from a combination of far-ultraviolet (FUV) emission and mid-infrared (mid-IR) emission. For that purpose, we use the $\Sigma_{\rm SFR}$ map from Leroy et al. (2019). We use the $\Sigma_{\rm SFR}$ map determined from FUV + 22 μm and convert to SFR by multiplying each value by the projected pixel surface area (0.075 kpc^2 for a 5 × 5 arcsec^2 pixel). We compare values coming within the radius of $\sim$1 kpc from the centre of NGC 3627, and from the rest of the mapped region. For the central region, we measure a SFR of $\sim$0.016 M$_\odot$ yr^{-1} from the extinction-corrected Hα emission and $\sim$0.286 M$_\odot$ yr^{-1} from FUV + 22 μm. For the rest of the NGC 3627, the SFR traced by the extinction-corrected Hα is $\sim$1.27 M$_\odot$ yr^{-1}, whereas the SFR traced by FUV + 22 μm is $\sim$1.55 M$_\odot$ yr^{-1}. The large difference in SFR from the centre of NGC 3627 is due to the fact that Hα emission associated with the AGN has been removed in the map used here, where it remains within the FUV + 22 μm SFR estimate. Whereas, in the rest of the galaxy, where both the FUV + 22 μm and Hα emission are expected to better trace the star formation, we estimate that they are in agreement (i.e. within 17 per cent). The small difference could be due to the high obscuration of the Hα emission from deeply embedded star-forming regions, not corrected for by the

Balmer decrement extinction correction, which then otherwise emit at longer wavelengths (i.e. as seen at 24 μm; e.g. see Kennicutt et al. 2009; Kim et al. 2021).

3 RESULTS

3.1 Integrated intensity maps

Fig. 1 shows the ancillary data (first row) towards NGC 3627 (Section 2.3) and the integrated intensity maps (second row) for HCN, ^{13}CO, and HCO$^+$. We show the remainder of the detected lines, HNC and C^{18}O, in the bottom row of Fig. 1. The overlaid contours in the top row show the 3σ, 5σ, and 10σ S/N of HCN emission. The median uncertainty of the HCN integrated intensity across the mapped region is 2 K km s^{-1}. The corresponding 3σ sensitivity threshold for HCN is then 6 K km s^{-1}, which, assuming a CO(1–0)/HCN ratio of 30 (Gao & Solomon 2004b) and a CO(1–0)-to-H$_2$ conversion factor of 1.2 M$_\odot$ (K km s^{-1} pc^{-2})$^{-1}$ calculated for NGC 3627 (Bolatto, Wolfire & Leroy 2013; Sandstrom et al. 2013), implies a mass sensitivity of $\sim$216 M$_\odot$ pc^{-2}.

In Fig. 2, we show the fraction of the total observed area that has significant detections from each of the observed molecular lines as a function of their effective critical density listed in Table 2. This area includes positions within the mosaic that have an integrated intensity value higher than three times the associated uncertainty (ranges for one and ten times the uncertainty are shown as error bars). In general, we find that the emission of high critical density lines is much more spatially compact than the CO(2–1) emission. The isotopologues of CO have a similar effective critical density, yet exhibit comparable coverage to the higher critical density lines. This can naturally be explained by the lower abundances of the CO isotopologues relative to ^{12}CO, which causes weaker line emission that falls below our detection limit. Of the observed lines, we see that the ^{13}CO line is the brightest and most spatially extended, whereas C^{18}O is the faintest and most compact (see Fig. 1).

3.2 Stacking procedure

In order to recover emission from the low signal/noise lines of sight, we stack individual spectra as a function of galactocentric radius, SFR surface density, and CO(2–1) integrated intensity following Schruba et al. (2011), Caldú-Primo & Schruba (2016), and Jiménez-Donaire et al. (2017, 2019). To do this, first we convolve our data cubes and maps to a common angular and spectral resolution of 1.95 arcsec and 5 km s^{-1}, respectively. Next, we regrid all data cubes and maps to a common world coordinate system (WCS). Last, we resample our line emission maps (including the ancillary data) on to the same hexagonal grid, where sampling points are spaced by half a beam size of the NOEMA observations ($\sim$1 arcsec), thus oversampling the data by a factor of 4.

Then we measure the average integrated intensity of each observed line in each bin. To do this, first we calculate the velocity at which the CO(2–1) spectrum peaks within all the lines of sight. In the next step, we shift the spectra of each line of sight within the NOEMA and ALMA CO(2–1) cubes by the velocity previously defined. This procedure results in cubes where all molecular line emission peaks at a velocity close to 0 km s^{-1}. Averaging the shifted lines will increase the S/N and by construction one knows where a (potentially weak) spectral line should build-up. It should be highlighted, however, that this method relies on the robust detection of at least one bright line to determine the line-of-sight velocity by which all other spectra will be shifted. Typically, CO(2–1) is the brightest line along each line of sight, so this is used as a prior. We exclude sightlines where CO(2–1) is not robustly detected, since we are unlikely to detect the weaker line emission towards these positions.

We integrate the stacked spectrum to determine the average integrated intensity of the line. We use stacked CO(2–1) spectra as a prior to determine the width of the integration window. First, we define the signal-free part of the spectrum. Next, we determine where the spectral line is defined using the masking technique described in Section 2.2. We select all channels with S/N above 4 and expand the mask to cover all neighbouring channels with S/N above 2. Finally, this velocity window is used as a mask that we apply to the stacked spectra of the rest of the observed molecular lines. The integrated intensity is then calculated as a sum over the integration window multiplied by the channel width. The uncertainty of the integrated intensity is computed using the equation (1). Because we estimate the noise from the signal-free region of the stacked spectrum itself, this uncertainty properly accounts for any spatial oversampling, as well as for the potential spatial and spectral correlation of the data. This implies that the uncertainty of the integrated intensity varies across different sightlines and from tracer to tracer. We take the integrated intensity of the stacked spectrum if the following criteria are not satisfied. In cases when CO(2–1) is detected, we measure the integrated intensity of the stacked spectrum, its peak, and the values in the two channels next to the peak. We then determine their S/N. If either of the S/Ns are below 3, the integrated intensity is taken as an upper limit of three times the uncertainty of the integrated intensity defined in equation (1). In cases where CO(2–1) is not detected (S/N $<$ 3) and therefore the velocity window cannot be determined, we calculate the integrated intensity as an upper limit of three times the uncertainty of the integrated intensity that is calculated as the rms noise of the line multiplied by a 30 km s^{-1} velocity window. The stacked spectra and integration windows are shown in Figs A1–A3 in Appendix A.

3.3 Stacking results

We stack the observed lines by the quantities measured at high spatial resolution: galactocentric radius, CO(2–1) integrated intensity, and SFR surface density. These stacked line profiles are shown in the top left-hand panels in Figs 3–5.

We define radial bins in linear space, using a radial bin size of 350 pc, which is approximately three times the beam size along the beam major axis. For stacking by CO(2–1) integrated intensity, we use data points with an S/N in CO(2–1) integrated intensity greater than 12 due to lack of the emission of dense molecular tracers at fainter sightlines. This threshold selects 70 per cent of data points that contain bright CO(2–1) emission. To stack by CO(2–1) and $\Sigma_{\rm SFR}$, we define bins with widths of $10^{0.2}$ (K km s^{-1}) and $10^{0.25}$ (M$_\odot$ yr^{-1} kpc^{-2}), respectively, in logarithmic space. To illustrate which parts of the galaxy entered which specific bin, we colour code data points that contribute to the same bin and show them in the bottom right-hand panels of Figs 3–5. The CO(2–1) bins are constructed in a way that the two brightest CO(2–1) bins contain the very central part of NGC 3627, the following bins contain sightlines from the bar ends, and finally, the remaining bins contain fainter CO(2–1) sightlines located along the spiral arms and the outskirts of the central region, bar, and the bar ends. The mid-high CO(2–1) bins are associated with a few largest $\Sigma_{\rm SFR}$ bins.

The galactocentric radius stacks are shown in the top left-hand panel of Fig. 3. In this figure, we label where different environments are located. Overall, all lines show the strongest emission in the centre of NGC 3627, after which their emission steadily decreases

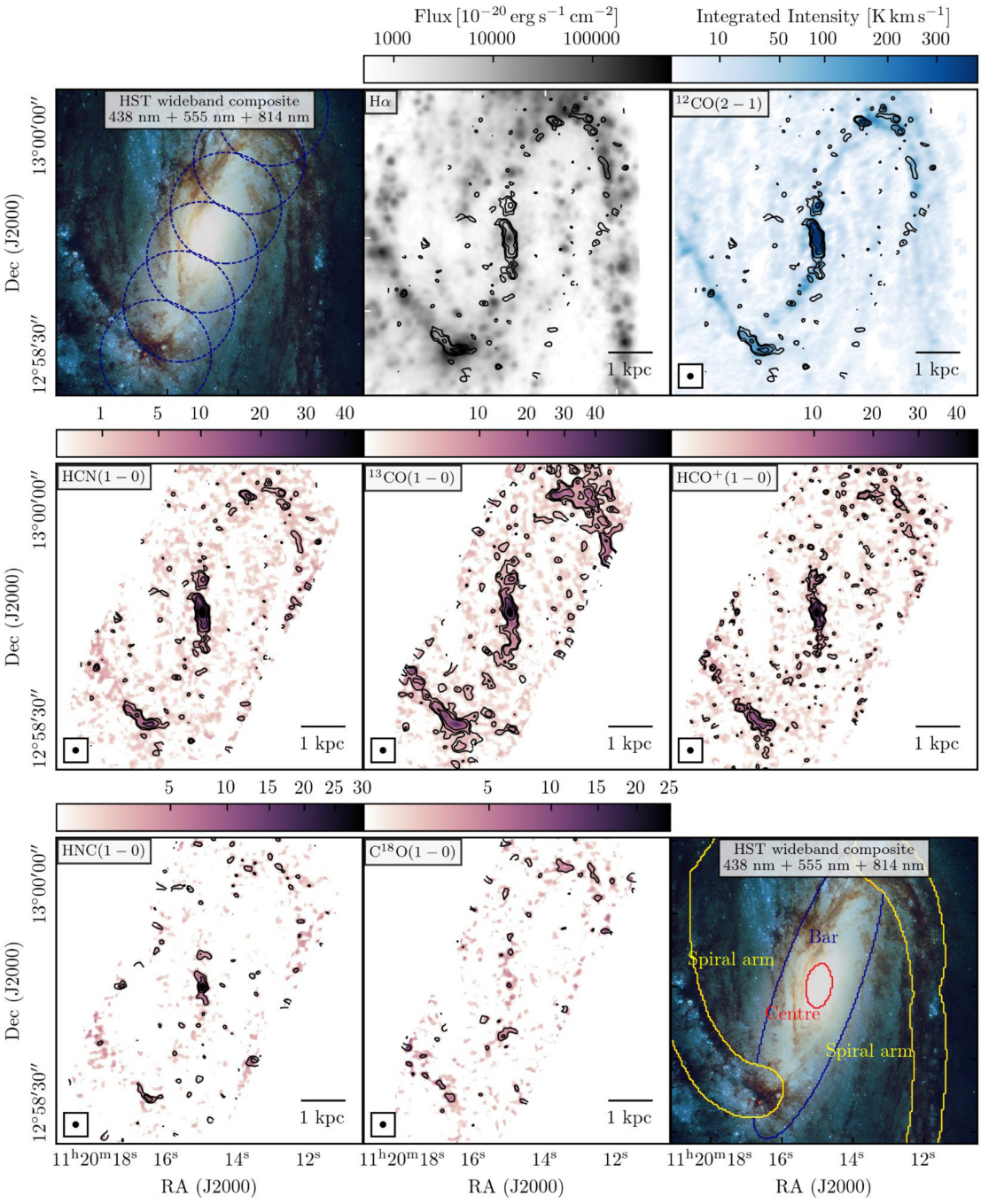

Figure 1. Top row: pointing pattern of the NOEMA mosaic corresponding to a frequency of 109.93 GHz overlaid on the wide field composite image of NGC 3627 obtained with the *Hubble Space Telescope* (left-hand panel; Lee et al. 2021), extinction-corrected Hα map at 1.86 arcsec (≈100 pc) resolution taken by the PHANGS-MUSE survey – we show all the Hα emission here, i.e. BPT and H II masking is applied to this image in a later step to recover actual SFR (middle panel, see Section 2.3; Emsellem et al., in preparation), CO(2–1) integrated intensity map at 1.95 arcsec (≈107 pc) taken by the PHANGS-ALMA survey (right-hand panel; Leroy et al. 2021b). Contours show HCN(1–0) integrated intensity at 3σ, 5σ, and 10σ levels (see below). Middle row: HCN, ^{13}CO, and HCO$^+$ integrated intensity map in K km s^{-1} observed by NOEMA at the working resolution of 1.95 arcsec (≈107 pc) adopted in this work. Bottom row: same as in the middle row but for HNC and C^{18}O. Contours in the middle and bottom row show levels of 3, 5, and 10 of S/N for each line. The circle on the bottom left-hand corner of the integrated intensity maps is the synthesized beam (1.95 arcsec). Bottom right-hand panel: same as in the top left-hand panel with overlaid contours of environmental masks (Querejeta, in preparation).

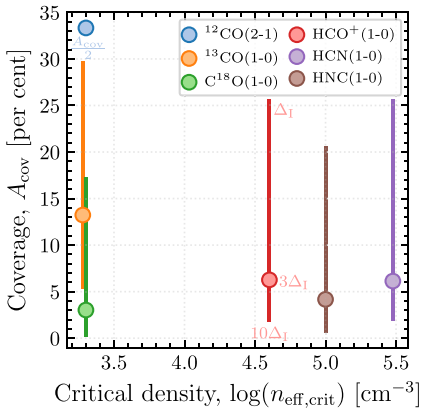

Figure 2. The percentage of pixels within the observed area that have significant values of the integrated intensity for each of the molecular lines, A_{cov}. We define significant integrated intensity values as being higher than three times their associated uncertainty (Δ_I; see Section 2.2). The error bars show the range of the percentage coverage for one and ten times the associated uncertainty. The variation between these limits for CO(2–1) line is small, therefore the error bar is not visible on the plot. The molecular line transitions are ordered as a function of the effective critical density of emission. We note that we offset the position of the ^{13}CO and C^{18}O values on the *x*-axis to avoid overlapping, due to their similar effective critical density (Table 2). We also note that the coverage of the ^{12}CO emission has to be reduced by a factor of 2 for plotting.

towards the bar where it reaches its minimum around 2 kpc (except for C^{18}O and HNC, where we do not recover emission). Line integrated intensities then increase towards the bar ends. The emission from the ^{13}CO line is recovered in almost all bins, up to ∼5 kpc. The ^{13}CO intensity increases towards the centre and the bar ends, but the centre appears to be brighter than the bar ends. Cormier et al. (2018) reported the opposite (i.e. brighter ^{13}CO in the bar ends than in the centre), but it was noted that this might be due to the low resolution at which the line was observed (∼1.5 kpc, compared to ∼100 pc in this work). Fig. 3 shows that the bright ^{13}CO at the bar ends covers a larger radial range than the emission at the centre.

HCN and HCO$^+$ emission are recovered along the bar (∼2 kpc). We find that HCN and HCO$^+$ have similar integrated intensities in the centre (26 and 21 K km s^{-1}, respectively) and across the disc of NGC 3627. This was also shown for the inner ∼4 kpc region in NGC 3627 by Gallagher et al. (2018b) and Jiménez-Donaire et al. (2019). Furthermore, we see bright and constant HCN and HCO$^+$ emission across the bar ends (∼3–4 kpc), where HCO$^+$ is slightly brighter than HCN. Similar emission is seen in HNC, but HNC is overall fainter than HCN by a factor of 2–3. C^{18}O is the faintest in the centre in comparison with other lines from our sample. Jiménez-Donaire et al. (2019) reported similar results for HNC and C^{18}O in this galaxy. We do not see a clear trend for C^{18}O and HNC, given their emission is only significant in the bar end and in the centre and bar end, respectively (see discussion in Section 4).

In the top left-hand panel of Fig. 4, we show the line integrated intensities as a function of CO(2–1) emission. The integrated intensity of all lines increases with increasing CO(2–1) integrated intensity. Taken at face value, this result implies that when more molecular gas is present, there is also more dense molecular gas. The brightest lines in our data set, ^{13}CO(1–0), HCN, and HCO$^+$, are recovered in all bins. We find that HCN and HCO$^+$ emission is considerably weaker in the lower CO(2–1) bins in comparison with ^{13}CO. Across all the CO(2–1) bins, HCN and HCO$^+$ show similar integrated intensities. HCO$^+$ emission is brighter than HCN for CO(2–1) integrated intensities less than 200 K km s^{-1}, whereas for the higher CO(2–1) values we find the opposite. At the very brightest CO(2–1) bin, HCN shows the brightest emission (∼110 K km s^{-1}), followed by ^{13}CO and HCO$^+$ (103 and 76 K km s^{-1}, respectively). HNC emission is recovered in almost all the CO(2–1) bins but is weaker than HCN and HCO$^+$. Finally, we recovered the emission of the faintest line in our data set, C^{18}O, in half of the CO(2–1) bins.

In the top left-hand panel of Fig. 5 we show line integrated intensities as stacked by SFR surface density. The emission of the stacked lines is recovered for about half of the Σ_{SFR} bins. We note that the central region (where the observed molecular lines peak) is excluded for analysis in this case due to the Hα emission not being sensitive to the presence of an embedded star formation present in this region (see Section 2.3). We find that at Σ_{SFR} values of 10^{-1}–1 M$_\odot$ yr^{-1} kpc^{-2} all the line intensities of denser molecular gas tracers are approximately flat, i.e. vary by a factor of ≤ 2. This behaviour is different from the one seen when stacking by CO(2–1) integrated intensity (Fig. 4). Overall, line intensities show a higher correlation with CO(2–1) than with Σ_{SFR}. In the bottom right-hand panel of Fig. 5, where we show a map of the SFR surface density plotted over the HCN integrated intensity map, we see that HCN emission is also present in regions where there is no star formation traced by Hα emission. 24 per cent of the total HCN (and 27 per cent of the CO(2–1)) flux is present in regions with star formation traced by Hα emission.

^{13}CO has overall the highest integrated intensity compared to the other observed 3 mm lines. For Σ_{SFR} of 5.3 M$_\odot$ yr^{-1} kpc^{-2}, ^{13}CO has an integrated intensity of 22 K km s^{-1}. The HCN and HCO$^+$ integrated intensities are a factor of ∼2 lower than the ^{13}CO (both ∼11 K km s^{-1}). Fig. 5 shows that the HCN integrated intensity is approximately constant over 1 dex in Σ_{SFR}, whereas for Σ_{SFR} greater than 1 M$_\odot$ yr^{-1} kpc^{-2}, HCN intensity increases by ∼0.6 dex. HNC emission appears to decrease from 0.2 to 1 M$_\odot$ yr^{-1} kpc^{-2}, but its emission increases at 1 M$_\odot$ yr^{-1} kpc^{-2} as the rest of the lines. The increasing trend of dense gas tracers with higher values of Σ_{SFR} we found is in agreement with Gallagher et al. (2018a) who showed that the denser gas mass traced by HCN correlates with SFR (in their work traced by Hα and 24 μm emission) in NGC 3627. Here we report similar results for the C^{18}O line as we have done in previous paragraphs. C^{18}O is the faintest line shown in Fig. 5, with emission only recovered in three Σ_{SFR} bins.

3.4 Comparison of the CO and HCN velocity dispersion

At low spatial resolution (≫100 pc), relative motions of the molecular gas caused by the galactic potential are thought to be the dominant factor broadening molecular line profiles. Hence, it is not possible to measure the intrinsic velocity dispersion of cold, denser clumps caused by their internal dynamics (e.g. turbulence and thermal motions). However, at scales of ∼100 pc, we probe smaller clumps. GMCs are also thought to decouple from the galactic dynamical environment at these spatial scales (e.g. Meidt et al. 2018; Chevance et al. 2020), and, hence, with high spatial resolution observations we might be able to measure these intrinsic properties.

Here we present the velocity dispersion of the HCN line emission, which we compare to the velocity dispersion of CO(2–1) emission. We conduct the following method to measure the velocity dispersions of these molecular lines. The velocity dispersion calculation is based

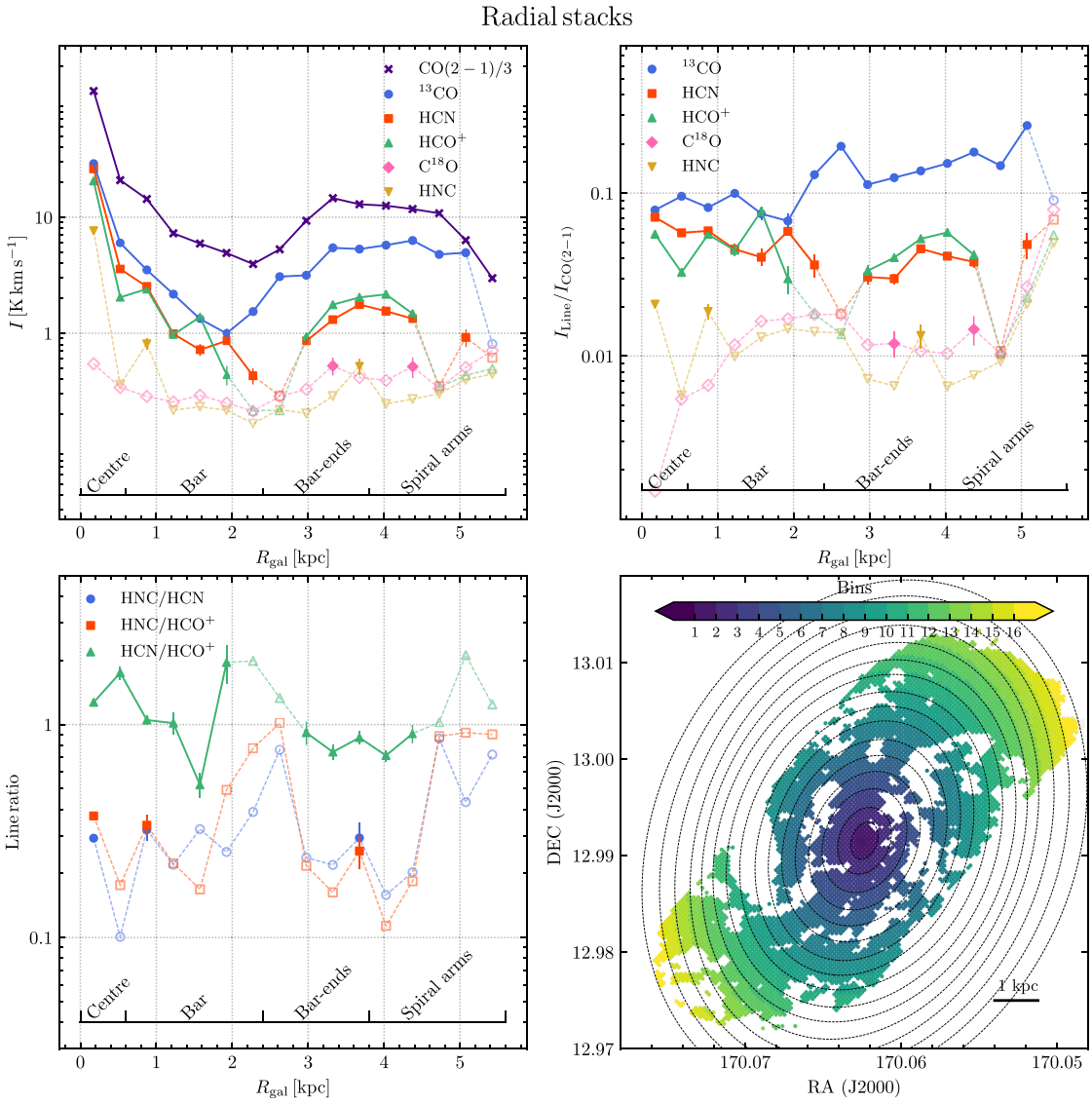

Figure 3. Stacked molecular line intensities binned by galactocentric radius. We show the integrated intensities of CO(2–1), CO isotopologues (^{13}CO and C^{18}O), and the dense gas tracers in the top left-hand panel and the line ratios of dense gas tracer per unit CO(2–1) in the top right-hand panel. Line ratios among the dense gas tracers are shown in the bottom left-hand panel. All significant measurements (characterized as good and satisfactory detections) are connected with solid lines, whereas for non-detections we plot $3\Delta_{\rm I}$ values as an open symbol that are connected with dashed lines. Error bars show 1σ uncertainties. Using the environmental mask, we label the location of each environment. The bottom right-hand panel shows a map of galactocentric radius, where we colour code each radial bin.

on the 'effective width' approach (Heyer, Carpenter & Snell 2001; Leroy et al. 2016, 2017a; Sun et al. 2018; Querejeta et al. 2019), in which the velocity dispersion is computed as

$$\sigma_{\rm Line} = \frac{I_{\rm Line}}{T_{\rm peak}\sqrt{2\pi}}, \tag{3}$$

where $I_{\rm Line}$ is the line integrated intensity in K km s^{-1}, and $T_{\rm peak}$ is the peak brightness temperature of the spectrum in units of K. The uncertainty of the velocity dispersion is calculated by propagating the corresponding uncertainties. The velocity dispersion is determined within lines of sight with S/N greater than 7 in both HCN and CO(2–1). We show our results in Fig. 6 where we colour code our points according to their CO(2–1) integrated intensity. We see that HCN line profiles become broader with brighter CO(2–1) emission. This is also the case for CO(2–1), which was previously highlighted by Sun et al. (2018, 2020). Here we also compare our results with velocity dispersion measures within the literature.

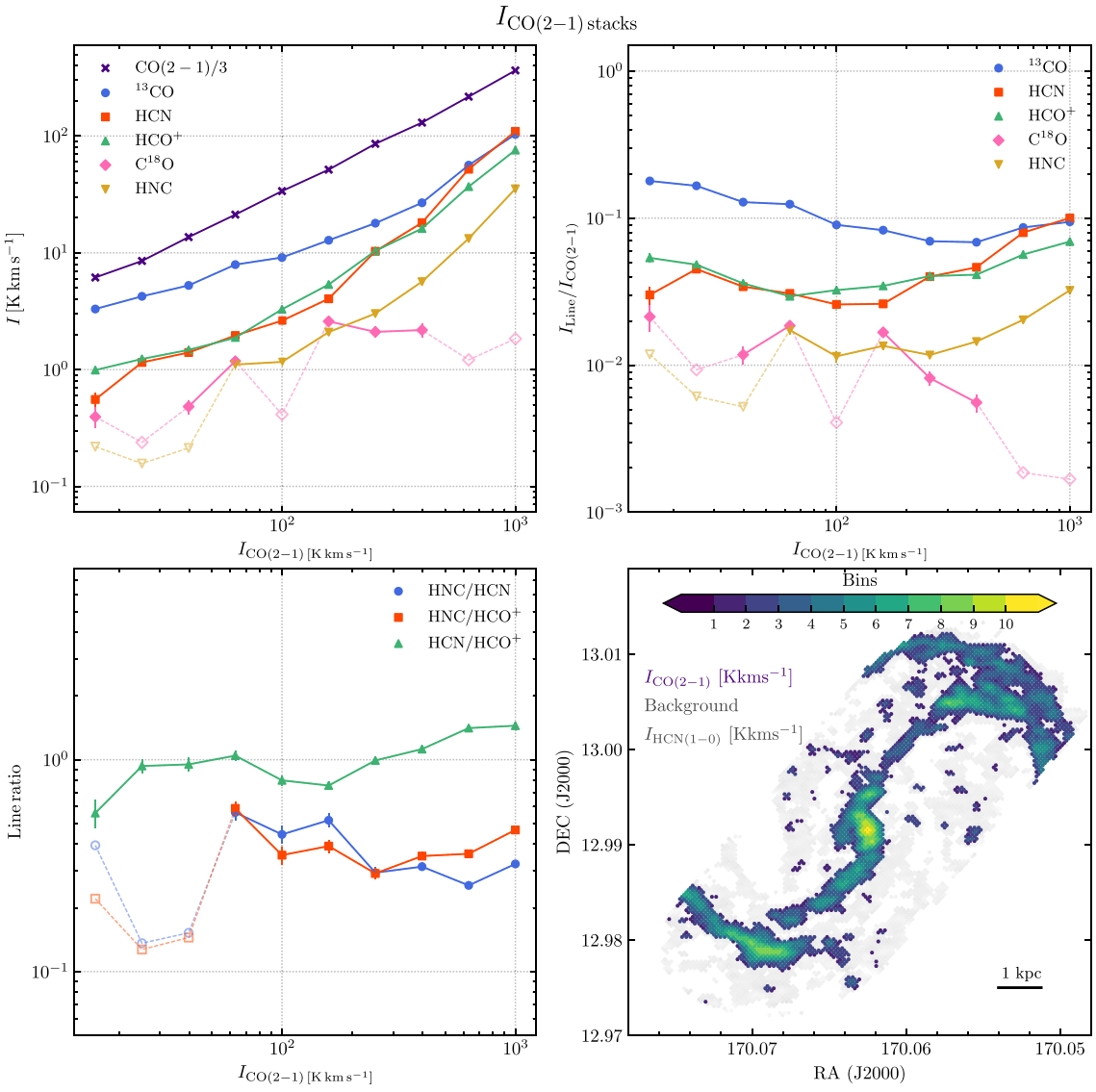

Figure 4. Same as Fig. 3, but stacked by CO(2–1). In this case, we only use data points with S/N > 12 in CO(2–1). We show the HCN integrated intensity map in grey in the bottom right-hand panel. Coloured points represent the lines of sight that contribute to CO(2–1) bins.

Several works within the literature have also made a similar comparison to that presented in this section, albeit over various spatial scales using fundamentally different observations and methods to determine the velocity dispersion. Hence, a direct comparison is difficult and should be taken with caution. Anderson et al. (2014) investigated the velocity dispersions of dense molecular clumps at 1.45 pc resolution in the 30 Doradus region within the Large Magellanic Cloud. Their result is that HCN and HCO$^+$ velocity dispersions of molecular clumps in 30 Doradus are comparable with CO velocity dispersions, concluding that the denser molecular gas is not dynamically decoupled from the bulk molecular gas. They also found a trend of increasing clump brightness with increasing velocity dispersion. Jiménez-Donaire et al. (2017) measured HCN, HCO$^+$, and ^{13}CO line widths in six galaxies, including NGC 3627, at 1 kpc resolution from a Gaussian fit of radially stacked spectra. They found narrower line widths in the discs of their galaxies than in their centres. In the case of NGC 3627, the reason for the broad line widths in the central region is that there are unresolved rotational motions in the centre, as well as the motions along the spiral arms and the bar.

Querejeta et al. (2019) investigated the velocity dispersions of dense gas tracers in M51 over spatial scales (∼100 pc) similar to those in our work. Importantly, this study used the same approach when calculating the 'effective' velocity dispersion, therefore we can

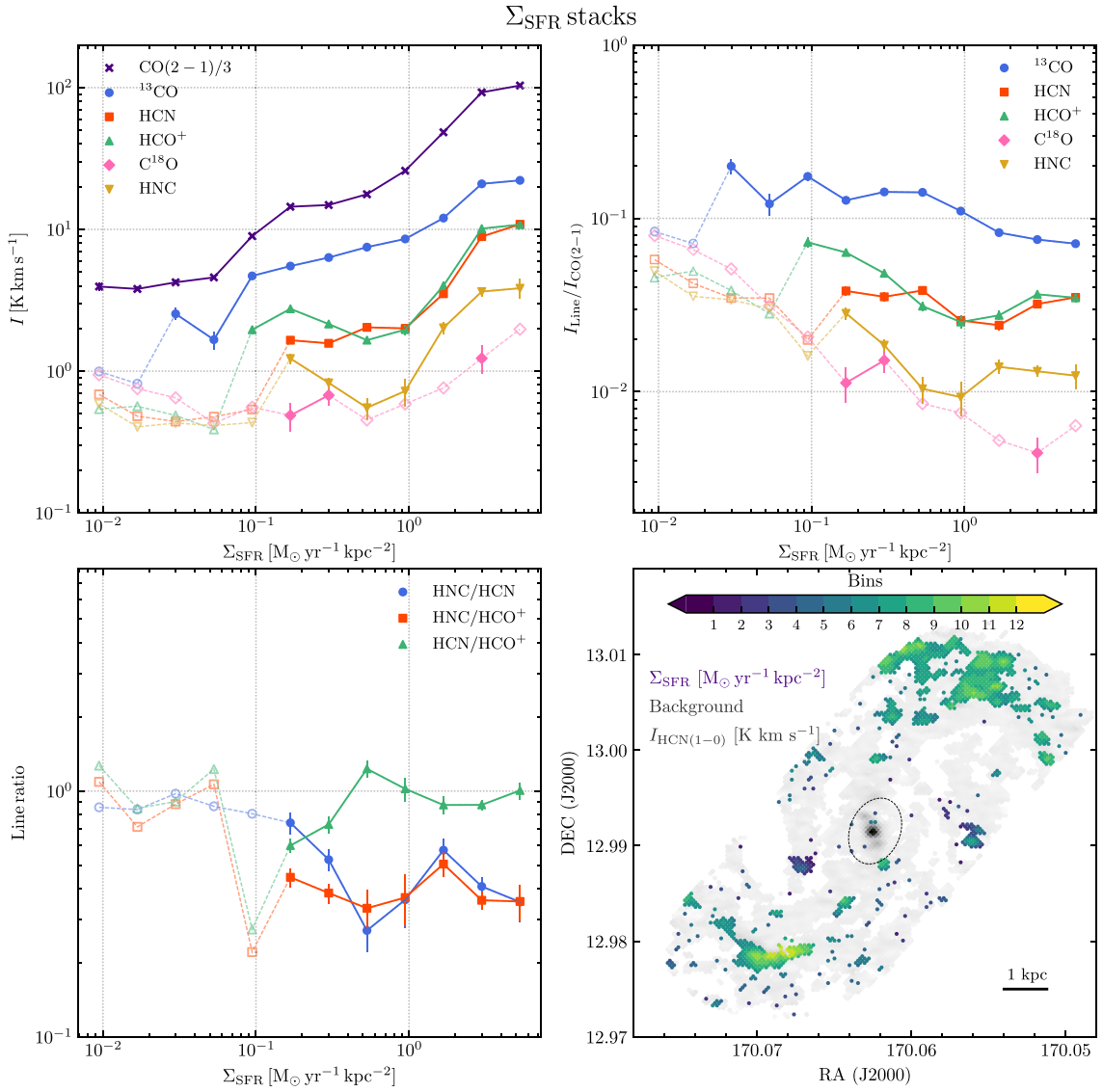

Figure 5. Same as Fig. 3, but for stacks by $\Sigma_{\rm SFR}$. We stack data points from regions where star formation is traced by Hα emission (Section 2.3). We exclude the centre (region within the circle with radius of ∼600 pc) where Hα emission may not exclusively trace recent star formation. We also show the HCN integrated intensity map in grey in the bottom right-hand panel.

directly compare our results with Querejeta et al. (2019). We show points from Querejeta et al. (2019) as grey circles in Fig. 6. The velocity dispersions seen for sightlines coming from NGC 3627 are higher than those seen in M51 in both HCN and CO(2–1). There seems to be a consistent picture, where broader profiles of HCN correlate with broader and brighter CO profiles, which is then suggestive that we probe multiple clouds along the line of sight. Thus our results are also in agreement with Querejeta et al. (2019) and the studies mentioned in the paragraph above.

In Fig. 6, we see that there is a deviation from the 1 : 1 relation as the HCN velocity dispersion is lower than the velocity dispersion of CO(2–1) emission. This behaviour likely arises due to the HCN emission being less spatially extended than the CO(2–1) (see Section 3.1 and Fig. 2), which is expected also to be seen in velocity space, or due to the presence of more gas traced by CO(2–1). Larger velocity dispersion can result from the presence of complex line profiles. We see only a few sightlines where velocity dispersions are higher in HCN than in CO(2–1) and these come from the sightlines with the brightest CO(2–1) emission in NGC 3627.

To compare velocity dispersion across different regions in NGC 3627, we label points coming from the centre of NGC 3627 as stars with a red outline, whereas the sightlines coming from the

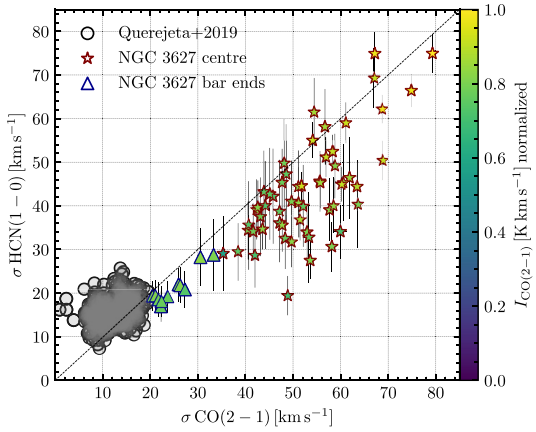

Figure 6. HCN velocity dispersion in comparison with CO(2–1) velocity dispersion. We show velocity dispersion measurements from Querejeta et al. (2019) as grey circles, whereas coloured points are sightlines from NGC 3627 colour coded according to their CO(2–1) integrated intensity. The dashed line shows where the points would lie in case of equal velocity dispersion in HCN and CO(2–1) emission. The points from the centre of NGC 3627 are marked as stars with a red outline, whereas points coming from the bar ends are labelled as blue triangles.

bar ends are marked as triangles with a blue outline in Fig. 6. Here we indeed see that velocity dispersions in the centre are higher than those from the bar ends. The deviation seen in the HCN–CO(2–1) velocity dispersion in the centre continues further from the centre.

There could be several explanations for these systematic differences in the HCN line profiles relative to the CO emission. Towards the centre and bright star-forming regions infrared pumping of HCN could also broaden the velocity dispersion relative to CO (Matsushita et al. 2015). Another explanation is that HCN and CO(2–1) may populate different orbits. CO(2–1) line profile exhibits multiple velocity components across some sightlines that can broaden the line. For complex line profiles, it is possible that HCN is not tracing all the velocity components in CO(2–1). The main difference in velocity dispersion seen in the centre and the bar ends is that in the very centre HCN and CO(2–1) trace the same molecular gas, i.e. the mean gas density in the centre might be higher than the HCN and CO(2–1) effective critical densities (Table 2). In the bar ends, however, the mean gas density is lower than the HCN effective critical density, therefore, HCN and CO(2–1) do not trace the same gas. In conclusion, the HCN velocity dispersion relative to CO(2–1) can be an identifier for complex line profiles. The importance of investigating each velocity component was demonstrated in Henshaw et al. (2020). We expand this analysis later, where we link the presence of complex line profiles in CO(2–1) with HCN emission in bar ends (Section 4.4).

3.5 Line ratios

In this section, we present the results for different velocity-integrated brightness temperature line ratios (hereafter line ratios). Investigating the line ratios, we are able to access the physics and chemistry that describes molecular gas better than investigating line intensities themselves. We derived these line ratios from the spectral stacking procedure, for bins of CO(2–1) integrated intensity, $\Sigma_{\rm SFR}$, and galactocentric radius (see Section 3.2). The error on the line ratio is calculated by the propagation of the uncertainties for the respective integrated line intensities,

$$\Delta_{\rm Line1/Line2} = \left|\frac{I_{\rm Line1}}{I_{\rm Line2}}\right| \sqrt{\left(\frac{\Delta_{\rm Line1}}{I_{\rm Line1}}\right)^2 + \left(\frac{\Delta_{\rm Line2}}{I_{\rm Line2}}\right)^2}, \quad (4)$$

where $I_{{\rm Line}\,i}$ is a given integrated line intensity and $\Delta_{{\rm Line}\,i}$ is its uncertainty within each bin (their computation is described in Section 3.2), both in units of K km s^{-1}. The computed line ratio and the associated uncertainty are non-dimensional.

In the following, we focus in more detail on the ratios of lines relatively to CO(2–1) and the ratios between denser gas tracers (HNC/HCN, HCN/HCO$^+$, and HNC/HCO$^+$).

3.5.1 Line ratios with respect to CO(2–1) integrated intensity

We examine how the line intensities over the CO(2–1) integrated intensity vary as a function of morphology across NGC 3627, CO(2–1) emission, where the CO(2–1) is assumed to trace the cloud-scale molecular surface density, $\Sigma_{\rm mol}$. We also look at how the ratio of the line intensities over the CO(2–1) varies as a function of SFR surface density, $\Sigma_{\rm SFR}$. These line ratios are shown in the top right-hand panels in Figs 3–5.

First, we discuss the line ratios of the CO isotopologues. In Fig. 3, we show line intensities over the CO(2–1) integrated intensity as a function of the galactocentric radius. We find that the ^{13}CO/CO(2–1) line ratio has the highest values across NGC 3627, with average values of 0.129 ± 0.005. We see that ^{13}CO/CO(2–1) is lower in the centre and inner bar than compared to the outer bar region and the bar ends. The variation of ^{13}CO/CO(2–1) is 0.6 dex across a radial range of ∼5 kpc.

In the top right-hand panel of Fig. 4, we show the line ratios as a function of CO(2–1) integrated intensity. The ^{13}CO/CO(2–1) ratio appears to slightly decrease with increasing CO(2–1) integrated intensity. The average ^{13}CO/CO(2–1) ratio over the CO(2–1) bins is 0.109 ± 0.002. We find that ^{13}CO/CO(2–1) varies over 0.4 dex, whereas the CO(2–1) integrated intensity varies by 2 dex.

Similarly, we find in the top right-hand panel of the Fig. 5 that the ^{13}CO(1–0)/CO(2–1) ratio decreases with increasing $\Sigma_{\rm SFR}$. The average ^{13}CO/CO(2–1) line ratio is 0.126 ± 0.006 and this line ratio varies over 0.4 dex whilst $\Sigma_{\rm SFR}$ varies over ∼3 orders of magnitude.

The C^{18}O/CO(2–1) line ratio has the lowest values compared to the remaining line ratios we show here and also the lowest number of significant points. We find a value for C^{18}O/CO(2–1) of $(12 \pm 2) \times 10^{-3}$ in the bar end of NGC 3627, and in the spiral arms it is $(14 \pm 3) \times 10^{-3}$ (top right-hand panel in Fig. 3). As a function of CO(2–1) and $\Sigma_{\rm SFR}$, the mean C^{18}O/CO(2–1) ratio is 0.014 ± 0.002.

We now discuss the ratios of the remaining line integrated intensities over CO(2–1) emission. These line ratios are used as a proxy of the dense gas fraction (e.g. HCN/CO). The HCN/CO(2–1) integrated intensity can also be used to describe the dense gas fraction, $f_{\rm dense}$, since the CO(2–1)/CO(1–0) is well studied (Sandstrom et al. 2013; Law et al. 2018; den Brok et al. 2021).

As a function of the environment (the top right-hand panel of Fig. 3), HCN/CO(2–1) line ratio has the highest measured value of 0.071 ± 0.001 in the centre of NGC 3627, after which slightly decreases towards the bar. The average line ratio across NGC 3627 is 0.046 ± 0.003. HCN/CO(2–1) in the central region is ∼2 times higher than in the bar ends. From the top right-hand panel in Fig. 4, we report mean HCN/CO(2–1) line ratio of 0.046 ± 0.001. The

biggest value of 0.100 ± 0.004, in this case, is found in the very centre of NGC 3627.

In case of CO(2–1) bins (top right-hand panel in Fig. 4), it appears that HCN/CO(2–1) has two regimes where the intersecting point is at the CO(2–1) integrated intensity of 100 K km s^{-1}. We find HCN/CO(2–1) is almost constant in the first regime where the CO(2–1) integrated intensity changes by an order of magnitude. In the second regime, we find that the HCN/CO(2–1) ratio varies by over 0.6 dex. In the top right-hand panel in Fig. 5, HCN/CO(2–1) ratio has significant points from Σ_{SFR} values of 10^{-1} M$_\odot$ yr^{-1} kpc^{-2}. Here HCN/CO(2–1) varies over 0.2 dex and the average line ratio is 0.035 ± 0.002. The maximum value of 0.038 ± 0.002 is found in the lowest recoverable Σ_{SFR} bin, while in the very last Σ_{SFR} we report a slightly lower value of this line ratio.

The rest of the line ratios (HCO$^+$/CO(2–1) and HNC/CO(2–1)) show a similar behaviour as the HCN/CO(2–1). HCO$^+$/CO(2–1) and HNC/CO(2–1) have average values of 0.047 ± 0.003 and 0.018 ± 0.002, respectively, across NGC 3627. We find higher values of HCN/CO(2–1) in the centre of NGC 3627 than the HCO$^+$/CO(2–1), whereas it becomes vice versa in the bar ends. At the high-intensity end HCN/CO(2–1) becomes overluminous compared to HCO$^+$/CO(2–1) (top right-hand panel in Figs 3 and 4). As a function of CO(2–1) emission (top right-hand panel in Fig. 4), both the HCO$^+$/CO(2–1) and the HNC/CO(2–1) vary over 0.4 dex. The average line ratios are 0.044 ± 0.001 for the HCO$^+$/CO(2–1) and 0.017 ± 0.001 for the HNC/CO(2–1). We report similar variation of these two line ratios as a function of Σ_{SFR} (Fig. 5), where HCO$^+$/CO(2–1) and HNC/CO(2–1) vary by ∼0.5 dex. The average line ratios in this case are 0.042 ± 0.002 for HCO$^+$/CO(2–1) and 0.015 ± 0.002 for HNC/CO(2–1).

Here we list our results and compare them with previous studies of NGC 3627 at lower spatial resolution. We find a peak HCN/CO(2–1) ratio of 0.076 in the very centre of NGC 3627, and a mean value of 0.058 ± 0.002 across the central 1 kpc (see Fig. 3). Similarly, across the central 1 kpc of NGC 3627, the studies of Gallagher et al. (2018b) and Jiménez-Donaire et al. (2019), who conduct a comparable stacking analysis, report mean a HCN/CO(1–0) ratio of ∼0.04. The HCO$^+$/CO(2–1) in the centre of NGC 3627 is 0.078, and 0.047 ± 0.002 the mean value in the inner 1 kpc region. For the HCO$^+$/CO(1–0) line ratio, Jiménez-Donaire et al. (2019) found a value of 0.017 at 1 kpc from the centre, whilst Gallagher et al. (2018a) reported a value of 0.039 in the centre and 0.01 at 1 kpc from the centre. Overall, our values towards the centre agree well with previous studies at lower spatial resolution, if we take into account the mean CO(2–1)/CO(1–0) ratio of 0.59 in NGC 3627 (den Brok et al. 2021). Comparing ratios determined here to the literature at larger Galactic radii is not possible, as our mosaic is not fully complete for bins >2 kpc (see lower right-hand panel of Fig. 3).

3.5.2 Line ratios of HCN, HNC, and HCO$^+$

In this section, we investigate the line ratios between the tracers of denser molecular gas, i.e. HNC/HCN, HCO$^+$/HCN, and HNC/HCO$^+$, as a function of three different stacking properties (bottom left-hand panels of Figs 3–5).

The HNC/HCN ratio is considerably lower than unity as a function of all the stacking properties. When considering only the significant points for the HNC/HCN ratio as a function of galactocentric radius (the bottom left-and panel in Fig. 3), the average HNC/HCN line ratio across NGC 3627 is 0.30 ± 0.03. The mean value of HNC/HCN ratio in the inner 1.2 kpc region is 0.30 ± 0.05 that is in agreement with the one reported by Jiménez-Donaire et al. (2019) for the inner 1.2 kpc region of five barred galaxies (0.4 ± 0.1). Watanabe et al. (2019) found a value of 0.3 ± 0.1. HNC/HCN does not vary with the CO(2–1) emission, but we report a slightly higher value of this line ratio for CO(2–1) integrated intensities below 200 K km s^{-1}. The mean HNC/HCN line ratio within all the CO(2–1) bins is 0.387 ± 0.024, whereas it is 0.46 ± 0.06 as a function of the Σ_{SFR}.

As a function of the environment in NGC 3627, we find HCN/HCO$^+$ greater than unity in the central region. We measure the highest value (1.9 ± 0.4) in the bar around 2 kpc, whereas we report values lower than unity in the bar ends where we measure the minimum value of this line ratio (0.42 ± 0.08). At the very centre of NGC 3627 we find HCN/HCO$^+$ to be 1.27 ± 0.02. Overall, we find the mean HCN/HCO$^+$ to be (1.31 ± 0.06) in the inner 1.2 kpc region, and both Jiménez-Donaire et al. (2019) and Watanabe et al. (2019) reported 1.3 ± 0.2. For the CO(2–1) stacks (the bottom left-hand panel in Fig. 4), we find values lower than unity at CO(2–1) integrated intensities below 200 K km s^{-1}, whereas regions with brighter CO(2–1) emission have HCN/HCO$^+$ values above unity. The variation of HCN/HCO$^+$ is 0.5 dex across two orders of magnitude in CO(2–1). From the bottom left-hand panel in Fig. 5, we find an average HCN/HCO$^+$ ratio of 0.91 ± 0.08. Here HCN/HCO$^+$ varies over 0.3 dex.

The HNC/HCO$^+$ ratio has a value below unity in all three cases. The mean HNC/HCO$^+$ ratio across NGC 3627 is 0.32 ± 0.04. The HNC/HCO$^+$ ratio varies over 0.3 dex as a function of CO(2–1) and over 0.2 dex as a function of Σ_{SFR}.

4 DISCUSSION

In this work, we observe high critical density molecules (HCN, HNC, and HCO$^+$) and CO isotopologues (^{13}CO and C^{18}O) across the disc of the star-forming galaxy NGC 3627 at scales of 100 pc comparable to individual GMCs. We use CO(2–1) data from PHANGS-ALMA as a bulk molecular gas tracer (Leroy et al. 2021b) and extinction-corrected Hα emission from PHANGS-MUSE as a star formation tracer (Emsellem et al., in preparation).

The observed molecular lines show emission about 10–100 times fainter than the CO(2–1) line. We directly detect HCN and HCO$^+$ emission in the brightest regions of NGC 3627 – the centre and bar ends. To recover the faint emission from the observed lines and increase the S/N, we make use of the stacking technique described in Section 3.2. Data are stacked by three different parameters that are measured at high resolution: galactocentric radius, CO(2–1) integrated intensity, and Σ_{SFR}. Our key results are presented in Section 3.

4.1 Integrated intensities

From the top left-hand panel of Fig. 3, we note that there is a lack of emission along the inner part of the bar (1.2–2.2 kpc), except for the brightest observed line in our sample, ^{13}CO. We investigate line intensity profiles across different environments where we were able to recover emission over significantly extended continuous areas (the brightest regions in NGC 3627: the inner 1.2 kpc region and the bar ends). In this section, we discuss how the line ratios vary within these two environments, as well as how the environment sets the star formation and denser gas fraction, and mention some caveats of our work.

Overall, we recover significant emission for all of our lines in bins of CO(2–1) intensity and Σ_{SFR}. We find that all lines show a positive correlation with CO(2–1) emission. They follow the structure of the

CO(2–1) emission, and show the brightest emission in the centre and the bar ends, as well where Σ_{SFR} is enhanced. Since CO(2–1) emission traces the molecular cloud scale surface density, our result is expected from the assumption that the denser molecular gas is found in regions where more gas is present.

4.2 Dense gas fraction across different environments: the centre and the bar end

Ratios involving HCN/CO(2–1), HNC/CO(2–1), and HCO^+/CO(2–1) can indicate how the gas is distributed across a range of densities, as these tracers have a high contrast of critical density (see Table 2 and Shirley 2015).

The HCN/CO line ratio, which is thought to be a good indicator of the dense gas fraction f_{dense}, appears to be bigger in regions of galaxies with high stellar mass surface density, high gas surface density, and high dynamical pressure (Usero et al. 2015; Bigiel et al. 2016; Jiménez-Donaire et al. 2017, 2019). This trend has been found with observations at ∼1 kpc resolution, whereas at the 100 pc spaces studied here we expect to see more variations with local environment and stochasticity (due to time evolution; Schruba et al. 2010; Querejeta et al. 2019). To first order, f_{dense} and SFE_{dense} are a function of galactocentric radius. A similar result has also been presented in recent studies at sub-kpc (∼500 pc) scales by Gallagher et al. (2018a,b) and Querejeta et al. (2019).

Gallagher et al. (2018b) found that the HCN/CO(2–1) ratio is higher in the inner kpc of four nearby galaxies (barred galaxies NGC 3351, NGC 3627, and NGC 4321 and unbarred galaxy NGC 4254). We find that the HCN/CO(2–1) ratio is elevated in the centre of NGC 3627 by approximately a factor of 2, compared to the bar-end regions (see Fig. 3). One possible explanation for this elevated HCN/CO(2–1) ratio, and hence higher denser gas fraction, is that the bar is driving a significant amount of gas towards the centre, which leads to an accumulation of (denser) molecular gas (Sheth et al. 2005; Krumholz & Kruijssen 2015; Sormani, Binney & Magorrian 2015a,b; Tress et al. 2020). It is worth mentioning that other effects may play a role in enhancing the HCN/CO(2–1) ratio (e.g. see Barnes et al. 2020a). For example, HCN emission can be enhanced relative to CO emission due to the presence of a very strong IR emitting source (i.e. via radiative IR pumping; e.g. Matsushita et al. 2015). CO(2–1) could have a high optical depth in some regions, which would cause a relative decrease in its emission relative to HCN emission. Moreover, the centre of NGC 3627 hosts an AGN (Filho et al. 2000).

Our results indicate that the HCN/CO(2–1) ratio, interpreted to trace the dense gas fraction f_{dense}, appears not to correlate with Hα emission on ∼100 pc scales in NGC 3627 (see Fig. 5). Gallagher et al. (2018a) showed that f_{dense} positively correlates with the star formation efficiency of molecular gas (SFE_{mol}) even though a significant scatter is present. These authors also found that f_{dense} correlates more strongly with the dense gas star formation efficiency (SFE_{dense}) as compared to SFE_{mol} (see figs 6 and 7 in Gallagher et al. 2018a). SFE_{dense} is a strong function of the environment, i.e. it appears to be reduced in regions of high molecular gas surface density and high stellar surface density (Shetty et al. 2014a; Shetty, Clark & Klessen 2014b). Murphy et al. (2015) found similar results for NGC 3627: they showed that SFE_{mol} anticorrelates with f_{dense} in the centre and the bar ends. This study also suggested that the dynamical state of dense gas sets this reduced star formation efficiency.

In Fig. 7, we compare the extinction-corrected Hα/HCN luminosity ratio as a function of the HCN/CO(2–1) luminosity ratio for all positions with significant CO and HCN emission. To extract sightlines from different environments, we apply environmental masks to our data: we assign points coming from the centre of NGC 3627 (inner radius of 600 pc region) and points that belong to the spiral arm or the bar (bar ends). The points are colour coded according to the environment from which they come. We find that central and bar-end positions have relatively similar values of HCN/CO(2–1) with mean f_{dense} ∼ 0.025 and ∼0.04, spanning less than an order of magnitude, f_{dense} ∼ 0.015–0.1. However, we find that they have significantly different Hα/HCN values with mean SFE_{dense} ∼ 0.01 and ∼0.1 in the centre and bar end, respectively. We recapitulate (see Section 2.3) that it is, however, likely that a large fraction of the Hα emission in the centre of NGC 3627 is not associated with star formation, rather could be attributed to AGN activity. Therefore, the Hα emission and, hence, SFE_{dense}, for the centre points, should be treated as upper limits (as highlighted in Fig. 7). We also highlight here a possibility of the obscured star formation in the centre, not traced by Hα emission (as discussed in Section 2.3).

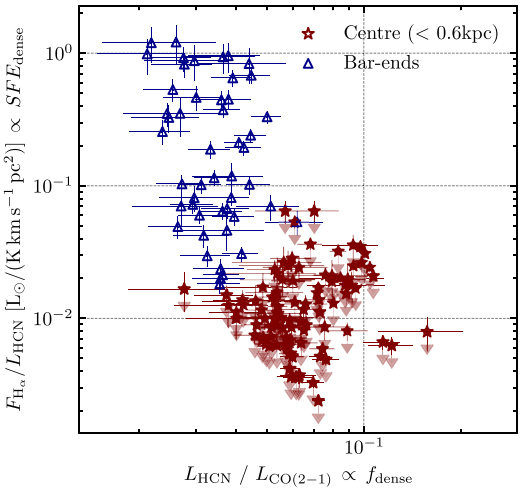

Figure 7. Hα/HCN luminosity ratio versus HCN/CO(2–1) luminosity ratio that can be thought of as proxies of SFE_{dense} and f_{dense}, respectively. Shown as red and blue points are independent sightlines we extract using the environmental masks (Querejeta, in preparation). These sightlines are coming from the centre and the bar ends of NGC 3627, respectively. The central SFE_{dense} points should be considered as upper limits due to the additional contribution of Hα emission not attributed to star formation (see Section 2.3.2).

The difference in these two environments may stem from the fact that the mean gas density in the centre may be much higher than the effective critical density of HCN (Leroy et al. 2017a), which increases f_{dense}. However, as previously mentioned, it has been proposed that it is the *relative* overdensities within the gas that are susceptible to gravitational collapse and form stars. That said, despite having a large f_{dense}, the galaxy centre would have a lower SFE_{dense}. Such a trend is observed within both the Milky Way's centre (e.g. Longmore et al. 2013; Kruijssen et al. 2014; Barnes et al. 2017) and other galaxy centres (e.g. Usero et al. 2015; Bigiel et al. 2016; Jiménez-Donaire et al. 2019). Helfer & Blitz (1997) explained a high HCN/CO(1–0) ratio in the centre of NGC 5194 by the presence of the AGN. HCN/CO(2–1) ratio found in the centre of NGC 3627 could be explained by invoking suppressed star formation. We also note that at the small spatial scales (∼100 pc) studied in this work, the scatter that

can be seen in Fig. 7 can be affected or driven by evolutionary effects in the gas–star cycle as the region separation lengths are ∼100–250 pc (Kruijssen & Longmore 2014; Kruijssen et al. 2018; Chevance et al. 2020). At the centre, however, that is most likely not the case as the fragmentation length of the gas reservoir is much smaller there as shown in e.g. Henshaw, Longmore & Kruijssen (2016), unless the entire centre goes through a feeding/starburst cycle (e.g. Kruijssen et al. 2014; Sormani & Barnes 2019; Barnes et al. 2020b). Other potential mechanisms regulating and suppressing star formation in the centre could be turbulence, suggested by the observed large velocity dispersions in both CO(2–1) and HCN (see Fig. 6), the effects of magnetic fields, and the increased gravitational potential of disc and bulge, though their roles are less clear (Krumholz & Kruijssen 2015). With this discussion in mind, however, it should be mentioned that a difference in the chemistry of these regions could also result in the observed scatter. Galactic Centres are known to harbour higher cosmic ionization rates than discs regions, which can lead to the formation and distinction of molecules, and increase or decrease their respective abundances (e.g. Harada et al. 2015). This is discussed further in the following section.

4.3 Line ratios between HCN, HNC, and HCO^+

Ratios among high critical density lines, i.e. HCN, HNC, and HCO^+, may encode information about density variations, radiation field, chemistry, and optical depth. The use of these line ratios to distinguish these properties is discussed in this section.

4.3.1 Does the HCN/HCO^+ ratio highlight X-ray-dominated regions?

The HCN/HCO^+ line intensity ratio is not driven by a single process, but it is more of an interplay between radiation field, column density, and gas density (Privon et al. 2015). The HCN/HCO^+ ratio is thought to be a good tracer of X-ray-dominated regions (XDRs; Murphy et al. 2015; Privon et al. 2015), because HCN abundance relative to CO and HCO^+ can be X-ray enhanced due to the presence of AGN (Jackson et al. 1993; Tacconi et al. 1994; Kohno et al. 2001; Usero et al. 2004), even though there are some sources with an AGN that do not show this. According to Meijerink, Spaans & Israel (2007), the HCN/HCO^+ ratio can be used to discriminate between XDR and photon-dominated region (PDR). Krips et al. (2008) found a systematic difference in HCN/HCO^+ between AGN and starburst-dominated systems. Moreover, Privon et al. (2015) concluded that global HCN enhancement is not necessarily a tracer of an AGN, whereas the presence of AGN does enhance HCN emission.

On the one hand, both HCN and HCO^+ are sensitive to cosmic rays. HCO^+ is produced predominantly by the $CO + H_3^+$ reaction, where H_3^+ is created by cosmic ray ionization of H_2 (Caselli et al. 1998). Therefore, we expect a higher HCO^+ abundance when the cosmic ray ionization rate is high. However, very high ionization rates may boost HCN emission by increasing the number of HCN–electron collisions (Kauffmann et al. 2017). On the other hand, HCO^+ as an ion tends to recombine and it is sensitive to the free electron abundance, although we would still expect the cosmic ray ionization rate to boost the HCO^+. HCN abundance, however, is not dependent on the free electron abundance (Papadopoulos 2007). Besides abundance and electron density, this line ratio can also be affected by the optical depth as shown by Jiménez-Donaire et al. (2017). This study calculated the optical depth of HCN ($\tau = 4.2 \pm 0.5$) and HCO^+ ($\tau < 5.2$) in NGC 3627 from the HCN/$H^{13}CN$ and HCO^+/$H^{13}CO^+$ line ratios. Moreover, if HCN and HCO^+ are optically thick (Jiménez-Donaire et al. 2017) and subthermally excited across the galaxy's disc (Knudsen et al. 2007; Meier et al. 2015), then the HCN/HCO^+ ratio may remain close to unity with small changes across the disc. Within resolved Galactic star-forming regions, the above effects combine to produce a spatial offset between HCN and HCO^+ that highlights this line ratio as a tool to trace fundamentally different environmental conditions (e.g. Pety et al. 2017; Barnes et al. 2020a). Murphy et al. (2015) reported a spatial offset between HCN and HCO^+ peak emission in NGC 3627's bar ends, implying that excitation effects may also play a role.

There is significant evidence to suggest that NGC 3627 harbours an AGN in its centre, which is classified as LINER/type 2 Seyfert galaxy (Ho et al. 1997; Filho et al. 2000; Véron-Cetty & Véron 2006). NGC 3627 hosts a strong X-ray source in its centre (Grier et al. 2011), which could affect the surrounding gas and impact the HCN/HCO^+ line ratio.

Our results show that the HCN/HCO^+ line ratio has values greater than or close to unity in the central region of NGC 3627 (see Fig. 3). HCN/HCO^+ ratio higher than unity is characteristic of either a high-density PDR ($n_H > 10^5$ cm^{-3}) or a low column density XDR ($N_H < 3.16 \times 10^{22}$ cm^{-2}; Meijerink et al. 2007). The presence of a XDR would cause CO(2–1)/CO(1–0) ratio being well above unity. Law et al. (2018) found a CO(2–1)/CO(1–0) ratio of ∼0.5–0.6 in the nuclear region of NGC 3627 combining a CO(2–1) observations from the Submillimeter Array (SMA) at 1 arcsec resolution and CO(1–0) from a BIMA Survey of Nearby Galaxies (BIMA SONG; Regan et al. 2001; Helfer et al. 2003) at 5 arcsec resolution. CO(2–1)/CO(1–0) ratio found in the centre of NGC 3627 is lower than the values found in XDR models (Meijerink et al. 2007), which is then suggestive that most of the CO(2–1) emission does not come from an XDR. Moreover, we estimate the X-ray flux from the AGN integrated over 2–10 keV (Ho et al. 1997; Filho et al. 2000). The flux is computed at a distance of approximately the beam size 100 pc from the AGN and it is $\sim 2.6 \times 10^{-3}$ erg cm^{-2} s^{-1}. This value is lower than the fluxes used in the Meijerink & Spaans (2005) models, which indicates that X-ray emission gets significantly absorbed very close (<100 pc) to the AGN, and, therefore, should not impact the HCO^+/HCN line ratio at larger radii.

We further consider possible composite XDR and PDR as explanations for the observed HCN/HCO^+ ratio. Privon et al. (2015) reported HCN/HCO^+ ratio of 1.84 for an AGN-dominated system, 1.14 for composite (high-density environments such as molecular cloud cores), and 0.88 for starburst systems. García-Burillo et al. (2014) found an average HCN/HCO^+ value of 2.5 in nuclear centre of NGC 1068 at 35 pc resolution. They reported the lowest HCN/HCO^+ value of 1.3. We report the average HCN/HCO^+ value in the centre of NGC 3627 to be 1.31 ± 0.06 and the lowest HCN/HCO^+ value of 1.07 ± 0.07 within the central region. According to Privon et al. (2015), the average HCN/HCO^+ in the central region of NGC 3627 is lying between the AGN-dominated and composite systems.

X-ray sources have also been found in the bar ends of NGC 3627 (Weżgowiec, Soida & Bomans 2012), where we report a mean HCN/HCO^+ ratio of ∼0.85. The X-ray luminosity from the bar ends integrated over 0–3 keV ($\sim 3.5 \times 10^{38}$ and 4×10^{38} erg s^{-1} for the southern and the northern bar ends, respectively) is comparable with the X-ray luminosity integrated over the same range from the centre ($\sim 2.75 \times 10^{38}$ erg s^{-1}; Weżgowiec et al. 2012). The X-ray emission in the bar ends could then also be influencing the HCO^+/HCN ratio within the bar ends, but at spatial scales lower than the beam size (∼100 pc).

4.3.2 HNC/HCN ratio as a temperature tracer

Recently, Hacar, Bosman & van Dishoeck (2020) have suggested that the HNC/HCN line ratio probes the gas kinetic temperature in the molecular interstellar medium (ISM). This dependence was, however, determined using high spatial resolution (<0.1 pc) observations of the Orion star-forming region. Hence, it is interesting to apply this probe to our NGC 3627 observations that cover a much larger dynamic range of environments both within the map and within the large beam (∼100 pc). Theoretical studies have suggested that the observed variations in HCN and HNC emission could be chemically controlled. HCN can be produced in neutral–neutral collisions (HNC + H ⟶ HCN + H), which when proceeding from left to right lowers the HNC/HCN abundance ratio. This reaction activates at a certain temperature, although there are some discrepancies between the observations and theoretical models. Schilke et al. (1992) calculated the activation temperature of 200 K, Talbi, Ellinger & Herbst (1996) found value of a 2000 K, whereas recent studies showed that this reaction could be activated at temperatures as low as ∼20 K (Graninger et al. 2014). Gas chemistry should also be taken into account, as it can enhance HCN abundance at temperatures between 30 and 60 K, and therefore influence HNC/HCN abundance ratio (Graninger et al. 2014).

Overall, we find the HNC/HCN line ratio to be less than unity within all three different types of bins shown in Figs 3–5. We also find that there is no correlation with CO(2–1) intensity, and the HNC/HCN ratio does not vary within the star formation bins; e.g. assuming star formation could correlate with gas temperature. Moreover, we see that the HNC/HCN ratio is higher in the bar end than in the centre. If we assume the temperature dependence of HNC/HCN in our case, as derived by Hacar et al. (2020) within the Orion integral shaped filament, we estimate a mean beam-averaged temperature in the centre and bar ends to be both 34 K. It is expected that higher temperatures should originate from the galactic centre region, e.g. due to the increased energetics (e.g. shocks) and/or radiation field within the central region. However, it is worth noting that NGC 3627 could be atypical as the bar ends are also very prominent in star formation and complex dynamics (i.e. that could also cause strong shocks; see Section 4.4), and it is not clear that one would then expect a relative increase in temperature towards the centre, or not a chemical, but a physical (density) effect.

Lastly, one may expect that a change in gas temperature could also affect the HCN/HCO^+ ratio in the same way as the HNC/HCN ratio (Jiménez-Donaire et al. 2019), albeit to a lesser degree, i.e. due to the HCN abundance variation with temperature. Indeed, we do observe larger values of the HCN/HCO^+ ratio within the centre compared to the disc. Yet, as previously discussed (Section 4.3.1), it is not clear if this is due to PDR and XDR, as opposed to the gas temperature.

4.4 Dynamical interaction enhancing star formation in the bar ends

We now investigate dynamical effects that can affect star formation within the bar ends of NGC 3627. Bar ends are thought to be the interface of gas populating two major sets of orbits, from either the bar or the spiral arms. The bar ends happen to be the apocentres of the orbits that are elongated parallel to the bar, as the gas flows on these orbits near the bar ends (Athanassoula 1992). At the apocentres, the gas slows down and piles up, which compresses the gas and enhances star formation. Orbital crowding and the intersection of gas on such orbits (e.g. via cloud–cloud collisions), followed by compression and collapse, are thought to enhance the SFR and the star formation efficiency in these regions (e.g. Benjamin et al. 2005; López-Corredoira et al. 2007; Renaud et al. 2015; Sormani et al. 2020).

The role of orbital motions on star formation in the northern and southern bar-end regions of NCG 3627 has been investigated by Beuther et al. (2017) using CO(2–1) line emission as a kinematic tracer. The CO(2–1) line was observed by the Plateau de Bure Interferometer (PdBI) and IRAM 30-m (Paladino et al. 2008; Leroy et al. 2009) at 1.6 arcsec (88 pc) resolution. They found that the positions of the brightest emission (i.e. integrated intensity peaks) exhibit the broadest line profiles, almost all of which consist of multiple (sometimes even more than two) velocity components in the cold denser molecular gas. These components are interpreted as resulting from the particular arrangement of the gas populating both bar and spiral orbits.

There are also a number of sightlines with lower line widths and only one velocity component. These are in agreement with the line width–size relation (Larson 1981; Solomon et al. 1987), indicating the presence of distinct molecular clouds from only one set of orbits. Single-peaked spectra at the northern bar end mainly trace the spiral component, whereas the bar component is observed in the single-peaked spectrum towards the southern bar end (Beuther et al. 2017). They then used the evidence of multiple velocity components to argue that converging flows and the resulting gas pile-up in this scenario lead to enhanced star formation in the bar ends of NGC 3627. This may stem from the influence of the interaction with the galaxy's companion NGC 3628 (Chemin et al. 2003) in the north, which might cause gas to be more strongly arranged by the spiral than by the bar. Law et al. (2018) reported higher CO(2–1)/CO(1–0) line ratios in the regions where the interaction is closer. The difference in magnetic field strength in bar ends may also play a role: Soida et al. (2001) found two magnetic field components in NGC 3627, with the magnetic field connected to the CO emission along the western arm.

In this work, we confirm that the northern and southern bar ends of NGC 3627 contain not only bright CO(2–1) but also HCN emission, implying that they are rich in both cold molecular and denser molecular gas. The southern bar end appears to be brighter in both lines and more extended. Something similar is seen in Hα emission suggesting that star formation is higher in this region. This supports the idea that these regions have ample fuel for intense star formation.

Our view of the kinematics of the denser gas in relation to the lower density gas traced by CO(2–1) adds another layer to the picture proposed by Beuther et al. (2017). Fig. 8 shows a comparison between the spatial and spectral distributions of the CO(2–1), HCN, and HCO^+ emission at the bar ends in NGC 3627. There we also highlight the distribution of Hα emission from MUSE observations, to serve as a probe of star formation.

The left-hand panels in the first two rows show the Hα maps of both bar-end regions overlaid with contours of Hα, CO(2–1), and HCN in white, blue, and red, respectively. We find that HCN peaks in a different position than Hα in the northern bar end, whereas a spatial offset between these two peaks is still present but smaller in the southern bar end.

We take averaged spectra within regions of a single beam (∼3 arcsec = 164 pc in radius) at several positions across both bar ends, which are presented in Fig. 8. We mark the peaks of HCN emission with red crosses and the peaks of Hα emission as white crosses. The spectra towards these two positions in both bar ends are shown in the right-hand panels of the top two rows and in the left-hand panels of the bottom two rows in Fig. 8.

The remaining panels in the bottom two rows show three different positions taken from Beuther et al. (2017, see their fig. 3). They

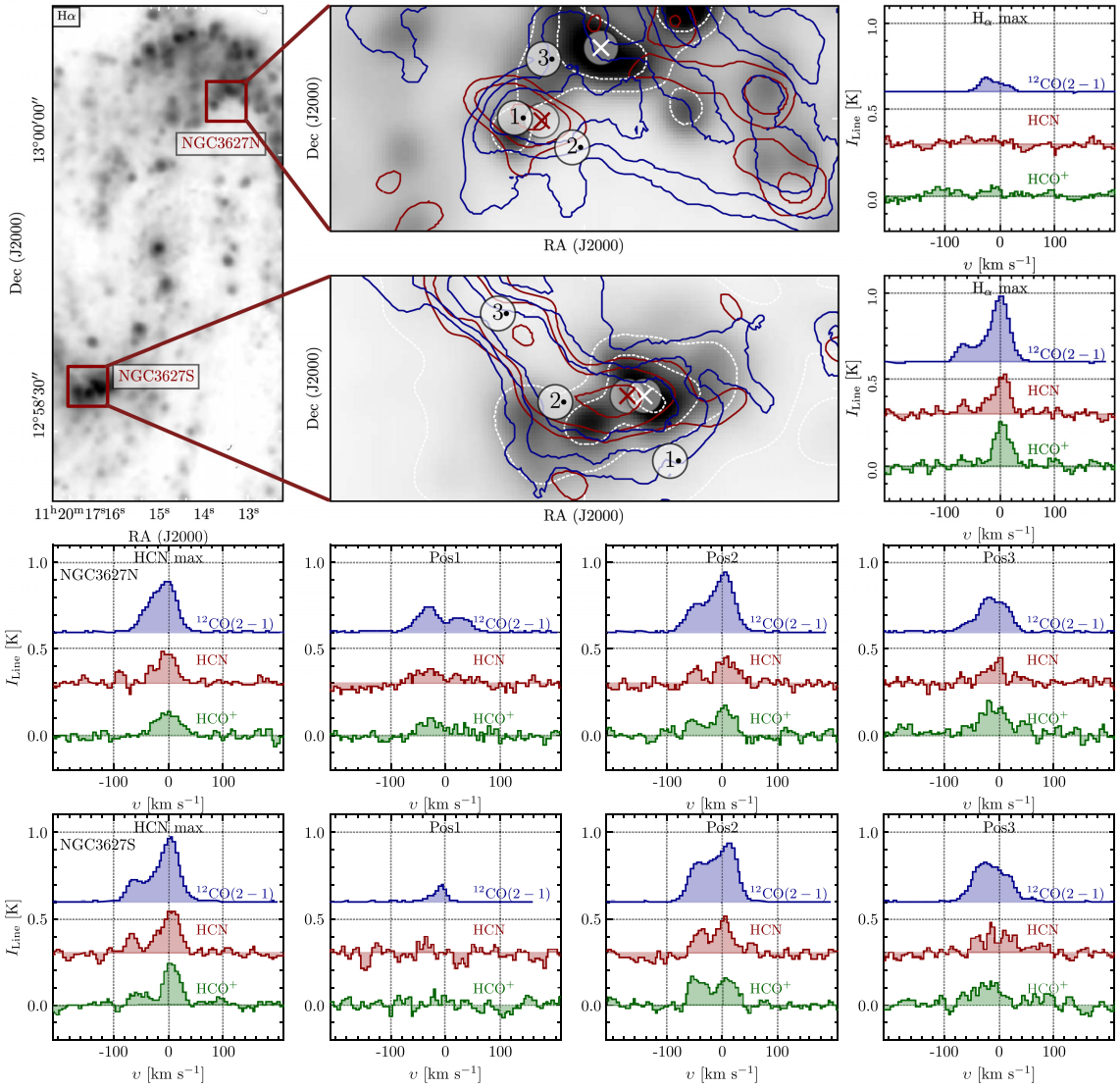

Figure 8. Bar-end regions within NGC 3627. The northern bar end (NGC 3627N) is shown in the top middle panel and the southern bar end (NGC 3627S) in the middle panel in the second row. We show Hα emission within these regions in grey scale and as white contours. Contours of CO(2–1) emission (of 50σ, 100σ, and 200σ) are shown in blue, and the HCN contours of 3σ, 5σ, and 10σ are in red. We indicate the position of the maximum of the Hα and HCN emission with a white cross and red cross, respectively. We show averaged spectra of CO(2–1), HCN, and HCO$^+$. In the first two rows in right-hand panels we plot spectra averaged over 3 arcsec (164 pc) region centred on the white crosses. The last two rows show averaged spectra over 3 arcsec (164 pc) region centred on the red crosses (left-hand panels), while the remaining panels show averaged spectra over 3 arcsec regions in three positions marked with numbers 1, 2, and 3 from both bar ends (each row, respectively, for NGC 3627N and NGC 3627S). These positions coincide with those analysed in Beuther et al. (2017).

identified one, two, and three CO(2–1) velocity components in the Pos1, Pos2, and Pos3 spectra, respectively. We see two or more velocity components in CO(2–1) within almost all regions shown. We also find that both the HCN and HCO$^+$ lines have two velocity components within several sightlines at the same velocities as CO(2–1).

We find that there are multiple velocity components in both HCN and HCO$^+$ emission, which appear to peak at a similar velocity and have comparable line widths to the components previously identified in CO(2–1) (Beuther et al. 2017). Moreover, we find double-peaked line profiles towards the peak of the HCN integrated intensity in both bar ends, and a double-peaked profile towards the Hα peak in the southern bar end. This result has two important implications. The first is the confirmation of these CO(2–1) components as real physical structures, rather than optical depth effects, as it is unlikely that both HCN and HCO$^+$ are severely optically thick and suffer from self-absorption on ∼100 pc scales. The second is then that the velocity components observed in CO(2–1), a molecular gas tracer, have significant dense gas tracer emission. This then highlights that the region contains both molecular gas and dense molecular gas that are distinct in velocity (and presumably space).

We ask then the question: How did these dense molecular gas components form? The profiles shown in Fig. 8 could suggest two scenarios. First, the dense gas could be created at the orbit intersection. Indeed, the peak of the dense gas emission within the centre of the bar-end regions would certainly point to this enhancement. Second, converging gas flows into the bar-end region could already be rich with dense gas before arrival. This could be evidence by the spectrum seen at Pos1 in the southern bar, which contains both HCN and HCO^+ emission, yet sits further upstream from the bars rotation, and the bright star-forming region. Answering this question is, therefore, somewhat speculative, and in reality, the scenario is likely that both some dense gas is delivered to the bar, which then is further compressed.

There is a final interesting point to note within the southern bar-end region. This is that the good correlation between Hα and HCN and CO emission at the leading edge of the bar end (i.e. centre right of the zoom-in panel in Fig. 8), yet the downstream material appears to be underluminous in Hα for a similar amount of HCN emission (i.e. upper left of zoom-in). This then may highlight that star formation is more efficient for a given amount of dense gas within the leading edge of the bar, compared to the trailing material. This then opens a question, if not just the amount of dense gas is important in fuelling star formation, but also the dynamics of the dense gas in limiting and/or driving its collapse? In particular, if the compressing motions of the leading bar edge are enhancing star formation, whilst the shearing forces of the trailing bar end are inhibiting star formation.

4.5 Systematic environmental density variations

Leroy et al. (2017a) investigated how the line intensity ratios of molecules trace molecular gas density. In extragalactic observations, reaching the necessary resolution and sensitivity while observing molecular lines fainter than CO is challenging. The line intensity integrated within a single beam encompasses a lot of different physical gas and contains information from a range of densities. The reason is that the line emits most at the 'effective critical density' ($n_{\rm eff,\,crit}$) as described in Leroy et al. (2017a), but it also emits from densities below $n_{\rm eff,\,crit}$ that frequently dominate the (subbeam) density distribution. Therefore, line intensity ratios can be used to infer density variations. We also note that optical depth, temperature, IR pumping, cosmic rays, and element abundance variations can affect the line ratios. Leroy et al. (2017a) coupled simple radiative transfer models and parametrized density probability density functions (PDFs) to quantify how changes in the subbeam density distributions affect the beam-averaged line emissivity. This study implemented two commonly considered density distributions to describe the density distribution of the cold phase of the ISM where our observed lines are produced: a pure lognormal distribution and a lognormal distribution with a power-law tail at high densities (Federrath & Klessen 2013; Girichidis et al. 2014; Kainulainen, Federrath & Henning 2014; Lombardi et al. 2014; Schneider et al. 2015a,b, 2016). They found that the subbeam density distribution affects the beam-averaged emissivity. This result is interpreted in a way that lines that trace denser gas (i.e. lines with high effective critical density) are the most sensitive to density changes. Therefore, ratios of these line's intensities to CO lead to more variation than lines that trace pure molecular or bulk molecular gas (^{13}CO, CO(2–1)). Such a line ratio shows a different behaviour that depends on the density distribution for a fixed abundance. The shape of the distribution of molecular gas also sets the variation of line ratios. For example, HCN/CO shows greater scatter when molecular gas is described with the lognormal distribution as opposed to the case when the lognormal distribution with a power-law tail describes molecular gas.

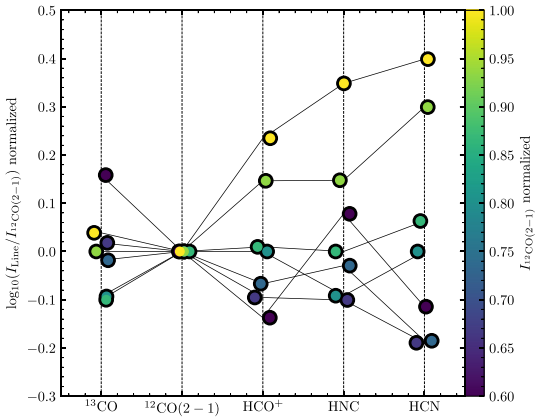

Figure 9. Line-to-CO(2–1) integrated intensity ratios. Individual data points are from stacking spectra by CO(2–1). We only show points at which all stacked intensities have signal/noise greater than 7 (see solid points in the top right-hand panel of Fig. 4). All points for each line ratio (same *x*-axis label) are normalized by their respective median value. Points are colour coded according to CO(2–1) integrated intensity (normalized) and are slightly offset along the *x*-axis for visualization purposes. All points with the same normalized CO(2–1) value are connected with a black line.

In this section, we investigate the scenario from Leroy et al. (2017a) that line intensity ratios can reflect changes in density distributions. In Fig. 9, we show how the line intensity ratios vary as a function of the CO(2–1) integrated intensity, used as a proxy for the volume density at cloud scales (Leroy et al. 2016; Sun et al. 2018). All intensities are determined by stacking in bins of CO(2–1) integrated intensity and only keeping significant measurements. We colour code each stacked line ratio measurement by the (normalized) CO(2–1) integrated intensity. Points with the same colour (similar 'density bin') are connected with a black line (see caption for details). We sort the line-to-CO(2–1) ratios according to their effective critical density listed in Table 2.

We show points at which the CO(2–1) integrated intensity is above $\sim$50 K km s^{-1}, because for these CO(2–1) intensity values the stacked line integrated intensities (except for C^{18}O) are classified as significant (the signal/noise is >7) according to our criteria explained in Section 2.3 (also see Fig. 4).

Overall, we find that HCN/CO(2–1) shows the highest scatter, followed by HNC/CO(2–1) and HCO^+/CO(2–1). The flaring pattern seen in Fig. 9 is consistent with the sensitivity of these line ratios to changes in mean gas density (here as traced by cloud-scale surface density). The higher the contrast of line critical densities, the more pronounced the flaring and dynamical range. This agrees with the modelling results found in Leroy et al. (2017a) and Puschnig et al. (in preparation). We note that the ^{13}CO/CO(2–1) ratio shows a reversed pattern, reflecting the lower ^{13}CO critical density compared to CO(2–1).

5 SUMMARY

We present new NOEMA observations towards a nearby, actively star-forming disc galaxy NGC 3627. These represent the current highest resolution (1.8 arcsec $\approx$ 100 pc) of molecular lines that

trace denser gas across a nearby spiral galaxy. Through this work, we investigate how the denser gas, using the following tracers HCN(1–0), HNC(1–0), HCO^+(1–0), ^{13}CO(1–0), and $C^{18}O$(1–0), is spatially distributed across NGC 3627 in comparison with the spatial distribution of bulk molecular gas (CO(2–1) emission) and star formation (Hα emission). We also investigate line profiles of denser molecular gas towards the bar ends. We list our key results here.

(i) We first investigate how the observed line intensities vary as a function of the CO(2–1) emission and, therefore, as a function of the bulk molecular gas. We find that all lines show brighter emission towards regions of brighter CO emission. To inspect the second-order deviations, we investigate the ratio of the lines with respect to CO. We find that the HCN, HNC, and HCO^+ to CO(2–1) ratios positively correlate with CO(2–1) emission, while the remaining lines (^{13}CO and $C^{18}O$) show the opposite trend and do not correlate with CO(2–1) emission. Moreover, we test if these line ratios can trace different density distributions and investigate the scatter in the ratio with increasing CO intensity. We find that HCN, HNC, and HCO^+ to CO(2–1) line ratios show greater scatter, which suggests that they trace densities above the mean molecular gas density, but it can also be driven by the other effects.

(ii) We investigate how the line intensities vary as a function of Hα emission. We find that all line intensities increase towards brighter Hα emission. Furthermore, we see that the line ratios to CO(2–1) do not vary significantly with Hα emission. Therefore, the line ratios show no correlation with recent star formation.

(iii) We detect significant emission in HCN, HCO^+, HNC, ^{13}CO, and $C^{18}O$ towards the brightest regions in NGC 3627 – the centre and the bar ends. Therefore, we check for trends with morphological features that describe the galaxy. The structure of the galaxy is influencing line intensities. We find that all lines show the brightest emission towards the centre and bar ends within NGC 3627. The line ratios reflect the environment: line to CO(2–1) ratios appear to be slightly higher in the centre than in the bar ends. This is a direct cause of what has been described in the former two points, i.e. looking at line intensities as a function of CO(2–1) and Hα. Stacking by these properties involves multiple different environments within the bins and therefore affects the trends we have seen.

(iv) We measure the velocity dispersion of HCN and CO(2–1) line emission for sightlines towards the centre and bar ends. Overall, HCN and CO(2–1) velocity dispersion increase with CO(2–1) line brightness, spanning ranges from 15 to 75 km s^{-1} (20–80 km s^{-1}) in HCN (CO(2–1)), while CO(2–1) changes by a factor of 1.4. The HCN velocity dispersion is lower by a few km s^{-1} than the velocity dispersion measured in CO(2–1). Sightlines towards the centre and bar ends are located in a different part of Fig. 6. Sightlines towards the bar end exhibit considerably lower HCN (from 15 to 30 km s^{-1}) and CO(2–1) velocity dispersions (from 20 to 35 km s^{-1}) than the sightlines from the centre (from $\sim$60 to 80 km s^{-1} in both HCN and CO(2–1)), despite having similar CO(2–1) intensity ($\sim$700 and 1000 K km s^{-1} towards bar ends and centre, respectively). The difference between measured HCN and CO(2–1) velocity dispersions in the centre and bar ends could be explained due to several effects, such as IR pumping of HCN in the centre, HCN and CO(2–1) populating different orbits, and the difference in the gas mean densities from the centre and bar ends.

(v) We have probed the role of the environment on setting the star formation and thus checked the variation of the star formation efficiency with respect to the dense gas fraction on $\sim$100 pc scales across two different environments (the centre and the bar ends). We see that they have different properties, e.g. the fraction of the denser gas to the bulk molecular gas does not change in the bar end as much as in the centre. The Hα/HCN ratio, however, depends on the environment and it appears to be higher in the bar ends than in the centre. These results agree well with previous studies of $f_{\rm dense}$ and $\rm SFE_{dense}$ at coarser resolutions (Usero et al. 2015; Bigiel et al. 2016; Jiménez-Donaire et al. 2019). One possible explanation is that HCN does not trace the same amount of the denser gas in these environments, i.e. it belongs to different parts of the density distributions that describe molecular gas within these regions (lognormal and power-law tail in the centre and in the bar end, respectively). Another interpretation of this result is that gas dynamics set the star formation on these scales and therefore set the star formation efficiency of the denser gas. Since we only use extinction-corrected Hα emission as the star formation tracer, our results might be biased in the centre of NGC 3627.

(vi) The dynamical effects in the bar ends of NGC 3627 can enhance collisions that trigger local star formation. To investigate this, we compare the spectra of CO(2–1), HCN, and HCO^+ towards the northern and the southern bar end. We find that HCN and HCO^+ have multiple velocity components associated with the CO(2–1) velocity components indicating that these gas motions coming from the spiral and the bar seen in CO(2–1) (Beuther et al. 2017) contain the denser gas. Furthermore, we note that denser gas can get piled up in the bar ends where it interacts and enhance the star formation.

Our work demonstrates the importance of pushing the observations towards high angular resolution and sensitivity to resolve and detect dense gas tracers on the scales of individual GMCs. In the future, we plan to further investigate the dynamics of the dense molecular gas, in order to understand the observed differences between environments in galaxies, such as the centre and the bar ends. It will be important to extend this work to even higher sensitivity observations, allowing us to begin to observe even fainter molecular lines in nearby galaxies (the high-J transitions of the dense molecular gas and even fainter tracers of dense molecular gas, i.e. N_2H^+). Doing so would further our understanding of the densest ISM phase(s), and its ability to form stars.

ACKNOWLEDGEMENTS

This work is based on IRAM/NOEMA observations carried out under project number W17BP, and the EMPIRE large program number 206-14 with the IRAM 30-m telescope. IRAM is supported by INSU/CNRS (France), MPG (Germany), and IGN (Spain). IB, ATB, FB, JPu, and JSdB would like to acknowledge the funding provided from the European Union's Horizon 2020 Framework Programme (grant agreement no. 726384/Empire). CE acknowledges funding from the Deutsche Forschungsgemeinschaft (DFG) Sachbeihilfe, grant number BI1546/3-1. JPe and CHC acknowledge support by the Programme National 'Physique et Chimie du Milieu Interstellaire' (PCMI) of CNRS/INSU with INC/INP, cofunded by CEA and CNES. The work of AKL is partially supported by the National Science Foundation under grants no. 1615105, 1615109, and 1653300. AU acknowledges support from the Spanish funding grants PGC2018-094671-B-I00 (MCIU/AEI/FEDER) and PID2019-108765GB-I00 (MICINN). ES, DL, IP, TS, and FS acknowledge funding from the European Research Council (ERC) under the European Union's Horizon 2020 Framework Programme (grant agreement no. 694343). AH was supported by the Programme National Cosmology et Galaxies (PNCG) of CNRS/INSU with INP and IN2P3, cofunded by CEA and CNES, and by the Programme National 'Physique et Chimie du Milieu Interstellaire' (PCMI) of CNRS/INSU with

INC/INP cofunded by CEA and CNES. CF is supported by the National Science Foundation under Award No. 1903946 and acknowledges funding from the European Research Council (ERC) under the European Union's Horizon 2020 Framework Programme (grant agreement no. 694343). KK gratefully acknowledges funding from the German Research Foundation (DFG) in the form of an Emmy Noether Research Group (grant number KR4598/2-1, PI: Kreckel). MC and JMDK gratefully acknowledge funding from the Deutsche Forschungsgemeinschaft (DFG, German Research Foundation) through an Emmy Noether Research Group (grant number KR4801/1-1) and the DFG Sachbeihilfe (grant number KR4801/2-1), and from the European Research Council (ERC) under the European Union's Horizon 2020 Framework Programme via the ERC Starting Grant MUSTANG (grant agreement number 714907). SCOG, RSK, and MCS acknowledge support from the Deutsche Forschungsgemeinschaft (DFG) via the Collaborative Research Center (SFB 881, Project-ID 138713538) 'The Milky Way System' (subprojects A1, B1, B2, and B8) and from the Heidelberg cluster of excellence (EXC 2181 - 390900948) 'STRUCTURES: A unifying approach to emergent phenomena in the physical world, mathematics, and complex data', funded by the German Excellence Strategy. RSK also thanks for funding form the European Research Council in the ERC Synergy Grant 'ECOGAL – Understanding our Galactic ecosystem: From the disk of the Milky Way to the formation sites of stars and planets' (project ID 855130). ER acknowledges the support of the Natural Sciences and Engineering Research Council of Canada (NSERC), funding reference number RGPIN-2017-03987. MCS acknowledges financial support from the German Research Foundation (DFG) via the Collaborative Research Centre (SFB 881, Project-ID 138713538) 'The Milky Way System' (subprojects A1, B1, B2, and B8). MQ acknowledges support from the research project PID2019-106027GA-C44 from the Spanish Ministerio de Ciencia e Innovación. TGW acknowledges funding from the European Research Council (ERC) under the European Union's Horizon 2020 Framework Programme (grant agreement no. 694343).

This paper makes use of the following ALMA data: ADS/JAO.ALMA#2015.1.00956.S. ALMA is a partnership of ESO (representing its member states), NSF (USA), and NINS (Japan), together with NRC (Canada), MOST and ASIAA (Taiwan), and KASI (Republic of Korea), in cooperation with the Republic of Chile. The Joint ALMA Observatory is operated by ESO, AUI/NRAO, and NAOJ. The National Radio Astronomy Observatory is a facility of the National Science Foundation operated under cooperative agreement by Associated Universities, Inc.

DATA AVAILABILITY

The data used in this paper will be shared on reasonable request to the corresponding author.

REFERENCES

Anand G. S. et al., 2021, MNRAS, 501, 3621
Anderson C. N. et al., 2014, ApJ, 793, 37
André P., Di Francesco J., Ward-Thompson D., Inutsuka S.-I., Pudritz R. E., Pineda J. E., 2014, in Beuther H., Klessen R. S., Dullemond C. P., Henning T., eds, Protostars and Planets VI. Univ. Arizona Press, Tucson, AZ, p. 27
Athanassoula E., 1992, MNRAS, 259, 345
Baldwin J. A., Phillips M. M., Terlevich R., 1981, PASP, 93, 5
Barnes P. J., Muller E., Indermuehle B., O'Dougherty S. N., Lowe V., Cunningham M., Hernandez A. K., Fuller G. A., 2015, ApJ, 812, 6
Barnes A. T., Longmore S. N., Battersby C., Bally J., Kruijssen J. M. D., Henshaw J. D., Walker D. L., 2017, MNRAS, 469, 2263
Barnes A. T. et al., 2020a, MNRAS, 497, 1972
Barnes A. T., Longmore S. N., Dale J. E., Krumholz M. R., Kruijssen J. M. D., Bigiel F., 2020b, MNRAS, 498, 4906
Benjamin R. A. et al., 2005, ApJ, 630, L149
Beuther H., Meidt S., Schinnerer E., Paladino R., Leroy A., 2017, A&A, 597, A85
Bigiel F. et al., 2016, ApJ, 822, L26
Bolatto A. D., Wolfire M., Leroy A. K., 2013, ARA&A, 51, 207
Brouillet N., Muller S., Herpin F., Braine J., Jacq T., 2005, A&A, 429, 153
Buchbender C. et al., 2013, A&A, 549, A17
Burton M. G. et al., 2013, Publ. Astron. Soc. Aust., 30, e044
Caldú-Primo A., Schruba A., 2016, AJ, 151, 34
Calzetti D., Armus L., Bohlin R. C., Kinney A. L., Koornneef J., Storchi-Bergmann T., 2000, ApJ, 533, 682
Calzetti D. et al., 2007, ApJ, 666, 870
Casasola V., Hunt L. K., Combes F., García-Burillo S., Neri R., 2011, A&A, 527, A92
Caselli P., Walmsley C. M., Terzieva R., Herbst E., 1998, ApJ, 499, 234
Chemin L., Cayatte V., Balkowski C., Marcelin M., Amram P., van Driel W., Flores H., 2003, A&A, 405, 89
Chen H., Braine J., Gao Y., Koda J., Gu Q., 2017, ApJ, 836, 101
Chevance M. et al., 2020, MNRAS, 493, 2872
Colombo D. et al., 2014, ApJ, 784, 3
Cormier D. et al., 2018, MNRAS, 475, 3909
Dame T. M., Hartmann D., Thaddeus P., 2001, ApJ, 547, 792
den Brok J. S. et al., 2021, MNRAS, 504, 3221
Domínguez A. et al., 2013, ApJ, 763, 145
Egusa F., Hirota A., Baba J., Muraoka K., 2018, ApJ, 854, 90
Engargiola G., Plambeck R. L., Rosolowsky E., Blitz L., 2003, ApJS, 149, 343
Evans N. J., II, Heiderman A., Vutisalchavakul N., 2014, ApJ, 782, 114
Faesi C. M., Lada C. J., Forbrich J., 2018, ApJ, 857, 19
Federrath C., Klessen R. S., 2012, ApJ, 761, 156
Federrath C., Klessen R. S., 2013, ApJ, 763, 51
Filho M. E., Barthel P. D., Ho L. C., 2000, ApJS, 129, 93
Gallagher M. J. et al., 2018a, ApJ, 858, 90
Gallagher M. J. et al., 2018b, ApJ, 868, L38
Gao Y., Solomon P. M., 2004a, ApJS, 152, 63
Gao Y., Solomon P. M., 2004b, ApJ, 606, 271
Gao Y., Carilli C. L., Solomon P. M., Vanden Bout P. A., 2007, ApJ, 660, L93
Garcia A. M., 1993, A&AS, 100, 47
García-Burillo S. et al., 2003, in Collin S., Combes F., Shlosman I., eds, ASP Conf. Ser. Vol. 290, Active Galactic Nuclei: From Central Engine to Host Galaxy. Astron. Soc. Pac., San Francisco, p. 423
García-Burillo S., Usero A., Alonso-Herrero A., Graciá-Carpio J., Pereira-Santaella M., Colina L., Planesas P., Arribas S., 2012, A&A, 539, A8
García-Burillo S. et al., 2014, A&A, 567, A125
Girichidis P., Konstandin L., Whitworth A. P., Klessen R. S., 2014, ApJ, 781, 91
Graciá-Carpio J., García-Burillo S., Planesas P., 2008, Ap&SS, 313, 331
Graninger D. M., Herbst E., Öberg K. I., Vasyunin A. I., 2014, ApJ, 787, 74
Gratier P. et al., 2012, A&A, 542, A108
Grier C. J., Mathur S., Ghosh H., Ferrarese L., 2011, ApJ, 731, 60
Hacar A., Bosman A. D., van Dishoeck E. F., 2020, A&A, 635, A4
Harada N. et al., 2015, A&A, 584, A102
Heiderman A., Evans N. J., II, Allen L. E., Huard T., Heyer M., 2010, ApJ, 723, 1019
Helfer T. T., Blitz L., 1997, ApJ, 478, 162
Helfer T. T., Thornley M. D., Regan M. W., Wong T., Sheth K., Vogel S. N., Blitz L., Bock D. C. J., 2003, ApJS, 145, 259
Henshaw J. D., Longmore S. N., Kruijssen J. M. D., 2016, MNRAS, 463, L122
Henshaw J. D. et al., 2020, Nat. Astron., 4, 1064
Herrera C. N. et al., 2020, A&A, 634, A121
Heyer M., Dame T. M., 2015, ARA&A, 53, 583
Heyer M. H., Carpenter J. M., Snell R. L., 2001, ApJ, 551, 852

Hirota A., Kuno N., Sato N., Nakanishi H., Tosaki T., Sorai K., 2011, ApJ, 737, 40
Ho L. C., Filippenko A. V., Sargent W. L. W., 1997, ApJS, 112, 315
Hughes A. et al., 2013, ApJ, 779, 46
Jackson J. M., Paglione T. A. D., Ishizuki S., Nguyen-Q-Rieu, 1993, ApJ, 418, L13
Jiang X.-J. et al., 2020, MNRAS, 494, 1276
Jiménez-Donaire M. J. et al., 2017, MNRAS, 466, 49
Jiménez-Donaire M. J. et al., 2019, ApJ, 880, 127
Jones P. A. et al., 2012, MNRAS, 419, 2961
Juneau S., Narayanan D. T., Moustakas J., Shirley Y. L., Bussmann R. S., Kennicutt R. C. J., Vanden Bout P. A., 2009, ApJ, 707, 1217
Kainulainen J., Federrath C., Henning T., 2014, Science, 344, 183
Kauffmann G. et al., 2003, MNRAS, 346, 1055
Kauffmann J., Goldsmith P. F., Melnick G., Tolls V., Guzman A., Menten K. M., 2017, A&A, 605, L5
Kennicutt R. C., Evans N. J., 2012, ARA&A, 50, 531
Kennicutt R. C., Jr et al., 2009, ApJ, 703, 1672
Kepley A. A., Leroy A. K., Frayer D., Usero A., Marvil J., Walter F., 2014, ApJ, 780, L13
Kepley A. A. et al., 2018, ApJ, 862, 120
Kewley L. J., Dopita M. A., Sutherland R. S., Heisler C. A., Trevena J., 2001, ApJ, 556, 121
Kim J. et al., 2021, MNRAS, 504, 487
Knudsen K. K., Walter F., Weiss A., Bolatto A., Riechers D. A., Menten K., 2007, ApJ, 666, 156
Kohno K., Matsushita S., Vila-Vilaró B., Okumura S. K., Shibatsuka T., Okiura M., Ishizuki S., Kawabe R., 2001, in Knapen J. H., Beckman J. E., Shlosman I., Mahoney T. J., eds, ASP Conf. Ser. Vol. 249, The Central Kiloparsec of Starbursts and AGN: The La Palma Connection. Astron. Soc. Pac., San Francisco, p. 672
Kreckel K. et al., 2019, ApJ, 887, 80
Krips M., Neri R., García-Burillo S., Martín S., Combes F., Graciá-Carpio J., Eckart A., 2008, ApJ, 677, 262
Kroupa P., 2001, MNRAS, 322, 231
Kruijssen J. M. D., Longmore S. N., 2014, MNRAS, 439, 3239
Kruijssen J. M. D., Longmore S. N., Elmegreen B. G., Murray N., Bally J., Testi L., Kennicutt R. C., 2014, MNRAS, 440, 3370
Kruijssen J. M. D., Schruba A., Hygate A. P. S., Hu C.-Y., Haydon D. T., Longmore S. N., 2018, MNRAS, 479, 1866
Kruijssen J. M. D. et al., 2019, Nature, 569, 519
Krumholz M. R., Kruijssen J. M. D., 2015, MNRAS, 453, 739
Lada C. J., Lada E. A., 2003, ARA&A, 41, 57
Lada C. J., Lombardi M., Alves J. F., 2010, ApJ, 724, 687
Lada C. J., Forbrich J., Lombardi M., Alves J. F., 2012, ApJ, 745, 190
Larson R. B., 1981, MNRAS, 194, 809
Law C. J., Zhang Q., Ricci L., Petitpas G., Jiménez-Donaire M. J., Ueda J., Lu X., Dunham M. M., 2018, ApJ, 865, 17
Lee J. C. et al., 2009, ApJ, 706, 599
Lee J. C. et al., 2021, preprint (arXiv:2101.02855)
Leroy A. K. et al., 2009, AJ, 137, 4670
Leroy A. K. et al., 2016, ApJ, 831, 16
Leroy A. K. et al., 2017a, ApJ, 835, 217
Leroy A. K. et al., 2017b, ApJ, 846, 71
Leroy A. K. et al., 2019, ApJS, 244, 24
Leroy A. K. et al., 2021a, ApJS, in press (arXiv:2104.07665)
Leroy A. K. et al., 2021b, ApJS, in press (arXiv:2104.07739)
Lombardi M., Bouy H., Alves J., Lada C. J., 2014, A&A, 566, A45
Longmore S. N. et al., 2013, MNRAS, 429, 987
López-Corredoira M., Cabrera-Lavers A., Mahoney T. J., Hammersley P. L., Garzón F., González-Fernández C., 2007, AJ, 133, 154
Maeda F., Ohta K., Fujimoto Y., Habe A., 2020, MNRAS, 493, 5045
Matsushita S., Trung D.-V., Boone F., Krips M., Lim J., Muller S., 2015, ApJ, 799, 26
Meidt S. E. et al., 2018, ApJ, 854, 100
Meier D. S. et al., 2015, ApJ, 801, 63
Meijerink R., Spaans M., 2005, A&A, 436, 397
Meijerink R., Spaans M., Israel F. P., 2007, A&A, 461, 793
Mizuno A., Fukui Y., 2004, in Clemens D., Shah R., Brainerd T., eds, ASP Conf. Ser. Vol. 317, Milky Way Surveys: The Structure and Evolution of our Galaxy. Astron. Soc. Pac., San Francisco, p. 59
Moriguchi Y., Yamaguchi N., Onishi T., Mizuno A., Fukui Y., 2001, PASJ, 53, 1025
Murphy E. J. et al., 2011, ApJ, 737, 67
Murphy E. J. et al., 2015, ApJ, 813, 118
Osterbrock D. E., 1989, Ann. New York Acad. Sci., 571, 99
Osterbrock D. E., 1993, ApJ, 404, 551
Paladino R., Murgia M., Tarchi A., Moscadelli L., Comito C., 2008, A&A, 485, 679
Papadopoulos P. P., 2007, ApJ, 656, 792
Pety J., 2005, in Casoli F., Contini T., Hameury J. M., Pagani L., eds, SF2A-2005: Semaine de l'Astrophysique Francaise. EDP Sciences, Les Ulis, France, p. 721
Pety J., Rodríguez-Fernández N., 2010, A&A, 517, A12
Pety J. et al., 2013, ApJ, 779, 43
Pety J. et al., 2017, A&A, 599, A98
Privon G. C. et al., 2015, ApJ, 814, 39
Querejeta M. et al., 2019, A&A, 625, A19
Regan M. W., Thornley M. D., Helfer T. T., Sheth K., Wong T., Vogel S. N., Blitz L., Bock D. C. J., 2001, ApJ, 561, 218
Renaud F. et al., 2015, MNRAS, 454, 3299
Rodriguez-Fernandez N., Pety J., Gueth F., 2008, Single-Dish Observation and Processing to Produce the Short-Spacing Information for a Millimeter Interferometer. Technical Report, IRAM Memo 2008-2
Rosolowsky E., 2007, ApJ, 654, 240
Rosolowsky E., Leroy A., 2006, PASP, 118, 590
Rosolowsky E., Engargiola G., Plambeck R., Blitz L., 2003, ApJ, 599, 258
Rosolowsky E. et al., 2021, MNRAS, 502, 1218
Sandstrom K. M. et al., 2013, ApJ, 777, 5
Schilke P., Walmsley C. M., Pineau Des Forets G., Roueff E., Flower D. R., Guilloteau S., 1992, A&A, 256, 595
Schinnerer E. et al., 2013, ApJ, 779, 42
Schinnerer E. et al., 2019, ApJ, 887, 49
Schneider N. et al., 2015a, A&A, 575, A79
Schneider N. et al., 2015b, A&A, 578, A29
Schneider N. et al., 2016, A&A, 587, A74
Schöier F. L., van der Tak F. F. S., van Dishoeck E. F., Black J. H., 2005, A&A, 432, 369
Schruba A., Leroy A. K., Walter F., Sandstrom K., Rosolowsky E., 2010, ApJ, 722, 1699
Schruba A. et al., 2011, AJ, 142, 37
Schruba A. et al., 2017, ApJ, 835, 278
Sheth K., Vogel S. N., Regan M. W., Thornley M. D., Teuben P. J., 2005, ApJ, 632, 217
Sheth K., Vogel S. N., Wilson C. D., Dame T. M., 2008, ApJ, 675, 330
Shetty R., Kelly B. C., Rahman N., Bigiel F., Bolatto A. D., Clark P. C., Klessen R. S., Konstandin L. K., 2014a, MNRAS, 437, L61
Shetty R., Clark P. C., Klessen R. S., 2014b, MNRAS, 442, 2208
Shirley Y. L., 2015, PASP, 127, 299
Soida M., Urbanik M., Beck R., Wielebinski R., Balkowski C., 2001, A&A, 378, 40
Solomon P. M., Rivolo A. R., Barrett J., Yahil A., 1987, ApJ, 319, 730
Sormani M. C., Barnes A. T., 2019, MNRAS, 484, 1213
Sormani M. C., Binney J., Magorrian J., 2015a, MNRAS, 449, 2421
Sormani M. C., Binney J., Magorrian J., 2015b, MNRAS, 451, 3437
Sormani M. C., Tress R. G., Glover S. C. O., Klessen R. S., Battersby C. D., Clark P. C., Hatchfield H. P., Smith R. J., 2020, MNRAS, 497, 5024
Stetson P. B., 1987, PASP, 99, 191
Sun J. et al., 2018, ApJ, 860, 172
Sun J. et al., 2020, ApJ, 901, L8
Tacconi L. J., Genzel R., Blietz M., Cameron M., Harris A. I., Madden S., 1994, ApJ, 426, L77
Talbi D., Ellinger Y., Herbst E., 1996, A&A, 314, 688
Thilker D. A., Braun R., Walterbos R. A. M., 2000, AJ, 120, 3070
Thuan T. X., Izotov Y. I., 2005, ApJS, 161, 240

Tress R. G., Sormani M. C., Glover S. C. O., Klessen R. S., Battersby C. D., Clark P. C., Hatchfield H. P., Smith R. J., 2020, MNRAS, 499, 4455
Usero A., García-Burillo S., Fuente A., Martín-Pintado J., Rodríguez-Fernández N. J., 2004, A&A, 419, 897
Usero A. et al., 2015, AJ, 150, 115
van der Tak F. F. S., Black J. H., Schöier F. L., Jansen D. J., van Dishoeck E. F., 2007, A&A, 468, 627
Véron-Cetty M. P., Véron P., 2006, A&A, 455, 773
Viaene S., Forbrich J., Fritz J., 2018, MNRAS, 475, 5550
Viti S. et al., 2014, A&A, 570, A28
Walter F. et al., 2017, ApJ, 835, 265
Watanabe Y., Nishimura Y., Sorai K., Sakai N., Kuno N., Yamamoto S., 2019, ApJS, 242, 26
Wężgowiec M., Soida M., Bomans D. J., 2012, A&A, 544, A113
Wu J., Evans N. J., II, Gao Y., Solomon P. M., Shirley Y. L., Vanden Bout P. A., 2005, ApJ, 635, L173
Wu J., Evans N. J., II, Shirley Y. L., Knez C., 2010, ApJS, 188, 313
Yamaguchi R., Saito H., Mizuno N., Mine Y., Mizuno A., Ogawa H., Fukui Y., 1999, PASJ, 51, 791

APPENDIX A: ADDITIONAL FIGURES

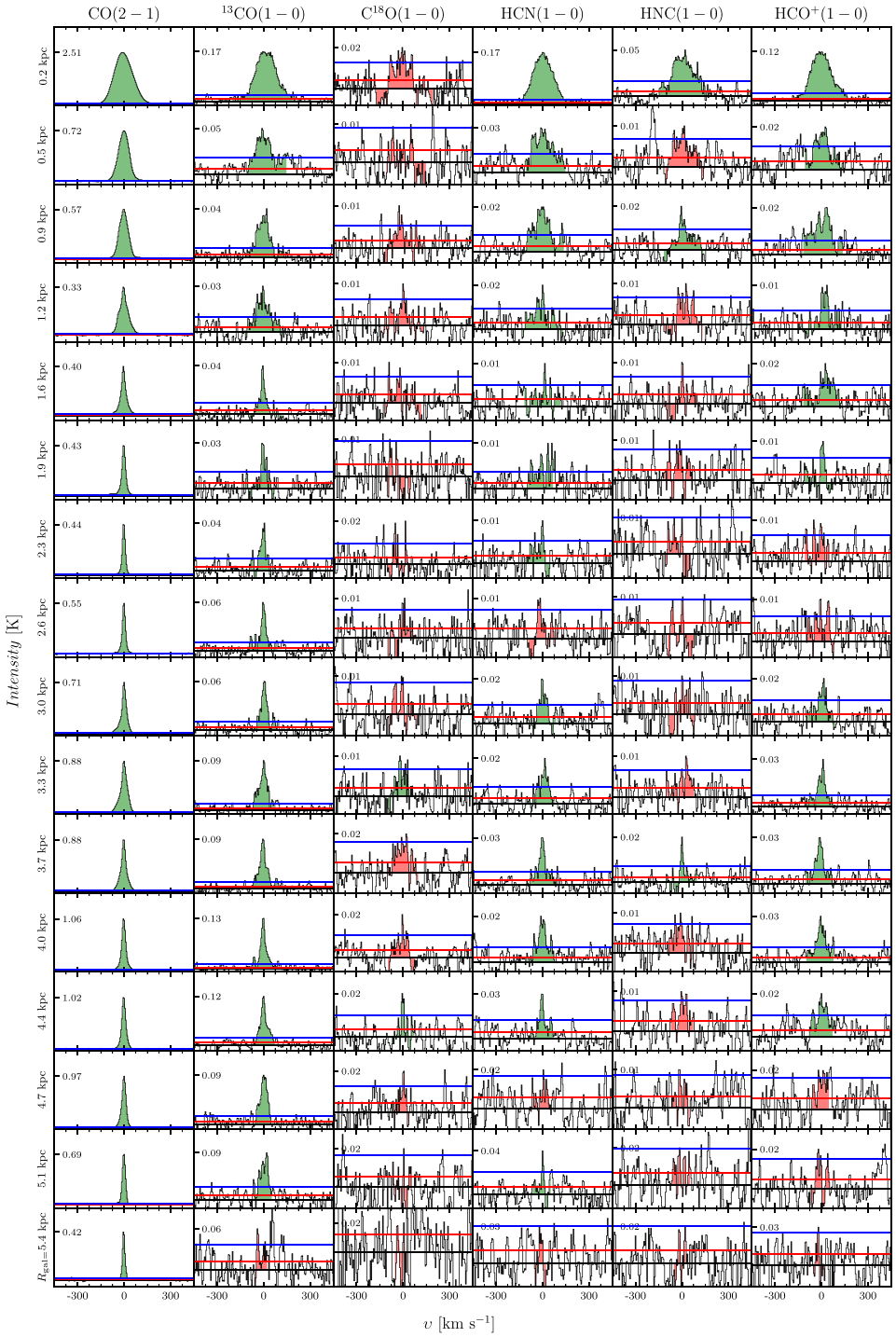

Figure A1. Radially stacked spectra of all lines (each column respectively). Median values of the radius for each bin are shown on the left-hand side of every row. Shaded regions show the integration window defined using CO(2–1) line. The colour of shaded regions corresponds to whether the integrated intensity of the stacked line is defined as an upper limit (red) or not (green), as described in Section 3.2. The black horizontal line shows the 0-level. The red horizontal line shows the rms of the stacked profile, whereas the blue line represents three times the rms.

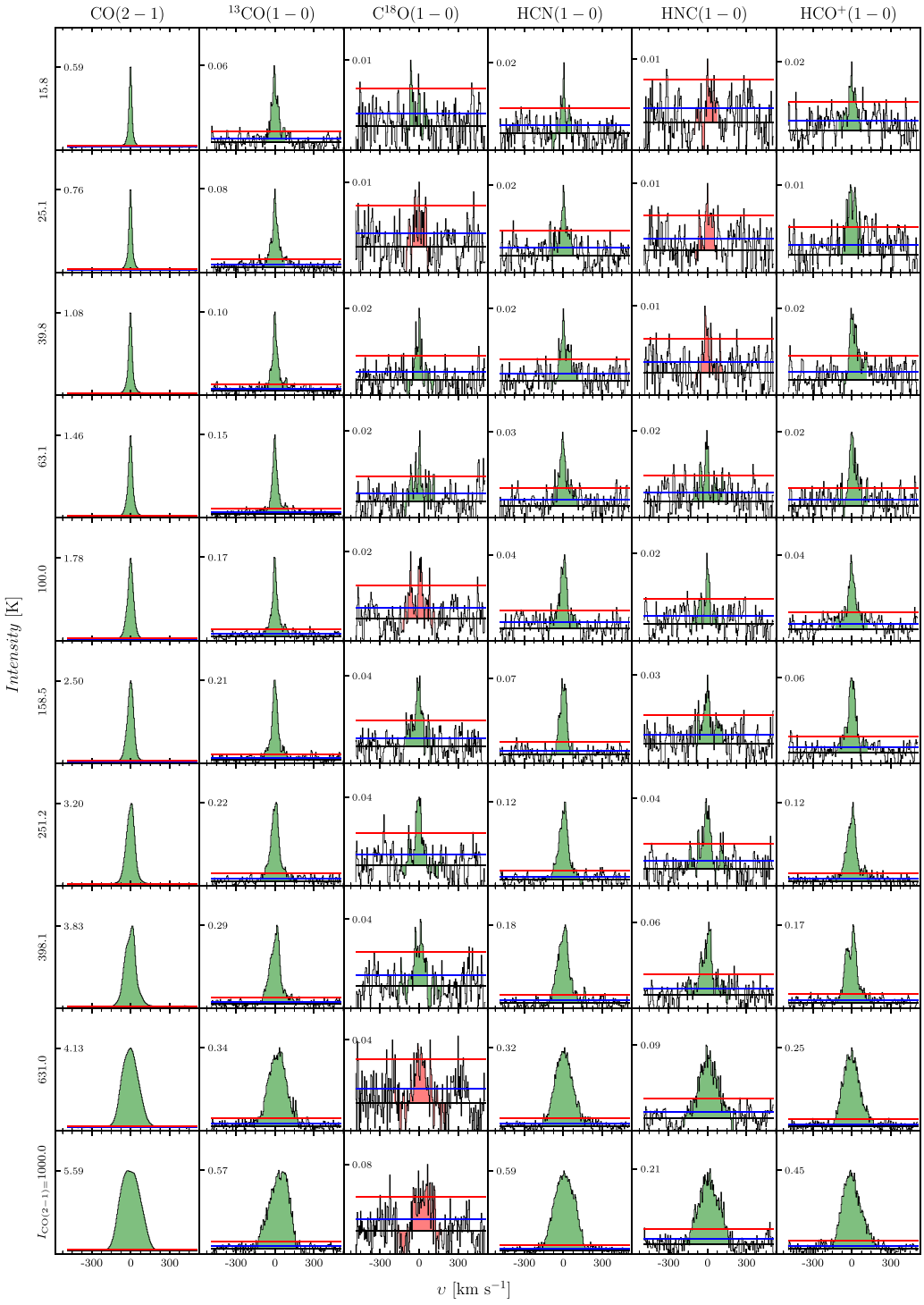

Figure A2. Same as in the Fig. A1, but for stacked spectra by the CO(2–1) integrated intensity. The CO(2–1) bins are in units of K km s^{-1}.

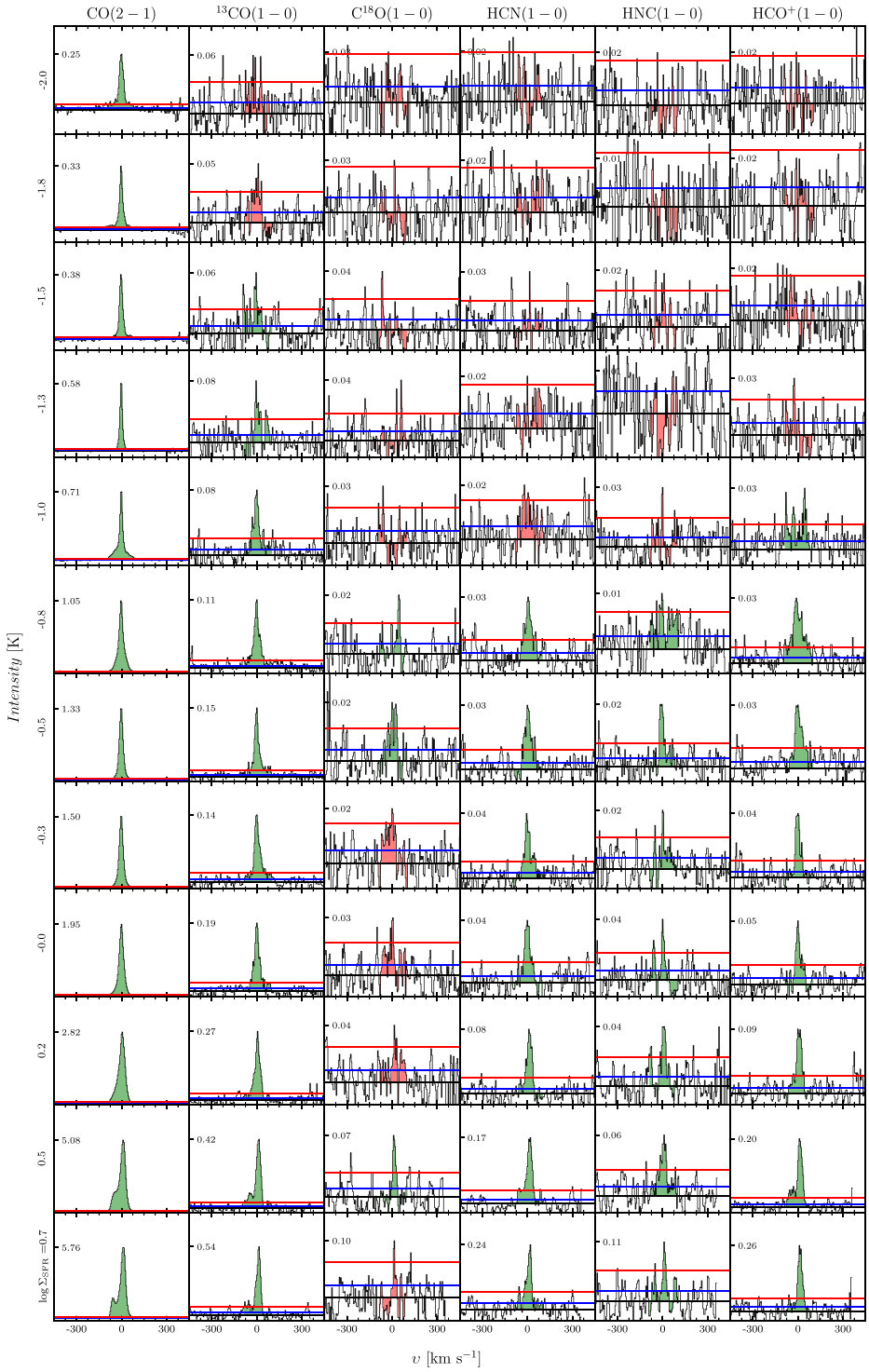

Figure A3. Same as in the Fig. A1, but for stacked spectra by the Σ_{SFR}. We show the Σ_{SFR} bins in logarithmic scale in units of $M_\odot$ yr^{-1} kpc^{-2}.

[1]*Argelander-Institut für Astronomie, Universität Bonn, Auf dem Hügel 71, D-53121 Bonn, Germany*
[2]*IRAM, 300 rue de la Piscine, F-38406 Saint Martin d'Hères, France*
[3]*LERMA, Observatoire de Paris, PSL Research University, CNRS, Sorbonne Universités, F-75014 Paris, France*
[4]*Department of Astronomy, The Ohio State University, 4055 McPherson Laboratory, 140 West 18th Avenue, Columbus, OH 43210, USA*
[5]*Observatorio Astronómico Nacional (IGN), C/ Alfonso XII 3, E-28014 Madrid, Spain*
[6]*Max Planck Institut für Astronomie, Königstuhl 17, D-69117 Heidelberg, Germany*
[7]*Sterrenkundig Observatorium, Universiteit Gent, Krijgslaan 281 S9, B-9000 Gent, Belgium*
[8]*European Southern Observatory, Karl-Schwarzschild Straße 2, D-85748 Garching bei München, Germany*
[9]*Univ Lyon, Univ Lyon1, ENS de Lyon, CNRS, Centre de Recherche Astrophysique de Lyon UMR5574, F-69230 Saint-Genis-Laval, France*
[10]*Université de Toulouse, UPS-OMP, F-31028 Toulouse, France*
[11]*CNRS, IRAP, Av. du Colonel Roche BP 44346, F-31028 Toulouse cedex 4, France*
[12]*Department of Astronomy, University of Massachusetts Amherst, 710 North Pleasant Street, Amherst, MA 01003, USA*
[13]*Astronomisches Rechen-Institut, Zentrum für Astronomie der Universität Heidelberg, Mönchhofstraße 12-14, D-69120 Heidelberg, Germany*
[14]*INAF – Osservatorio Astrofisico di Arcetri, Largo E. Fermi 5, I-50157 Firenze, Italy*
[15]*Institut für Theoretische Astrophysik, Zentrum für Astronomie, Universität Heidelberg, Albert-Ueberle-Straße 2, D-69120 Heidelberg, Germany*
[16]*Research School of Astronomy and Astrophysics, Australian National University, Canberra, ACT 2611, Australia*
[17]*ARC Centre of Excellence for All Sky Astrophysics in 3 Dimensions (ASTRO 3D), Mount Stromlo Rd Stromlo, Australian Capital Territory 2611, AU, Australia*
[18]*Interdisziplinäres Zentrum für Wissenschaftliches Rechnen, Universität Heidelberg, Im Neuenheimer Feld 205, D-69120 Heidelberg, Germany*
[19]*4-183 CCIS, University of Alberta, Edmonton, AB T6G 2E1, Canada*
[20]*Max Planck Institut für Extraterrestrische Physik, Giessenbachstraße 1, D-85748 Garching, Germany*

This paper has been typeset from a TEX/LATEX file prepared by the author.

APPENDIX B

The dense gas properties and kinematics of one the closest starburst galaxies (NGC253) observed with ALMA

B.1 Quality assessment

This document is based on the quality assesment that has been done for the PHANGS-ALMA CO(2–1) data cubes, and it has been created to do the quality assurance of ALMA Cycle 7 data. In particular, the 3 mm ACA observations of NGC 253. This data set has been processed using PHANGS pipeline in CASA (Leroy et al., 2021a). The cleaning was done using single-scale algorithms, and the user-defined CO(2–1) signal mask. To extract the HCN emission used in analysis (Chapter 5), we flagged HCN(1–0), HCO^+(1–0) and HNCO(4-3) line in the respective spectral window (Figure 5.2).

B.1.1 Summary of input files

This table lists the files that were used for the analysis.

Table B.1: List of Input Files.

Type	File
Data	ngc0253_7m_hcn10.fits
Noise	ngc0253_7m_hcn10_noise.fits
Mask	ngc0253_7m_hcn10_mask.fits
Residuals	ngc0253_7m_hcn10_residual.fits

B.2 Properties of input cube

This table summarises the basic parameters of the data cube.

Table B.2: Basic parameters of input cube.

Galaxy name	PIX SIZE [as] [as]	Channel width [km/s] [km/s]	BMAJ [as] [as]	BMIN [as] [as]	BPA [deg] [deg]	BUNIT	CASA	NX	NY	NZ
ngc0253	3.00	9.91	19.99	10.10	84.22	Jy/beam	CASA 5.6.1-8	240	240	90

B.2.1 Total Flux And Peak Values In/Outside Mask

This table summarises the integrated flux and peak statistics of the data cube (whole cube, inside, and outside the mask).

Table B.3: Basic parameters of input cube.

Galaxy name	Flux [10^4 Jy/beam km/s pix]	Peak [Jy/beam]	Flux_in [%]	Peak_in [Jy/beam]	Flux_out [%]	Peak_out [Jy/beam]
ngc0253	1.65	1.53	102.16	1.53	2.16	0.17

B.2.2 Statistics

Figures B.1, B.2 show the histogram of pixel values in the data and the residuals cubes. Values for the whole cube (black) and inner quarter (blue) are shown.

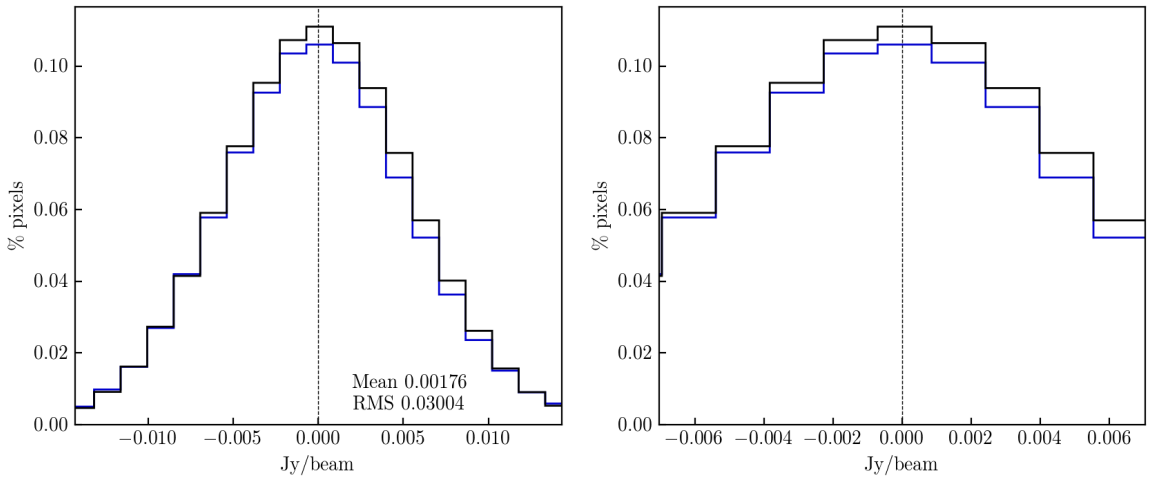

Figure B.1: Histogram of pixel values in the entire data cube (black), inner quarter of FoV of data cube (blue). The two panels show the same data, but the range of the x-axis is modified to investigate behaviour at low intensities. The x-axis of the top panel extends to the 0.5th percentile, and in the bottom panel to the 10th percentile.

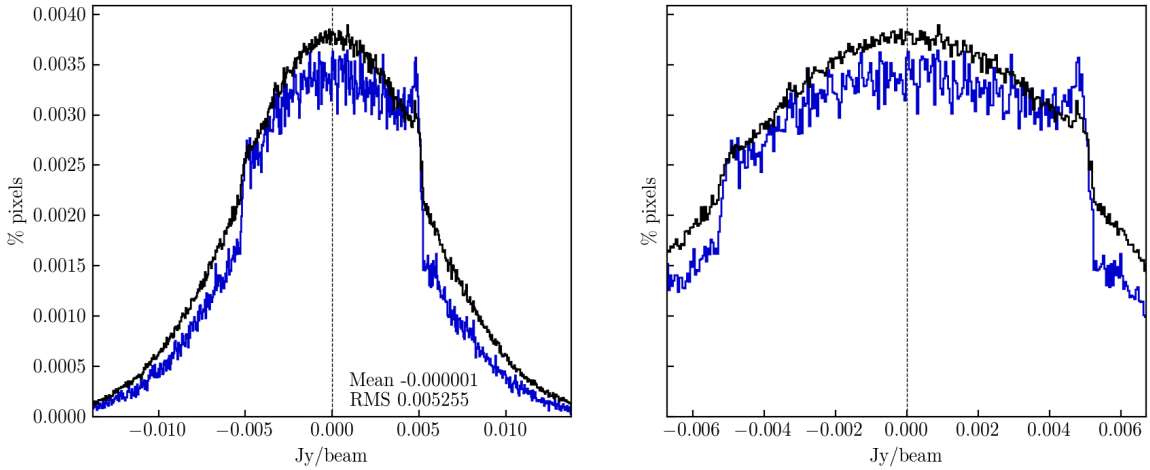

Figure B.2

B.2.3 2D Density Spectra

Figures B.3, B.4, B.5, B.6 show a 2D histogram of pixel values in the data and residuals cubes. The median value in each channel is traced by the black line. The 1st, 25th, 75th and 99th percentiles of the data values in each channel are traced by the white lines. The purple line indicates the peak of the 1D-histogram corresponding to each channel slice. The blue lines indicate 3σ deviation from the median, where σ is a robust sigma estimate of the pixel values, calculated channel-by-channel. RMS0 is defined as the median noise value inside the deconvolution mask (i.e. value is obtained from the noise cube).

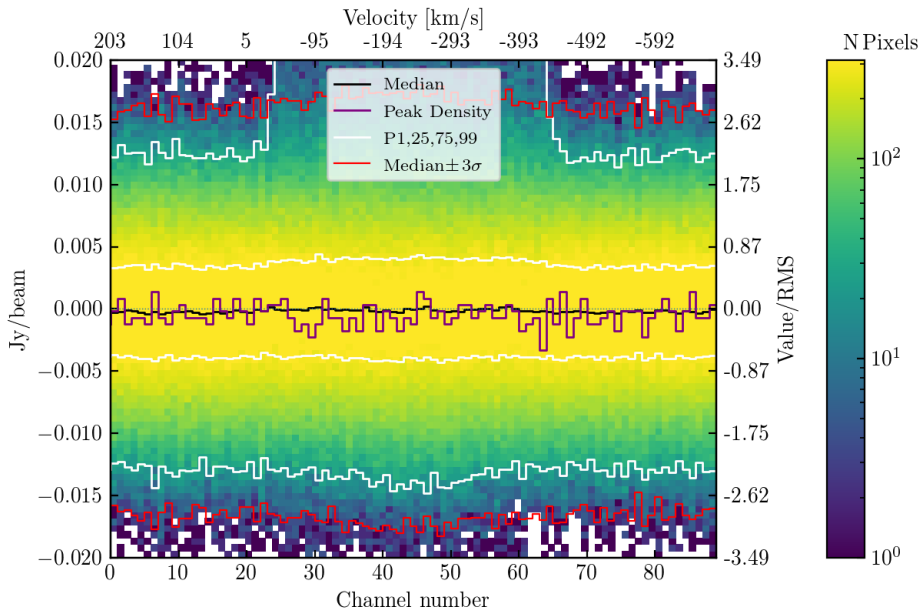

Figure B.3: 2D histogram of pixel values and statistics per channel of the data cube.

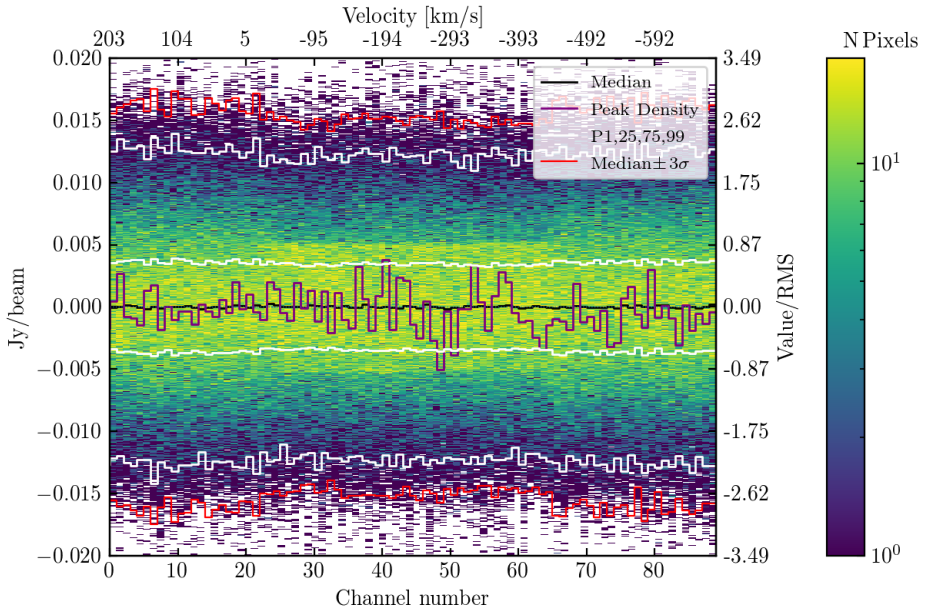

Figure B.4: 2D histogram of pixel values and statistics per channel of the residual cube.

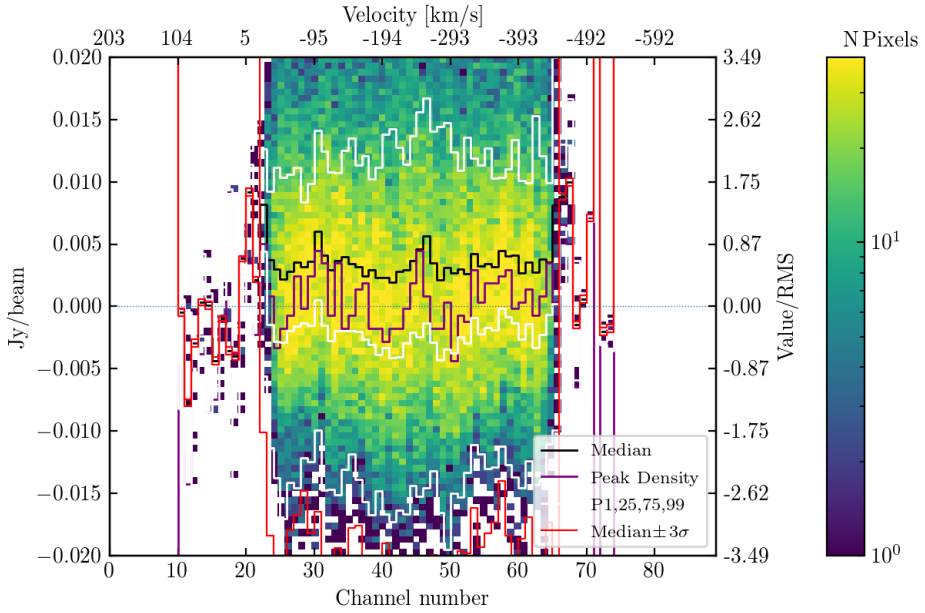

Figure B.5: 2D histogram of pixel values and statistics per channel of the data cube inside the clean mask only.

B.2.4 Noise characterization

The first plot (Figure B.7) shows a two-dimensional pixel density plot and "per-channel" representation of the noise. The second plot (Figure B.8) shows the histogram of noise values in a 2-Dimensional map of the noise (constructed as the mean of the channels in the noise cube).

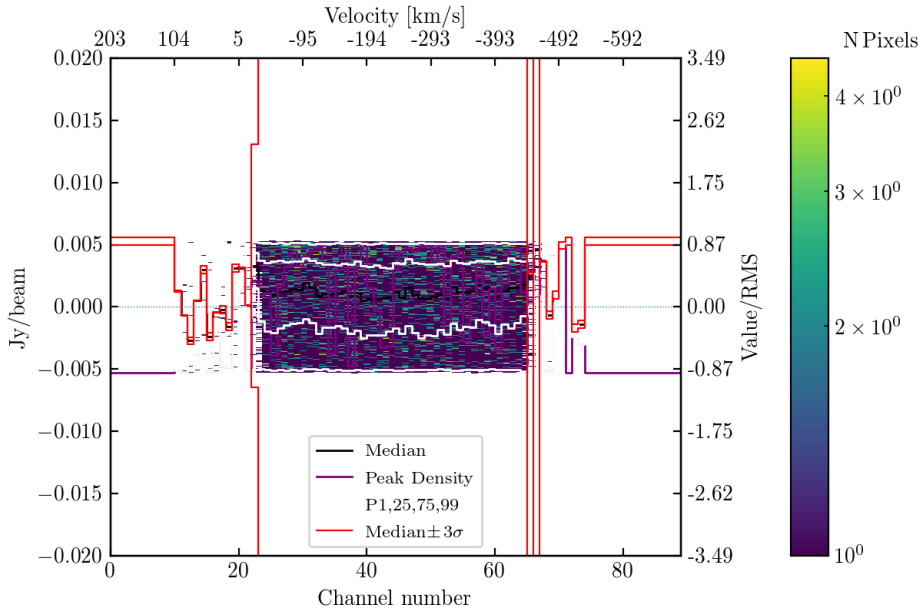

Figure B.6: 2D histogram of pixel values and statistics per channel of the residual cube inside the clean mask only.

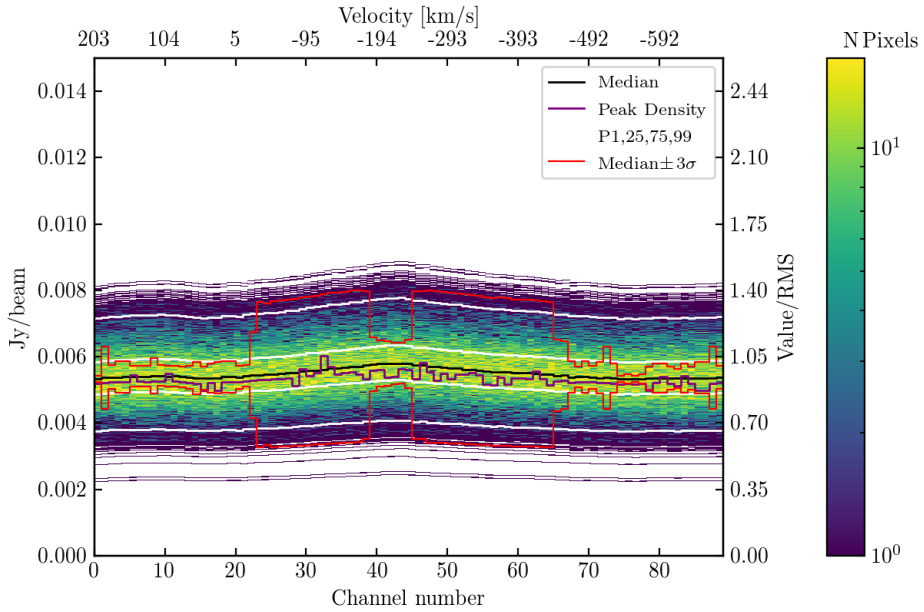

Figure B.7: 2D histogram of pixel values and statistics per channel of the noise cube.

B.2.5 Moment 0 Map

Figure B.9 shows a simple integrated intensity map (direct integration over the entire velocity range). The top (bottom) panel uses a color stretch with a maximum value set to the 10th (30th) percentile.

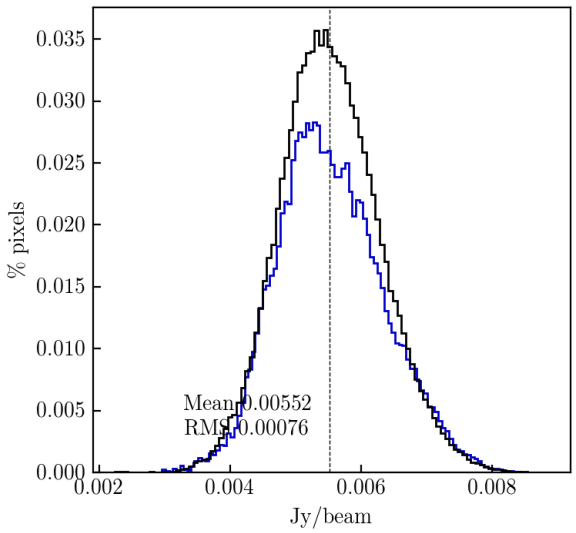

Figure B.8: Per-channel estimates of the r.m.s. from the data cube (red), and the average noise (blue).

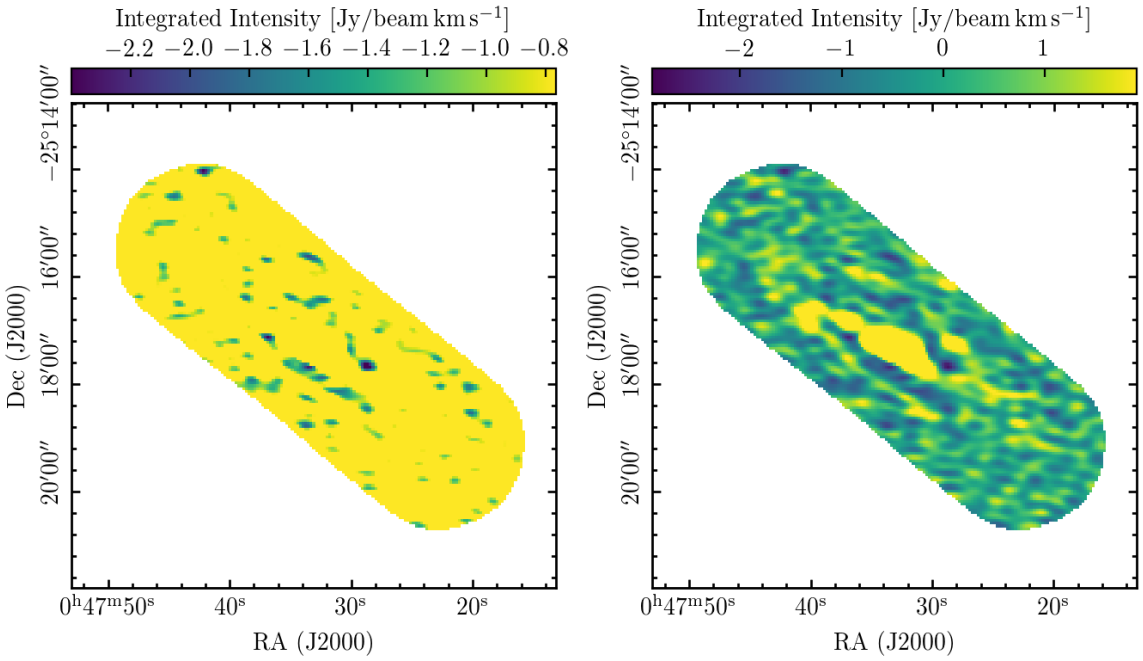

Figure B.9: Simple moment-0 map. Color stretch max is 10th (left) and 30th (right) percentile of pixel intensities.

B.2.6 Channel maps

The following figures (Figure B.10 and later) show the individual channels of the data cube (left), signal-to-noise (middle left), residuals (middle right), and ratio (=signal/residuals) cubes (right).

Table B.4: Properties of 3 mm molecular line observations obtained by ACA across NGC 253.

Line	Transition	Frequency [GHz]	B_{maj} ["]	B_{min} ["]	BPA [deg]	$\Delta\upsilon$ [km s^{-1}]	rms [mK]	Critical density [cm^{-3}]
HCN	1 - 0	88.63	21.40	10.36	83.51	1.65	6.98	2×10^5
HCO^+	1 - 0	89.19	21.40	10.36	83.51	1.64	6.95	4×10^4
$HC^{13}N$	1 - 0	86.34	21.76	10.63	84.95	1.69	7.18	9.7×10^6
$HC^{13}O^+$	1 - 0	86.75	21.76	10.63	84.95	1.69	6.99	6.7×10^5
SiO	2 - 1	85.85	21.76	10.63	84.95	1.68	6.74	10^5
CS	2 - 1	97.98	18.87	9.19	84.88	1.5	8.20	7×10^4
HC_3N	11 - 10	100.07	19.04	8.97	85.67	1.46	8.51	5×10^5

B.3 Additional molecular lines detected by ACA in NGC 253

B.4 SCOUSE

In our work, we use the Semi-automated multi-COmponent Universal Spectral-line fitting Engine (SCOUSE) (Henshaw et al., 2016a, 2019), which is the spectral decomposition algorithm that defines where the line is located within the spectrum and describes such lines using Gaussian fitting. SCOUSE consists of four steps. In the first step, we define a spatial area over which we want to fit the spectra by creating a grid of macropixels, called Spectral Averaging Areas (SAAs). The size of a SAA is a free parameter. In our case, each SAA contains 4 pixels. The spectrum of each SAA represents the averaged spectrum of all the spectra within pixels contained in the SAA. In the second phase, SCOUSE fits the spectrum of each SAA and suggest a model solution assuming the Gaussian line profile. The model solution within each SAA consists of the detected number of Gaussian components, and the fitting parameters: the amplitude, the centroid velocity, and the line width. The criteria for the fit to be considered as successful is that the signal-to-noise ratio of the XX is at least 3. In case when SCOUSE cannot find a proper solution for a fit, the user can manually change the requested signal-to-noise ratio in order for fitting parameters to converge, or fit the respective spectrum manually by selecting the location of spectral line within the spectrum, its peak, and the brightness temperature at which the spectrum reaches the 50 % of its peak. After completing the second phase, SCOUSE has a model solution of each SAAs' spectrum and uses these to fit pixels within each SAA. The third phase is where the user checks the SCOUSE's model solutions for each pixel. Similar to the second phase, the user can change the number of Gaussian components and its fitting parameters. The location of each pixel in the map, and SCOUSE solutions for their spectrum are saved in the textual file in the final, fourth phase.

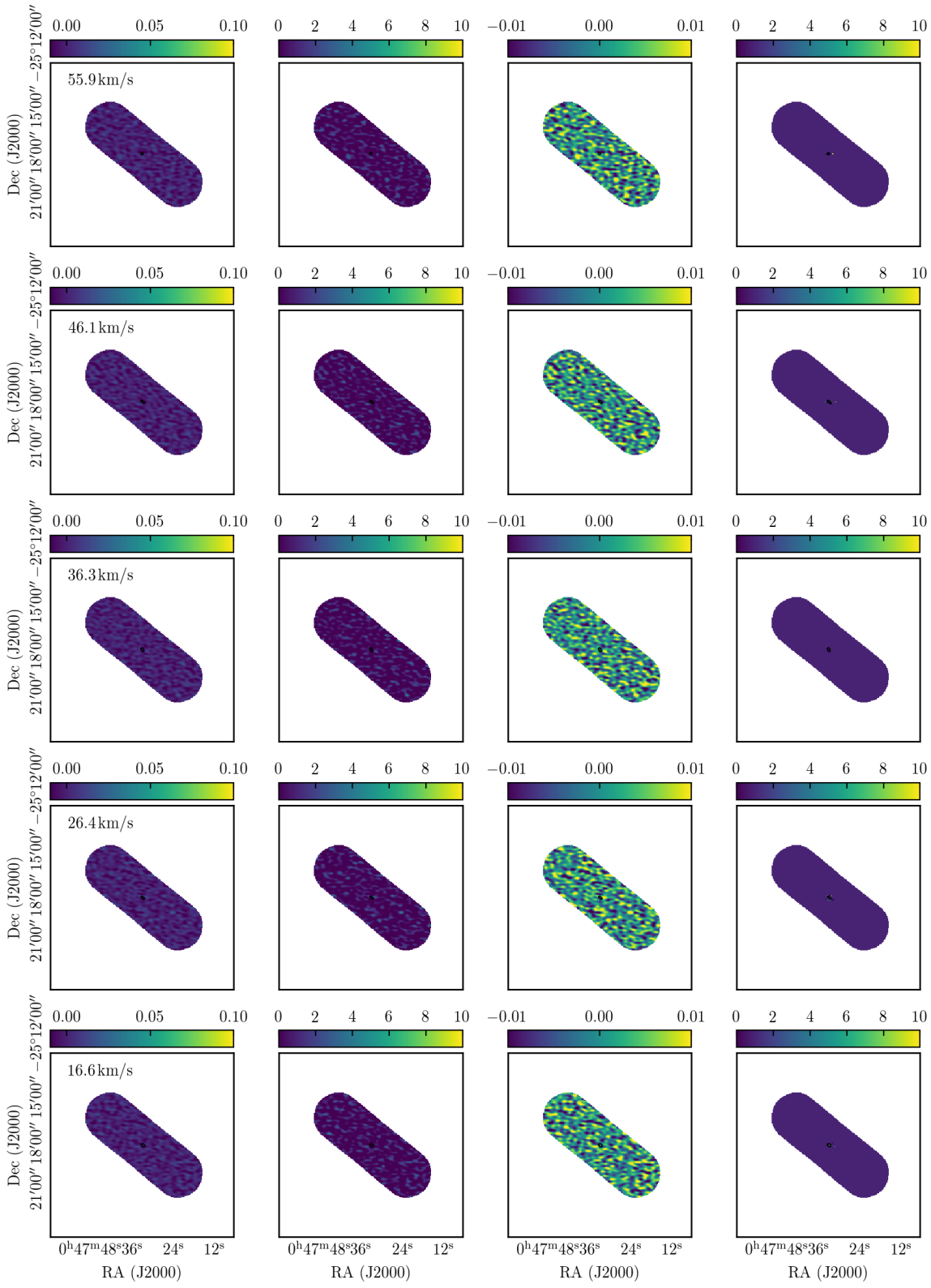

Figure B.10: Channel maps of the HCN data cube (left), signal-to-noise ratio (middle left), residuals (middle right), and ratio of signal and residuals cubes (right). Deconvolution mask is overplotted (black contours).

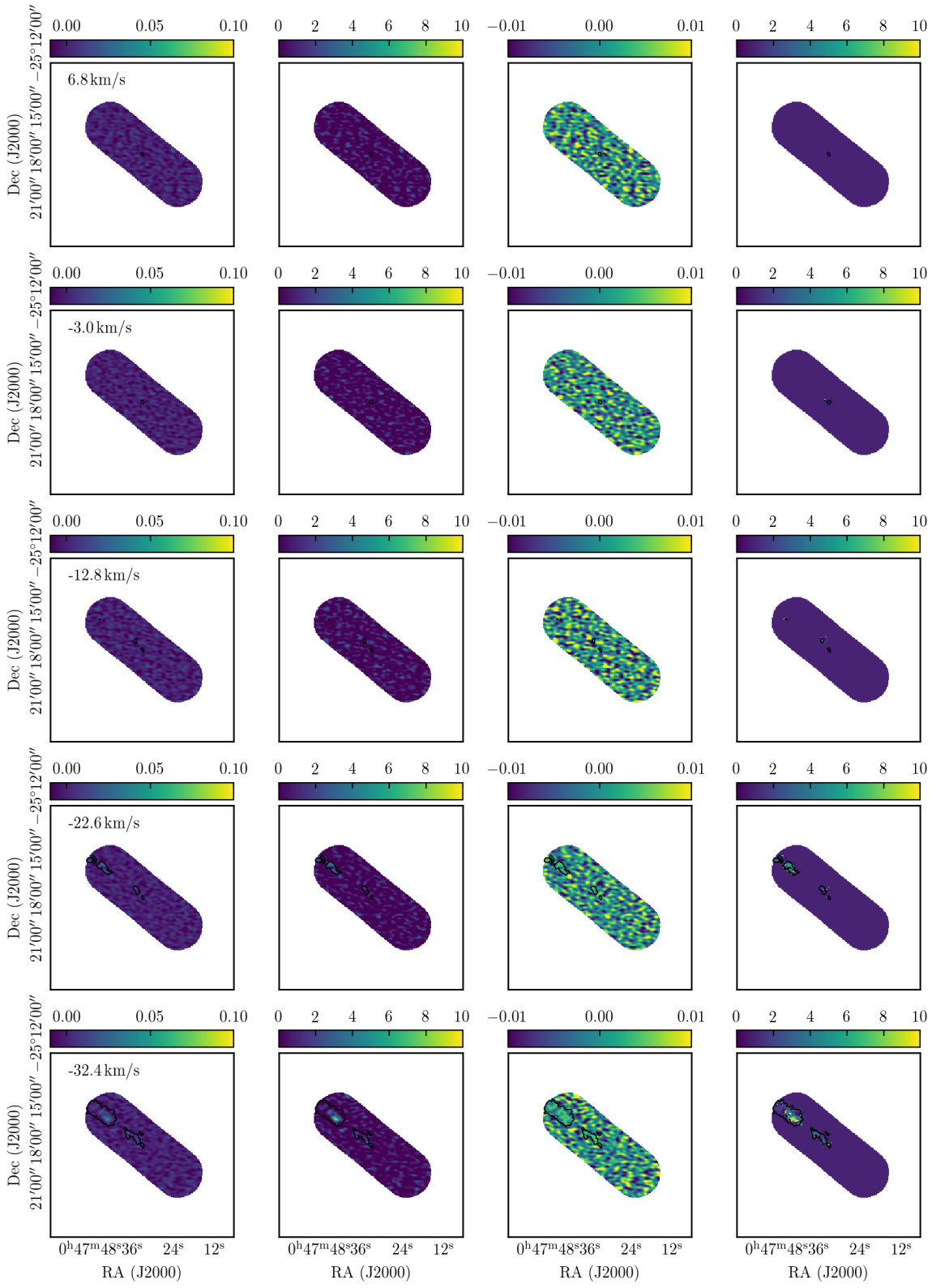

Figure B.11: Same as in Figure B.10.

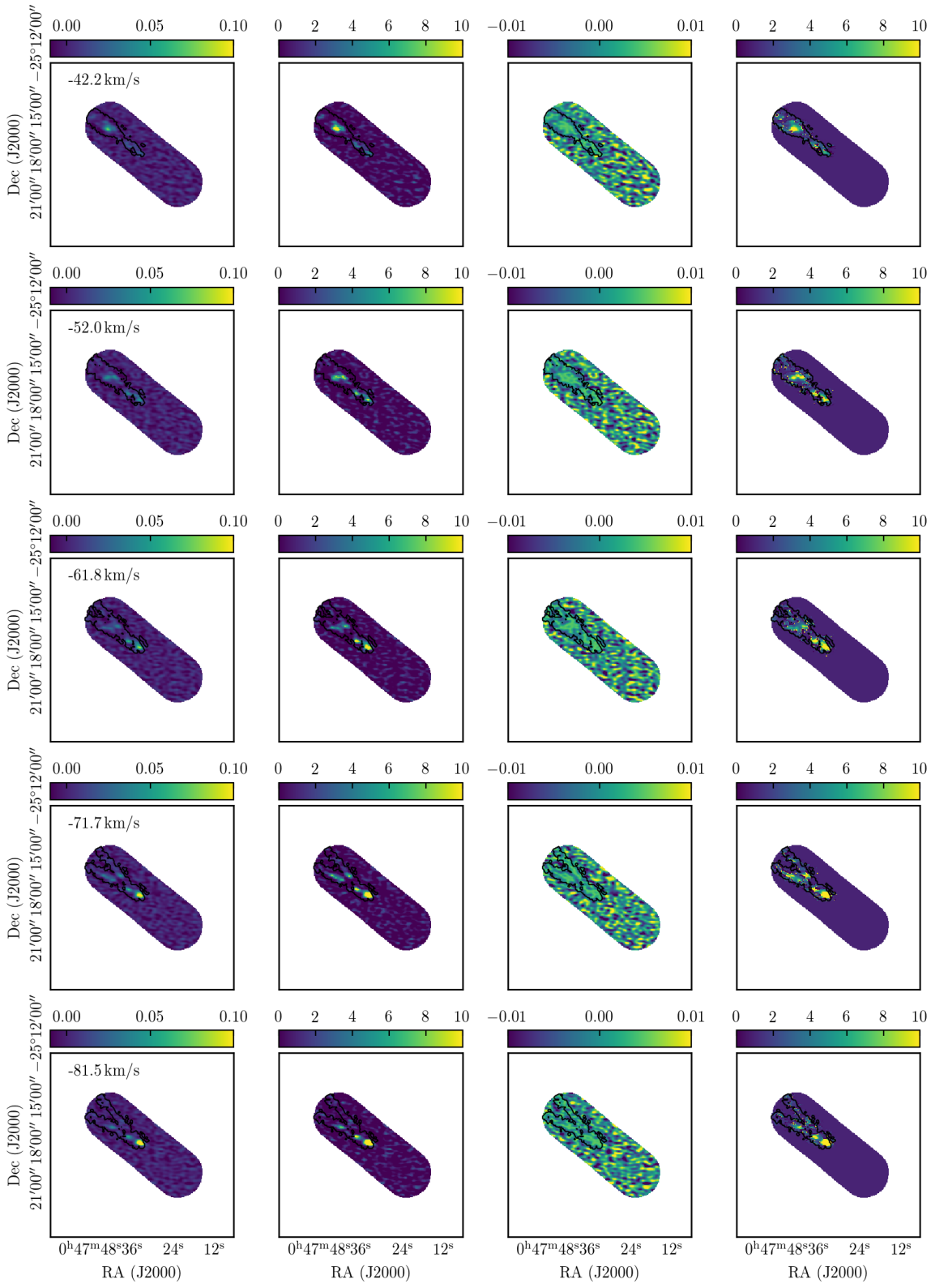

Figure B.12

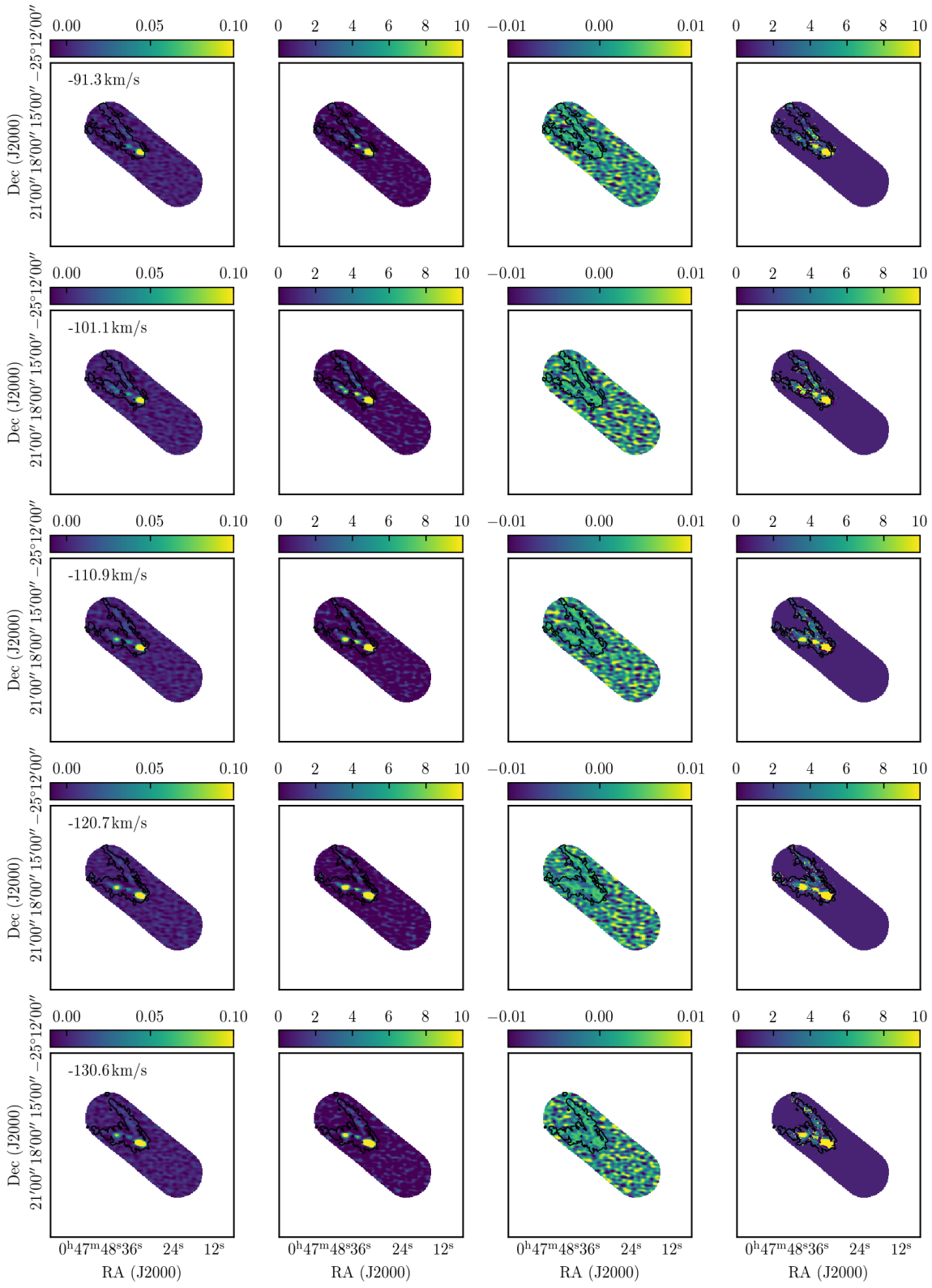

Figure B.13

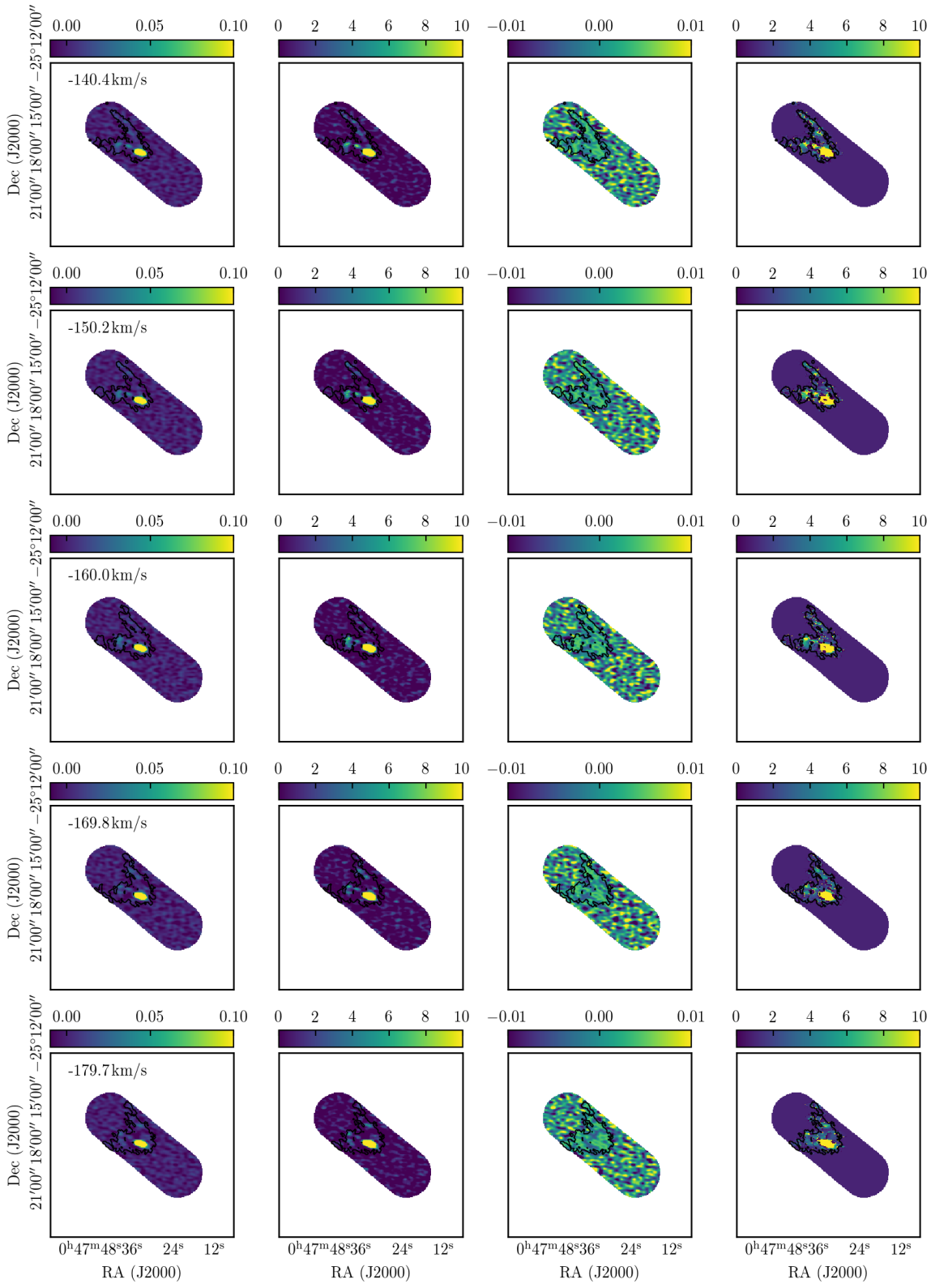
-140.4km/s
-150.2km/s
-160.0km/s
-169.8km/s
-179.7km/s
Dec (J2000)
RA (J2000)

Figure B.14

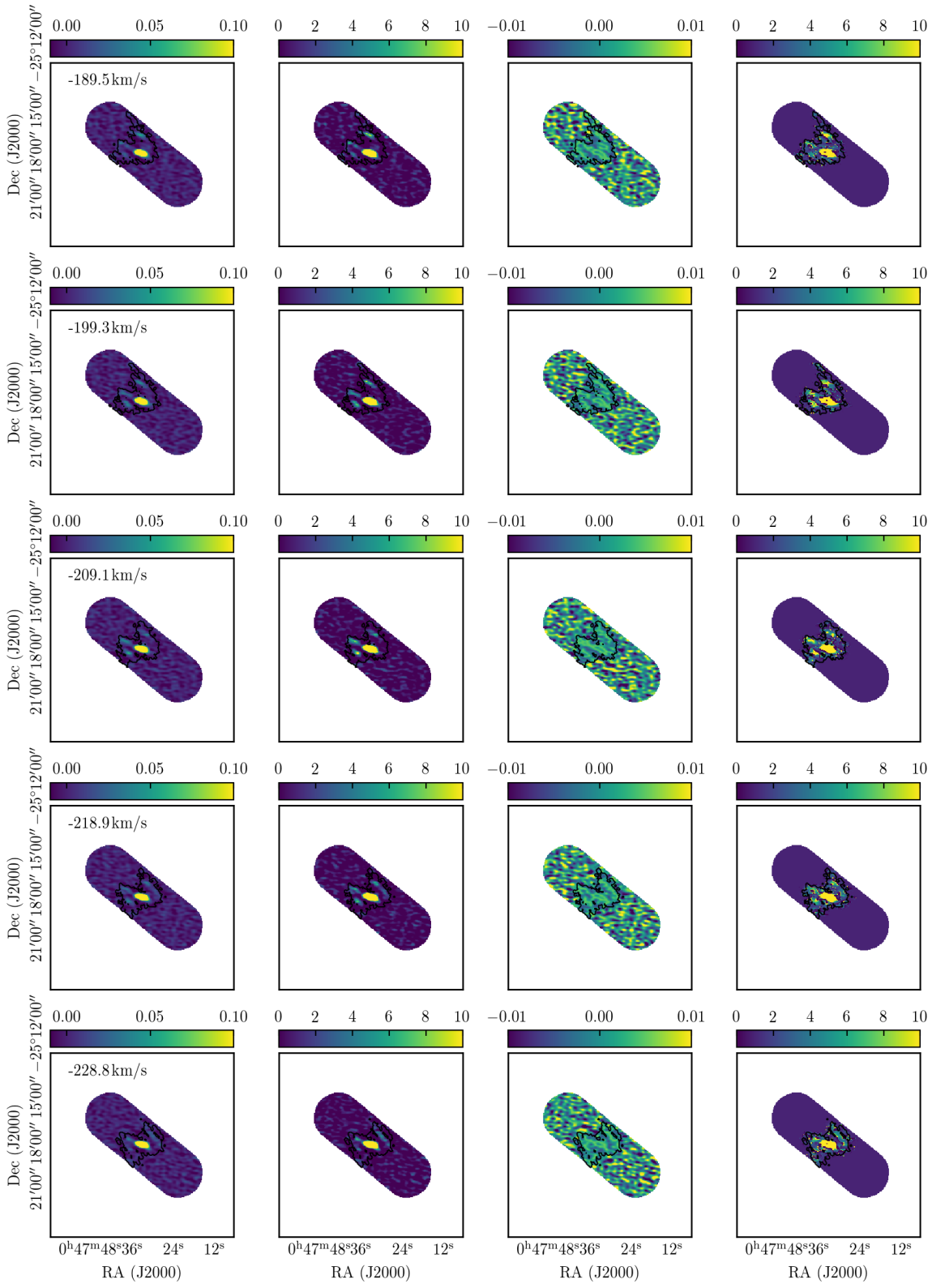
-189.5 km/s
-199.3 km/s
-209.1 km/s
-218.9 km/s
-228.8 km/s
Dec (J2000)
RA (J2000)

Figure B.15

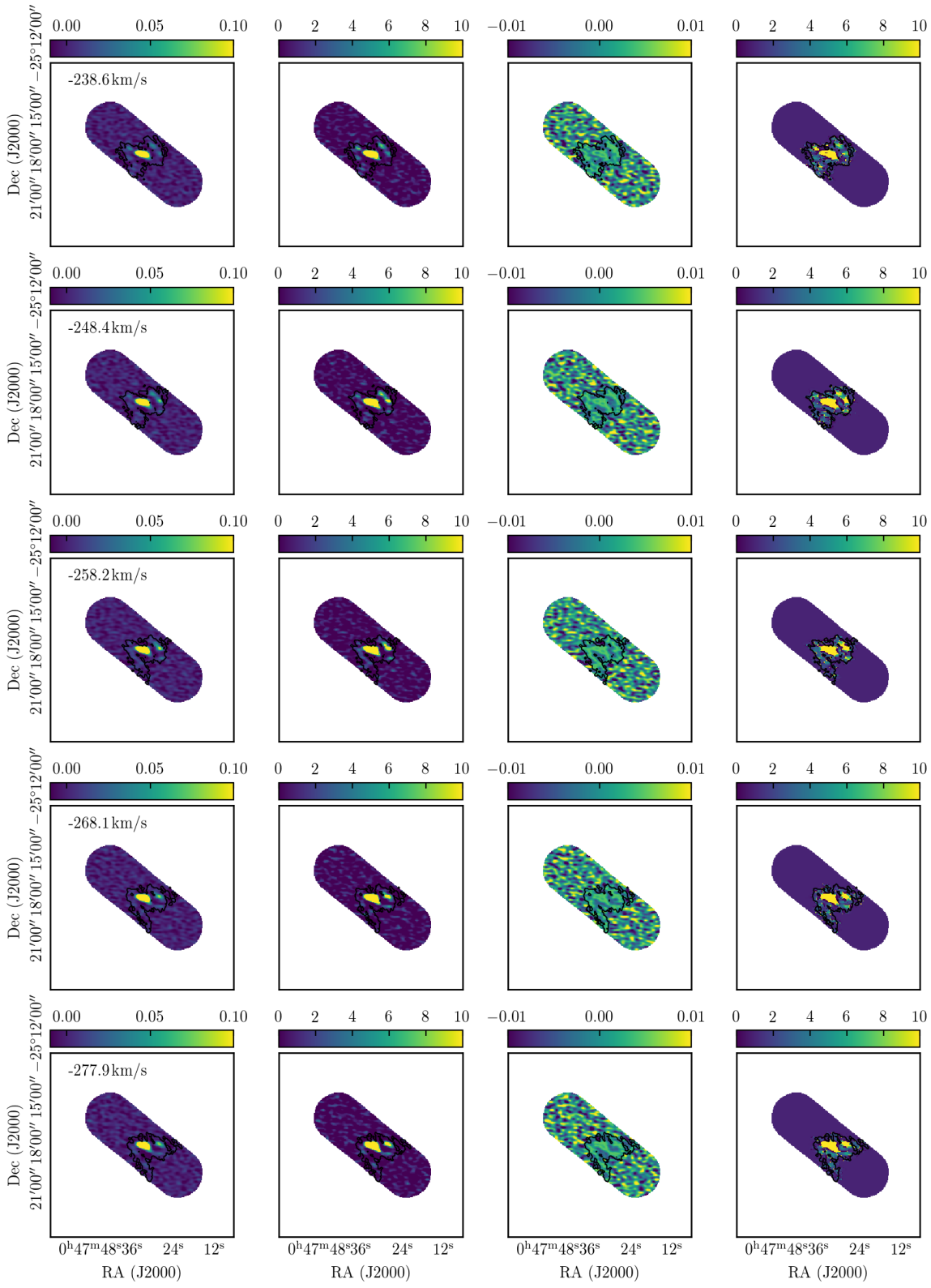
-238.6km/s
-248.4km/s
-258.2km/s
-268.1km/s
-277.9km/s
Dec (J2000)
RA (J2000)

Figure B.16

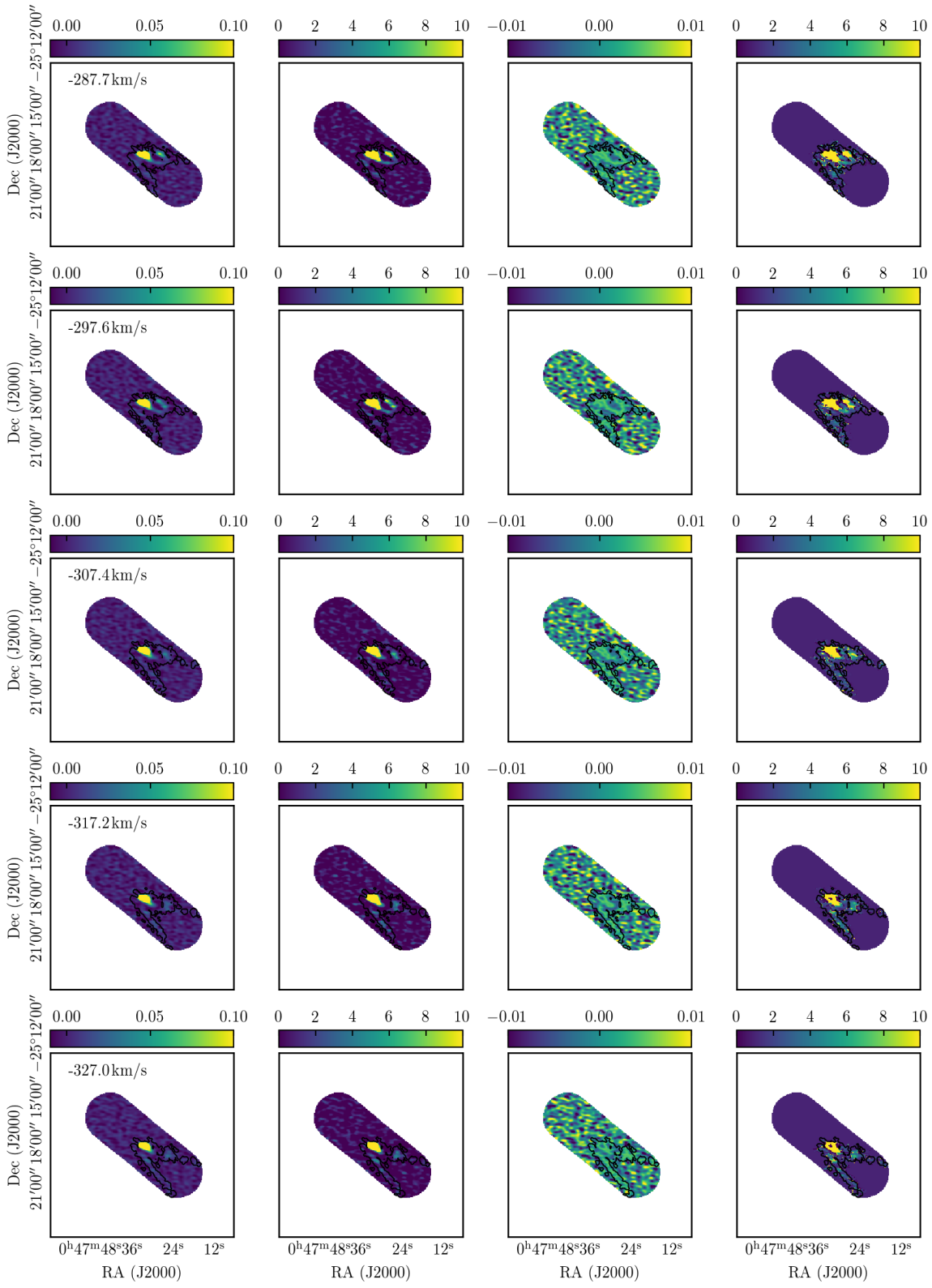
-287.7km/s
-297.6km/s
-307.4km/s
-317.2km/s
-327.0km/s
Dec (J2000)
RA (J2000)

Figure B.17

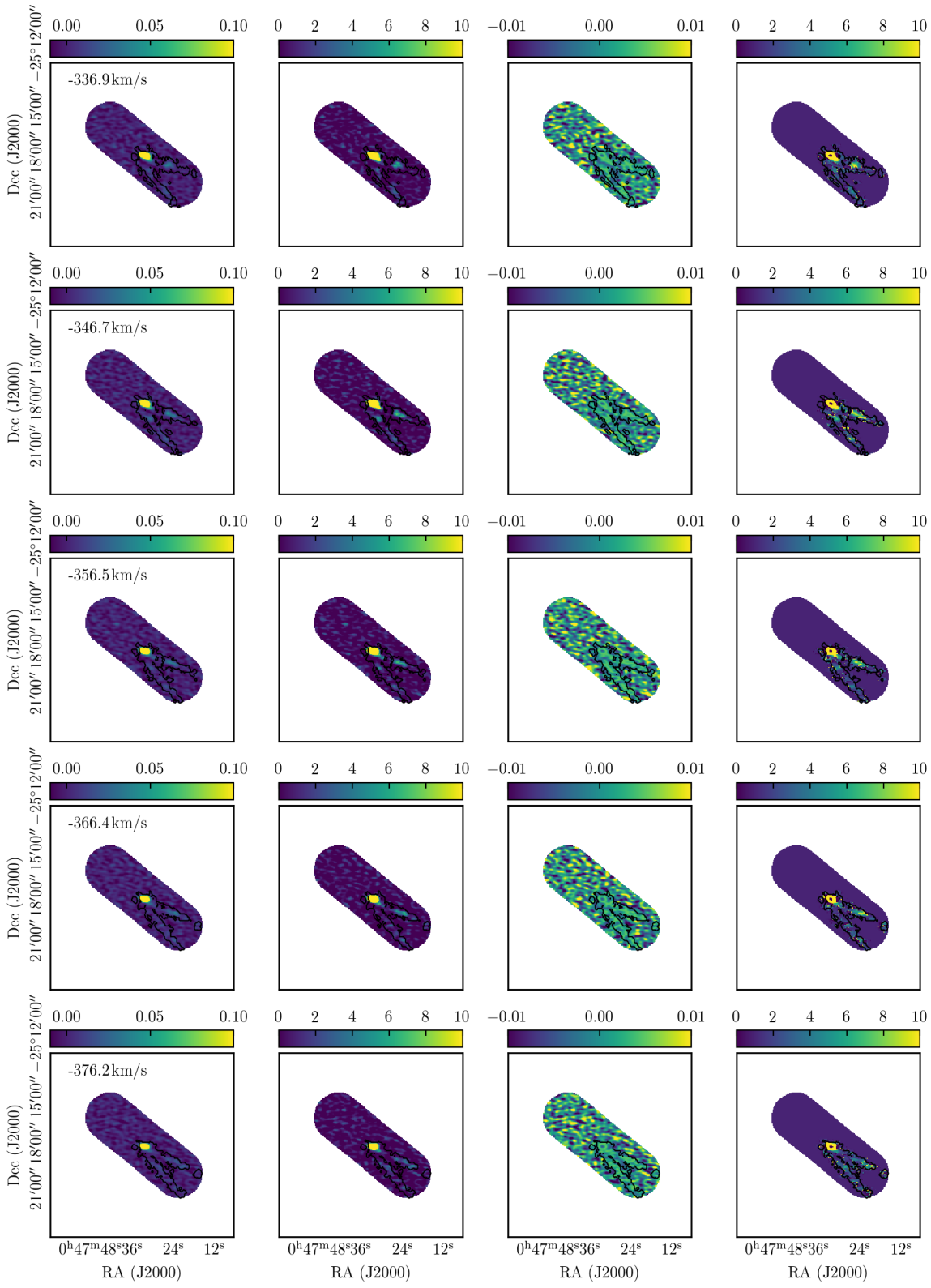
-336.9km/s
-346.7km/s
-356.5km/s
-366.4km/s
-376.2km/s
Dec (J2000)
RA (J2000)

Figure B.18

List of Figures

List of Tables

Acknowledgements

"*So long, and thanks for all the fish.*"
— Douglas Adams, "The Hitchhiker's Guide to the Galaxy"

This doctoral thesis presents a personal milestone. During the last four years of my doctoral studies, I gained significant experience: I had the chance to live in Heidelberg and Bonn, meet many people, travel to places I had never been before, and spend several weeks observing in person at IRAM 30-meter telescope and then remotely sitting in my office during holidays and weekends during the lockdowns.

I want to thank my supervisor, Prof Dr Frank Bigiel, firstly for the opportunity to do a doctoral thesis in his group, for scientific support, and for encouragment to write observing proposals, visit the IRAM 30-meter telescope and observe, co-advise master and bachelor projects.

Next, I would like to thank Dr Ashley Thomas Barnes for the outstanding scientific support, advice, encouragement to be curious, proofreading proposals, papers and thesis chapters, and for bringing excitement when discussing possible ideas for future projects. To Dr Johannes Puschnig, who taught me how to observe using IRAM 30-meter telescope, and many great discussions about science and detailed feedback every time I asked for help.

I would also like to thank all the members of Prof Dr Frank Bigiel's group. Cosima Eibensteiner, Jakob den Brok and Lukas Neumann, for numerous discussions, working on joint projects, writing proposals, and scientific support. In addition, I would like to thank all master's and bachelor's students from our group because I learned a lot by helping with their projects.

I want to thank all collaborators from PHANGS, especially Adam Leroy and Antonio Users, for being there to provide a piece of advice and scientific support.

Thanks to all my colleagues from the Argelander Institute for Astronomy and IMPRS. Time spent with all of you was precious, and Friday evenings we spent in Fiddlers, barbeques at Alter Zoll and travels is something I will never forget.

Dr Maria Jesus Jimenez-Donaire, for great support and encouragement, to not give up and give my best. To Manali Jeste, Than Hoang Dat, Ivalu Barlach Christensen, Jovana Gudžić for being there for me, for girls evenings, Harry Potter movie nights and the great time we spent together.

I want to thank Dr Jens Erler, Dr Kevin Harrington, Dr Arshia Jakob, Dr Jan Luca van de Busch, Dr Eric Jiménez Andrade and Basilio Solís Castillo and David Aguilera for being there to provide support during the writing period of this thesis. I am grateful for all the great advice you gave me and for being honest and sharing your experience with me.

Everything I have achieved so far I owe to my family and friends in Serbia. To my parents, who never questioned my choices even though I was stepping far out of my and their comfort zone, to my siblings, whose support and jokes means to me more than anything in this world, and to my boyfriend, who always supported me to pursue my dreams. To Sanja, Teodora, Neda and Zorana for always being there for me, and for teaching me to value friendships even more.

This work is based on IRAM/NOEMA observations carried out under project number W17BP, and the EMPIRE large program number 206-14 with the IRAM 30m telescope. IRAM is supported by INSU/CNRS (France), MPG (Germany) and IGN (Spain). IB would like to acknowledge the funding provided from the European Union's Horizon 2020 research and innovation programme (grant agreement No 726384/Empire).

This doctoral thesis makes use of the following ALMA data: ADS/JAO.ALMA#2015.1.00956.S and ADS/JAO.ALMA#2019.2.00236.S. ALMA is a partnership of ESO (representing its member states), NSF (USA) and NINS (Japan), together with NRC (Canada), MOST and ASIAA (Taiwan), and KASI (Republic of Korea), in cooperation with the Republic of Chile. The Joint ALMA Observatory is operated by ESO, AUI/NRAO and NAOJ. The National Radio Astronomy Observatory is a facility of the National Science Foundation operated under cooperative agreement by Associated Universities, Inc.